

**ON THE TOPOLOGY OF GLOBAL CORONAL MAGNETIC
FIELDS**

Sarah Jane Edwards

**A Thesis Submitted for the Degree of PhD
at the
University of St Andrews**



2014

**Full metadata for this item is available in
Research@StAndrews:FullText
at:**

<http://research-repository.st-andrews.ac.uk/>

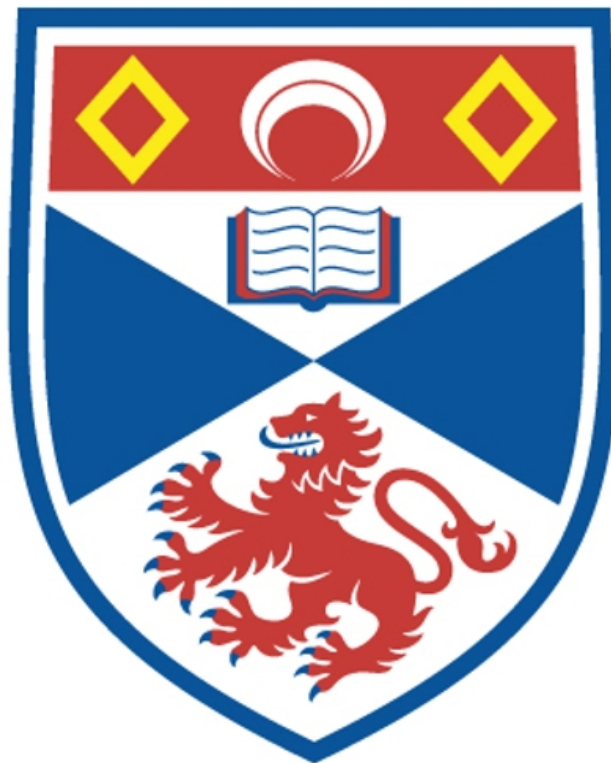
Please use this identifier to cite or link to this item:

<http://hdl.handle.net/10023/5896>

This item is protected by original copyright

On the Topology of Global Coronal Magnetic Fields

Sarah Jane Edwards



This thesis is submitted in partial fulfilment for the degree of
PhD
at the
University of St Andrews

28TH OCTOBER 2014

Abstract

This thesis considers the magnetic topology of the global solar corona. To understand the magnetic topology we use the magnetic skeleton which provides us with a robust description of the magnetic field. To do this we use a Potential Field model extrapolated from observations of the photospheric magnetic field. Various measurements of the photospheric magnetic field are used from both ground-based observatories (Kitt-Peak and SOLIS) and space-based observatories (MDI and HMI).

Using the magnetic skeleton we characterise particular topological structures and discuss their variations throughout the solar cycle. We find that, from the topology, there are two types of solar minimum magnetic field and one type of solar maximum. The global structure of the coronal magnetic field depends on the relative strengths of the polar fields and the low-latitude fields. During a strong solar dipole minimum the heliospheric current sheet sits near the equator and the heliospheric current sheet curtains enclose a large amount of mixed polarity field which is associated with many low-altitude null points. In a weak solar dipole minimum the heliospheric current sheet becomes warped and large scale topological features can form that are associated with weak magnetic field regions. At solar maximum the heliospheric current sheet is highly warped and there are more null points at high altitudes than at solar minimum.

The number of null points in a magnetic field can be seen as a measure of the complexity of the field so this is investigated. We find that the number of nulls above 10Mm falls off with height as a power law whose slope depends on the phase of the solar cycle.

We compare the magnetic topology we found at particular times with observations of the Doppler velocity and intensity around particular active regions to see if it is possible to determine whether plasma upflows at the edge of active regions are linked to open field regions.

Declarations

I, Sarah Jane Edwards, hereby certify that this thesis, which is approximately 38000 words in length, has been written by me, and that it is the record of work carried out by me, or principally by myself in collaboration with others as acknowledged, and that it has not been submitted in any previous application for a higher degree.

I was admitted as a research student in September 2011 and as a candidate for the degree of PhD in September 2011; the higher study for which this is a record was carried out in the University of St Andrews between 2011 and 2014.

Date signature of candidate

I hereby certify that the candidate has fulfilled the conditions of the Resolution and Regulations appropriate for the degree of PhD in the University of St Andrews and that the candidate is qualified to submit this thesis in application for that degree.

Date signature of supervisor.....

In submitting this thesis to the University of St Andrews I understand that I am giving permission for it to be made available for use in accordance with the regulations of the University Library for the time being in force, subject to any copyright vested in the work not being affected thereby. I also understand that the title and the abstract will be published, and that a copy of the work may be made and supplied to any bona fide library or research worker, that my thesis will be electronically accessible for personal or research use, and that the library has the right to migrate my thesis into new electronic forms as required to ensure continued access to the thesis. I have obtained any third-party copyright permissions that may be required in order to allow such access and migration. No embargo on print or electronic copies.

Date signature of candidate.....

signature of supervisor.....

Acknowledgements

I would like to thank first of all my supervisor, Clare Parnell, for all her help with all my PhD studies. Secondly, I would like to thank Solmaz, Gordon, Karen, Greg and Julie who have made studying in St Andrews such a fantastic experience.

I would like to thank my family for all their support. In particular I would like to thank my mum for inspiring me to continue to study. I would also like to thank my Dad, and wish he could be here to see me finish.

Finally, I would like to thank my husband, Harri. I really could not have done any of this without him. Thank you, Harri, for listening to all my moaning and helping motivate me through the second year blues.

"All your people must learn before you can reach for the stars."
-Captain Kirk, Gamesters of Triskellion

Publications

The following published paper includes material from Chapters 3 and 4 of this thesis (published in my maiden name, S. J. Platten):

- S. J. Platten, C. E. Parnell, A. L. Haynes, E. R. Priest and D. H. Mackay. “The solar cycle variation of topological structures in the global solar corona”, *Astron. Astrophys.* Volume 565, 2014

Contents

1	Introduction	1
1.1	Solar cycle	4
1.2	Active regions	6
1.3	Solar wind	8
1.4	Magnetic Field Structure - An Overview	12
1.4.1	Maxwell's Equations and Ohm's Law	12
1.4.2	Null Points	14
1.4.3	The Magnetic Skeleton and Separators	16
1.4.4	Quasi-separatrix surfaces	18
1.4.5	Magnetic reconnection	18
1.5	Outline	19
2	Models and Methods	21
2.1	Force-free models	21
2.2	Potential Field Source Surface Model	23
2.3	Magnetogram data	26
2.3.1	Kitt-Peak data	26
2.3.2	Michelson Doppler Imager (MDI) data	28
2.3.3	Heliospheric Magnetic Imager (HMI) data	28
2.4	Finding the magnetic topology of our global potential field models	29
2.4.1	Trilinear method for finding null points	29
2.4.2	Finding null-point properties	33
2.4.3	Method for finding separatrix surfaces	34
3	Topological Configurations in the Global Solar Corona	35
3.1	HCS and HCS curtain	35
3.2	Pseudostreamers	36
3.3	Bald-patch separatrix surfaces	38
3.4	Global separatrix surface structures	39
3.4.1	Separatrix domes	39
3.4.2	Separatrix Curtains	40
3.4.3	Separatrix caves and tunnels	41
3.5	Example Topological Structures in Global Magnetic Fields	43

3.5.1	Separatrix dome from one separatrix surface	43
3.5.2	Separatrix dome from two separatrix surfaces	46
3.5.3	Separatrix cave	48
3.5.4	Separatrix tunnel	50
3.5.5	Closed separatrix curtain from one null point	50
3.5.6	Transition from a single pseudostreamer to a double helmet streamer	52
4	Solar Cycle Variations of Topological Properties	57
4.1	Motivation	57
4.2	Magnetogram data	58
4.3	Typical solar maximum and solar minimum global topology	59
4.3.1	Typical solar minimum topologies	61
4.3.2	Typical Solar Maximum Topology	70
4.4	Cycle variations in topological properties	73
4.4.1	Tilt angle of the HCS	73
4.4.2	Closed separatrix curtains	75
4.4.3	Null Points	77
4.4.4	Separators	80
4.5	Discussion	83
5	Long-term Trends in Topological Structures	85
5.1	Isolated separatrix domes from one null and open separatrix surfaces	86
5.2	Null-Separator networks	88
5.3	Classifying topological structures	94
5.3.1	Double caves	96
5.3.2	Dome-Tunnels	98
5.4	Discussion	99
6	Data Comparison	101
6.1	Magnetogram data	101
6.2	SOLIS high-res vs. low-res	101
6.2.1	Solar minimum comparison - CR2083	102
6.2.2	Solar maximum comparison - CR2130	107
6.2.3	Quantitative comparison of low-resolution and high-resolution structures	112
6.2.4	Temporal comparison	114
6.3	Conclusions	116
7	Null point distribution and density	121
7.1	Null point column density with time	123
7.2	Null point column density	123
7.3	Statistical analysis of null point distribution	126
7.4	Null volume density variation with height	132

7.4.1	Null butterfly diagrams	135
7.5	Example Carrington rotations	137
7.5.1	MDI, SOLIS and HMI extrapolations comparison - CR2100	137
7.5.2	MDI sample Carrington rotations	141
7.6	Conclusions	145
8	Open Fields Around Active Regions	147
8.1	Introduction	147
8.2	PFSS extrapolations from HMI	148
8.3	Active Regions and Observational Data	149
8.4	AR11271 - 21st August 2011	149
8.5	AR11419 - 17th February 2012	150
8.6	AR11427 - 2nd March 2012	153
8.7	AR11445 - 28th March 2012	157
8.8	AR11553 29th August 2012	161
8.9	AR11569 15th September 2012	164
8.10	AR11575 23rd September 2012	164
8.11	Discussion and Conclusions	168
9	Summary and Future Work	171
9.1	Topological Configurations and Cycle Variations	171
9.1.1	Future work	172
9.2	Null point statistics	173
9.2.1	Future work	173
9.3	Active region topology	173
9.3.1	Future Work	174

Chapter 1

Introduction

The Sun is the star at the centre of our solar system. It is approximately 4.5 billion years old and has a mass of about 2×10^{30} kg which accounts for over 99% of the total mass of the solar system [Priest, 1982]. In terms of stars, the Sun is not unusual, however its proximity to the Earth enables us to study it in much greater detail than other stars.

People have been observing the Sun in an astronomical sense for millennia, through eclipse and naked-eye sunspot observations. Since the invention of the telescope and more recently with satellite capability, interest in observations of the Sun has rocketed. During the last twenty years we have gained the ability to produce high-resolution images from the Sun in many different wavelengths, as well as measurements of the solar surface magnetic field and in-situ measurements of plasma composition, velocity and magnetic field in the heliosphere from a variety of space missions.

At the centre of the Sun nuclear fusion takes place fusing hydrogen together to form helium and other heavier elements. This occurs in the *core* which is very hot, approximately 1.5×10^7 K, and very dense, approximately 1.6×10^5 kg m⁻³ [Priest, 1982]. The core extends out to about a quarter of the Sun's radius. The fusion processes in the core release a great deal of energy which is transported to the solar surface, first through radiation out from the core to about $0.7R_{\odot}$ (where R_{\odot} is the radius of the Sun which is approximately 696Mm) through a region known as the *radiative zone*. Following that, this energy is transported via convection to the solar surface through the *convective zone* and then out into the solar atmosphere above. The high pressure in the core and the radiative zone cause them to rotate as a solid body, but the convective zone and the solar atmosphere can rotate as a fluid. These layers rotate at a speed that varies with latitude according to a profile known as *differential rotation* that is fastest at the equator and slowest at the poles. This means that between the radiative and convective zone in a layer known as the *tachocline* there is a steep velocity gradient which is believed to play an important role in generating the solar magnetic field [Deluca and Gilman, 1991].

Above the convective zone is the solar atmosphere which consists of four layers: the photosphere, chromosphere, transition region and corona. The solar atmosphere and

its magnetic field is the focus of this thesis. The lowest layer of the solar atmosphere is the *photosphere*. This layer, similar to the interior of the Sun, is optically thick, unlike the rest of the atmosphere above and hence it is called the surface of the Sun. The photosphere is a thin layer just 500km deep and has a density of $4 \times 10^{-7} \text{ g cm}^{-3}$ and a temperature of about 6000K. It can be observed in white light and also a range of different wavelengths from which measurements of the photospheric magnetic field can be taken.

The next layer is a couple of megametres thick and is known as the *chromosphere*. Here the density drops to $8 \times 10^{-8} \text{ g cm}^{-3}$, which allows light to pass through. The temperature falls off in the chromosphere to around 3800K. Between the chromosphere and the *corona*, which stretches out into interplanetary space, is a layer known as the transition region where the temperature rises steeply to reach temperatures of the order of 10MK in the low corona [Aschwanden, 2005]. Plasma at these temperatures can be observed in various Extreme Ultra-Violet (EUV) wavelengths. Further above the temperature begins to fall off again. Through the solar atmosphere the density falls off rapidly, dropping to about $10^{14} \text{ g cm}^{-3}$ in the low corona [Gibson, 1973].

In both the solar interior and the solar atmosphere the high temperatures are sufficient to ionise the gases present such that they become a *plasma*. This means charged particles are present which carry an electric current and gives rise to a magnetic field. It is the magnetic field in the solar atmosphere that this thesis considers.

Figure 1.1 shows various observations of the solar atmosphere from the 20th June 2014 taken by the Atmospheric Imaging Assembly (AIA) and the Heliospheric Magnetic Imager (HMI) aboard the Solar Dynamics Observatory (SDO) satellite. The radial component of the photospheric magnetic field is shown in Figure 1.1a, field going into the sun is black and out of the sun is white. The strong black and white patches are *active regions* and the weak dappled areas are known as the *quiet sun*. There is also a weaker dipolar magnetic field aligned in the north south direction present.

Figure 1.1b shows a white light image of the Sun. Two small blemishes can be seen on the solar disc and these are known as *sunspots*. Plasma at chromospheric temperatures can be viewed in a wavelength of 304 \AA , Figure 1.1c. In this wavelength we can see *prominences* which are volumes of cool plasma that are suspended above the solar surface by the magnetic field. These can be seen on the limb or as dark lines on the solar disc, where they are sometimes referred to as *filaments*. Such structures can become unstable and erupt releasing energy and plasma. Prominence eruptions are one type of *Coronal Mass Ejection* (CME) which is a dynamic event that involves an ejection of a large amount of matter into the solar wind.

Figure 1.1d and e show plasma at coronal temperatures. Here we can see bright magnetic field loops that connect within active regions. Also, visible are dark patches of the solar surface, these are known as *coronal holes* and correspond to regions where field lines are open into interplanetary space.

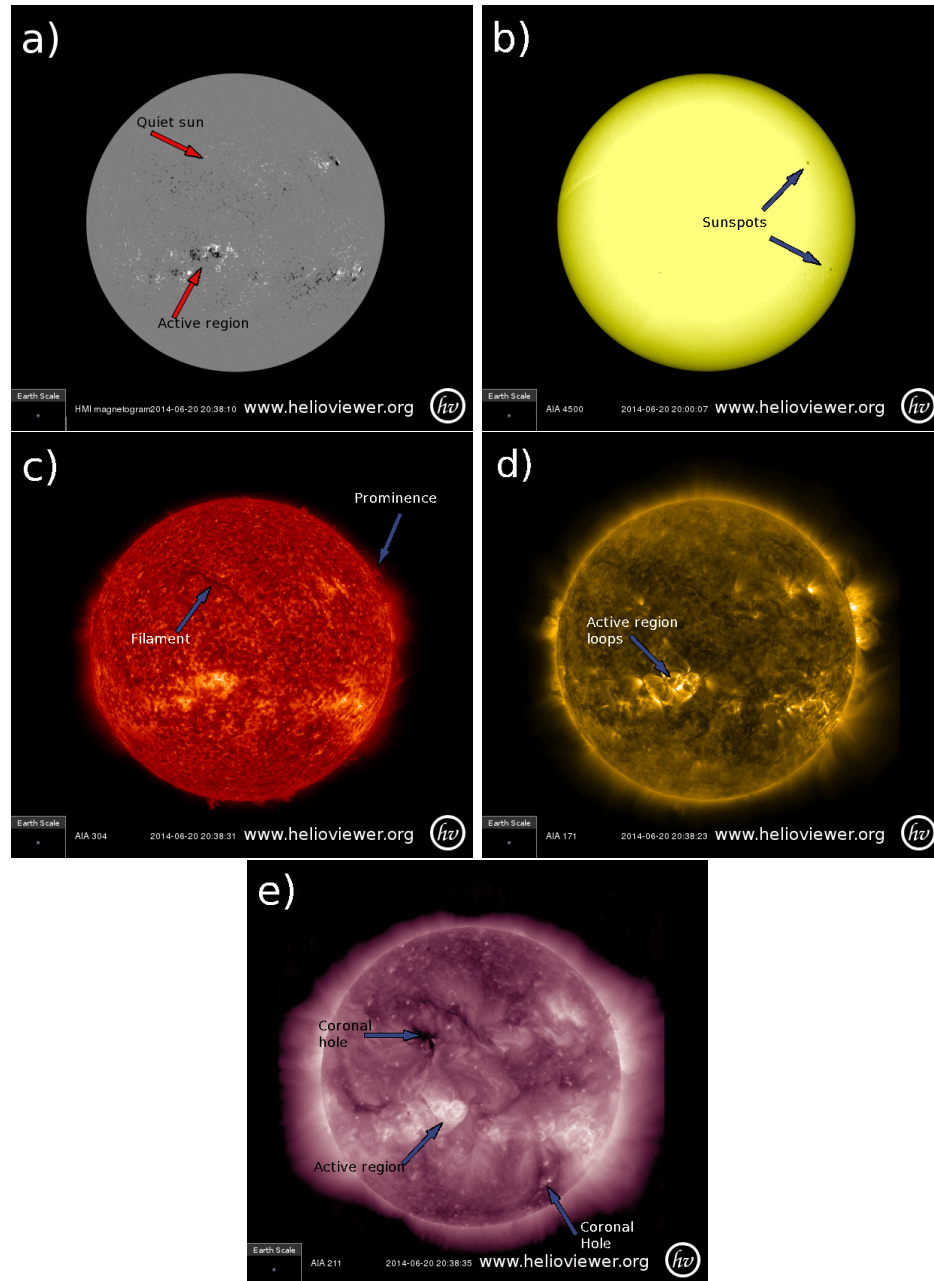


Figure 1.1: Observations of the solar surface and atmosphere from AIA and HMI. (a) shows the full disc magnetogram, (b) 4500 Å, (c) 304 Å, (d) 173 Å and (e) 211 Å. Images from helioviewer.org.

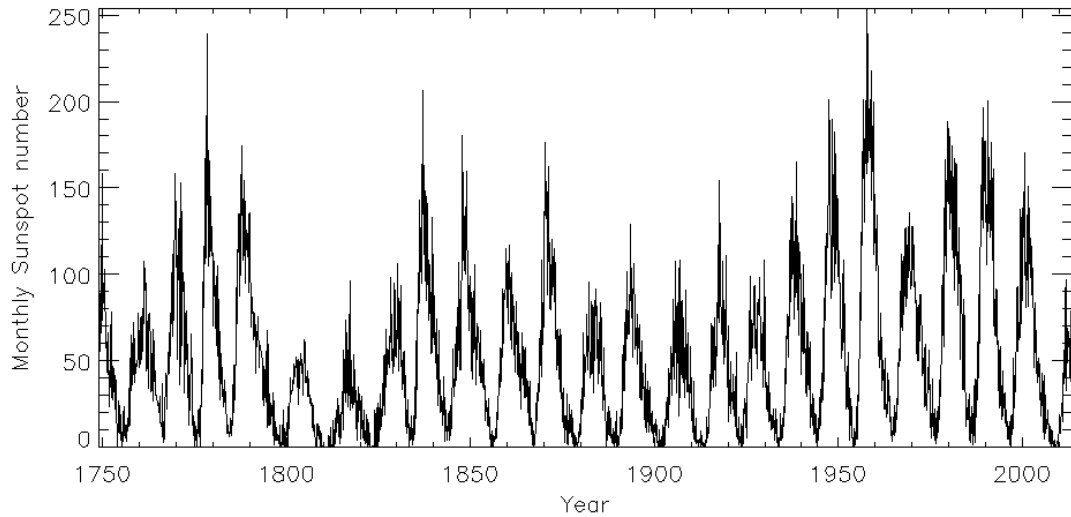


Figure 1.2: Graph of the number of sunspots recorded per month since 1749. Data from the Royal Greenwich Observatory up until 1977 and then afterwards from the US Air Force Solar Optical Observing Network: http://solarscience.msfc.nasa.gov/greenwch/spot_num.txt.

1.1 Solar cycle

It has been known for over a century that the amount of activity on the Sun changes over time with a periodic nature [Schwabe, 1844]. Ever since the invention of the telescope there has been a record of the numbers of sunspots observed on the solar disc each day. This record shows a clear periodicity with a period of approximately 11 years (see Figure 1.2), although each cycle has its own characteristics which vary, including the length which can be as long as 15 years [e.g., Hathaway, 2010]. The period of time when the sunspot number is at its highest is called *solar maximum*. There are various estimates of when the peak of each solar maximum occurs and these usually range within a couple of years [e.g., Hathaway, 2010]. Similarly, the time when the sunspot number has a local minimum is called *solar minimum*. Solar minima can often last slightly longer than maxima. During every solar maximum the polarity of the dipole magnetic field of the Sun changes [e.g., Hathaway, 2010]. For the Sun to go through a complete magnetic polarity change, and return to the dipolar configuration with which it started, takes two 11 year solar cycles, so the *magnetic solar cycle* is around 22 years [Babcock, 1959].

Although the length of the solar cycle is usually approximately 11 years, the amount of activity in each solar maximum, the number of spotless days at each solar minimum and the length of the solar cycle (within a couple of years) varies. In the current cycle (cycle 24) there have been relatively few sunspots present at solar maximum in comparison with the previous three solar cycles (see Figure 1.2). Since

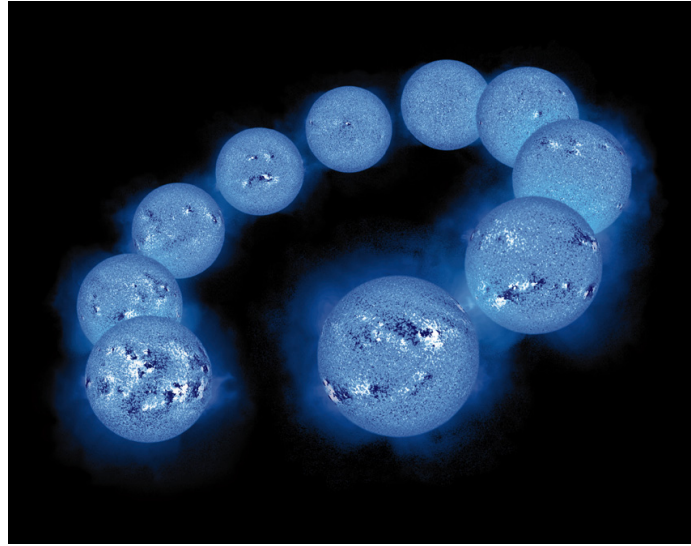


Figure 1.3: Images of the photospheric magnetic field taken at one year intervals throughout the solar cycle. Image Credit: Lockheed Martin Solar & Astrophysics Lab, Yohkoh SXT and Kitt Peak National Solar Observatory (http://www.nasa.gov/images/content/150799main_magcycle.jpg).

sunspot records began there have been several long periods when there have been consecutive cycles having very few or no active regions at solar maximum. Notably, between 1645 and 1715, there were very few sunspots observed. This period is known as the *Maunder Minimum* [Eddy, 1976] and corresponded to a period of much lower than average temperature in most of Europe. Although the connection between solar activity and temperature on Earth is still an open question, it is clear changes in solar activity can effect the climate here on Earth [Haigh, 2007]. Another example of a period of low activity is the *Dalton Minimum* that occurred at the beginning of the 19th Century (see Figure 1.2), however it should be noted that during the Dalton minimum the numbers of sunspots still varied considerably with a clear solar cycle modulation whereas in the Maunder minimum this did not happen. It is also possible to look back further than the invention of the telescope by examining, for example, the levels of the isotope carbon-14 collected in wood or proxy measurements of the cosmic ray flux [Usoskin, 2013]. Sustained periods of low solar activity or *grand minima* occur with reasonable frequency although with no apparent periodicity [Usoskin, 2013].

The magnetic field of the Sun (the cause of sunspots, as described in the next section) varies dramatically throughout the solar cycle. Figure 1.3 shows the variation in the observed magnetic field on the solar disc with one snapshot per year throughout an eleven year cycle. Black indicates field directed into the Sun and white indicates field directed out of the Sun. The strongest magnetic field regions correspond to the location of sunspots. These are primarily seen at cycle maximum whereas at cycle minimum there are few or none of these regions and the solar surface is covered with a dappling of weak, mixed-polarity magnetic field known as the *quiet sun*.

1.2 Active regions

The solar surface often has regions where the magnetic field is much stronger than the surroundings (see Figure 1.3), during solar maxima there can be many of these regions and during solar minima there are few or none. These regions are known as *active regions* and are often associated with sunspots. Active regions occur when convective motions in the interior cause loops of magnetic flux to emerge through the photosphere into the corona, as such they often appear on the photosphere as a large bipolar region (see Figure 1.4b).

In the corona the field lines connecting regions of opposite polarity form loops. Loops associated with active regions can be filled with plasma which is often much hotter than the surrounding plasma, reaching temperatures greater than 2MK [Aschwanden, 2005].

On the photosphere the foot-points of the active region loops are cooler than the surrounding plasma. This means that when larger active regions are viewed in white light they appear as visible blemishes on the solar disc that are darker than their surroundings and are referred to as *sunspots*.

The most westerly pole¹ of the bipole is known as the *leading polarity* due to the direction of the solar rotation. The orientation of the bipole usually follows two rules: *Joy's Law* and *Hale's Law* [Hale et al., 1919]. Joy's Law states that the leading polarity of the bipole will be closer to the equator than the following polarity and Hale's law states that the leading polarity will be the same polarity as the pole in the hemisphere in which it emerges (see Figure 1.4a). Hale's Law also implies that bipoles emerging on opposite sides of the equator will have opposite leading polarities. The line between regions of opposite polarity across which the gradient of the radial magnetic field component is maximised is called the *polarity inversion line* (PIL) and the tilt of the active region can sometimes be described by the tilt of the PIL.

It should be noted that bipoles do not always emerge with the orientation suggested by Joy's and Hale's law. Occasionally subsurface motions can twist the emerging flux so the bipole emerges contrary to these laws.

As well as the number of active regions changing through the solar cycle the location of active regions also changes. We can see this in a *magnetic butterfly diagram* (Figure 1.5). A butterfly diagram is produced by averaging the signed radial component of the magnetic field at the photosphere over all longitudes for each latitude and plotting this against time. A latitude that has a strong magnetic feature of either positive or negative polarity will appear white or black, respectively.

From Figure 1.5 we can see that active regions begin emerging at about 40° latitude at the start of the cycle and as the cycle progresses they emerge closer to the equator. This phenomenon is sometimes known as *Spörer's Law* [Maunder, 1903] and is thought to be brought about by the wrapping of subsurface magnetic field around the sun as the cycle progresses due to *differential rotation* [Gibson, 1973]. At the

¹It should be noted that on the Sun, when looking from earth, west is to the right of the solar disc and east is to the left

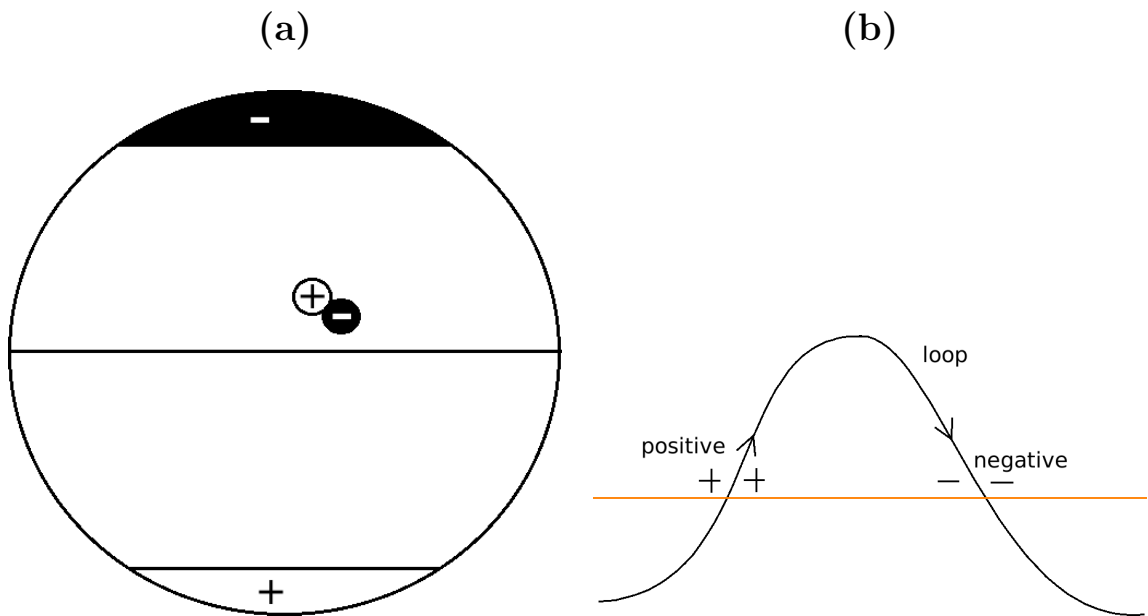


Figure 1.4: (a) Diagram of a bipole emerged in the Northern hemisphere which in this instance has a negative pole and following Joy's Law and Hale's Law. (b) Diagram of loop of magnetic field protruding through the photosphere to produce a bipole field.

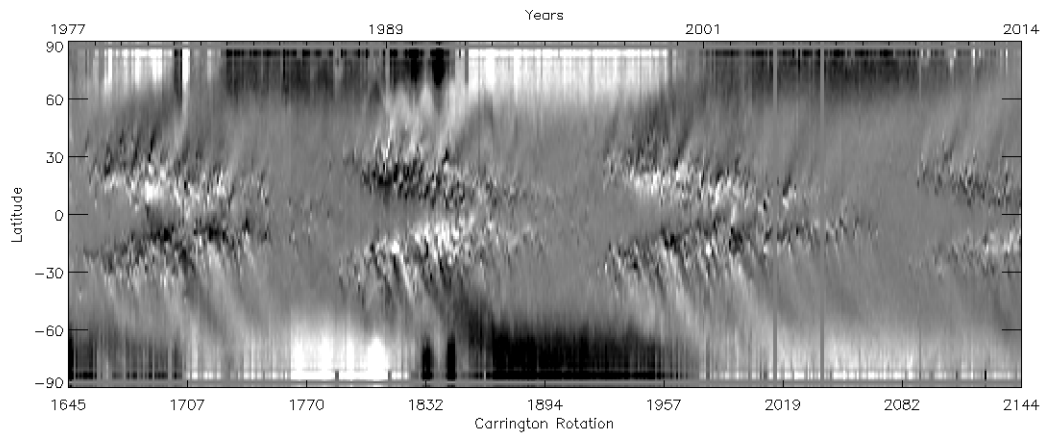


Figure 1.5: Magnetic Butterfly diagram of the average signed radial magnetic field over all longitudes for each latitude and for each Carrington rotation over the last 3 solar cycles. Data from National Solar Observatory Kitt-Peak.

start of some cycles active regions start emerging in one hemisphere before the other (e.g., in cycle 24 active regions emerged in the northern hemisphere before the south, see Figure 1.5 circa Carrington rotation 2090).

Figure 1.5 also shows Joy’s and Hale’s Laws. The inner edge of the “wings” of the butterfly in each hemisphere are always of the same polarity as the pole in that hemisphere at the start of the cycle. This is formed by the cumulative effect of the emergence of active regions with tilt according to Joy’s Law and polarity according to Hale’s Law.

Once the active regions have emerged they evolve due to flux cancellation (the mutual loss of flux from neighbouring flux regions of opposite polarity), coalescence (the combining of two neighbouring flux features of the same sign into one large feature) and fragmentation (the splitting up of one flux feature into two or more smaller features). These processes ultimately lead to dispersal of the active region. Meridional flow pushes the higher latitude magnetic elements poleward (see streaks in Figure 1.5). Joy’s law tells us that the part of a large magnetic feature that is closest to the pole will be of the opposite polarity to the flux in the pole towards which it is being pushed. Therefore when the remnants of the trailing polarity reach the poles it causes cancellation of flux eventually leading to polar field reversal at cycle maximum [Babcock, 1961]. This can be seen in the black and white bands at the poles in Figure 1.5. The leading sunspots from each hemisphere disperse across the equator where they too cancel.

1.3 Solar wind

There is a constant stream of plasma leaving the Sun along field lines that extend out into interplanetary space. This stream is known as the *solar wind*.

The solar wind as we know it was first discovered through observations in the 1950s by Biermann of comet tails that stream away from the Sun rather than behind the trajectory of the comet [Biermann, 1951, 1957]. Previously, it had been noticed that particles stream out from the Sun intermittently. In particular, Carrington noted in 1859 that following the very large flare he observed in white light there was an increase in auroral activity which was already understood to be correlated with geomagnetic disturbances [Carrington, 1859, Hodgson, 1859].

Magnetic field lines anchored in the photosphere can either map to other points in the photosphere (such field lines are referred to as *closed*) or extend out into interplanetary space in which case they are referred to as *open*. It is the plasma on these open field lines that gives rise to the solar wind. When the corona is observed in certain extreme ultra-violet (EUV) wavelengths the areas of open field appear as dark patches since the density of plasma along these field lines is lower than along closed field lines. Hence, these dark open-field regions are often termed *coronal holes*. However, it is important to note that the term “coronal hole” refers to an observed phenomenon seen in images of the solar corona and so when describing the behaviour

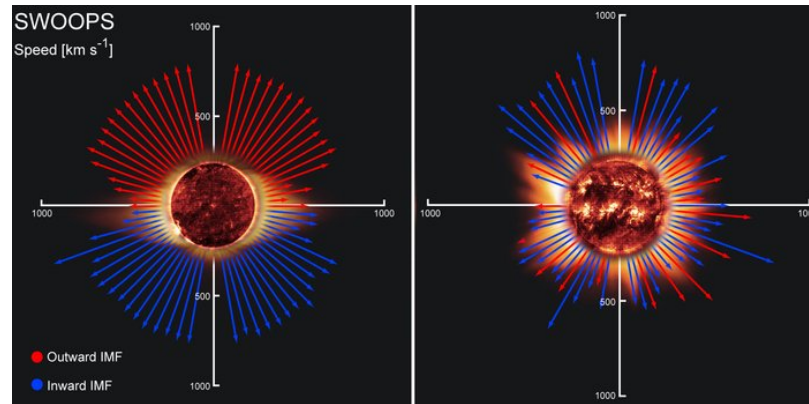


Figure 1.6: Schematic of measurements taken of the solar wind speed during solar minimum on the first orbit of ULYSSES (left panel) and solar maximum on the second orbit of ULYSSES (right panel). Image credit: http://www.esa.int/spaceinimages/Images/2008/06/Solar_wind_speeds_measured_by_Ulysses

of the magnetic field we will always refer to places where the magnetic field is open as *open-field regions*.

The first solution for a solar wind came from Parker [1958] who sought to find an analytic solution for the expanding corona. The solution he derived predicted a supersonic solar wind. This was confirmed by the observations of the Mariner 2 spacecraft in 1962 [Neugebauer and Snyder, 1962].

Parker's model assumed an isothermal plasma and a radially expanding solar wind. A consequence of this is that a faster than radial expansion (for example along expanding flux tubes) would produce a faster solar wind and hence that open magnetic flux tubes that had a large expansion factor would produce the highest solar wind speeds. However, observations have since indicated that this is not the case. Since then, more realistic solutions have been found for the solar wind that allow the temperature to vary as it does in the corona [e.g., Meyer-Vernet, 2007].

A key space mission for investigating the solar wind was the ULYSSES mission which was launched in 1990 and during its period of operation carried out three polar orbits of the Sun. The first orbit was during the minimum at the end of solar cycle 22 (Figure 1.6 left panel), the second during the maximum of cycle 23 (Figure 1.6 right panel) and the third during the minimum following cycle 23. There are two types of solar wind: the fast solar wind has speeds of around 700km/s and the slow solar wind has typical speeds of around 450km/s. ULYSSES showed that the fast solar wind is fastest at solar minimum when it emanates from the large polar coronal holes (see Figure 1.6 left panel). At solar minimum the slow wind is present around the streamer belt near the equator. At solar maximum the fast wind is typically slower with spikes of fast and slow wind originating from all over the Sun (Figure 1.6 right panel). The magnetic field at the polar regions at solar minimum have a relatively low expansion factor in comparison to the open field regions at solar maximum. Since

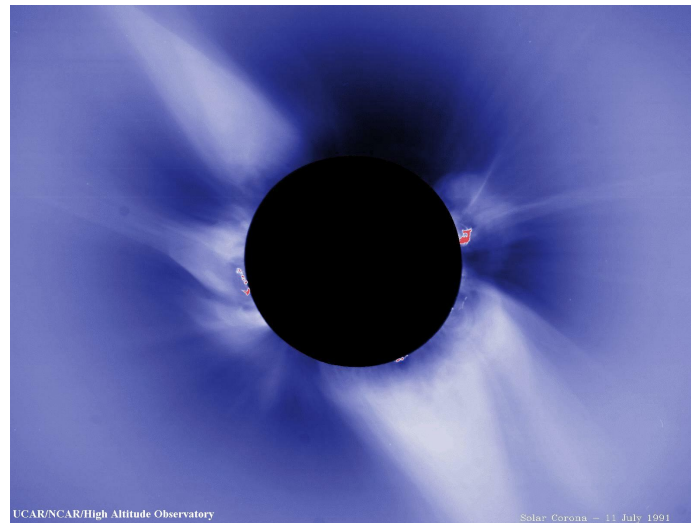


Figure 1.7: Image of the corona in white light from 11th July 1991 which was in the decline phase of solar cycle 22. The helmet streamer belt can be seen as the white tilted structure. Image credit: <http://solarscience.msfc.nasa.gov/corona.shtml>

the solar minimum shows the highest solar wind speeds this contradicts the Parker solar wind model.

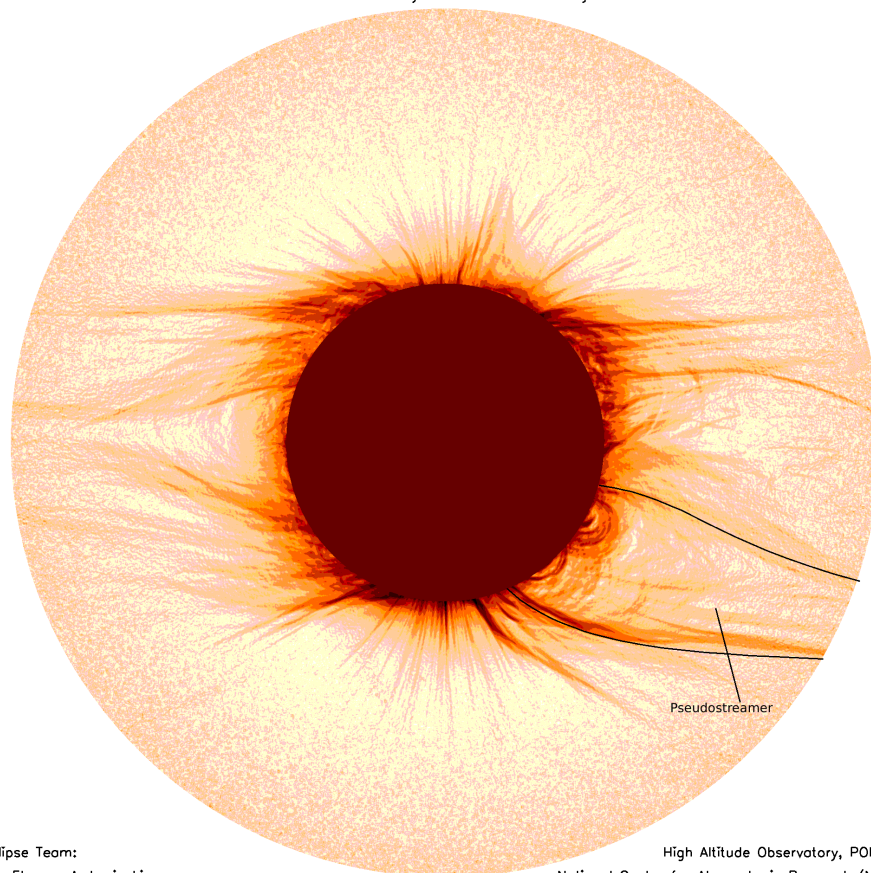
The fast solar wind is most evident at solar minimum and it is present around the polar coronal holes. Near the equator, at solar minimum, elongated bright structures can be seen in the corona these are known as *streamers* or *helmet streamers* which are due to plasma held on the very large scale loops that are associated with the solar magnetic dipole (see Figure 1.7). These loops are dragged outwards by the solar wind in the open field regions at the poles to create the elongated streamer structures. Helmet streamers have been observed in eclipses since medieval times [Priest, 1982] and have been studied in connection with the solar wind since the 1960s [e.g., Parker, 1964]. Magnetic field lines on both sides of the streamer belt are open into interplanetary space and are oppositely directed leading to currents building up at the top of the streamer and forming the *heliospheric current sheet* [Howard and Koomen, 1974].

More recently, streamers that do not have a change of polarity in the field either side of them have been discovered [e.g., Wang et al., 2007]. These are called *pseudostreamers* or *unipolar streamers*. An example of such a structure is shown in Figure 1.8. When pseudostreamers are observed close to the limb of the sun a characteristic pattern of two lobes is seen underneath the streamer which extends out into space (see Figure 1.8). More explanation of the structure of pseudostreamers is presented in Chapter 3.

Pseudostreamers have been found to be important sites for acceleration of the slow solar wind [e.g., Crooker et al., 2012, Wang et al., 2012] and also sites that are favourable for eruptions [e.g., Titov et al., 2012].

26 February 1998 eclipse, Curacao, Netherlands Antilles

Fine structure in this intensity data has been numerically enhanced.



Eclipse Team:
D. Elmore, A. Lecinski,
G. Card, B. Lites, K. Streander, S. Tomczyk

High Altitude Observatory, POISE98
National Center for Atmospheric Research (NCAR)
NCAR is sponsored by the U.S. National Science Foundation.

Figure 1.8: Image of the 26th February 1998 eclipse taken by the High Altitude Observatory's POISE98 instrument. This is in the rise phase of cycle 23. A pseudostreamer structure is visible on the south west limb and is labelled. Image credit: http://mlso.hao.ucar.edu/images/haoeclipse1998scarab_2033x2628.gif

1.4 Magnetic Field Structure - An Overview

The structure of a magnetic field is important in determining the way it can evolve. This section will first give an overview of the equations that govern a magnetised plasma, such as that found on the Sun, with particular attention paid to the equation that describes the evolution of a magnetic field. Then I will consider the different elements of magnetic field structure before giving a detailed description of the *magnetic skeleton* which provides us with a robust and clear way of analysing and understanding the magnetic field structure. Describing the field structure in this way enables us to identify likely sites for the important energy release process of *magnetic reconnection*.

1.4.1 Maxwell's Equations and Ohm's Law

All magnetic fields are governed by a set of laws known as *Maxwell's Equations* [Clerk Maxwell, 1865]. These are given here in SI units.

The first of these is the solenoidal constraint which precludes the existence of magnetic monopoles,

$$\nabla \cdot \mathbf{B} = 0, \quad (1.1)$$

where \mathbf{B} is the magnetic field vector.

Faraday's law links the changes in time of the magnetic field, \mathbf{B} , with the curl of the electric field, \mathbf{E} .

$$\nabla \times \mathbf{E} = -\frac{\partial \mathbf{B}}{\partial t}, \quad (1.2)$$

where \mathbf{E} is the electric field and t is time. From this we can see that dimensionally:

$$\frac{E_0}{l_0} \approx \frac{B_0}{t_0}, \quad (1.3)$$

where E_0 and B_0 are typical electric and magnetic field strengths, respectively, l_0 is a typical length scale and t_0 is a typical time-scale.

The magnetic field is associated with an electric current, \mathbf{j} , through *Ampere's Law*:

$$\nabla \times \mathbf{B} = \frac{1}{c^2} \frac{\partial \mathbf{E}}{\partial t} + \mu_0 \mathbf{j}, \quad (1.4)$$

where c is the speed of light, $\mu_0 = 4\pi \times 10^{-7} \text{Hm}^{-1}$ is the permeability of free space, \mathbf{E} is the electric field and t is time. The speeds of motion of the magnetic field and the plasma are typically much less than the speed of light so we have:

$$v_0 \ll c, \quad (1.5)$$

where v_0 is a typical speed. Supposing t_0 is a typical time and l_0 is a typical length scale then, since $t_0 = l_0/v_0$, after applying a dimensional argument to the first term on the right hand side of 1.4 we get:

$$\frac{1}{c^2} \frac{\partial \mathbf{E}}{\partial t} \approx \frac{1}{c^2} \frac{E_0}{t_0} \approx \frac{v_0}{c^2} \frac{E_0}{l_0}. \quad (1.6)$$

Using Equation (1.3) we have:

$$\frac{v_0 E_0}{c^2 l_0} \approx \frac{v_0 B_0}{c^2 t_0} = \frac{v_0^2 B_0}{c^2 l_0} \ll \frac{B_0}{l_0} \approx \nabla \times \mathbf{B}. \quad (1.7)$$

This means that we can neglect the $\frac{1}{c^2} \frac{\partial \mathbf{E}}{\partial t}$ term and consider Ampere's law to be:

$$\nabla \times \mathbf{B} = \mu_0 \mathbf{j}. \quad (1.8)$$

In the case where the current is zero then we say the field is *potential*. Further discussion on the relevance of potential fields in the solar corona can be found in Section 2.1.

In addition to Maxwell's Equations we also have resistive Ohm's Law:

$$\mathbf{j} = \sigma (\mathbf{E} + \mathbf{v} \times \mathbf{B}), \quad (1.9)$$

where σ is the electric conductivity.

Rearranging (1.9) for \mathbf{E} gives:

$$\mathbf{E} = \frac{\mathbf{j}}{\sigma} - \mathbf{v} \times \mathbf{B}. \quad (1.10)$$

Substituting this into (1.2) gives:

$$\nabla \times \left(\frac{\mathbf{j}}{\sigma} - \mathbf{v} \times \mathbf{B} \right) = -\frac{\partial \mathbf{B}}{\partial t} \quad (1.11)$$

$$\Rightarrow \frac{\partial \mathbf{B}}{\partial t} = -\frac{1}{\sigma} \nabla \times \mathbf{j} + \nabla \times (\mathbf{v} \times \mathbf{B}). \quad (1.12)$$

Now substituting for \mathbf{j} using (1.8) we get:

$$\frac{\partial \mathbf{B}}{\partial t} = \frac{-1}{\mu_0 \sigma} \nabla \times (\nabla \times \mathbf{B}) + \nabla \times (\mathbf{v} \times \mathbf{B}), \quad (1.13)$$

which following a vector identity substitution gives

$$\frac{\partial \mathbf{B}}{\partial t} = \nabla \times (\mathbf{v} \times \mathbf{B}) + \eta \nabla^2 \mathbf{B}, \quad (1.14)$$

where $\eta = \frac{1}{\mu_0 \sigma}$ is the magnetic diffusivity. It should be noted that this derivation assumes η is a constant in space which is not always the case. Equation (1.14) is known as the induction equation and it describes the changes in the magnetic field in terms of advection ($\nabla \times (\mathbf{v} \times \mathbf{B})$) and diffusion ($\eta \nabla^2 \mathbf{B}$) terms. In most places in the solar corona the advection term dominates and field lines are "frozen in" to the plasma [Alfvén, 1943]. However, in places where large currents are built up over small length scales the diffusion term can dominate which means the field lines can slip through the plasma and magnetic reconnection can occur.

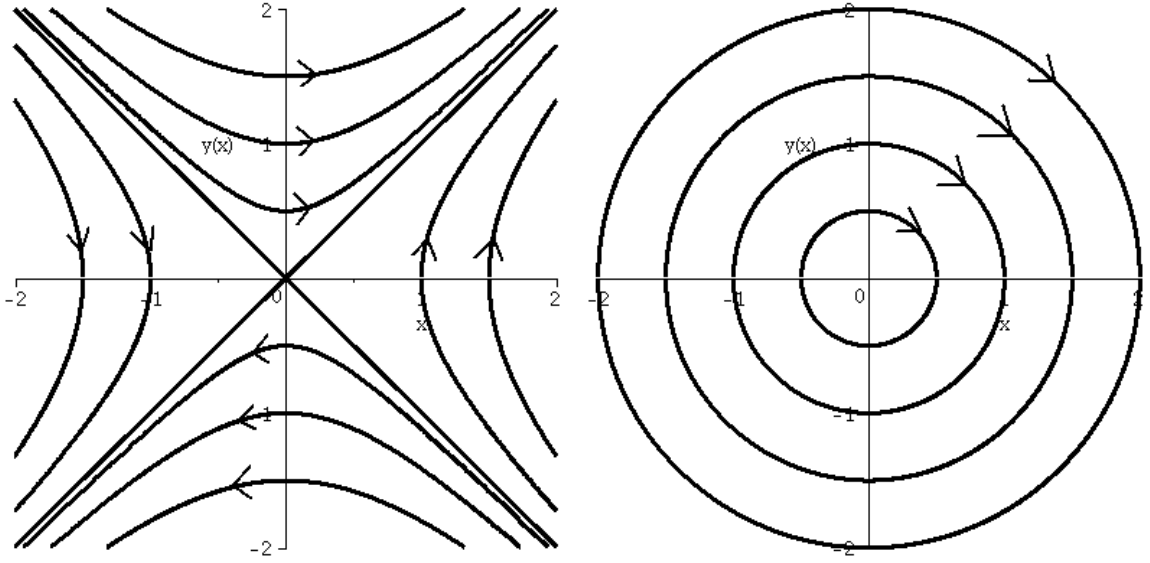


Figure 1.9: Examples of field lines around 2D null points. (left) X-type null and (right) O-type null

1.4.2 Null Points

Magnetic null points are points in space where the magnetic field, \mathbf{B} , equals zero. Null points are a crucial part of the magnetic field structure. They are places where reconnection can occur and in 3D they are associated with separators which are also possible magnetic reconnection sites.

We can linearise about a null point located at a position \mathbf{r}_0 to obtain an expression for the local magnetic field about the null:

$$\mathbf{B} = \nabla \mathbf{B}|_{\mathbf{r}_0} \cdot (\mathbf{r} - \mathbf{r}_0), \quad (1.15)$$

where \mathbf{r} is position in space whose i^{th} component is x_i and $\nabla \mathbf{B}|_{\mathbf{r}_0}$ is the Jacobian matrix evaluated at $\mathbf{r} = \mathbf{r}_0$ with $\nabla \mathbf{B}_{i,j} = \partial B_i / \partial x_j$. From this point on we will refer to $\nabla \mathbf{B}|_{\mathbf{r}_0}$ as \mathbf{M} , an $n \times n$ matrix where n is the dimension of the space we are considering (i.e., 2 or 3).

Null Points in 2D

In two dimensions, magnetic null points can be one of two forms: an X-point (Figure 1.9 left) or an O-point (Figure 1.9 right). There is also the degenerate case where the null collapses to a 1D null line separating anti-parallel field lines which is not considered here. The type of null depends on the nature of the eigenvalues of \mathbf{M} .

In 2D,

$$\mathbf{M} = \begin{pmatrix} \partial B_1 / \partial x_1 & \partial B_1 / \partial x_2 \\ \partial B_2 / \partial x_1 & \partial B_2 / \partial x_2 \end{pmatrix} = \begin{pmatrix} a_{11} & a_{12} \\ a_{21} & a_{22} \end{pmatrix}, \quad (1.16)$$

since $\nabla \cdot \mathbf{B} = 0$, $a_{11} = -a_{22}$. So there are only 3 parameters specifying the local field.

From Ampere's Law (1.8) the current is

$$\begin{aligned} \mathbf{j} &= \frac{1}{\mu_0} \nabla \times \mathbf{B} \\ &= \frac{1}{\mu_0} (0, 0, a_{21} - a_{12}), \end{aligned} \quad (1.17)$$

where $\mu_0 = 4\pi \times 10^{-7} \text{Hm}^{-1}$ is the permeability of free space.

This means that currents are present at the null if and only if \mathbf{M} is non-symmetric. The eigenvalues of \mathbf{M} are $\lambda_{1,2} = \pm \sqrt{a_{11}^2 + a_{12}a_{21}}$. This means that if $a_{11}^2 + a_{12}a_{21}$ is negative then the local field around the null forms concentric rings or ellipses: this is known as an O-point. Similarly, if $a_{11}^2 + a_{12}a_{21}$ is positive non-zero the field lines are hyperbolic and an X-point is formed.

2D Potential Nulls If the field is potential then \mathbf{M} must be symmetric. This means that $a_{12} = a_{21}$ which limits the number of free parameters to 2.

$$\mathbf{B} = \begin{pmatrix} a_{11} & a_{12} \\ a_{12} & -a_{11} \end{pmatrix} \cdot \begin{pmatrix} x \\ y \end{pmatrix}, \quad (1.18)$$

The eigenvalues of \mathbf{M} are $\lambda_{1,2} = \pm \sqrt{a_{11}^2 + a_{12}^2}$. Both the eigenvalues are real and they are opposite and equal. The eigenvectors will be:

$$\mathbf{v}_1 = (-a_{12}, a_{11} - \sqrt{a_{11}^2 + a_{12}^2}) \quad (1.19)$$

$$\mathbf{v}_2 = (a_{11} + \sqrt{a_{11}^2 + a_{12}^2}, a_{12}) \quad (1.20)$$

This means that the field lines will be rectangular hyperbolae. This will form an X-type null point.

Null Points in 3D

In three dimensions, the field lines passing through a null point form a *spine line* and a *fan plane* structure [e.g., Cowley, 1973, Lau and Finn, 1990, Parnell et al., 1996, Priest and Titov, 1996]. The sign of a null point in 3D depends on the direction of the field lines in the fan plane. If the field lines go away from the null in the fan and into the null along the spine then the null is positive. Likewise, if the field lines go towards the null in the fan and out of the null along the spine then the null is negative.

To determine the field locally about the null we again linearise as we did in 2D. To first order, in spherical coordinates, for a null point at $\mathbf{r}_0 = (r_0, \theta_0, \phi_0)$, this gives us,

$$\mathbf{B} = (B_r, B_\theta, B_\phi) = \nabla \mathbf{B}|_{\mathbf{r}_0} (\mathbf{r} - \mathbf{r}_0) = \mathbf{M} \cdot (\mathbf{r} - \mathbf{r}_0) \quad (1.21)$$

where \mathbf{r} is the displacement from the origin and $\mathbf{M} = \nabla\mathbf{B}|_{\mathbf{r}_0}$. The direction and location of the spine and the fan are determined by the eigenvectors and eigenvalues of \mathbf{M} .

From Parnell et al. [1996], if \mathbf{M} is diagonalisable then we have the equation of a field line in the vicinity of the null parametrised by k ,

$$\mathbf{r}(k) = Ae^{\lambda_1 k}\mathbf{x}_1 + Be^{\lambda_2 k}\mathbf{x}_2 + Ce^{\lambda_3 k}\mathbf{x}_3 + \mathbf{r}_0, \quad (1.22)$$

where λ_i are the eigenvalues and \mathbf{x}_i are the associated eigenvectors of \mathbf{M} . To follow a field line out from the null we let $k \rightarrow \infty$. To follow a field-line that is directed into the null we let $k \rightarrow -\infty$. Field lines going into the null will tend to eigenvectors with negative eigenvalues, in particular the eigenvector with the largest negative eigenvalue. Field lines going out of the null will tend to eigenvectors with positive eigenvalues, in particular the eigenvector with the largest positive eigenvalue.

Positive null points will have two positive eigenvalues and one negative eigenvalue. Therefore, field lines traced backwards along the field from close to the null will all tend to the eigenvector corresponding to the negative eigenvalue, this forms the spine. Field lines traced forwards along the field from close to the null will initially head out in the plane described by the two eigenvectors corresponding to the positive eigenvalues, this forms the fan plane. Similarly for negative nulls, tracing the field lines backwards from the null forms the fan-plane and tracing forwards from the nulls forms the spine.

It is clear that for the solenoidal constraint (Equation 1.1) to be satisfied then the trace of the Jacobian matrix, \mathbf{M} , and also the eigenvalues of \mathbf{M} , must sum to zero. This means that the set of eigenvalues of the null may be one of the following three cases: (1) three real eigenvalues, (2) one real eigenvalue and two that are complex conjugates and (3) one eigenvalue is zero and two that are equal but opposite in sign. The third case is a degenerate case where the 3D null has collapsed to a 2D null line with ‘‘X-point’’ type field around it if the two non-zero eigenvalues are real and ‘‘O-point’’ type field around it if the two non-zero eigenvalues are imaginary.

The remaining two cases correspond to genuine 3D nulls. The sign (positive or negative) of the null is governed by the sign of the real part of the eigenvalues as described above. In the case where all the eigenvalues are real the field lines in the fan plane are not spiral. In the case where two of the eigenvalues are complex conjugates the field lines in the fan will spiral into or out of the null [Parnell et al., 1996]. If the field is potential then the matrix \mathbf{M} will be symmetric and so will have all real eigenvalues.

1.4.3 The Magnetic Skeleton and Separators

When the field lines in the fan-plane of a null are traced away from the null they form a surface, known as a *separatrix surface* which divides space into two *topologically distinct flux domains*. A *topologically distinct flux domain* (TDFD) is a simply connected volume bounded by separatrix surfaces or the boundaries of the whole magnetic domain

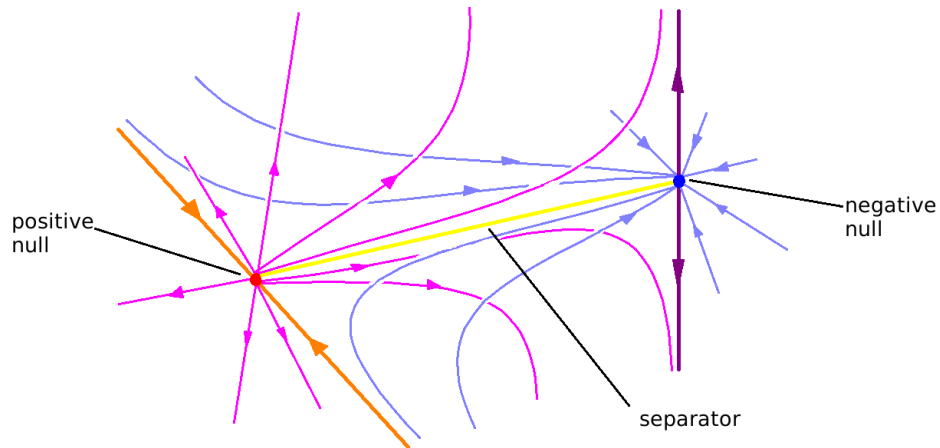


Figure 1.10: Sketch of the field lines from two 3D null points intersecting to form a separator. The red and blue circles are the positive and negative nulls respectively. The pink and blue lines are the field lines in the separatrix surfaces of the positive and negative nulls respectively and the orange and purple lines are the spines. The intersection of the two separatrix surfaces (separator) is the yellow line.

and containing field lines that have the same connectivity. Within a *simply connected volume* lines can be continuously deformed into one another [Longcope and Klapper, 2002, Beveridge and Longcope, 2005].

When the separatrix surfaces from nulls of opposite sign intersect one another they intersect on a field line that connects the two nulls; this line is called a *separator* [e.g., Baum and Bratenahl, 1980, Lau and Finn, 1990] and it lies on the dividing line between four topologically distinct flux domains. Figure 1.10 shows a cartoon of the intersection of two separatrix surfaces. The blue lines are field lines in the separatrix surface from the negative null (blue dot) and the pink lines are field lines in the separatrix surface from the positive null (red dot), their intersection is the separator (yellow line).

Separators are important sites for magnetic reconnection [e.g., Priest and Titov, 1996, Galsgaard et al., 2000, Longcope, 2005, Parnell et al., 2010]. Reconnection can occur anywhere along the length of a separator [e.g., Galsgaard et al., 2000, Parnell et al., 2010] and will occur where the separators pass through regions of high parallel electric field.

The *magnetic skeleton* is the name given for the network of null points, separatrix surfaces, spines and separators which robustly describe the magnetic field structure [Priest et al., 1996]. Methods for finding the magnetic skeleton of a magnetic field are discussed later in Section 2.4.

By considering the TDFDs rather than just the connectivity of the system we can see more of the structure of the field. For instance, it is possible to differentiate between field lines connecting different patches within a continuous flux distribution such as the solar surface. The magnetic skeleton is also stable in the sense that

continuous ideal movement of the magnetic field will not change the topology of the magnetic field, hence, not change its magnetic skeleton.

1.4.4 Quasi-separatrix surfaces

In addition to separatrix surfaces, there is a lot of interest in regions where the field lines that start close together are mapped to points far apart. A thin layer where the field line mapping has a large gradient is known as a *Quasi Separatrix Layer* (QSL) [Priest and Démoulin, 1995]. Quasi-separatrix layers and their intersections, quasi-separators, are known to be important sites for reconnection in the corona [e.g., Démoulin et al., 1996, Mandrini et al., 1996, Titov et al., 2008, Baker et al., 2009]. To find QSLs a parameter known as the squashing factor, Q , is calculated. The squashing factor is found by tracing field lines from a circle on one boundary and measuring the eccentricity of the ellipse formed when the field lines hit the other boundary. Obviously geometric effects of the choice of boundaries can influence the value obtained for Q so, to reduce these effects, a generalized squashing factor has been developed by Titov [2007].

All separatrix surfaces will also be layers of high or infinite Q since the mapping of field lines across a separatrix surface will either be discontinuous or will have a large gradient. Therefore, by finding and investigating the separatrix surfaces we are able to find most locations where Q is high and also exclude the possibility of finding regions that have a high Q due to geometric effects.

1.4.5 Magnetic reconnection

Magnetic reconnection is the process by which magnetic field lines can “break” and form new connections [e.g., Priest and Forbes, 2000]. This is one of the primary ways in which magnetic energy can be released into the corona and has long been known to be a mechanism for energy release in solar energetic events such as flares [Giovannelli, 1946, Hoyle, 1949]. In 2D, magnetic reconnection happens at null points, in particular X-type null points. Field lines from flux domains that are opposite one another are pushed into the null where they reconnect and form a new pair of field lines. In this way flux is transferred from one pair of topologically distinct flux domains to another.

In 3D magnetic reconnection can happen at null points [e.g., Lau and Finn, 1990, Craig et al., 1995, Priest and Titov, 1996, Masson et al., 2009, Pontin et al., 2013], separators [e.g., Galsgaard et al., 2000, Parnell et al., 2010] or in the presence of neither of these [e.g. Hesse and Schindler, 1988, Priest and Démoulin, 1995, Démoulin et al., 1996]. Three-dimensional magnetic reconnection does not match pairs of reconnected field lines instead it happens continuously within a volume.

The main condition that needs to be satisfied for reconnection to occur in 3D is that the electric field component that is parallel to the magnetic field lines needs to be high [Schindler et al., 1988] and the integrated parallel electric field component along the field lines through the diffusion region needs to be non-zero. From Ohm’s

law (Equation 1.9) we can see there will only be a component of \mathbf{E} parallel to \mathbf{B} if a current, \mathbf{j} , is present and if that current has a component along the magnetic field.

1.5 Outline

This thesis considers global potential field extrapolations of the Sun’s coronal magnetic field. To do this we employ a model known as the Potential Field Source Surface (PFSS) model. The methods and codes used both for the PFSS extrapolations and for finding the magnetic skeleton within these extrapolations are described in Chapter 2.

Chapter 3 explains different topological features that have been identified as being important to the global coronal magnetic skeleton. We describe both the well known features such as the Heliospheric Current Sheet (HCS) and bald-patches, as well as introducing terminology to describe more complex structures seen in our models.

In Chapter 4, the long term changes in the global magnetic topology of potential fields is studied. We consider potential magnetic fields extrapolated from the magnetograms that have been produced for the last 37 years by the National Solar Observatory (NSO) at Kitt-Peak, Arizona. Initially in this chapter a qualitative analysis of the “typical” types of topology seen at solar minimum and solar maximum is presented. Following this, an in-depth study looks at the prevalence and location of certain topological features in PFSS extrapolations from the long term Kitt-Peak/Solar Optical Long-term Investigations of the Sun (SOLIS) low-resolution data.

In Chapter 5, we again use PFSS extrapolations from the Kitt-Peak and SOLIS magnetograms to look into the cycle variation of particular topological structures. We consider the global network of separators and null points and characterise topological configurations such as isolated separatrix domes and double separatrix caves from properties of this network. We also consider long-term trends in particular aspects of the separator network.

Since 2003 the magnetograms produced by the SOLIS telescope at the Kitt-Peak observatory have come in two resolutions, so Chapter 6 analyses the topological differences between extrapolations from these two data sets with differing resolutions. In particular, we note the differences in open-field regions.

In Chapter 7, we extrapolate high-resolution global potential magnetic fields from magnetograms from the Michelson Doppler Imager (MDI) and use these to carry out a detailed study of the distribution of null-points in the solar corona and its variation in time. For comparison, we also consider extrapolations from magnetograms from the Heliospheric Magnetic Imager (HMI) and SOLIS.

As well as categorising the long term trends in the topology it is also of interest to investigate the topology at particular periods of time. For example, in Chapter 8 we present topological analysis of the extrapolated global coronal potential magnetic field surrounding large active regions from which plasma up-flows have been observed.

First, an overview of the observations of these active regions is given. These observations have been carried out by Louise Harra and Len Culhane (Mullard Space Science Laboratory). Following this details of the extrapolations around these active regions is presented with particular note given to whether field lines from the area in which up-flows are observed are open and hence a source of the solar wind.

Finally, Chapter 9 provides a summary and conclusions of the work in this thesis as well as providing insight into future work that could be undertaken on the topics addressed here.

Chapter 2

Models and Methods

This chapter describes some of the models and methods used in this thesis. First I explain the global coronal magnetic field model used and the observational input it requires, before going on to describe the methods used to find the three-dimensional topology of these extrapolated magnetic fields.

2.1 Force-free models

Many models have been used to describe the global magnetic field of the Sun based on various assumptions. These can be categorised into force-free and non-force-free models. Examples of non-force-free models are fully magneto-hydrodynamic models [e.g., Riley et al., 2006, DeVore and Antiochos, 2008, Lionello et al., 2009, Downs et al., 2010, Feng et al., 2012] but these are extremely computationally intensive and as such cannot be easily driven by observations or run at a high-resolution. The compromise we make is by introducing the force-free approximation which is described below.

The equation of motion for an inviscid plasma is

$$\underbrace{\rho \frac{D\mathbf{v}}{Dt}}_{(1)} = \underbrace{-\nabla p}_{(2)} + \underbrace{\mathbf{j} \times \mathbf{B}}_{(3)} + \underbrace{\rho \mathbf{g}}_{(4)} \quad (2.1)$$

where ρ is the plasma density, \mathbf{v} is the plasma velocity, p is the plasma pressure, \mathbf{j} is the current, \mathbf{B} is the magnetic field and \mathbf{g} is the gravity vector.

If we compare the magnitudes of term (1) ($\rho D\mathbf{v}/Dt$) and the Lorentz force, term (3) ($\mathbf{j} \times \mathbf{B}$) we get

$$\left| \rho \frac{D\mathbf{v}}{Dt} \right| : |\mathbf{j} \times \mathbf{B}| \quad (2.2)$$

$$\frac{\rho_0 v_0}{t_0} : \frac{B_0^2}{\mu_0 l_0}, \quad (2.3)$$

where $\rho_0, v_0, B_0, l_0, t_0$ are all typical quantities. To neglect term (1) in favour of term (3) we want

$$\frac{\rho_0 v_0}{t_0} \ll \frac{B_0^2}{\mu_0 l_0} \Rightarrow v_0^2 \ll \frac{B_0^2}{\mu_0 \rho_0} = v_A^2, \quad (2.4)$$

where v_A is the typical Alfvén speed. In the corona, we have typical values of B_0 between 20G and 100G, $\mu_0 = 4\pi \times 10^{-7}$ H m⁻¹ and ρ_0 varies from 10^{-10} kg m⁻³ in the low corona to 10^{-15} kg m⁻³ at $2.5R_\odot$. This gives an Alfvén speed of around 10^6 m s⁻¹. Typically the velocities in the corona are about 10^4 m s⁻¹ and so forces due to acceleration of the plasma are small in comparison to the Lorentz force.

If we compare the magnitudes of term (2) and term (3) then we get

$$|-\nabla p| : |\mathbf{j} \times \mathbf{B}| \quad (2.5)$$

$$\frac{p_0}{l_0} : \frac{B_0^2}{\mu_0 l_0} \quad (2.6)$$

In order to neglect term (2) in favour of term (3) we want

$$\frac{p_0}{L} \ll \frac{B_0^2}{\mu_0 L} \Rightarrow \frac{p_0 \mu_0}{B_0^2} \ll 1 \Rightarrow \beta \ll 1, \quad (2.7)$$

where $\beta = \frac{2p_0 \mu_0}{B_0^2}$ is the *plasma-beta*. This is a reasonable assumption to make since typically in the corona $p_0 = 0.1$ pascal which produces $\beta = 0.001$ which is much less than one so forces due to pressure gradients can be neglected. We should note that around a null point where the magnetic field drops to zero β will be locally very high but on average it is fair to make the assumption that it is low.

If we compare term (4) and term (3) we get

$$|\rho \mathbf{g}| : |\mathbf{j} \times \mathbf{B}| \quad (2.8)$$

$$\rho_0 g : \frac{B^2}{\mu_0 l_0}. \quad (2.9)$$

In order to neglect term (4) in favour of term (3) we want

$$\rho_0 g \ll \frac{B^2}{\mu_0 l_0}. \quad (2.10)$$

We define the pressure scale height $H = p_0/\rho_0 g$. Then dividing Equation 2.10 by p_0

$$\frac{\rho_0 g}{p_0} \ll \frac{B^2}{\mu_0 l_0 p_0} \Rightarrow \quad (2.11)$$

$$\frac{1}{H} \ll \frac{1}{l_0 \beta} \quad (2.12)$$

$$l + 0 \ll \frac{H}{\beta}. \quad (2.13)$$

This is a reasonable assumption to make since β is very small in much of the corona so its reciprocal is very large.

This then leaves us with

$$\mathbf{j} \times \mathbf{B} = 0. \quad (2.14)$$

This means that $\mathbf{j} \parallel \mathbf{B}$.

There are three ways in which this can be satisfied. First, by assuming the field is potential, such that $\mathbf{j} = \mathbf{0}$ which satisfies $\mathbf{j} \times \mathbf{B} = \mathbf{0}$ trivially.

Second, there is the linear force-free approach where the current is set to be some constant times the magnetic field, i.e.,

$$\mu_0 \mathbf{j} = \alpha \mathbf{B} \quad (2.15)$$

where α is constant in space.

In order for Ampere's Law to be satisfied then we need:

$$\nabla \times \mathbf{B} = \alpha \mathbf{B} \quad (2.16)$$

and since the divergence of a curl must always be zero

$$\nabla \cdot (\nabla \times \mathbf{B}) = 0 \quad (2.17)$$

$$\nabla \cdot \alpha \mathbf{B} = 0 \quad (2.18)$$

$$\alpha \nabla \cdot \mathbf{B} + \mathbf{B} \cdot \nabla \alpha = 0 \quad (2.19)$$

$$\Rightarrow \mathbf{B} \cdot \nabla \alpha = 0 \quad (2.20)$$

which means α is constant along field lines. The third approach is the non-linear force-free approach which lets the parameter, α , vary over space. Non-linear force-free models have been widely used in studying coronal fields [e.g., van Ballegoijen et al., 2000, Mackay and van Ballegoijen, 2006, Wiegmann, 2007, Contopoulos et al., 2011, Yeates and Mackay, 2012].

The following section describes the potential-field source-surface model which, for a given set of boundary conditions, provides a unique, simple, force-free global coronal magnetic field model. It allows us to study the magnetic field of the global solar corona over a long time period and also at high resolution whilst being relatively computationally tractable. As input it simply requires the normal component of the magnetic field at the photosphere to produce a unique solution whereas the other non-potential force-free models produce non-unique solutions unless information can be provided about α on all boundaries. The disadvantages of using a potential field model are that it fails to replicate twisted features that are often seen in the corona such as flux ropes or sheared field lines or any features where strong currents build up.

2.2 Potential Field Source Surface Model

The simplest solution of the force-free constraint is $\mathbf{j} = \mathbf{0}$ which produces a potential magnetic field. A potential field model of the global coronal magnetic field can be

found by taking a synoptic magnetogram as the radial component of the magnetic field on the lower boundary and imposing the constraint that all field becomes radial at the outer boundary. This is known as the Potential-Field Source-Surface (PFSS) model [Altschuler and Newkirk, 1969, Schatten et al., 1969]. The outer boundary is known as the *source surface* and is usually set at $2.5R_\odot$ as this is where the field is observed to be largely radial from eclipse observations and coronagraphs [e.g., Mackay and Yeates, 2012]. However, it has been suggested that it should be set at a lower height such as $1.8R_\odot$ or $1.6R_\odot$ [e.g., Lee et al., 2011]. In this thesis we will set the outer boundary to be at $2.5R_\odot$ in all our models except those models presented in Chapter 8 where it will be set to $2.0R_\odot$ to give a larger estimate for the amount of open field.

The derivation of the potential field source surface model which is presented below follows Mackay and Yeates [2012].

For a potential field we must have:

$$\nabla \times \mathbf{B} = 0, \quad (2.21)$$

this means we can write \mathbf{B} in terms of a scalar potential Ψ

$$\mathbf{B} = -\nabla\Psi. \quad (2.22)$$

Since we have $\nabla \cdot \mathbf{B} = 0$, Ψ must satisfy Laplace's equation

$$\nabla^2\Psi = 0, \quad (2.23)$$

and we have the boundary conditions that the normal component of the magnetic field at the lower boundary is defined by a magnetogram and the field at the top boundary, the source surface, is assumed to be radial. Therefore,

$$\left. \frac{\partial\Psi}{\partial r} \right|_{R_\odot} = B_r(R_\odot, \theta, \phi), \quad \left. \frac{\partial\Psi}{\partial\theta} \right|_{R_{SS}} = 0, \quad \left. \frac{\partial\Psi}{\partial\phi} \right|_{R_{SS}} = 0. \quad (2.24)$$

The solution of Laplace's equation in spherical harmonics can be found using separation of variables and is found to be

$$\Psi(r, \theta, \phi) = \sum_{l=0}^{\infty} \sum_{m=-l}^l (f_{lm}r^l + g_{lm}r^{-(l+1)}) P_l^m(\cos\theta)e^{im\phi}, \quad (2.25)$$

where $P_l^m(\cos\theta)$ are the *associated Legendre polynomials*, l and m specify the degree and f_{lm} and g_{lm} are constants that vary for different l, m and are found by applying the boundary conditions.

The boundary condition that $(\partial\Psi/\partial\phi)|_{R_{SS}} = 0$ means that $f_{lm}R_{SS}^l + g_{lm}R_{SS}^{-(l+1)} = 0$ for all (l, m) . Therefore, $g_{lm} = -f_{lm}R_{SS}^{(2l+1)}$.

The lower boundary condition, given by the magnetogram, implies

$$\begin{aligned} \left. \frac{\partial \Psi}{\partial r} \right|_{R_\odot} &= B_r(R_\odot, \theta, \phi) \Rightarrow \\ &\sum_{l=0}^{\infty} \sum_{m=-l}^l f_{lm} \left(l R_\odot^{(l-1)} + (l+1) R_{SS}^{2l+1} R_\odot^{-l-2} \right) P_l^m(\cos \theta) e^{im\phi} \\ &= B_r(R_\odot, \theta, \phi) \end{aligned} \quad (2.26)$$

In order to satisfy this condition we set f_{lm} to be related to the normal component of the magnetic field at the solar surface taken from the magnetograms, $B_r(R_\odot, \theta, \phi)$, via the spherical harmonic coefficients of this field, b_{lm}

$$\Rightarrow f_{lm} = \left(l R_\odot^{(l-1)} + (l+1) R_{SS}^{2l+1} R_\odot^{-l-2} \right)^{-1} b_{lm}. \quad (2.27)$$

This means we get an expression for the scalar potential,

$$\Psi(r, \theta, \phi) = \sum_{l=0}^{\infty} \sum_{m=-l}^l b_{lm} d_l(r) P_l^m(\cos \theta) e^{im\phi}, \quad (2.28)$$

$$\Rightarrow B_r(r, \theta, \phi) = \sum_{l=0}^{\infty} \sum_{m=-l}^l b_{lm} c_l(r) P_l^m(\cos \theta) e^{im\phi}, \quad (2.29)$$

$$B_\theta(r, \theta, \phi) = - \sum_{l=0}^{\infty} \sum_{m=-l}^l b_{lm} d_l(r) \frac{dP_l^m(\cos \theta)}{d\theta} e^{im\phi}, \quad (2.30)$$

$$B_\phi(r, \theta, \phi) = - \sum_{l=0}^{\infty} \sum_{m=-l}^l \frac{im}{\sin \theta} b_{lm} d_l(r) P_l^m(\cos \theta) e^{im\phi}, \quad (2.31)$$

where,

$$c_l(r) = \left(\frac{r}{R_\odot} \right)^{-l-2} \left[\frac{l+1 + l(r/R_{SS})^{2l+1}}{l+1 + l(R_\odot/R_{SS})^{2l+1}} \right], \quad (2.32)$$

$$d_l(r) = \left(\frac{r}{R_\odot} \right)^{-l-2} \left[\frac{r(1 - (r/R_{SS})^{2l+1})}{l+1 + l(R_\odot/R_{SS})^{2l+1}} \right]. \quad (2.33)$$

In order to calculate these we use the code described by van Ballegooijen et al. [1998]. In practice it is not possible to sum up an infinite number of harmonics so we need to truncate the sum at some finite l . The more harmonics included, the higher the resolution of the model. However, numerical errors in the summation of the small, higher-order harmonics can cause a “ringing” effect known as *Gibbs’ phenomenon*. This means a balance needs to be found between obtaining sufficient resolution and reducing spherical ringing. The number of harmonics used, l_{max} , depends on the resolution of the synoptic magnetogram used at the lower boundary. We find the optimum number of harmonics by trial and error using several constraints.

- First we make sure that the resolution of the extrapolation at the photosphere is not greater than the resolution of the input data. This means $N_x < 4(l_{max} + 1)$ and $N_y < 2(l_{max} + 1)$ where N_x and N_y are the resolution of the input magnetogram in the longitudinal and latitudinal directions respectively.
- Second we want the highest resolution possible without causing ringing so we take a number l_{max} that satisfies the previous constraint and is suitably large and perform the extrapolation and investigate for visual signs of ringing. In particular this will occur around active regions with strong magnetic field that are surrounded by quiet sun.
- Third we need to choose a number of harmonics that will produce an extrapolation suitable for the memory capacity of the computer. In particular we need to be able to load at least one frame in its entirety in order to perform the topological analysis of the extrapolated magnetic field.

Once the number of harmonics has been determined we calculate the potential field on a grid that has a resolution of $4(l_{max} + 1) + 1$ grid points in longitude $2(l_{max} + 1) + 1$ grid points in latitude and radial spaced gridpoint calculated depending on the height used for the source surface.

2.3 Magnetogram data

The lower boundary, from which the PFSS model is calculated, is taken from synoptic magnetograms. In this thesis, data from various sources is used including the Kitt-Peak synoptic magnetograms, Heliospheric Magnetic Imager (HMI) high-resolution synoptic magnetograms (both daily update and Carrington rotation maps), Michelson Doppler Imager (MDI) synoptic magnetograms, and low-resolution and high-resolution synoptic magnetogram maps from the Solar Optical Long-term Investigations of the Sun (SOLIS) telescope.

2.3.1 Kitt-Peak data

The National Solar Observatory (NSO) at Kitt-Peak, Arizona, USA, has been producing synoptic magnetogram maps since 1975. For almost 30 years the original vacuum telescope was used and then, in August 2003, this was replaced with the Solar Optical Long-term Investigations of the Sun (SOLIS) telescope. Both these telescopes create synoptic maps from solar disc observations taken every day for one *Carrington rotation*. A Carrington rotation is approximately 27 days and it corresponds to an estimate of the rotational period of the mid-latitudes of the Sun. The observations from each day are weighted and shifted to the appropriate Carrington longitude and combined to give a map of the entire solar surface for that Carrington rotation. These maps have a grid spacing that is even in longitude and sine latitude meaning every pixel represents an equal area on the Sun.

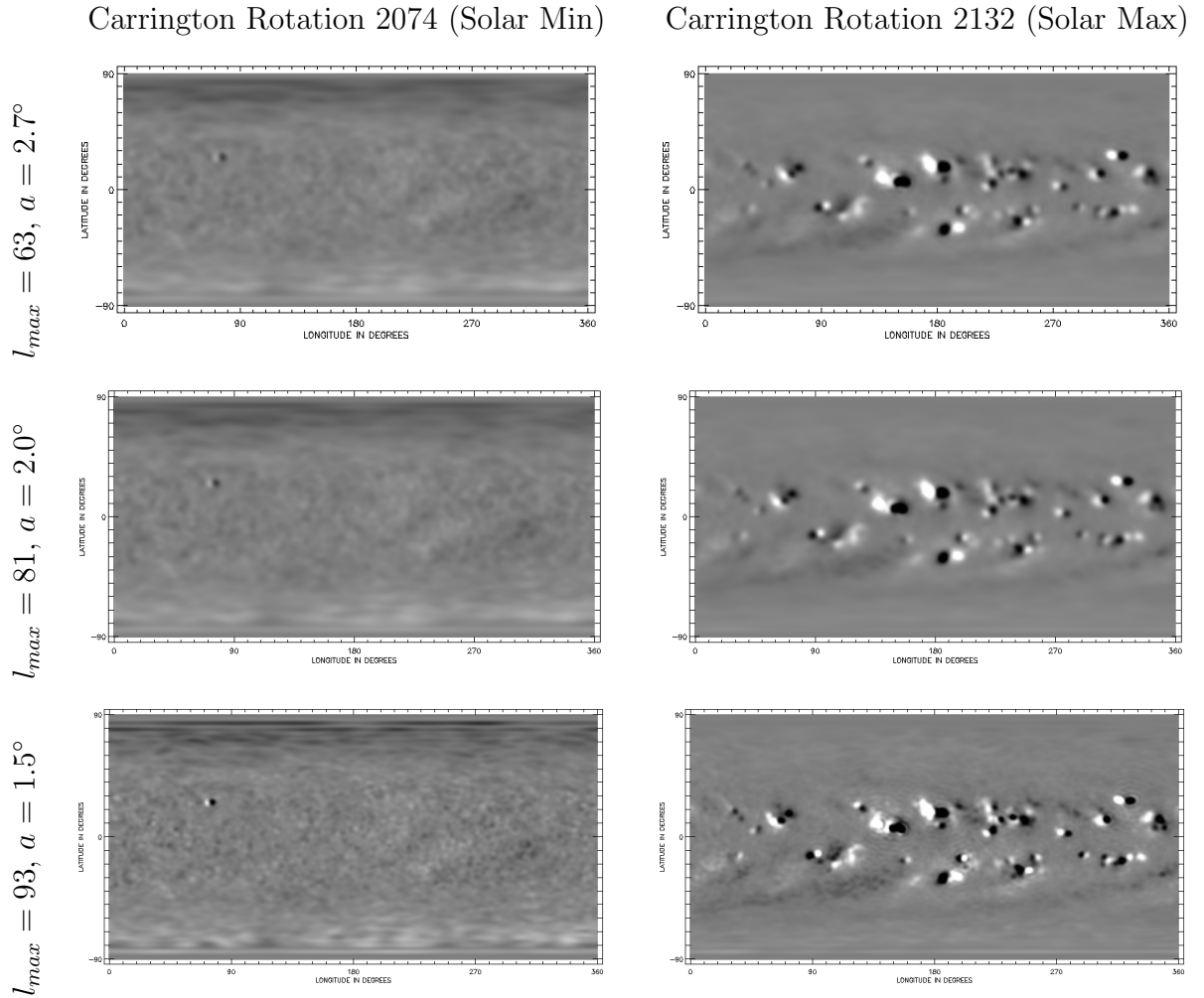


Figure 2.1: Constructed radial component of the magnetic field at the photosphere from the PFSS model for typical solar minimum and solar maximum frames and for three different harmonic numbers.

The original vacuum telescope produced maps that have a resolution of 360 grid-points in equal steps of longitude and 180 grid-points in equal steps of sine latitude. This series of 360 by 180 maps was continued by the SOLIS telescope, producing a continuous 36 year period of observations that can be studied. Several different combinations of harmonic numbers (l_{max}) and Gaussian smoothing widths (a) were tried, three of these are shown in Figure 2.1 for a typical solar minimum and solar maximum Carrington rotation. We see that using $l_{max} = 63$ gives a very smoothed image which does not replicate well the mixed polarity field at solar minimum. Using $l_{max} = 93$ (Figure 2.1 bottom row) replicates the mixed polarity solar minimum field well but at solar maximum around the strong active-region fields significant ringing is found (can be seen as ripples in the field). Using $l_{max} = 81$ gives us a good compromise between good resolution and the introduction of spherical ringing.

As well as producing maps of the same resolution as the original Kitt-Peak vacuum telescope, SOLIS also produces a series of high-resolution synoptic maps. The high-resolution maps have 1800 grid points in longitude and 900 in sine latitude. The maximum number of harmonics used in the PFSS model with this data is $l_{max} = 301$ which is selected in the same way as for the Kitt-Peak/low-res SOLIS data.

2.3.2 Michelson Doppler Imager (MDI) data

The Michelson Doppler Imager (MDI) is an instrument aboard the SOlar and Heliospheric Observatory (SOHO) which was operational between 1996 and 2010. Carrington rotation synoptic maps from its data have been produced. These have a resolution of 3600×1080 grid-points and from this we can extrapolate a potential field using a maximum of $l_{max} = 351$ harmonics. The main constraint here is memory for computing rather than ringing in the constructed magnetogram. Before calculating the potential field extrapolation we smooth the data with a Gaussian filter with width 0.5 degrees. The smoothing width and the maximum number of harmonics are found as described for Kitt-Peak/SOLIS data.

2.3.3 Heliospheric Magnetic Imager (HMI) data

The Solar Dynamics Observatory (SDO) was launched in 2010. The magnetic imager on-board is the Heliospheric Magnetic Imager (HMI). The observations from HMI briefly overlapped with those of SOHO between May 2010 and November 2010 (Carrington rotations 2097 to 2104). HMI produces Carrington rotation synoptic maps of a resolution of 3600×1440 . Initially we average adjacent pixels to reduce the resolution by half for ease of computation. Then the maps are smoothed with a Gaussian filter of 0.5 degrees and an extrapolation is performed using a maximum harmonic number $l_{max} = 351$ which gives an extrapolation of the same resolution as that from MDI.

Also, HMI produces daily updated synoptic maps. To produce these daily maps the full time-averaged Carrington rotation map is taken and shifted so that the central longitude at 12:00:00 on the given day is at 60 degrees. Then a 120 degree wedge centred on this longitude is replaced by observations taken over a 12 hour period on that day. These maps are used in Chapter 8 to extrapolate the global field associated with an active region.

A graph showing the number of harmonics used in each extrapolation and the period from which observations are available for each source of magnetogram is shown in Figure 2.2.

It should be noted that for all the synoptic magnetograms the radial component of the magnetic field is calculated from measuring the magnetic field in the line of sight. This means that at the poles the coverage is not so good as the radial field component becomes perpendicular to the line of sight at the poles. The data from

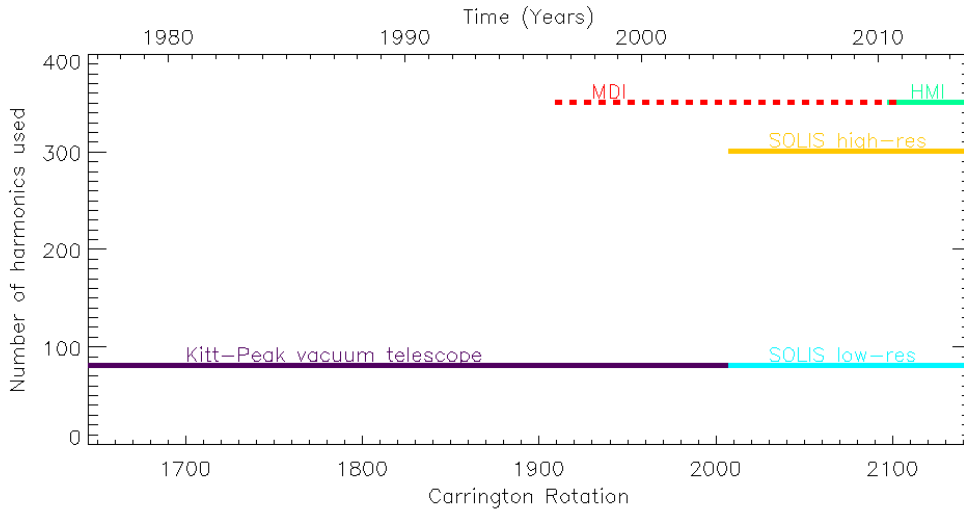


Figure 2.2: Graph showing the time period and number of harmonics for each of the different PFSS models used in this thesis.

Kitt-Peak and SOLIS include considerable polar field correction.

2.4 Finding the magnetic topology of our global potential field models

In order to find all the features of the magnetic topology of a magnetic field in a numerical grid we use three steps. First we need to find the null points. We do this by using the trilinear method [Haynes and Parnell, 2007]. Secondly, we need to characterise the null points and determine their properties which we do by linearisation of the field close to the null. Finally, we apply the separatrix-surface finding code [Haynes and Parnell, 2010] to trace out the separatrix surfaces and find the separators and spines and hence the magnetic skeleton. These three steps are described in detail in this section.

2.4.1 Trilinear method for finding null points

Given a vector field specified over a numerical grid it is desirable to interpolate this field to sub-grid resolution in order to trace field lines and to find null points in the field. Generally, provided the field is reasonably well resolved, it is adequate to approximate the field within a grid cell using trilinear interpolation [Haynes and Parnell, 2007]. The null finding method used here employs the trilinear method to interpolate the field to sub-grid resolution. This method has been shown to be more accurate than other null finding methods, such as Greene’s method, for numerical magnetic fields that are non-linear [Haynes and Parnell, 2007].

The trilinear null finding method has three steps to it. The first step is a reduction phase where every cell that definitely does not contain a null is excluded. The second phase identifies which of the remaining cells really does contain a null point and the third stage finds the sub-grid resolution position of the null point. To begin, we describe trilinear interpolation which is used in the second and third stages.

Trilinear Interpolation

We begin by considering a function, f , specified on the corners of a grid cell which we normalise so each cell has a length of 1 in every dimension. We first interpolate linearly along an edge of the grid cell where we have $f(0)$ and $f(1)$ specified at the corners of this edge, such that

$$f(x) = f(0) + x(f(1) - f(0)), \quad x \in [0, 1] \quad (2.34)$$

where x is the proportion of the way along the grid cell edge. We can then expand this to two variables where we know $f(x, y)$ at $(x, y) = \{(0, 0), (1, 0), (0, 1), (1, 1)\}$. We let $p_1(x)$ be the value of f at the point $(x, 1)$ on the top edge of the cell and $p_0(x)$ be the value of f at the point $(x, 0)$ on the bottom edge of the cell. Thus, from 2.34,

$$p_0(x) = f(0, 0) + x(f(1, 0) - f(0, 0)) \quad (2.35)$$

$$p_1(x) = f(0, 1) + x(f(1, 1) - f(0, 1)). \quad (2.36)$$

We can then interpolate linearly in $y \in [0, 1]$ between $p_1(x)$ and $p_0(x)$ to find,

$$\begin{aligned} f(x, y) &= p_0(x) + y(p_1(x) - p_0(x)) \\ &= f(0, 0) + (f(1, 0) - f(0, 0))x + (f(0, 1) - f(0, 0))y \\ &\quad + (f(1, 1) - f(0, 1) - f(1, 0) + f(0, 0))xy. \end{aligned} \quad (2.37)$$

Thus, from the values of f at each 2D grid cell corner we can find f at any given point (x, y) in the cell.

We wish to not only find the value of f at any position, but to determine the location of null points where the components of the magnetic field equal zero. To do this we will need to know how to locate zeros of any two components of the magnetic field on one of the faces of a 3D grid cell. So let us now consider the pair of bilinear simultaneous equations:

$$f_1(x, y) = a_1 + b_1x + c_1y + d_1xy = 0 \quad (2.38)$$

$$f_2(x, y) = a_2 + b_2x + c_2y + d_2xy = 0, \quad (2.39)$$

combining these we get quadratic equations in x and y which we can solve to give us the locations at which $f_1 = f_2 = 0$:

$$\begin{vmatrix} a_1 & a_2 \\ c_1 & c_2 \end{vmatrix} + \left(\begin{vmatrix} a_1 & a_2 \\ d_1 & d_2 \end{vmatrix} + \begin{vmatrix} b_1 & b_2 \\ c_1 & c_2 \end{vmatrix} \right) x + \begin{vmatrix} b_1 & b_2 \\ d_1 & d_2 \end{vmatrix} x^2 = 0 \quad (2.40)$$

$$\left| \begin{array}{cc} a_1 & a_2 \\ b_1 & b_2 \end{array} \right| + \left(\left| \begin{array}{cc} a_1 & a_2 \\ d_1 & d_2 \end{array} \right| + \left| \begin{array}{cc} b_1 & b_2 \\ c_1 & c_2 \end{array} \right| \right) y + \left| \begin{array}{cc} c_1 & c_2 \\ d_1 & d_2 \end{array} \right| y^2 = 0. \quad (2.41)$$

These equations will give us two solutions for x and two for y which we can match to find correct pairs of solutions.

Similarly, we can extend this analysis to find f at a point $f(x, y, z)$ in a 3D grid cell by interpolating linearly in the z direction, by considering two points: $q_0(x, y)$ on the surface $z = 0$ and $q_1(x, y)$ on the surface $z = 1$. For ease we will now let $f(x, y, z)$ be represented by f_{xyz} .

$$\begin{aligned} f(x, y, z) = f_{xyz} &= q_0(x, y) + z (q_1(x, y) - q_0(x, y)) \\ &= f_{000} + (f_{100} - f_{000})x + (f_{010} - f_{000})y \\ &\quad + (f_{110} - f_{010} - f_{100} + f_{000})xy \\ &\quad + z [f_{001} + (f_{101} - f_{001})x + (f_{011} - f_{001})y \\ &\quad + (f_{111} - f_{011} - f_{101} + f_{001})xy \\ &\quad - (f_{000} + (f_{100} - f_{000})x + (f_{010} - f_{000})y \\ &\quad + (f_{110} - f_{010} - f_{100} + f_{000})xy)] \\ &= f_{000} + (f_{100} - f_{000})x + (f_{010} - f_{000})y \\ &\quad + (f_{001} - f_{000})z + (f_{110} - f_{100} - f_{010} + f_{000})xy \\ &\quad + (f_{101} - f_{100} - f_{001} + f_{000})xz + (f_{011} - f_{010} - f_{001} + f_{000})yz \\ &\quad + (f_{111} - f_{110} - f_{101} - f_{011} + f_{100} + f_{010} + f_{001} - f_{000})xyz \end{aligned} \quad (2.42)$$

This gives us a trilinear field specified within each grid cell. In the spherical system we are using we let the proportion of the way along the grid cell in the r -direction, θ -direction and ϕ -direction be x , y and z respectively.

The three steps describing the trilinear null finding method are as follows:

Step 1: Reduction Phase

Since a null point is a point where $\mathbf{B} = 0$, this means at this point, all components $B_i = 0$ for i , the coordinate system directions. A cell is bounded by eight corner grid-points at which B_r, B_θ, B_ϕ are specified. Assuming the field components do not go through more than one change of sign in the cell then for a component B_i to be zero somewhere in the cell it must change sign between at least 2 corners of the cell. If one or more magnetic field components are positive at all eight corners or negative at all eight corners then the cell definitely does not contain a null.

Step 2: Ascertaining Whether a Cell Contains a Null

Regions where a single magnetic field component, B_i , equals zero forms a surface in 3D space. These surfaces intersect the sides of the grid cell containing the null as

lines. When two of these surfaces intersect in a grid cell they intersect as a line. There are two possibilities either (1) this line forms a circuit inside the cell or (2) the line of intersection stretches through the sides of the cell and cuts two or more of the faces of the cell. We can neglect case (1) as it implies considerable sub-grid structure.

Considering case (2), first we find the lines where the two magnetic field components equal zero on the faces of the cell by interpolating the two magnetic field components on the faces of the cell using bilinear interpolation. As mentioned previously it is possible to solve a pair of bilinear equations to find the point of intersection of the lines $B_i(x, y) = B_j(x, y) = 0$, where x and y are the coordinates on the cell face (see Equations (2.38), (2.40) and (2.41)).

Once these equations have been solved to find a point of intersection we look at the sign of the third component of the magnetic field at the two intersection points on the faces. If there is a change of sign then we know that the cell contains a null point, but if there is no change in sign then we conclude that the cell does not contain a null point.

Step 3: Converging on the Exact Location of the Null Point

Once it has been decided that a cell contains a null point we need to find the position of the null within the cell to sub-grid resolution. We do this by applying a 3D Newton-Raphson method.

Since close to the null we have, $\mathbf{B} = \nabla\mathbf{B}|_{\mathbf{r}_0} \cdot (\mathbf{r} - \mathbf{r}_0)$, where \mathbf{r} is the position vector and \mathbf{r}_0 is the location of the null. Then $\mathbf{r} - (\nabla\mathbf{B}|_{\mathbf{r}_0})^{-1} \mathbf{B} = \mathbf{r}_0$.

We can obtain \mathbf{r}_0 by using successive approximations:

$$\mathbf{r}_{n+1} = \mathbf{r}_n - (\nabla\mathbf{B}|_{\mathbf{r}_n})^{-1} \mathbf{B}|_{\mathbf{r}_n}. \quad (2.43)$$

Near the null $\mathbf{B} \approx \mathbf{0}$ so $\mathbf{r}_n \rightarrow \mathbf{r}_0$.

Limitations of the Trilinear Null Finding Method

As with any null-finding method, this method works well as long as the grid is sufficiently fine. If the grid is not fine enough, for instance if there is more than one null in one cell then the trilinear method will not necessarily find both (or any of the nulls).

In this thesis a spherical grid is used which means the grid cell size increases with radius. However, the trilinear method should still be appropriate to use at all radial distances as the complexity of the field falls off with radius. However, the field close to the surface has a great deal of structure and so a pair of nulls could sit within a single grid cell. If we know that the structure is fine in a certain area it is valid to use trilinear interpolation to interpolate points between the grid-points to make a finer mesh. This finer mesh will allow for more complexity within a cell and hence find more of the null points if they exist.

2.4.2 Finding null-point properties

In order to find the separatrix surface from a null point several pieces of information about the properties of the null need to be found. We need to find the approximate direction of the spine and the plane of the fan, and whether the null is positive or negative. We can find all this information from the eigenvectors and eigenvalues of the matrix describing the linearised field around the null (see Section 1.4.2). The numerical method used to find these depends on whether the model is potential or non-potential. In this thesis only potential fields are considered so only this method is detailed here.

Potential nulls - power method

To find the null points in a potential field we use the power method (which is detailed below) to find the first two eigenvectors and eigenvalues and then we use the orthogonality of the eigenvectors in a potential field to find the third.

For a general vector \mathbf{u} and a diagonalisable 3×3 matrix \mathbf{M} with eigenvalues λ_1, λ_2 and λ_3 and eigenvectors $\mathbf{v}_1, \mathbf{v}_2$ and \mathbf{v}_3 , respectively, we can write

$$\mathbf{u} = c_1\mathbf{v}_1 + c_2\mathbf{v}_2 + c_3\mathbf{v}_3, \quad (2.44)$$

where c_i are the components of \mathbf{u} in eigenvector space. Pre-multiplying this by \mathbf{M} gives

$$\mathbf{M} \cdot \mathbf{u} = c_1\lambda_1\mathbf{v}_1 + c_2\lambda_2\mathbf{v}_2 + c_3\lambda_3\mathbf{v}_3. \quad (2.45)$$

Repeating this step n times gives

$$\mathbf{M}^n \cdot \mathbf{u} = c_1\lambda_1^n\mathbf{v}_1 + c_2\lambda_2^n\mathbf{v}_2 + c_3\lambda_3^n\mathbf{v}_3. \quad (2.46)$$

Given $|\lambda_1| \geq |\lambda_2| \geq |\lambda_3|$ then as $n \rightarrow \infty$ the term involving λ_1 will dominate therefore:

$$\mathbf{M}^n \cdot \mathbf{u} \approx \mathbf{M}^n \cdot c_1\mathbf{v}_1 \approx c_1\lambda_1^n\mathbf{v}_1. \quad (2.47)$$

Hence, by using Equation 2.47 with sufficiently large n we find a vector parallel to the eigenvector corresponding to the dominant eigenvalue. The eigenvalue can then be found quite easily from the ratio of $\mathbf{M} \cdot c_1\mathbf{v}_1$ to $c_1\mathbf{v}_1$.

The second eigenvector-eigenvalue pair is found using a similar method. If λ_i is an eigenvalue of \mathbf{M} with corresponding eigenvector \mathbf{v}_i then $1/\lambda_i$ will be an eigenvalue of \mathbf{M}^{-1} . So by using the power method on \mathbf{M}^{-1} we can find the smallest eigenvalue of \mathbf{M} and its corresponding eigenvector.

The third eigenvector is found by using the fact that for a potential magnetic field all the eigenvectors are orthogonal. The third eigenvalue is found so $\nabla \cdot \mathbf{B} = 0$, which implies $\lambda_1 + \lambda_2 + \lambda_3 = 0$. If two eigenvalues are positive and one is negative then the null is positive and if two eigenvalues are negative and one is positive then the null is negative.

2.4.3 Method for finding separatrix surfaces

To find the separatrix surfaces we use the separatrix-surface finding code by Haynes and Parnell [2010]. This code takes as input: the numerical grid of magnetic field components; coordinates specifying the spatial separation of grid points; the locations of all the null points in the grid and for each null point: the sign of the null; a vector approximating the local direction of the spine and two vectors approximating the local plane of the fan surface.

The separatrix surface finding code begins by taking a ring of points close to the null in a plane given by the vectors that approximate the fan surface. Field lines are then traced from these points away from the null a small distance giving a new set of points. This new set of points is joined up to form a ring. Where gaps between neighbouring points in the ring are large extra points are added into the ring. Field lines are then traced out from the points on this ring to form a second new ring and this process is continued until the ring either hits the boundary of the grid or another null. If the ring encounters another null then it is broken. Either side of the null the points on the ring are moved to the spine of this null and the two pieces of the ring begin to propagate separately, one along each spine of the null.

The field line between the two nulls is traced backwards by linking points on the previous rings and this is marked as a separator. Each separator can be counted twice: once from the first null to the second and once from the second null to the first. We find a list of unique separators by finding the maximal distance between two separators that connect the same two nulls and if this distance is sufficiently small then we say that they are the same separator.

In addition to null points, our global coronal model has two other structures that we would like to trace surfaces from: the HCS null-line as described in Section 3.1 and bald-patch separatrix surfaces as described in Section 3.3. The separatrix surface finding code enables us to trace out other surfaces from these lines which we call *rakes*. These surfaces are traced out in a similar way as separatrix surfaces but instead of starting on a circle in the fan-plane of a null they start on a specified line. Also, when rake surfaces intersect with other rake surfaces we do not classify them as separators.

Chapter 3

Topological Configurations in the Global Solar Corona

In this thesis, since we are only looking at potential fields where there are no twisted structures we use the term *magnetic topology* to refer to the structure and form of the magnetic skeleton.

By studying the magnetic topology or magnetic skeleton we can find a robust description of the magnetic field that can only be altered by reconnection processes. We investigate the topology by using the magnetic skeleton as described in Section 1.4.3. Magnetic topology in three dimensions can become very complex. In this Chapter, features seen in global coronal magnetic field models are described with particular emphasis on configurations found in the potential-field source-surface (PFSS) model which was described in Section 2.2.

3.1 HCS and HCS curtain

As described in the previous chapter, at the boundary of the PFSS model the magnetic field becomes purely radial. This means that any inversion in the direction of the magnetic field will form a line of null points known as a *null line*. The assumption in the PFSS model is that this null line forms the base of the *heliospheric current sheet* which extends out into the heliosphere. We can trace field lines forward and backwards from the null line down to the solar surface. We call the surfaces created by these field lines the *HCS curtains*. It should be noted that the heliospheric current sheet is a well known and observed feature and is not only associated with the PFSS model. Figure 3.1 shows a cartoon of the HCS curtains which separate closed field on the Sun from open field associated with the global dipole. The outlines of these HCS curtains can be seen in white-light coronagraphs (see Figure 1.7, Section 1.3) and are known as *streamers* or *helmet streamers*.

In reality of course, the surface at which the field becomes approximately radial is not a perfect sphere as has been assumed in the PFSS model. However, a fairly good correlation has been found between the location of the source surface null line from

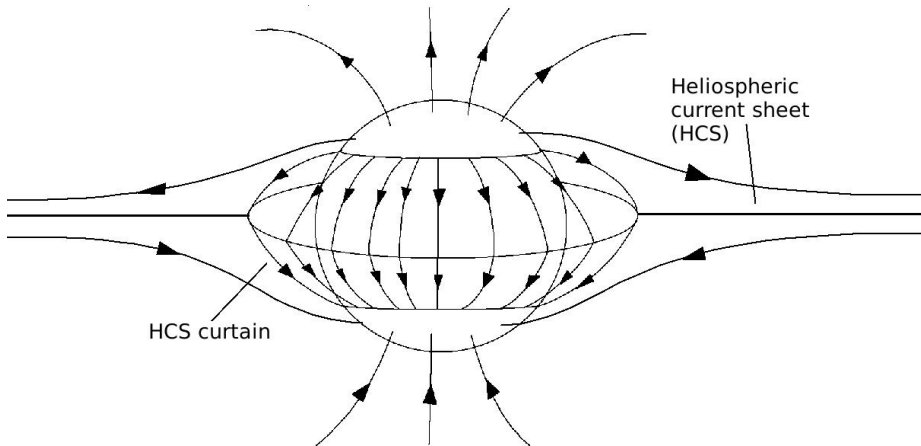


Figure 3.1: Cartoon of field lines traced from heliospheric current sheet (HCS) forming the HCS curtain.

PFSS models and the observed HCS from in-situ measurements [e.g., Burton et al., 1994].

3.2 Pseudostreamers

Sometimes streamers are seen that are not associated with the heliospheric current sheet, these are called pseudostreamers. An example of an observation of a pseudostreamer is given in Figure 1.8. These differ from helmet streamers in that they have two lobe structures underneath them as opposed to one. A helmet streamer has just one primary polarity inversion line along the photosphere underneath it whereas a pseudostreamer has two. Figure 3.2 shows a cartoon of the magnetic configurations of different kinds of streamers. Figure 3.2a shows an isolated helmet streamer. The current sheet (red line) forms as the two open field regions either side of it are oppositely directed. Figure 3.2b shows a pseudostreamer, there is no current sheet associated with this structure as all the open field is orientated in the same direction. Instead the enhanced plasma density that is observed in coronagraphs is centred around a separatrix surface (orange line). There are two closed field lobes below the pseudostreamer and two polarity inversion lines. However, two polarity inversion lines do not guarantee a pseudostreamer. Figure 3.2c shows a structure with two helmet streamers side by side which we call a *double streamer* [e.g., Crooker et al., 1993, Rachmeler et al., 2014]. This double streamer has the same number of PILs as the pseudostreamer but the centre polarity in this case is strong enough or large enough to become open field [see for example Priest, 1982].

Three-dimensional topological features that could be associated with pseudostreamers are described in Sections 3.5.4, 3.5.5 and 3.5.6.

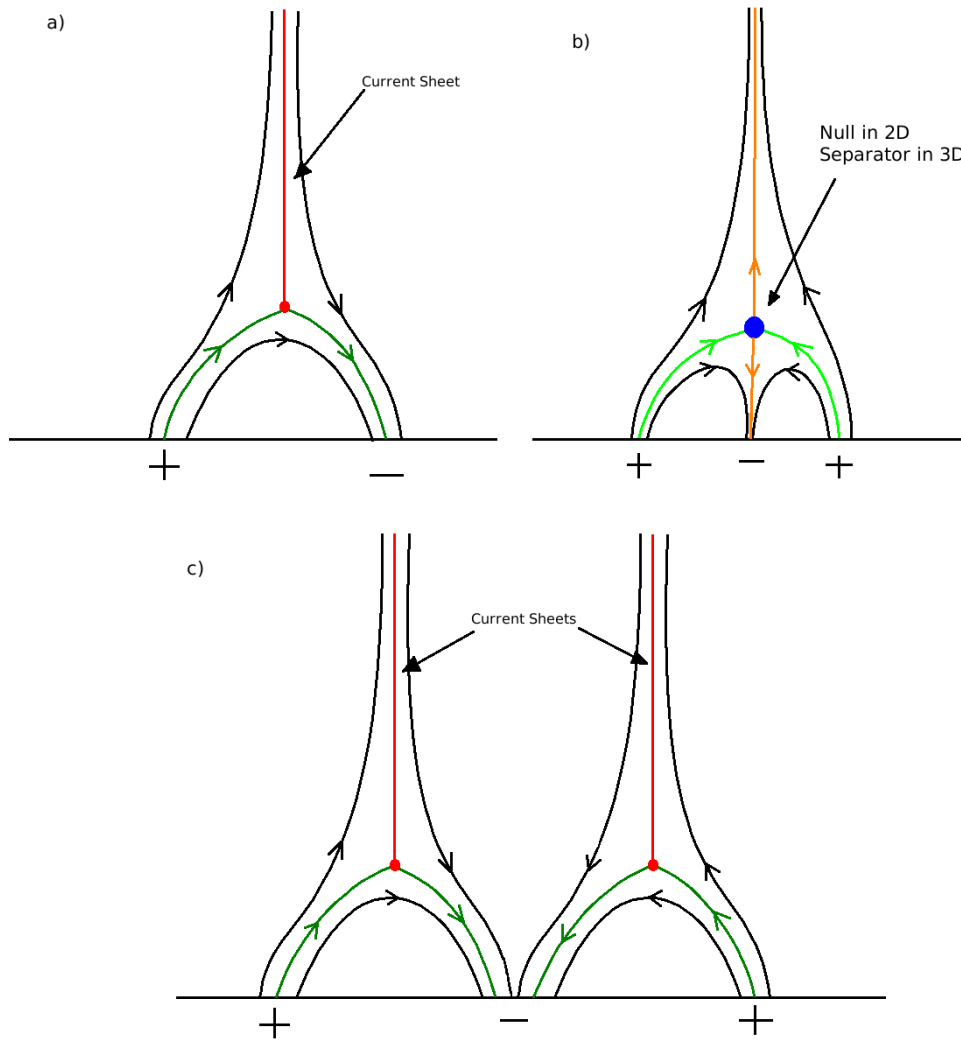


Figure 3.2: Cartoon of different types of streamers. (a) shows a helmet streamer, there is one arch of field lines below a null line (red dot) and current sheet (red line), the HCS curtains are shown as dark green lines. (b) shows a pseudostreamer there are two arches of field lines below a null-line or separator (blue dot) there is no current sheet but there is a separatrix surface dividing the two open field regions (orange and green lines). (c) shows two helmet streamers side by side, sometimes called a double streamer, colours as in (a).

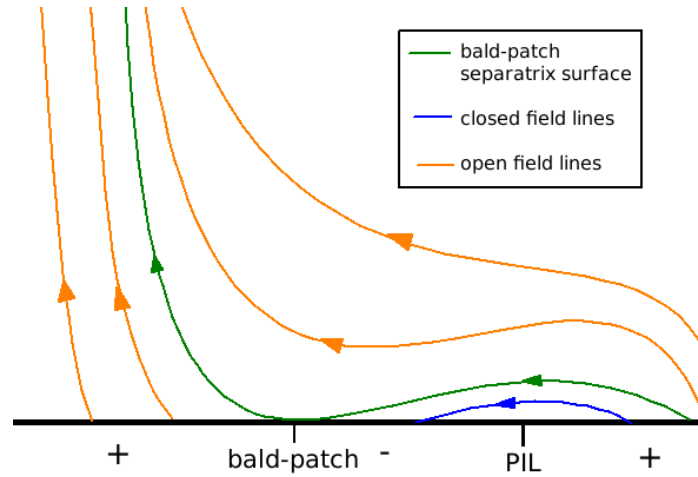


Figure 3.3: Cartoon of field lines around a bald-patch. Green line is bald-patch field-line, blue line is a closed field-line and orange lines are open field-lines.

3.3 Bald-patch separatrix surfaces

In addition to considering separatrix surfaces from null points and the HCS null line we can also consider separatrix surfaces associated with *bald-patches* [Titov et al., 1993, 2011]. A bald-patch occurs when a field line touches the solar surface and is concave upwards. Figure 3.3 shows a 2D bald-patch separatrix surface (BPSS). The point where the field line touches the photosphere is called a bald-patch. In three dimensions, a bald-patch would be a line on the photosphere with the BPSS traced from it in both directions along the magnetic field.

To find bald-patches we iterate through three steps. A schematic of this method is shown in Figure 3.4. First, we find all polarity inversion lines on the photosphere (lines separating positive and negative polarity magnetic field: black line in Figure 3.4 left panel), then for each point on the polarity inversion line we calculate the direction of the field a small distance above it. If the magnetic field above the polarity inversion line is directed from negative to positive, we have a bald patch (see Figure 3.4).

Using this method we generate line segments on the solar surface from which we can trace separatrix surfaces. The number of bald-patches is related to the complexity of the photospheric magnetic field and, as such, in extrapolations from high-resolution data (such as that from MDI and HMI) there are too many bald-patches for us to calculate. With this in mind we only look for bald-patches and their associated separatrix surfaces in low-resolution extrapolations such as those from Kitt-Peak and low-resolution SOLIS data.

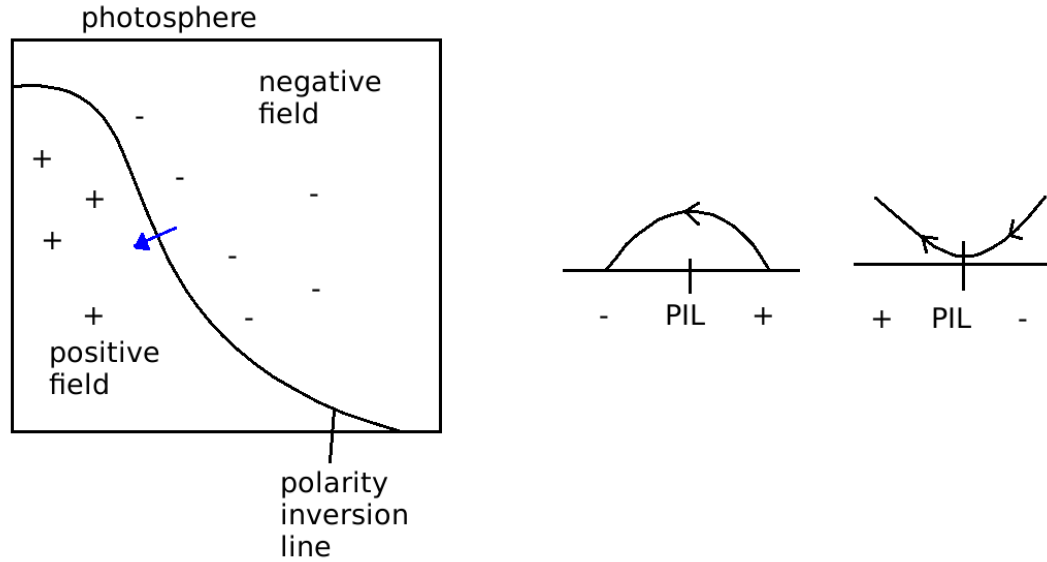


Figure 3.4: Schematic of finding bald patches by checking the field above the polarity inversion line.

3.4 Global separatrix surface structures

As described in Section 1.4.3, separatrix surfaces are formed in 3D from field lines passing through a null point and lying in the null's fan plane. The shape of separatrix surfaces is affected by the coronal magnetic field. In the corona, these separatrix surfaces can be bounded by spines from a null of opposite sign or the photosphere. Additionally, in our model they can be bounded by the outer boundary (source surface) and one of the HCS curtains. This section will describe several examples of the kinds of separatrix surface structures that are found.

3.4.1 Separatrix domes

Separatrix domes [e.g., Close et al., 2005, Titov et al., 2011] are closed domes made up of one or more separatrix surfaces that enclose completely a patch of field on the photosphere. Reconnection at the null point of such structures have been studied in detail by many authors [e.g., Antiochos et al., 1999, Masson et al., 2009, 2012, Zhang et al., 2012, Baumann et al., 2013, Pontin et al., 2013] and it has been found that large amounts of flux can be transferred from open to closed regimes and visa versa at such a location. Separatrix domes form over a patch of magnetic polarity on the photosphere that is stronger and of the opposite sign to the surrounding field: this is often called a *parasitic polarity*.

The simplest case is a dome made from a single separatrix surface originating from one null point (see Figure 3.5a). A separatrix dome intersects with the solar surface

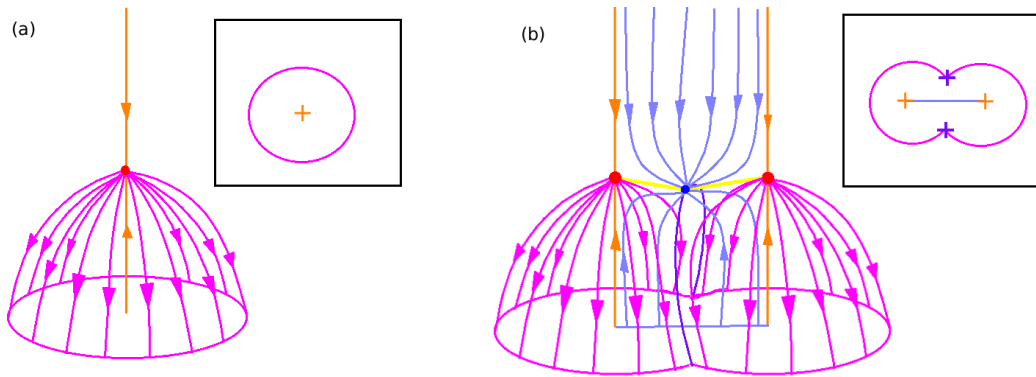


Figure 3.5: Cartoon of separatrix domes. Pink field lines show the separatrix surfaces of positive nulls, orange field lines show the spines of positive nulls, blue and purple field lines show the separatrix surface and spine lines of negative nulls, respectively, and yellow lines represent separators. (a) shows a separatrix dome made of the separatrix surface from a single null, (b) shows a separatrix dome made from the separatrix surfaces of two nulls and cut by an open separatrix curtain from a third null of opposite sign. The footprints of these field structures are shown in the black boxes where the pink and blue lines correspond to the intersection of positive and negative separatrix surfaces, respectively, with the photosphere and the orange and purple crosses correspond to the intersection of positive and negative spines, respectively, with the photosphere.

forming a closed loop. This means that all field lines with foot-points inside this loop map back down to the photosphere to points inside this loop. Such a loop can be made from the intersection of multiple separatrix surfaces with the photosphere. In this case, these separatrix surfaces meet along the spines from nulls of opposite sign. In the case of a separatrix dome made from two separatrix surfaces (see Figure 3.5b), three nulls are present, two of the same sign whose separatrix surfaces form a dome and the one of opposite sign, whose separatrix surface is bounded by the spines of the two dome nulls and creates an *open separatrix curtain* (Section 3.4.2). The spines of the separatrix curtain null intersect with the photosphere.

In Figure 3.5 the spines of the dome nulls extend out to the outer boundary of the model, however, in reality many domes form in closed field regions such as underneath the HCS curtains and so their spines trace back down to the photosphere. In the examples in Section 3.5.1 we see both types.

3.4.2 Separatrix Curtains

Separatrix curtains [Titov et al., 2011] are separatrix surfaces that intersect with the source surface and are referred to as *open* if they do not form a *disconnected open field region* and *closed* if they do.

Open separatrix curtains are separatrix surfaces that intersect with the source

surface in a line segment. They are bounded above by the source surface, below by the photosphere and to the side by either two spines or one spine and the HCS curtain. An example of an open separatrix curtain bounded by two spines is given in Section 3.5.2 (Figure 3.9) which forms between the spines of the two nulls whose separatrix surfaces form the separatrix dome. An example of a magnetic field configuration with an open separatrix curtain bounded by one spine and the HCS is given in Section 3.5.3 (Figure 3.10). Open separatrix curtains do not create topologically distinct flux domains and thus do not create disconnected open field regions.

Closed separatrix curtains are separatrix surfaces that intersect with the outer boundary forming either a closed loop or are connected on both ends to the HCS curtains. These closed separatrix curtains map down to the photosphere and enclose field from the photosphere all the way to the source surface, thus creating a disconnected open field region. Examples of a closed separatrix curtain made from the separatrix surface from one null and two nulls are given in Sections 3.5.4 and 3.5.5, respectively.

3.4.3 Separatrix caves and tunnels

In the case of a separatrix dome made from two separatrix surfaces from two nulls the configuration contains two nulls of one polarity and one of the opposite polarity. This opposite polarity null has spines that both map down to the photosphere. The separatrix surfaces of the two dome nulls then meet along the spines of this null. If we have a configuration with only two nulls of opposite polarity to each other with the separatrix surface of one of them closed to the photosphere and bounded by the spine of the other null then a topological configuration can emerge where the separatrix surface does not form a closed curve on the photosphere but rather a curve with a break. If the curve has one break in it then it is referred to as a *separatrix cave*. Figure 3.6a shows a cartoon of the topology of a separatrix cave. In this case the separatrix surface from the positive null point is closed to the photosphere and also bounded by the spines of the negative null, so it forms a cave-like, as opposed to dome-like structure. The separatrix surface from the negative null forms an open separatrix surface.

Figure 3.6b shows a cartoon of a separatrix tunnel. Here the configuration has three null points: two with closed spines and one with an open spine. There are two breaks in the intersection of the negative separatrix surface with the photosphere creating a tunnel feature. This tunnel structure is similar to the structure described by Titov et al. [2011] that creates a disconnected open field region. A separatrix tunnel and associated closed separatrix curtain is one example of a topological structure that could be observed as a *pseudostreamer* in a coronagraph image. It has been suggested that these pseudostreamer structures could be important for eruptions [e.g., Titov et al., 2012].

The pattern of polarities on the photosphere underneath a separatrix tunnel is the same as the pattern of polarities on the photosphere underneath two helmet streamers side by side and the resulting configuration depends on the strength and separation

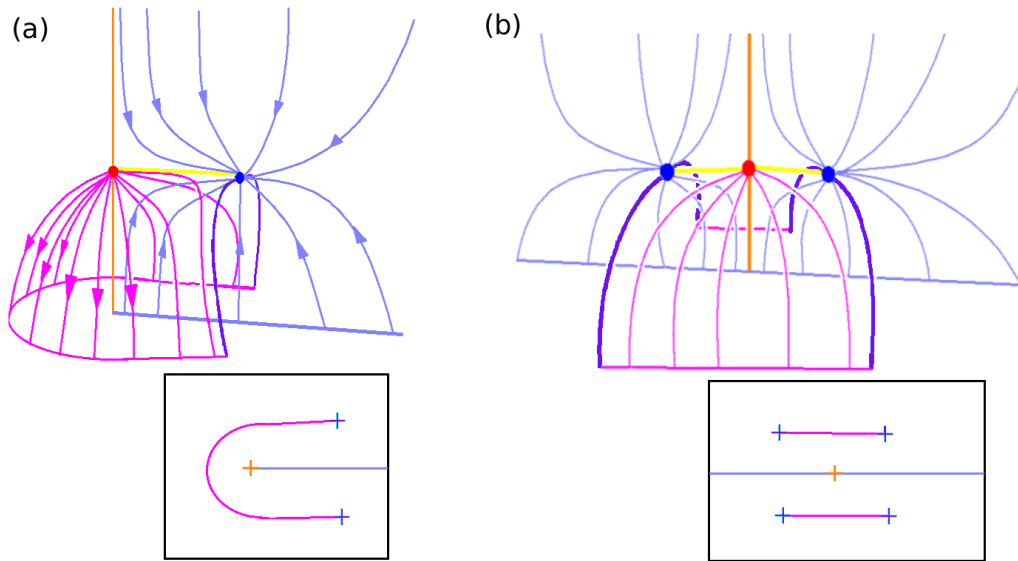


Figure 3.6: Cartoon of a separatrix cave (a) and a separatrix tunnel (b). Pink field lines show the separatrix surfaces of positive nulls, blue field lines show the separatrix surfaces of negative nulls. Orange and purple field lines show the spine lines of positive and negative nulls respectively. Yellow lines show separators. The footprints of these field structures are shown in the black boxes where the pink and blue lines correspond to the intersection of positive and negative separatrix surfaces, respectively, with the photosphere and the orange and purple crosses correspond to the intersection of positive and negative spines, respectively, with the photosphere.

of the sources.

3.5 Example Topological Structures in Global Magnetic Fields

By inserting regions of positive or negative polarity onto the surface of a sphere the topological structures discussed above can be recreated. To begin with, we form a grid of 360 points in longitude and 180 points in sine latitude. We then apply a gradient that goes from -10G at the south pole to 10G at the north pole which is constant in the longitudinal direction and increases linearly in the sine latitude direction in order to form a global dipole field. We then insert patches of field of different sizes and magnetic field strengths and smooth using the IDL smooth function with a width of 10. The patches of field inserted have the form:

$$B(x, y) = B_k \forall(x, y) : \left(\frac{x - a}{b} \right)^2 + \left(\frac{y - c}{d} \right)^2 = l, \quad (3.1)$$

where B_k is the field strength of the patch in Gauss, a and c are the grid coordinates of the centre of the patch in longitude and sine latitude coordinates, respectively, and b, d and l determine the size of the patch. We ensure flux balance on the photosphere by calculating the imbalance of flux and distributing it evenly across the synthetic magnetogram. The resulting synthetic magnetogram is then used as the boundary condition in the PFSS extrapolation code described in Section 2.2 to create the magnetic field in the corona.

3.5.1 Separatrix dome from one separatrix surface

A separatrix dome created from a single separatrix surface is associated with a coronal null point residing over a region of the photosphere of opposite polarity flux to the surrounding region. To create this field a single polarity patch is inserted onto the dipolar synthetic magnetogram. We use the parameters $B_1 = -30$, $a = 200$, $c = 160$, $l = 10$ and $b = d = 1$. A 3D plot of the topology of this configuration is shown in Figure 3.7. This separatrix dome sits outside the HCS curtain. The footprint of the separatrix dome can be seen by taking a cut in the separatrix surface at the photosphere (see Figure 3.7b). This example is chosen because the dome sits outside the HCS curtains to enable it to be seen clearly, however, many domes occur under the HCS curtains. An example of such a dome is shown in Figure 3.8 and is produced using the following patches of field:

- First patch: $B_1 = 5$, $a = 200$, $c = 120$, $l = 10$ and $b = 2.0$ and $d = 1$
- Second patch: $B_2 = -5$, $a = 200$, $c = 140$, $l = 10$ and $b = 3.0$ and $d = 1$.

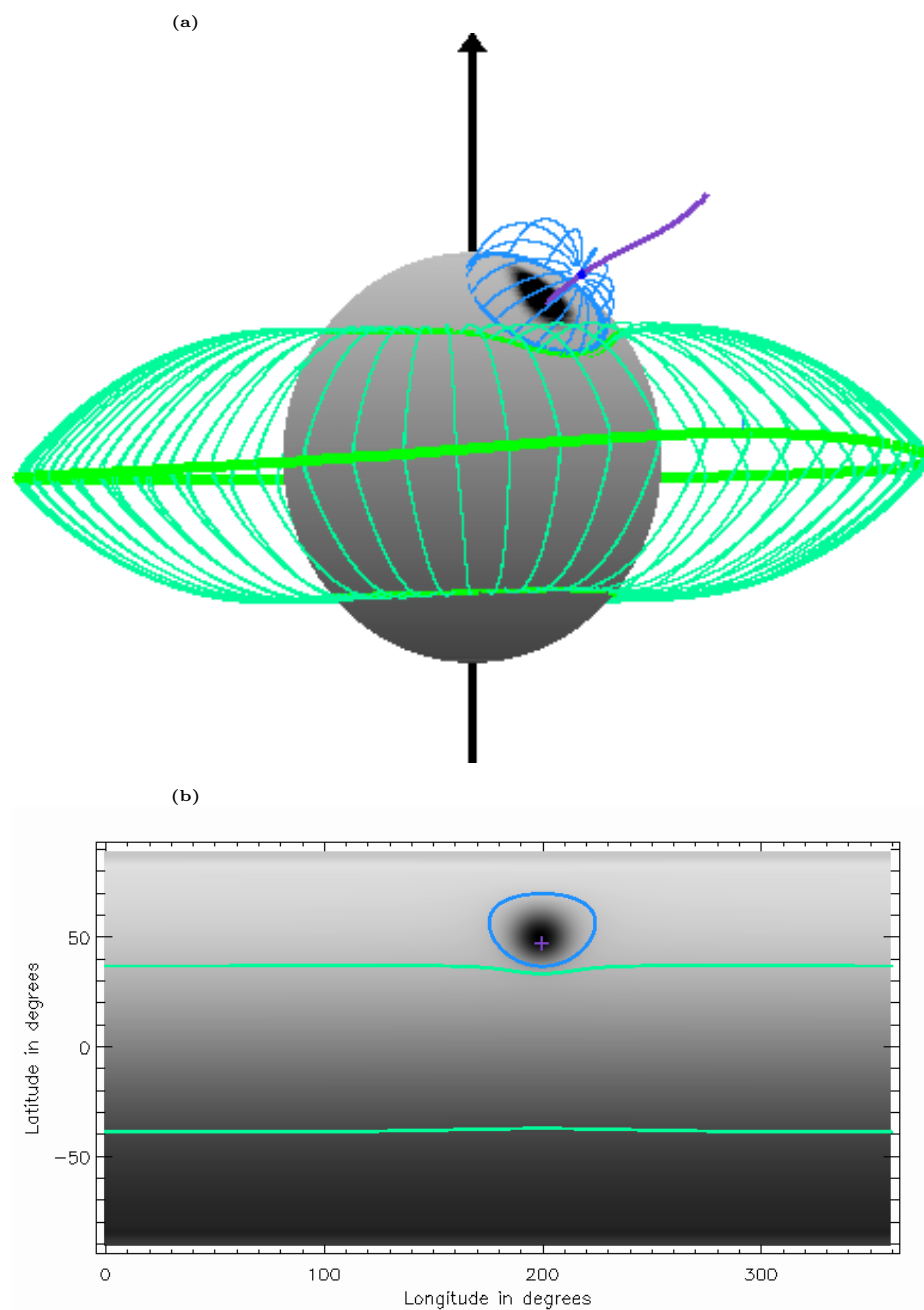


Figure 3.7: Example of topology of a separatrix dome from one separatrix surface from one negative null near the north pole. (a) shows the 3D global topology: blue dot is the negative null, purple line is the spine from this null, light blue lines are field lines in the separatrix surface and green lines are field lines in the HCS curtain. (b) shows the footprint of this topology: the background is shaded with the radial component of the magnetic field at the photosphere saturated at $\pm 30 \text{ Mx/cm}^2$, green lines are the intersection of the HCS curtain with the base, blue lines are the intersection of the separatrix surface with the base, purple cross is the intersection of the spine with the base.

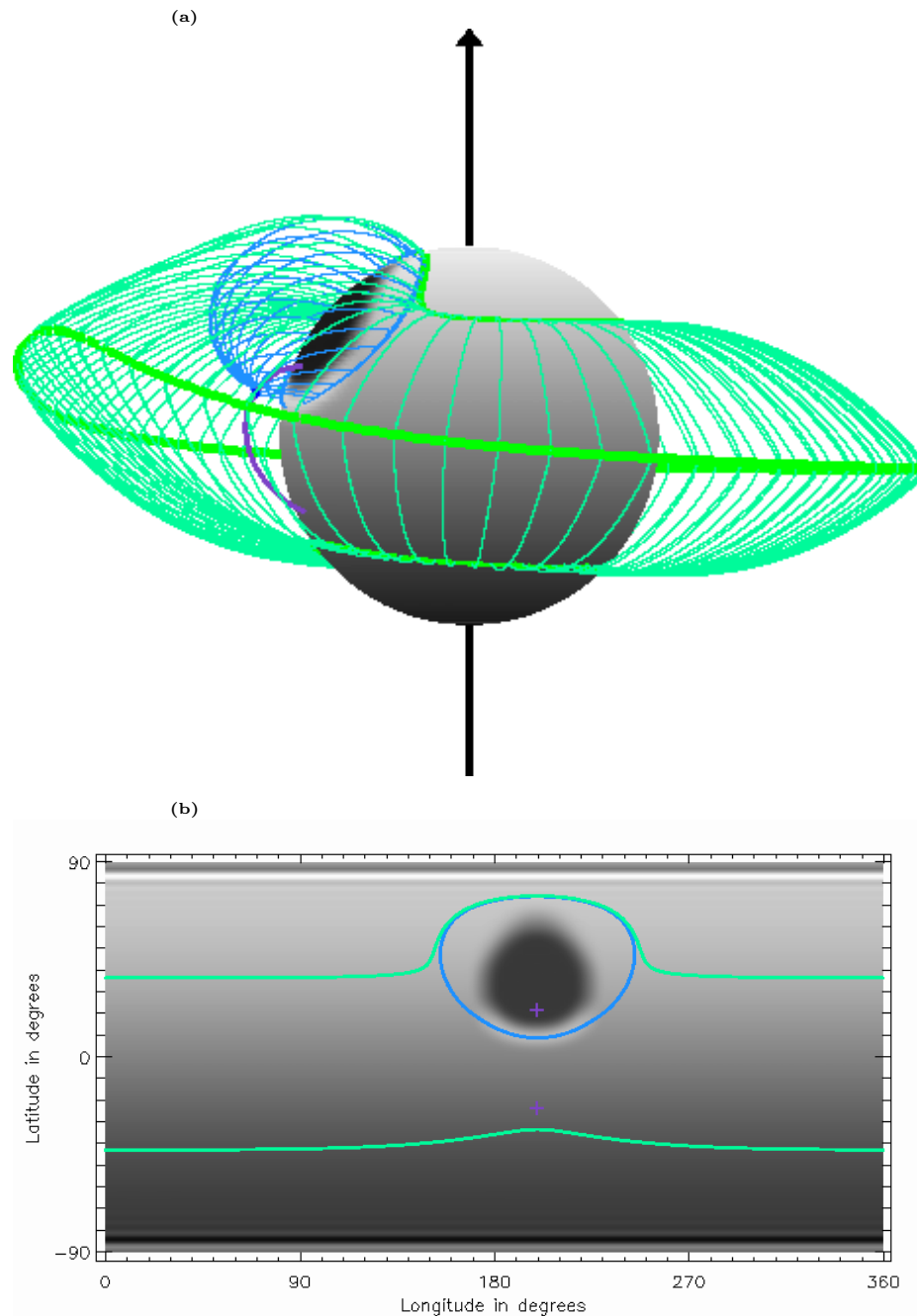


Figure 3.8: Example of a topology of a separatrix dome under the HCS curtains from the separatrix surface from one negative null near the north pole. (a) shows the 3D global topology: blue dot is the negative null, purple line is the spine from this null, blue lines are field lines in the separatrix surface and green lines are field lines in the HCS curtain. (b) shows the footprint of this topology: the background is shaded with the radial component of the magnetic field at the base saturated at $\pm 15 \text{ Mx/cm}^2$, green lines, blue lines and purple crosses are the intersection of the HCS curtain, negative separatrix surface and negative spines with the base.

For a separatrix dome under the HCS curtains both spines connect back down to the photosphere (purple crosses in Figure 3.8b).

We can characterise domes from one null point by checking only one condition, namely, do any separators connect to the null point. The only configuration in our global field models that can arise from a null point with no separator connections is the case of an isolated separatrix dome.

3.5.2 Separatrix dome from two separatrix surfaces

A separatrix dome from two separatrix surfaces can be associated with two parasitic polarity regions sitting very close to one another. In order to create such a topological configuration six patches of magnetic field have been inserted into the synthetic magnetogram with a dipolar field. They are inserted in ascending numerical order and only the field strength of the uppermost patch is used if several overlap. The parameters for these patches are given as follows:

- First patch: $B_1 = -10$, $a = 200$, $c = 145$, $l = 10$ and $b = 2.5$ and $d = 1$
- Second patch: $B_2 = -10$, $a = 200$, $c = 160$, $l = 10$ and $b = 2.5$ and $d = 1$
- Third patch: $B_3 = 20$, $a = 200$, $c = 150$, $l = 10$ and $b = 2.5$ and $d = 1$
- Fourth patch: $B_4 = -20$, $a = 170$, $c = 150$, $l = 10$ and $b = 2.5$ and $d = 1$
- Fifth patch: $B_5 = -20$, $a = 230$, $c = 150$, $l = 10$ and $b = 2.5$ and $d = 1$
- Sixth patch: $B_6 = 15$, $a = 200$, $c = 110$, $l = 10$ and $b = 5$ and $d = 1$.

Figure 3.9(a) shows the 3D structure of the potential field extrapolated from this photospheric field. The separatrix dome is made of the separatrix surfaces from two negative null points which are bounded by the spine of a positive null point that sits between them and the photospheric surface. The separatrix surface from this positive null point is bounded by the spines of the two negative nulls and intersects the source surface at $2.5R_\odot$ in a segment that is not connected to the HCS neutral line and hence is referred to as an *open separatrix curtain*. The separatrix surface from the positive null point intersects the separatrix surfaces of the two negative null points producing a pair of separators that link the three nulls in a line.

The footprint on the photosphere of this topological structure is shown in Figure 3.9b. The open separatrix curtain extends down below the separators to the photosphere and its intersection with the photosphere is shown by the pink curve. It is bounded by the spines from the two negative nulls. The separatrix dome forms a closed curve in its intersection with the photosphere which means that it completely encloses all field inside this dome. The footprint of the open separatrix surface is contained within the dome's closed loop.

Similar to the dome formed from a single separatrix surface, this type of dome can also form within the HCS curtains. If this is the case, the open separatrix curtain

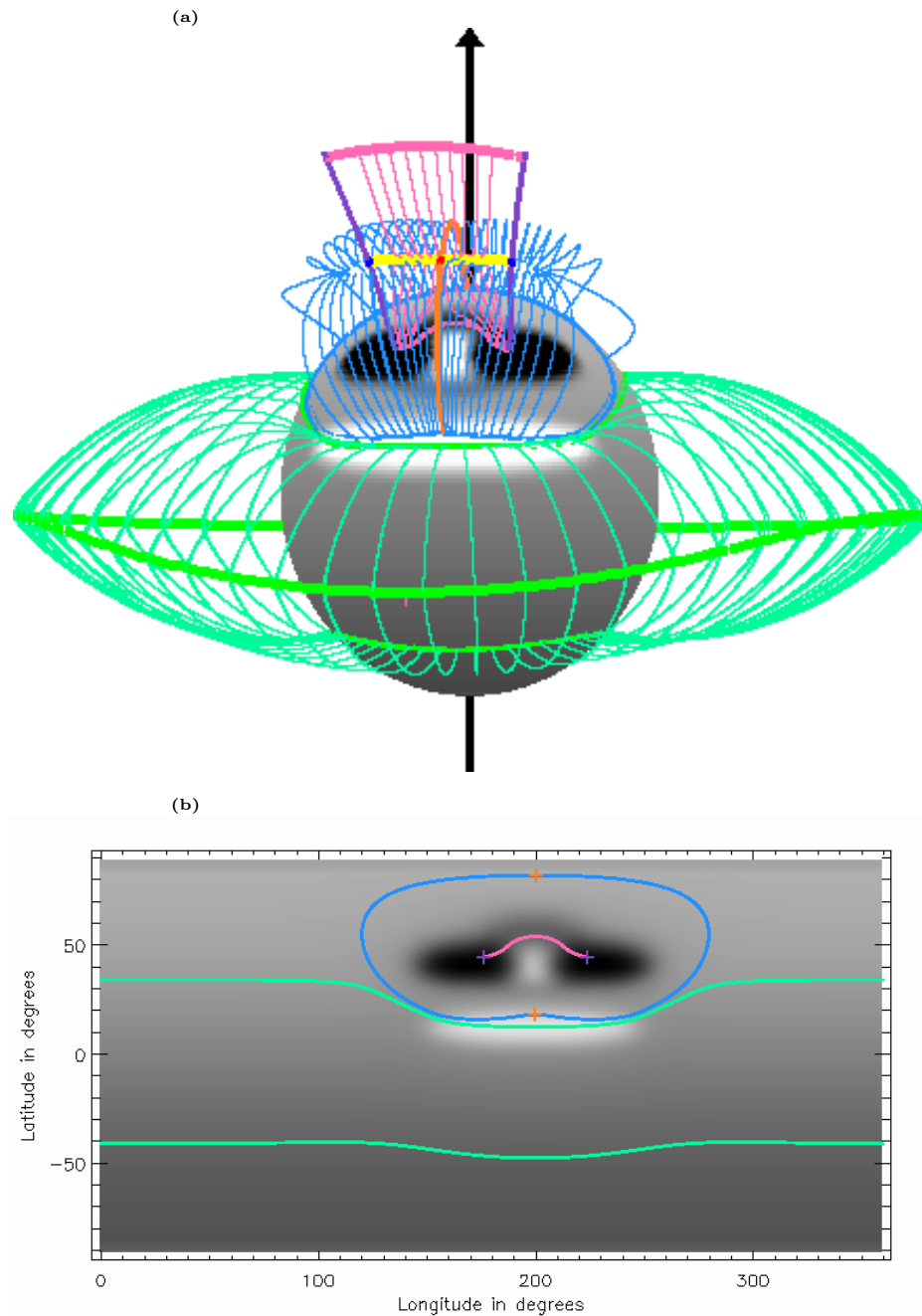


Figure 3.9: Example of a magnetic topology with a negative separatrix dome made from the separatrix surfaces from two negative nulls and bounding the separatrix surface of a positive null. (a) shows the 3D global topology: blue/red dots are negative/positive nulls, purple/orange lines are the spines from negative/positive nulls, blue/pink lines are field lines in the separatrix surfaces from negative/positive nulls and green lines are field lines in the HCS curtain. (b) shows the footprint of this structure on the photosphere: the background is shaded with the radial component of the magnetic field and is saturated at $\pm 20 \text{ Mx/cm}^2$, blue/pink lines are the intersection of the negative/positive separatrix surfaces with the photosphere, purple/orange crosses are the spines from negative/positive nulls and green lines are the intersection of the HCS curtain with the photosphere.

would fold back down to the photosphere forming a closed tunnel-type structure (such structures are discussed later in this thesis in Chapter 5) Also, separatrix domes can be formed from more than two separatrix surfaces to create more elongated or irregularly shaped dome-type structures.

If a separatrix dome has a spine (or spines) that are open in the sense that it intersects with the source surface such as the examples given in Figures 3.7 and 3.9, reconnection at the null point can lead to transfer of flux between open and closed field regimes.

3.5.3 Separatrix cave

A separatrix dome will always form a closed loop in its intersection with the photosphere. A separatrix surface that forms a closed loop with one opening in its intersection with the photosphere is referred to as a *separatrix cave*. The opening can form in a variety of different circumstances including where the cave joins on to the HCS curtain. An example of such a separatrix cave (Figure 3.10) can be created using patches of the form shown in Equation (3.1) and the parameters:

- First patch: $B_1 = 20$, $a = 205$, $c = 90$, $l = 10$ and $b = 3.0$ and $d = 1$
- Second patch: $B_2 = -20$, $a = 200$, $c = 130$, $l = 10$ and $b = 5.0$ and $d = 2.0$
- Third patch: $B_3 = 15$, $a = 200$, $c = 170$, $l = 10$ and $b = 2.5$ and $d = 1$
- Fourth patch: $B_4 = -15$, $a = 230$, $c = 85$, $l = 10$ and $b = 1.0$ and $d = 2.5$.

Figure 3.10 shows an example of a separatrix cave topology. There are two coronal null points of opposite polarity in this field. The separatrix surface from the positive null is bounded by the spines of the negative null and the photosphere, which it intersects in a curve (see Figure 3.10b). The separatrix surface from the negative null extends up to the outer boundary above and down to the photosphere below. It is also bounded on one side by the HCS curtain and on the other by the spine of the positive null. Since this separatrix surface does not intersect the outer boundary as part of a closed curve we refer to this as an *open separatrix curtain*. The mouth of the separatrix cave opens out into the region underneath the HCS curtains. This must be the case since field-lines within the cave are closed and there is no separatrix barrier across the cave opening, therefore there can not be a discontinuous field-line mapping across the cave mouth so field-lines that cross the cave mouth must also be closed. As in the cases of the separatrix domes with open spines, reconnection at either of the nulls and/or the separators associated with the separatrix cave could lead to the creation of open magnetic field. This means that a separatrix cave and associated open separatrix curtain is a global topological structure could be associated with an eruptive event such as a coronal mass ejection or eruptive flare.

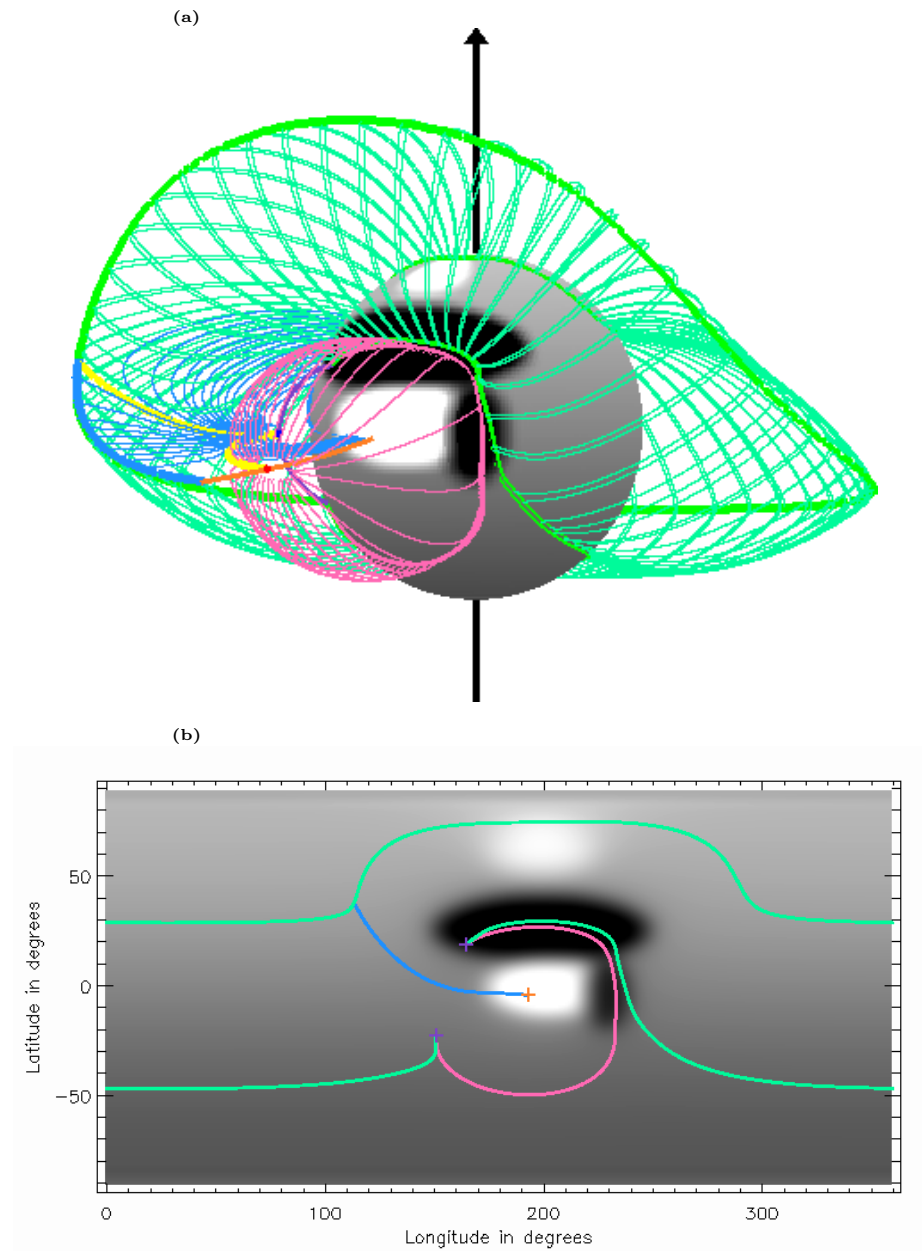


Figure 3.10: Example of a potential magnetic field with a separatrix cave formed from a positive separatrix surface to the south of the HCS curtain and a negative open separatrix curtain. (a) shows the 3D topology, (b) shows the footprint of the structure at the photosphere over contours of the radial magnetic field saturated at $\pm 15 \text{ Mx/cm}^2$. The colouring is the same as Figure 3.9

3.5.4 Separatrix tunnel

A separatrix tunnel can connect on both ends to the HCS curtains and in this case forms along with a closed separatrix curtain made of multiple separatrix surfaces. This means that a separatrix tunnel is more likely to form if the HCS becomes distorted, as it does during periods of solar maximum. To create an example field containing a separatrix tunnel, three patches of field need to be inserted into the dipolar synthetic magnetogram field using the scheme in Equation (3.1) and the parameters:

- First patch: $B_1 = 10$, $a = 200$, $c = 90$, $l = 10$ and $b = 2.5$ and $d = 1$
- Second patch: $B_2 = -20$, $a = 200$, $c = 130$, $l = 10$ and $b = 5.0$ and $d = 1$
- Third patch: $B_3 = 15$, $a = 200$, $c = 170$, $l = 10$ and $b = 2.5$ and $d = 1$

These flux patches cause the HCS to buckle towards the north pole and so creates a separatrix tunnel to the south. Figure 3.11a shows a 3D image of the topology of the potential field extrapolated from this synthesised magnetogram. In this configuration there are three coronal null points: two negative and one positive linked together by separators. The two negative nulls also connect to the HCS null line via null-HCS separators. The separatrix surface from the positive null is bounded by the spines of the two negative nulls and by the photosphere. The separatrix surfaces from the two negative nulls are bounded to the sides by the spine of the positive null and the HCS curtain and otherwise extend from the photosphere up to the source surface. Together these two negative separatrix surfaces form a separatrix curtain (blue surface) that is connected at both ends to the HCS curtains and maps down to the photosphere thus forming a *closed separatrix curtain*. This means any open field line that is traced from a negative patch on the photosphere will always stay the same side of this separatrix curtain. So, the closed separatrix curtain forms a disconnected open field region. The footprint of this configuration is shown in Figure 3.11b and it is clear that the two patches of negative open field are not connected to one another at the photosphere. Often it is easier to observe the structure by taking a cut in the separatrix surfaces at the outer boundary (see Figure 3.11c). The signature of this separatrix tunnel at the outer boundary is a closed separatrix curtain (blue line) connected on both ends to the HCS null line (green line) and composed of the separatrix surfaces from two nulls meeting at the spine of a null of opposite sign (purple cross).

3.5.5 Closed separatrix curtain from one null point

The separatrix tunnel is a way that a closed separatrix curtain made of two separatrix surfaces can form. However, in most cases closed separatrix curtains are only made up of one separatrix surface. We produce an example like this by setting up two patches:

- First patch: $B_1 = 5$, $a = 200$, $c = 120$, $l = 10$ and $b = 2.0$ and $d = 1$

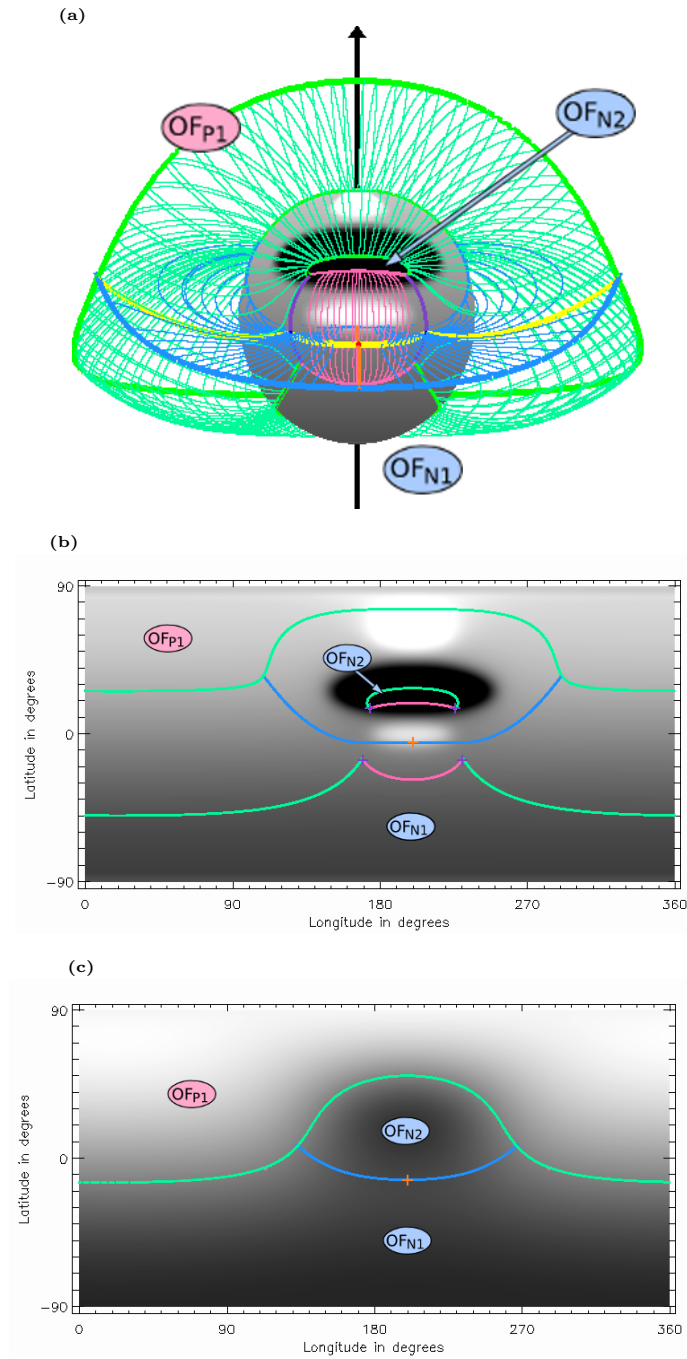


Figure 3.11: Example of a potential magnetic field with separatrix tunnel which has a positive null to the south of the HCS curtain forming a disconnected negative open field region. (a) shows the 3D topology, (b) shows the footprint of the structure at the photosphere plotted over contours of the radial magnetic field component saturated at $\pm 15 \text{ Mx/cm}^2$, (c) shows the intersection of the structure with the outer boundary plotted over contours of the magnetic field at the source surface. The colouring is the same as Figure 3.9. The open field regions are labelled OF_{P1} , OF_{N1} and OF_{N2} for the one positive and two negative open field regions respectively.

- Second patch: $B_2 = -10$, $a = 200$, $c = 140$, $l = 10$ and $b = 3.0$ and $d = 1$.

This synthetic magnetogram is very similar to the one used to produce the separatrix dome underneath the HCS curtains (Section 3.5.2) except the strength of the second patch has been doubled. This patch of stronger field is strong enough to displace the HCS and cause a disconnected open-field region to form.

In this example there is one negative null point. Its separatrix surface stretches down to the photosphere and up to the source surface and its spines are both anchored on the photosphere: one in each negative open field region. There are two null-HCS separators present where the separatrix curtain intersects with the HCS curtains.

The structure of a closed separatrix curtain means that there is a separatrix surface separating two open field regions of the same polarity which is characteristic of a pseudostreamer (see Section 3.2). If lines along the magnetic field components in the plane of sky are traced for this model when the null point is in the plane of sky, a similar pattern to observations of pseudostreamers is seen (see Figure 3.13 and compare with Figure 1.8). The top of a helmet streamer is a null-line in our model (green dots in Figure 3.13) but the top of the loops of a pseudostreamer forms a separator (red star in Figure 3.13).

3.5.6 Transition from a single pseudostreamer to a double helmet streamer

As described in the previous two examples, closed separatrix curtains form structures that are seen as pseudostreamers. Also, in Section 3.1, we saw that the HCS and the associated HCS curtains are analogous to helmet streamers. When two helmet streamers are present beside each other on one limb of the Sun it is known as a double streamer, such structures have been discussed by e.g., Crooker et al. [1993] and Rachmeler et al. [2014].

Although the magnetic structure in the corona cannot be observed directly many of the field lines are illuminated by hot dense plasma. Rachmeler et al. [2014] observed a long lived pseudostreamer structure in white light that morphed along its length into a double streamer structure. This Section describes a PFSS extrapolation from a synthesised magnetogram that could produce such a structure.

The magnetic topological structure given here is also an example of an instance where the HCS null line has split into two separate loops on the source surface. This structure is produced using the following patches of field inserted into a dipolar synthetic magnetogram as Equation (3.1).

- First patch: $B_1 = 15$, $a = 20$, $c = 150$, $l = 10$ and $b = 3.0$ and $d = 2.5$
- Second patch: $B_2 = 15$, $a = 380$, $c = 150$, $l = 10$ and $b = 3.0$ and $d = 2.5$
- Third patch: $B_3 = 25$, $a = 200$, $c = 80$, $l = 10$ and $b = 4.0$ and $d = 2.5$
- Fourth patch: $B_4 = -25$, $a = 200$, $c = 130$, $l = 10$ and $b = 5.0$ and $d = 3.0$

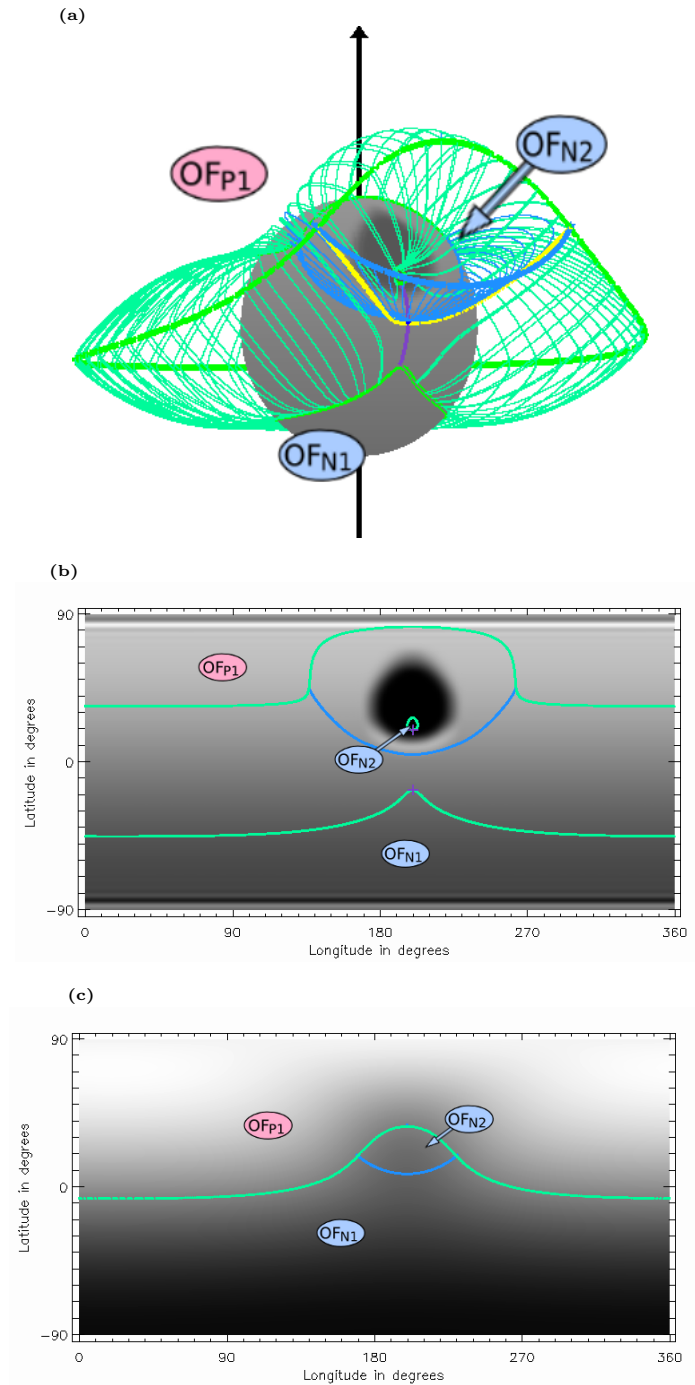


Figure 3.12: Example of a potential magnetic field of a closed separatrix curtain forming a disconnected negative field region. (a) shows the 3D topology, (b) shows the footprint of the structure at the photosphere plotted over contours of the radial magnetic field component saturated at $\pm 7 \text{ Mx/cm}^2$, (c) shows the intersection of the structure with the outer boundary plotted over contours of the magnetic field at the source surface. The colouring is the same as Figure 3.9. The open field regions are labelled OF_{P1} , OF_{N1} and OF_{N2} for the one positive and two negative open field regions respectively.

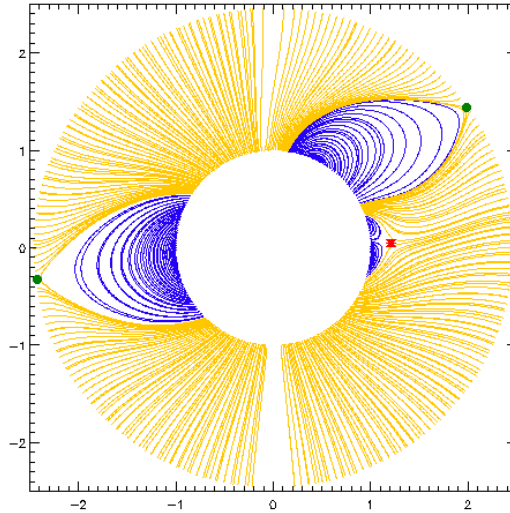


Figure 3.13: Lines traced along the components of the magnetic field in the plane of sky for a closed separatrix curtain on the limb. Closed field lines are in blue, open field lines are in yellow. The intersection of a separator with the plane is a red star and the intersections of the HCS null line with the plane are green dots.

- Fifth patch: $B_5 = 15$, $a = 200$, $c = 170$, $l = 10$ and $b = 4.0$ and $d = 1.0$

Figure 3.14(a) shows a 3D representation of the structure which is symmetric and has two HCS null line loops at the source surface. One is associated with the global dipole and the other is associated with a large positive polarity patch (third patch listed above). The cut in the separatrix surfaces at the photosphere (Figure 3.14b) shows four open field regions: two positive (OF_{P1} and OF_{P2}) and two negative (OF_{N1} and OF_{N2}). The area occupied by OF_{P1} at the photospheric level is too small to be seen plotted at this resolution and is between the green lines. At the outer boundary (Figure 3.14c) all four distinct open field regions are apparent and the two HCS null line loops are clear. The negative separatrix surfaces each connect to the two HCS curtains and it is these that form the pseudostreamers.

If we take lines traced along the components of the magnetic field in the plane of sky for three different angles of view of this model we can see the pseudostreamer and double streamer structures (Figure 3.15). The separator forms at the apex of the pseudostreamer lobes (left panel) and these lobes get taller along the structure as the separator rises up to the HCS null line (centre panel) then, further along the structure, the second HCS null line loop appears on the limb and the HCS curtains form two distinct helmet streamer belts (right panel).

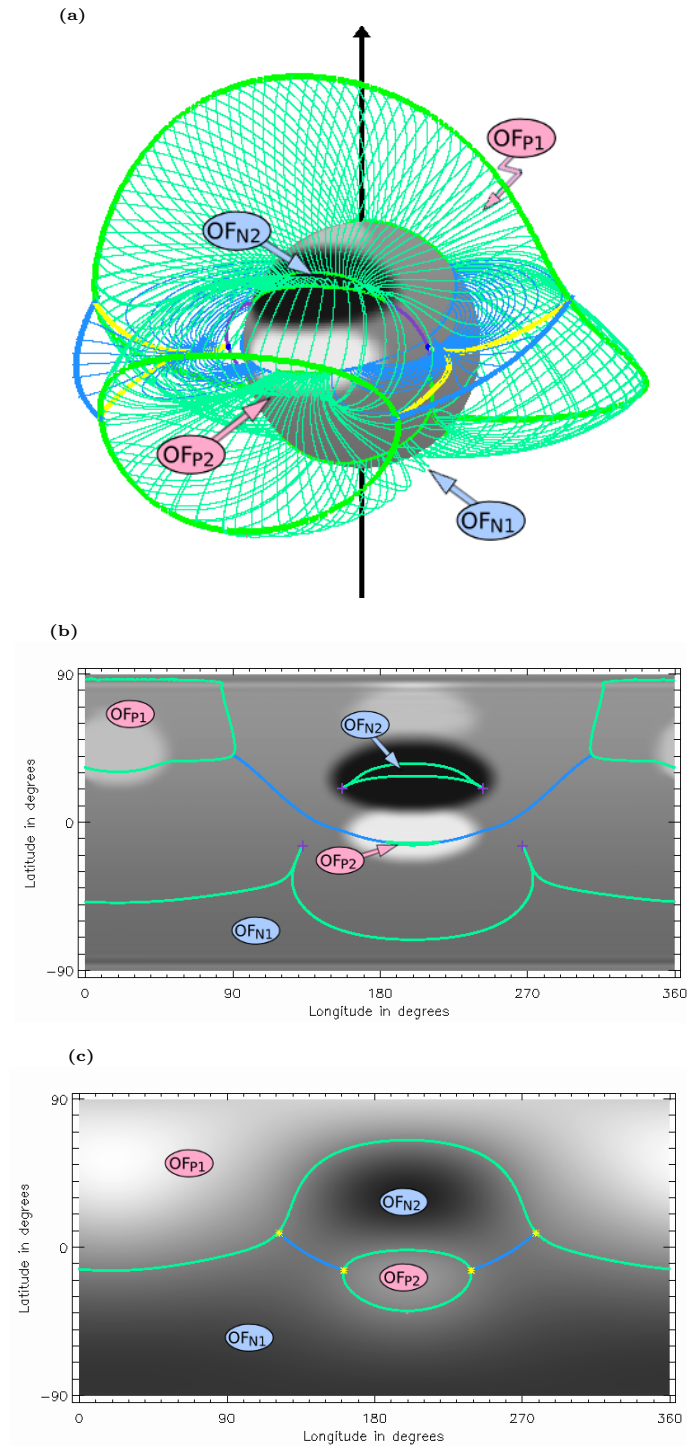


Figure 3.14: Example of a simple potential magnetic field configuration that includes a bifurcated HCS and a pseudostreamer and helmet streamer configuration. (a) shows the 3D topology, (b) shows the footprint of the structure at the photosphere plotted over contours of the radial magnetic field component in the photosphere saturated at $\pm 15 \text{ Mx/cm}^2$. (c) shows the footprint of the structure at the source surface overplotted on a contour map of the magnetic field at the source surface. The colouring is the same as Figure 3.9. The open field regions are labelled OF_{P1-2} , OF_{N1-2} for the two positive and two negative open field regions respectively.

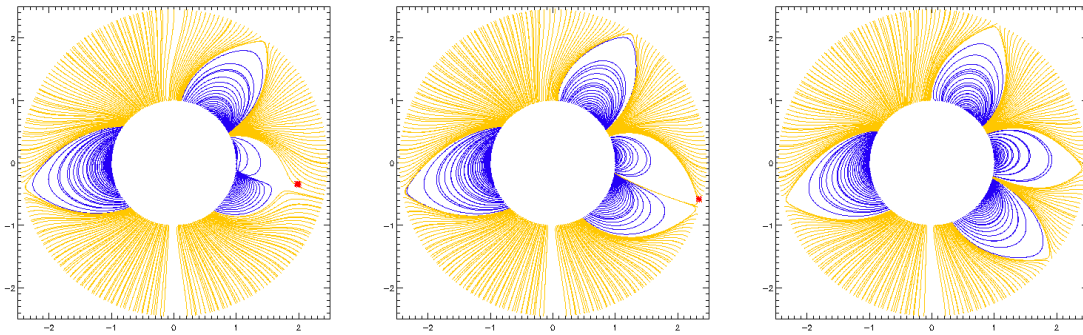


Figure 3.15: Lines along the components of the magnetic field in the plane of sky for three points in the rotation of the 3D representation in Figure 3.14. Yellow lines are open field lines, blue lines are closed field lines. The red star is the location of the intersection of the separator with the plane. Central longitudes from left: 40 degrees, 51 degrees and 110 degrees.

Chapter 4

Solar Cycle Variations of Topological Properties

The topology of the global PFSS models of the coronal field for every Carrington rotation over the last 37 years are created using the synoptic magnetograms from the National Solar Observatory (NSO) at Kitt-Peak in Arizona. From 1976 to 2003 data was taken by the vacuum telescope and from 2003 onward data is taken by the Solar Optical Long-term Investigations of the Sun (SOLIS) telescope. The SOLIS telescope produces data at two different resolutions, the lower of these resolutions is the same as that of the vacuum telescope so it is used in this chapter for continuity. This chapter firstly explores three case studies, a typical solar maximum and two kinds of solar minimum topologies, before moving on to a study of the long-term trends in topological features and properties over the full 37 years.

4.1 Motivation

Although PFSS extrapolations (see Section 2.2) have been around for a long time, it is only recently that people have begun to study their topology and compute their magnetic skeletons [e.g., Titov et al., 2011]. The importance of global coronal separatrix surfaces and quasi-separatrix layers (QSLs) for the solar wind has been described by Antiochos et al. [2011] and Crooker et al. [2012]. They suggest that the slow solar wind can be heated and accelerated by a web of coronal separatrix surfaces and quasi-separatrix layers which they call the “S-web”.

The separatrix surface finding method [Haynes and Parnell, 2010] has been used to find the magnetic skeleton of PFSS extrapolations for particular instances [e.g., DeRosa et al., 2011, van Driel-Gesztelyi et al., 2012]. However, a long term study of the changes in the global coronal magnetic skeleton has not previously been undertaken.

Many topological features have been shown to play a key role in dynamic events such as flares and CMEs. For instance, the breakout model for CMEs [Antiochos et al., 1999] requires the presence of a coronal null point. Also, reconnection around

a coronal null has been used to explain the Bastille day flare of 1998 [Aulanier et al., 2000] and the flare occurring in AR10191 on 16th November 2002 [Masson et al., 2009]. In addition to reconnection at null points, reconnection around QSLs and separatrix surfaces from bald-patches and null points have been associated with dynamic coronal events [e.g., Aulanier et al., 2007].

The number of null points in the global solar corona has previously been studied by Cook et al. [2009]. They looked at the number of null points in a PFSS model over 2 solar cycles using magnetic flux transport models to determine the photospheric field. Their study showed the number of null points to vary in phase with the solar cycle however they missed a large number of null points by using a smooth simulated magnetogram rather than realistic photospheric magnetic field measurements. To create their simulated magnetograms Cook et al. [2009] inserted bipoles into a smooth dipole field. This process meant that they ignored quiet-sun and weak mixed polarity fields which give rise to greater numbers of null points.

We use observed synoptic magnetograms of a resolution considerably higher than those used by Cook et al. [2009] and this allows us to get a higher resolution PFSS extrapolation by using a larger number of harmonics. Cook et al. [2009] used a surface diffusion term in their flux transport simulation that smoothed out small-scale features. Since small-scale features cover a large part of the solar surface at solar minimum we would expect to find many more nulls than Cook et al. [2009] at solar minimum and also some more at solar maximum.

Other studies of the number of coronal null points include Longcope and Parnell [2009], who found numbers of the order of 0.003 nulls per square Megametre over a quiet sun region in the corona by extrapolating the potential magnetic field above a large number of high-resolution MDI magnetograms. Since our resolution is much lower than that used by Longcope and Parnell [2009] we would expect to find fewer of the low altitude nulls than they find. Also, since we consider the whole solar surface we include large unipolar regions such as parts of active regions and polar open-field regions. These regions will have a lower density of coronal nulls above them as there is less mixing of magnetic field in these regions.

4.2 Magnetogram data

The PFSS model described in Section 2.2 takes synoptic magnetogram maps as a lower boundary condition from which the potential magnetic field of the global corona is generated. The data used in this chapter are synoptic magnetograms from the Kitt Peak observatory. Between 1976 and 2003 the magnetograms are from the vacuum telescope and from 2003 onwards the Solar Optical Long-term Investigations of the Sun (SOLIS) telescope is used. The resolution of the synoptic magnetograms from the vacuum telescope is 360 pixels in equal steps of longitude and 180 pixels in equal steps of sine latitude. The SOLIS telescope produces two resolutions of synoptic magnetogram, the lower of these resolutions is the same as that from the

Colour	Linestyle	Topological feature
Blue	Dot	Negative null point
Red	Dot	Positive null point
Light blue	Thin lines	Negative separatrix surface
Pink	Thin lines	Positive separatrix surface
Green	Thin lines	HCS curtain
Green	Thick line	HCS null-line
Purple	Thick lines	Negative spines
Orange	Thick lines	Positive spines
Olive green	Thin lines	Bald-patch separatrix surface
Yellow	Thick lines	Separators

Table 4.1: Colours used for 3D topology images

vacuum telescope so it provides us with an uninterrupted 37 year data set of the same resolution.

The PFSS model requires the selection of the number of harmonics to use in the extrapolation, based on the resolution of the input magnetograms (see Section 2.2). For this resolution we set $l_{max} = 81$. This gives us a potential field source surface extrapolation with 329 points equally spaced in longitude, 165 points equally spaced in latitude and 48 points exponentially spaced with radius. We select the source surface to be at a radial distance of $2.5R_{\odot}$ for the whole 37 year period of this study.

4.3 Typical solar maximum and solar minimum global topology

This section examines typical examples of the kinds of global topology seen in the potential fields at solar minimum and solar maximum. Figure 4.1 describes the scheme used to visualise the topology found using methods from Haynes and Parnell [2007, 2010]. Small red and blue dots represent positive and negative null points, respectively. The field lines in the separatrix surfaces traced from these nulls are pink for positive nulls and blue for negative nulls. Similarly the spine lines are drawn as orange and purple lines for positive and negative null points, respectively. Field lines in separatrix surfaces from bald patches (if present) are olive green. Field lines that connect a pair of null points (separators) are represented by thick yellow lines. Field lines in the HCS curtain are bright green. For reference the colour scheme is listed in detail in Table 4.1. The surface of the Sun is shaded with the radial component of the photospheric magnetic field set at an appropriate saturation to highlight the magnetic features. The axis of rotation is shown by the black arrow.

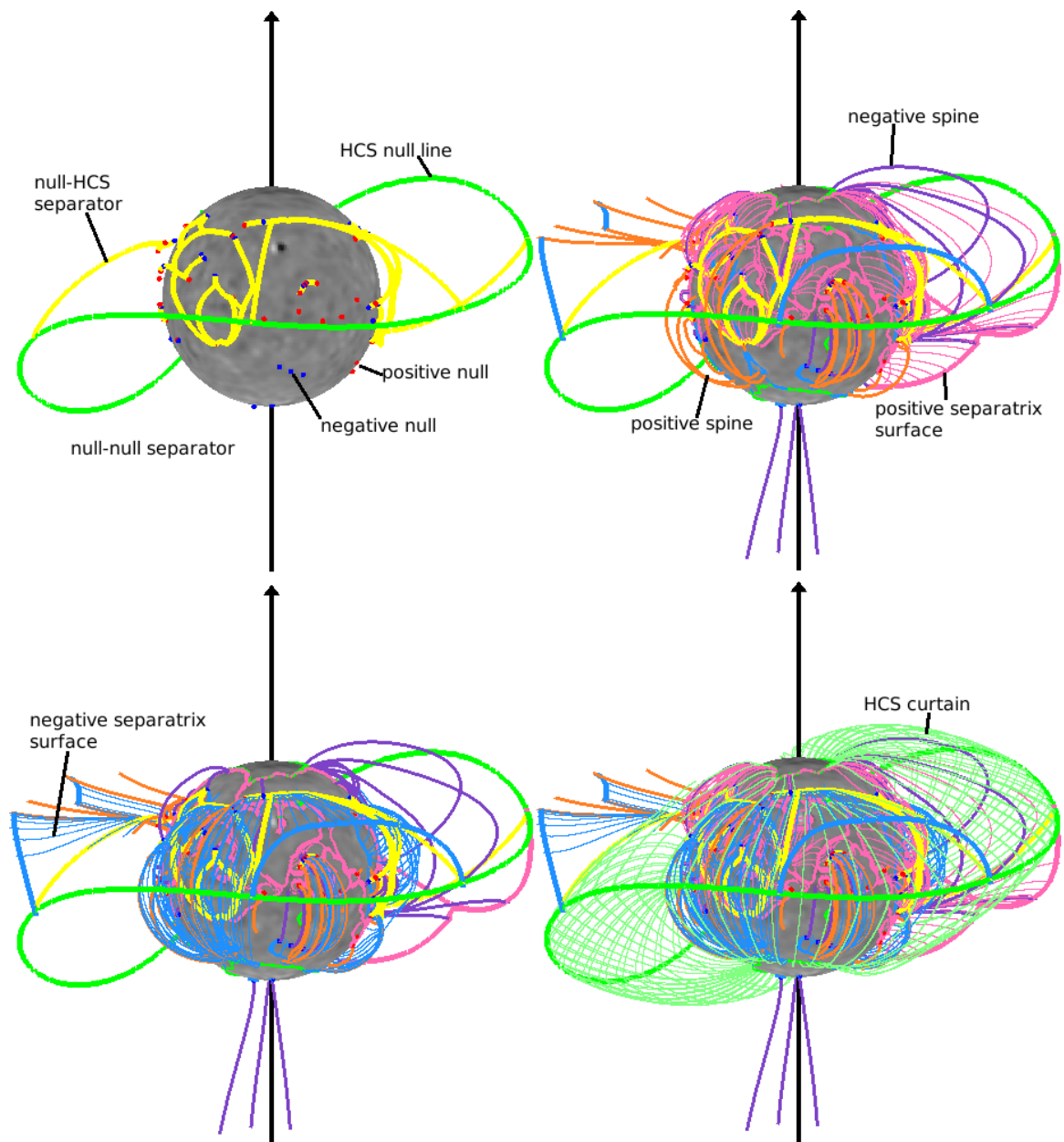


Figure 4.1: The building blocks of global coronal topology. This example is Carrington Rotation 2074 (August 2008, solar minimum cycle 23/24). The Sun is shaded with the radial component of the magnetic field at the photosphere. Red and blue dots represent positive and negative null points. Separators are thick yellow lines. Separatrix surfaces are traced from the nulls as well as from the null-line at the base of the heliospheric current sheet (HCS) at the upper boundary of the model (green line) and from bald patches at the lower boundary of the model. The HCS curtain is represented by the green field lines, bald patch separatrix surfaces (if present) are represented by the olive green field lines, separatrix surfaces from positive/negative nulls are represented by pink/blue field lines. Spine lines from positive/negative nulls are orange/purple.

4.3.1 Typical solar minimum topologies

Solar minimum is the time at which there are few or no large active regions on the surface of the Sun. Instead, much of the solar surface is covered by small magnetic elements of mixed polarity which is referred to as the *quiet sun*. In the absence of active regions, the typical global configuration of magnetic topology present at solar minimum depends on the strength of the global dipole. In this section, I will consider one case from the minimum between cycles 22 and 23 which is an example of a minimum with a strong global dipole and one case from the minimum between cycles 23 and 24 (a minimum where the global dipole is comparatively weak).

Strong global dipole solar minimum

If the global dipole is strong, such as was the case for the cycle 21/22 minimum and cycle 22/23 minimum, then it dominates over small-scale field structures. In this case, null points sit low in the corona, the HCS lies near to the equator and is almost circular and the HCS curtains map down, from the HCS, to enclose almost all mixed-polarity field at low latitudes. The strong polar field creates large open-field regions over the poles and few additional disconnected open-field regions are present.

Figure 4.2 shows an example of the topology of such a minimum from the PFSS model from Carrington rotation 1904 (beginning 20th December 1995) which is at the end of cycle 22. In this frame the HCS lies very close to the equator (thick green line at outer boundary) and there is only one separatrix curtain present (pink surface intersecting with top boundary labelled OSC). This separatrix surface is from a positive null point and is *open*, as described in Chapter 3: it is bounded by the HCS curtain on one side and the spine of a negative null on the other side. Since it is bounded by a spine to which no other separatrix curtains connect, it does not form a disconnected open-field region. There is only one positive and one negative open-field region present. The positive open-field region covers the north pole (OF_{P1}) and the negative open-field region covers the south pole (OF_{N1}). Globally the field appears close to bipolar with almost all of the features enclosed under the HCS curtain. To examine the features underneath the HCS curtain cuts at constant radius are taken at different altitudes. These cuts are then flattened into longitude/latitude maps of the topological structures at this height. We examine cuts at the outer boundary ($2.5R_{\odot}$), midway though the model ($1.44R_{\odot}$) and just above the photosphere ($1.02R_{\odot}$), Figure 4.3a, b and c, respectively¹.

Very few separatrix features intersect with the top boundary. The green line in Figure 4.3a is the neutral line at the base of the HCS which sits close to equator at almost constant latitude. There is one separatrix curtain made of a single separatrix surface intersecting with the top boundary (labelled OSC) and in this cut it is clear that it is open at the end bounded by the negative spine (purple cross).

¹Note that, for the cuts at the lower boundary, we take a cut at approximately $1.02R_{\odot}$ as it is numerically difficult to evaluate the intersections of the separatrix surfaces exactly on the lower boundary

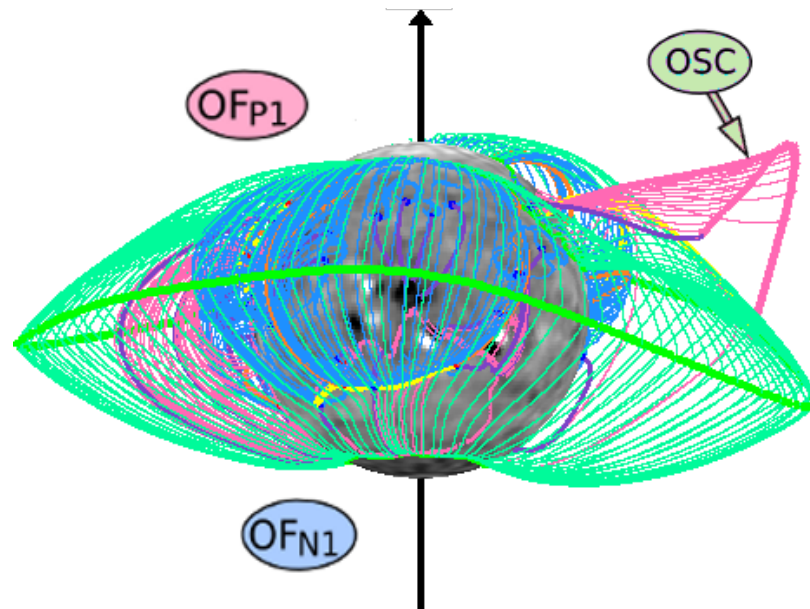


Figure 4.2: Strong global dipole solar minimum topology of PFSS extrapolation from Carrington rotation 1904. The red/blue dots are positive/negative null points, the pink/blue surfaces are separatrix surfaces from positive/negative null points, the green surface is the HCS curtain and the olive green surfaces (if visible) are bald patch separatrix surfaces. The orange/purple lines are the spines of positive/negative null points and the yellow lines are separators. The open-field regions are labelled OF_{P1} for the open-field region with positive polarity and OF_{N1} for the open-field region with negative polarity. There is one open separatrix curtain present labelled OSC.

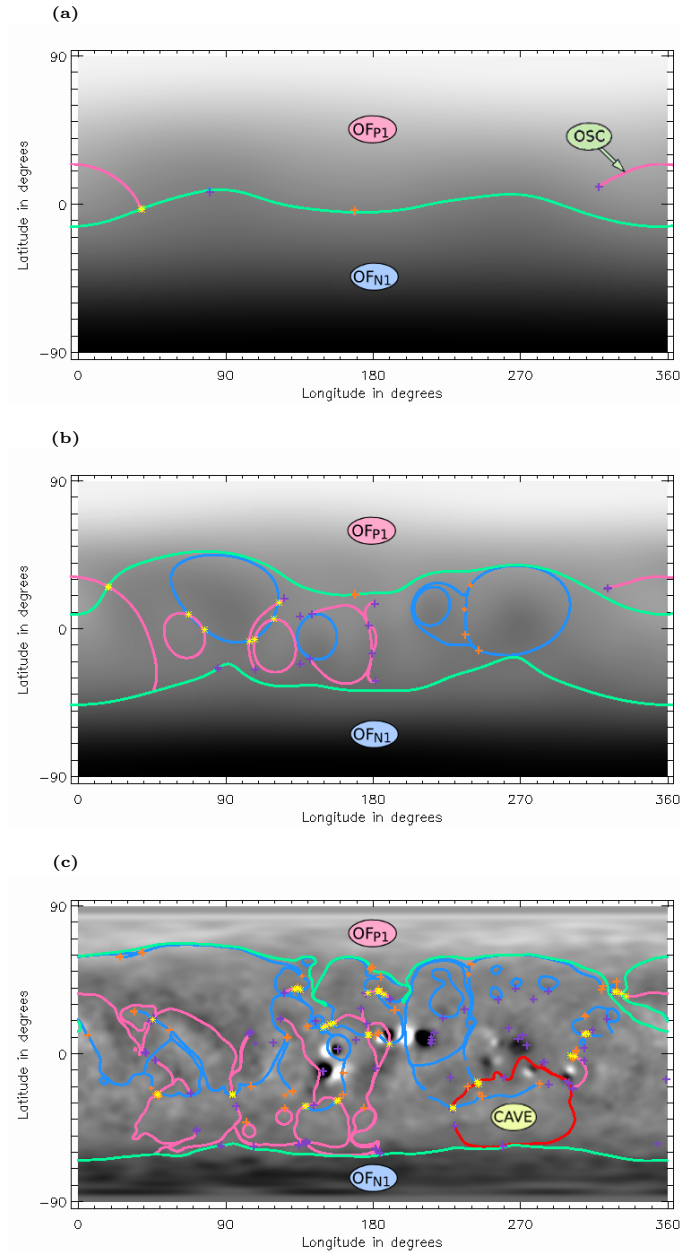


Figure 4.3: Cuts in the separatrix surfaces at heights of (a) $r = R_{ss} = 2.5R_{\odot}$, (b) $r = 1.44R_{\odot}$ and (c) $r = 1.02R_{\odot}$. Background is coloured with the radial component of the magnetic field at that height. The pink/blue lines are the intersection of the positive/negative separatrix surfaces with the cut. The orange/purple crosses are the intersection of positive/negative spines with the cut. Yellow stars are the intersection of separators with the cut. Green lines are the intersection of the HCS curtain with the cut and the olive green lines (if present) are the intersection of bald patch separatrix surfaces with the cut. The polar open-field regions are the only open-field regions present and have been labelled OF_{P1} and OF_{N1} . There is one separatrix curtain in (a) labelled OSC and a separatrix cave in (c) labelled $CAVE$.

The background of the maps in Figure 4.3 are shaded with the radial component of the magnetic field at the altitude of each cut, where black is negative and white is positive. At the outer boundary all of the field is in the radial direction and we can see that it is a bipolar configuration with the negative pole at the south pole and the positive pole at the north pole.

At $1.44R_{\odot}$ the two curtains from the HCS are visible as two green lines that lie either side of the equator and approximately 50° apart from each other at all longitudes. Some topological features are present at this height in the atmosphere between the HCS curtains. Several large rings are visible which are cuts through large separatrix domes at this radial distance. At this height we also see several separatrix surfaces bounded by spines which produce arching structures that close back to the surface between the HCS curtains. Thirteen separatrix surfaces reach up to $1.44R_{\odot}$ (Figure 4.3(b) and produce seven separators.

Near the solar surface (Figure 4.3c) there are many more separatrix features present. One feature of note at this height is the footprint of a separatrix cave (as shown in Section 3.5.3) made from the separatrix surfaces of several positive nulls intersecting with two separatrix surfaces from negative nulls and becoming bounded by their spines (labelled CAVE). The boundaries of the cave are coloured in red, the cave structure is completely enclosed under the HCS curtains so is not associated with an open separatrix curtain.

The HCS curtain encloses almost all field between $\pm 60^{\circ}$ and so globally the field is very close to bipolar and the global structure is very simple. At the photosphere (Figure 4.3c), the HCS curtain makes three notable deviations from $\pm 60^{\circ}$. These deviations are all in the northern hemisphere and occur where the HCS curtain twists around large separatrix domes. The largest of these is at about 330° longitude and 30° latitude and is associated with the base of the separatrix curtain (OSC in Figure 4.3a)

From the cuts we can see that there are many separators low down in the atmosphere but few of these reach up high into the atmosphere. Only null-HCS separators reach up to the upper boundary. Figure 4.4 summarises the heights reached by the nulls and the null-null separators. There are 58 coronal nulls present in this frame and 33 null-null separators. The highest null point sits at $1.21R_{\odot}$ (146Mm above the solar surface), but the highest null-null separator reaches $1.56R_{\odot}$ (389Mm above the solar surface). Although there are many separator connections most null-null separators are below $1.2R_{\odot}$ which corresponds to a height of 139Mm above the solar surface.

Weak Global Dipole Solar Minimum

On the other hand, if the global dipole is weak, such as during the recent solar minimum [e.g., Wang et al., 2009], then the global topology at solar minimum appears quite different because the magnetic influence of small-scale magnetic elements can reach high in the atmosphere since they are not restricted by the strong dipole field.

Figure 4.5 shows the global topology at Carrington rotation 2083 beginning May

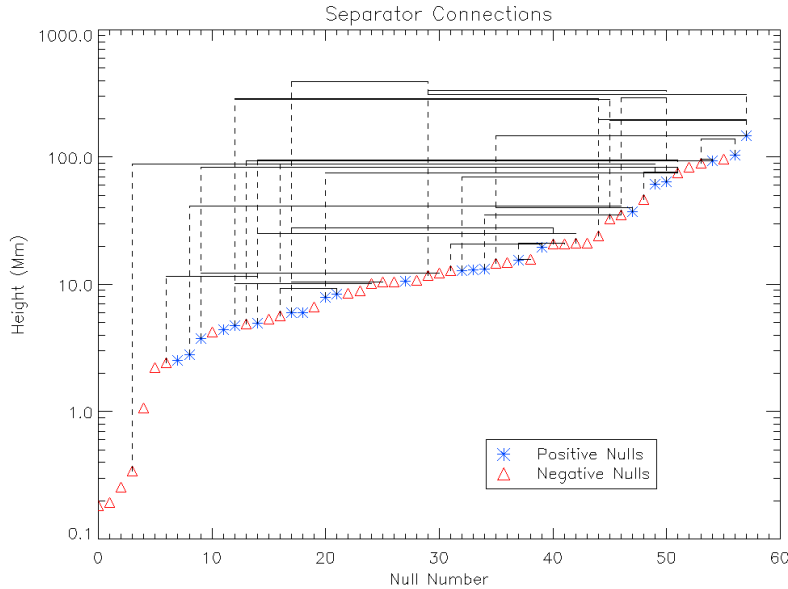


Figure 4.4: Diagram of separator connections between null points. Null points are represented as blue stars and red triangles for positive and negative nulls respectively. If there exists a separator between two nulls a line is drawn from the first null up to the maximum height reached by the separator and then along and down to the second null.

3rd 2009 (between cycles 23/24). The large-scale topology is much more complex than at CR 1904. The HCS is still fairly close to the equator (although it switches back and forth across the equator multiple times reaching latitudes of $\pm 30^\circ$) and the polar regions are open. There are many separatrix curtains most of which are closed (connected to the HCS at both ends) which means that they form disconnected open-field regions. In Figure 4.5, there are 6 negative separatrix curtains visible: 4 are closed and bound open-field regions (OF_{N2-5}), and 2 are open. The openings of 6 disconnected open-field regions are visible. There are three negative open-field regions (OF_{N2} , OF_{N3} and OF_{N5}) which are bounded to the south by the HCS curtain and to the north by closed negative separatrix curtains. There is also one open-field region visible (OF_{N4}) which is bounded to both the north and south by negative separatrix curtains. Two of the open-field regions are associated with the global dipole and these are OF_{P1} at the South pole and OF_{N1} at the North pole.

Figure 4.6 shows maps of cuts at constant radii through the topological features from Carrington rotation 2083. At the source surface (Figure 4.6a), the openings of the open-field regions have been labelled as in Figure 4.5. In addition to the 6 open-field regions visible in Figure 4.5, there are a further four open-field regions: 3 positive (OF_{P2} , OF_{P3} and OF_{P4}) and one negative (OF_{N6}). Negative open-field regions can be bounded by a combination of negative separatrix surfaces, the HCS curtain and bald-patch separatrix surfaces. Similarly positive open-field regions are

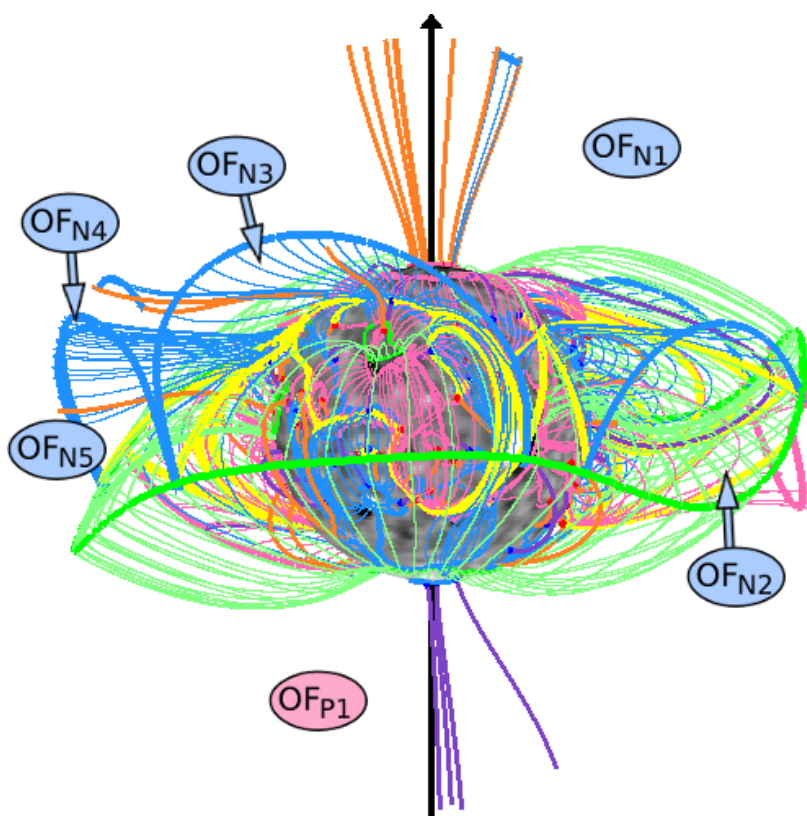


Figure 4.5: Weak global-dipole minimum topology of PFSS extrapolation from Carrington rotation 2083. Features are coloured as in Figure 4.2. There are 5 negative open-field regions visible labelled OF_{N1-5} and one positive open-field region visible, labelled OF_{P1} .

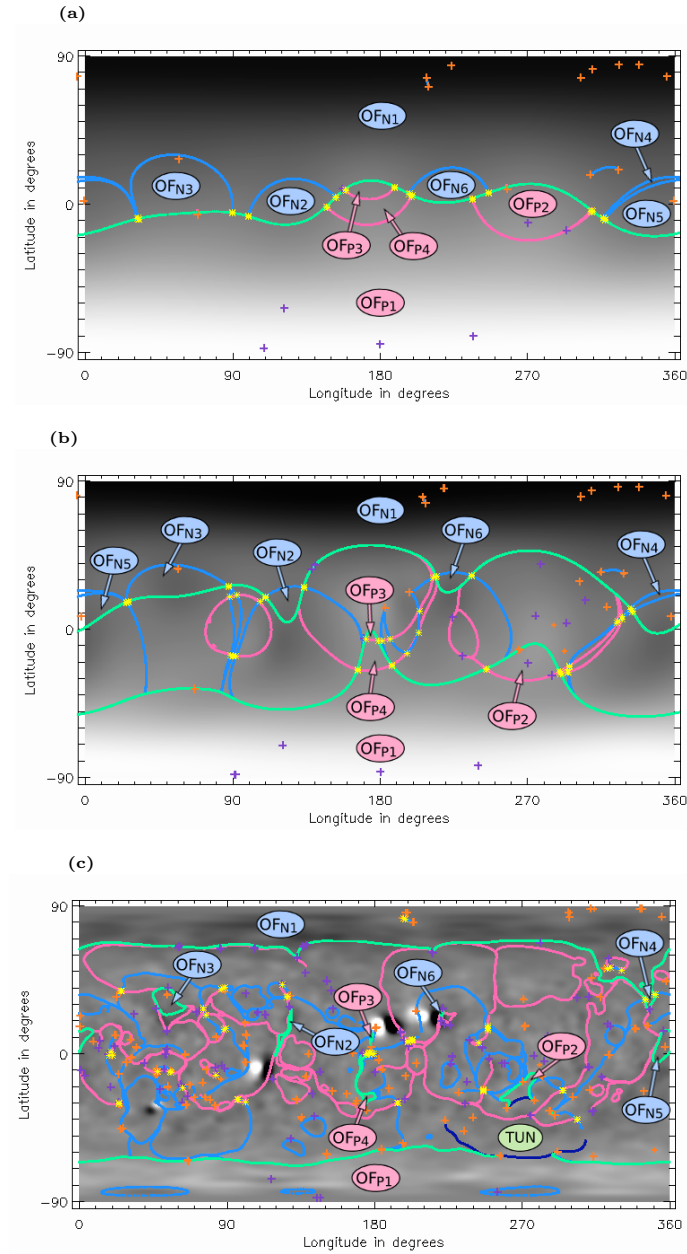


Figure 4.6: Cuts in the separatrix surfaces at heights of (a) $r = R_{ss} = 2.5R_{\odot}$, (b) $r = 1.44R_{\odot}$ and (c) $r = 1.02R_{\odot}$. Features are coloured as in Figure 4.3. There are six negative open-field regions (labelled OF_{N1-6}) and four positive open-field regions (labelled OF_{P1-4}). The separatrix tunnel dividing OF_{P1} and OF_{P2} is labelled as TUN and highlighted in royal blue.

bounded by a combination of positive separatrix surfaces, the HCS curtain and bald-patch separatrix surfaces.

The open-field regions can be tracked through the atmosphere, using the cuts, to their foot-points on the photosphere (labelled in Figure 4.6a, b and c). Many open-field regions that connect to large open areas at the source surface come from regions at the photosphere that are so small they cannot be seen when lines are plotted to outline them (e.g, OF_{P3} , OF_{N2}).

Figure 4.6b shows a cut at $1.44R_{\odot}$, here the open-field regions have shrunk considerably. The separatrix curtains intersect with one of the HCS curtains to form a null-HCS separator (yellow stars on green line) and are bounded by the other HCS curtain.

From the lower boundary cut (Figure 4.6c) we can identify features such as those described in Chapter 3. At 270° longitude and around -50° latitude at the lower boundary (Figure 4.6c) there is a channel of negative separatrix surfaces with a positive separatrix surface intersecting it (labelled TUN). This is the footprint of a separatrix tunnel (see Figure 3.11) and a closed separatrix curtain made of two separatrix surfaces. If we track this curtain to the source surface it becomes the boundary for disconnected open-field region OF_{P2} . At the lower boundary, OF_{P2} is separated from the polar open-field region OF_{P1} by this separatrix tunnel. There is no clear field line path from the foot-points of OF_{P1} to those of OF_{P2} contrary to Antiochos et al. [2007] who proposed the hypothesis that all open-field regions of the same polarity are connected at the photospheric level and which Titov et al. [2011] demonstrated is not always the case.

If we consider only the intersection of the HCS curtains with a surface of constant radius of $1.02R_{\odot}$ (Figure 4.7) then we can see that, for the most part, the HCS curtains sit at $\pm 70^{\circ}$. However, the small rings and lines seen within these latitudinal bands show how parts of the HCS curtain deviate towards the equator and form open-field regions that can have very low latitudes. In particular, there is an open-field region between 350° and 10° longitude that spans the equator and is the foot-point of open-field region OF_{N5} .

From these cuts we can see that there are many separators present (yellow stars in Figure 4.6) at all heights. There are 73 null-null separators in total and 121 coronal nulls. The highest null is at a height of $1.35R_{\odot}$ (244Mm above the solar surface) and the highest null-null separator extends even higher (to $1.95R_{\odot}$, 661Mm above the solar surface). Figure 4.6c shows many null-null separators, however, most of these do not extend high into the atmosphere so few separators are visible at $1.44R_{\odot}$ (Figure 4.6b). At the source surface (Figure 4.6a), only separators arising from the intersection of the HCS curtain and separatrix surfaces from nulls occur.

Figure 4.8 shows the heights and connections of the null-null separators. There are many connections, as in Carrington rotation 1904 (Figure 4.4), and, although the null points still sit low in the atmosphere, some of the separators that connect them arch up high in the corona to much greater heights than when a strong global dipole is present. This is due to the weak polar field allowing magnetic structures to expand.

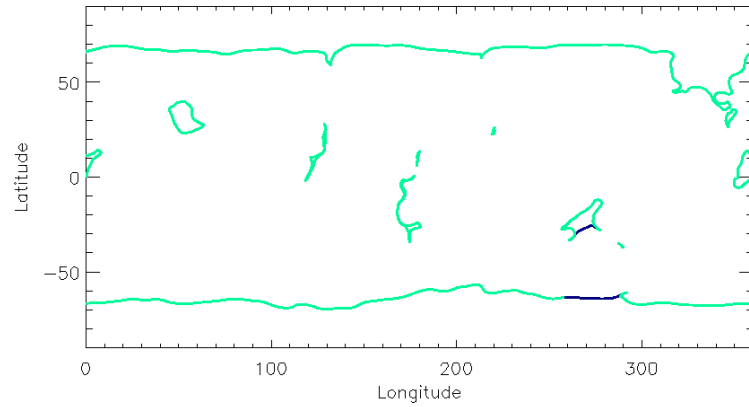


Figure 4.7: Intersection of the HCS curtains with a surface of radius $1.02R_{\odot}$. Green lines show HCS curtain, blue lines show sides of separatrix tunnel labelled in Figure 4.6c.

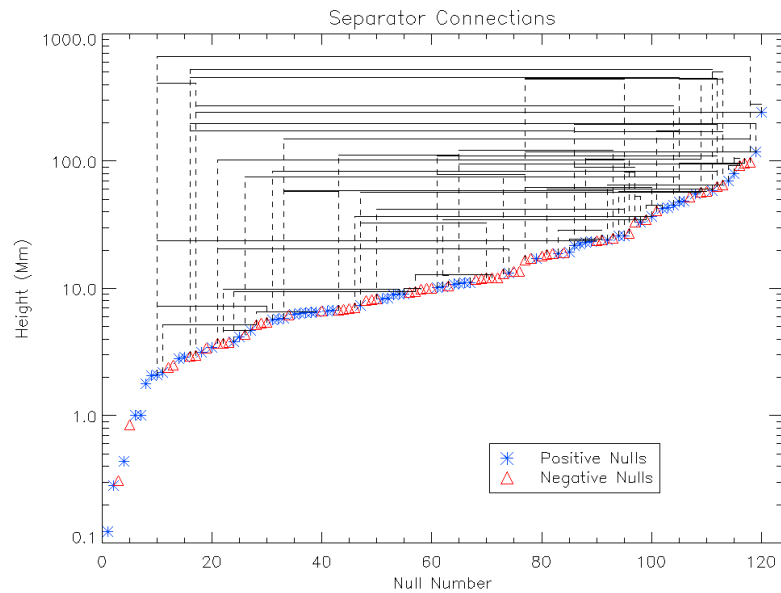


Figure 4.8: Diagram of separator connections between null points for Carrington rotation 2083. Null points are represented as blue stars and red triangles for positive and negative null points respectively. If there exists a separator between two nulls a line is drawn from the first null up to the maximum height above the photosphere reached by the separator and then along and down to the second null.

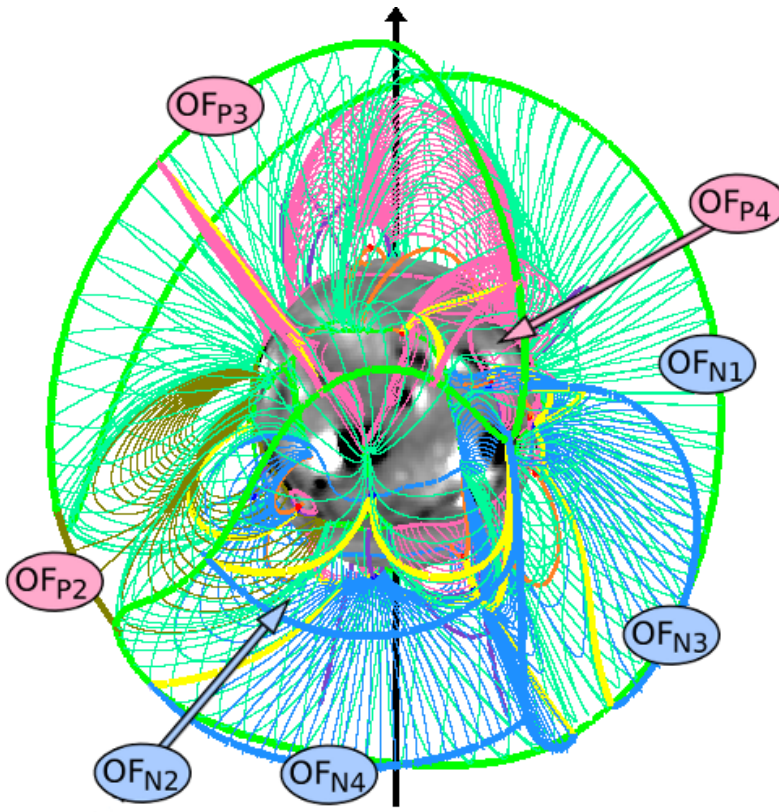


Figure 4.9: Topology of potential field extrapolation from Carrington Rotation 1957 (Solar Maximum). The same notation as Figure 4.2 is used. There are three positive polarity open-field regions visible (OF_{P2} , OF_{P3} , OF_{P4}) and four negative polarity open-field regions visible (OF_{N1} , OF_{N2} , OF_{N3} , OF_{N4}).

4.3.2 Typical Solar Maximum Topology

At solar maximum many active regions are present on the solar surface. Much of the flux in the leading polarity of an active region will cancel with other active regions (often across the equator). This leaves a remnant polarity which, due to Hale's law, will be of the opposite polarity to the polar field in that hemisphere. Meridional flows tend to push these remnant active regions poleward which serves to weaken the polar field [Babcock, 1961]. Eventually this culminates in the polar field reversal. The relative strength of the large number of active regions in comparison to the polar fields causes the HCS to become severely buckled [Titov et al., 2011] such that the field at the poles can become closed. This allows the footprints of open-field regions to occur anywhere on the surface of the Sun, including equatorial regions.

Figure 4.9 shows the global topology of a typical solar maximum field taken from CR1957, beginning 5th December 1999, at the maximum of cycle 22. There are a total of 7 open-field regions visible from this view: three with positive polarity (OF_{P2-4})

and four with negative polarity (OF_{N1-4}). These are bounded by separatrix curtains of which there are 7 visible in this Figure. Six of the separatrix curtains shown are from null points and one is from a bald patch (olive green surface bounding the left hand end of OF_{P2}). In this Carrington rotation all of the separatrix curtains are closed and, in total, they divide the source surface up into 9 disconnected open-field regions. These can be seen outlined in cuts taken at three heights in the corona (Figure 4.10). At the source surface (Figure 4.10a) all field is open so the separatrix curtains separate the field from each disconnected open-field region. Using these cuts, open-field regions can be tracked through the atmosphere to find the origins of these regions on the photosphere.

The source surface cut at this time is drastically different to those seen in either of the cases from minimum. The magnetic field does not have a north-south dipole and the HCS null line (green line in Figure 4.10a) does not follow close to the equator forming a single line across the source surface map, as seen in solar minimum. Instead, between 220° and 300° longitude it is absent and forms a closed loop that on one side covers both poles and on the other a section of the equator. This warping of the HCS is due to the active-region magnetic fields dominating over the polar fields. In this Carrington rotation the HCS forms a highly distorted single loop. However, at many times during solar maximum the HCS can split to form multiple loops as a quadrupolar configuration from active region fields dominates over the dipolar configuration from the polar fields [e.g., Wang et al., 2014].

Figure 4.10b and c show cuts at $r = 1.44R_\odot$ and $r = R_\odot$, respectively. Further down in the atmosphere the regions of open field shrink and become highly distorted. At the photosphere (Figure 4.10c), the positive-polarity open-field region OF_{P4} and the negative-polarity open-field region OF_{N2} have shrunk so much that they appear as a line when plotted in an image of this size. A few rings corresponding to separatrix domes are seen at the photosphere (Figure 4.10c), some of which are seen to occur outside the HCS curtain. In particular, there is a large negative separatrix dome that further reduces the region of open field labelled OF_{P1} . The limited occurrence of small separatrix domes is because the topology is governed by large active-region magnetic fields rather than the small-scale intermingling of flux that we see on the quiet Sun.

The organisation of the magnetic field into large active regions at solar maximum means that few null points form: in this frame there are 33 present up to heights of $1.40R_\odot$ (278Mm above the photosphere). Similarly, the number of separators is lower as there are fewer null-null connections (see Figure 4.11). The null-null separators that are present do not extend into the corona much higher than the null points they connect. In total, there are only 8 null-null separators present as there are few null points and these are widely-spaced around the Sun so are unlikely to have connections. The highest height reached by a null-null separator is $1.39R_\odot$ (271Mm). It should be noted that there are many separators high in the corona at solar maximum, but these are usually null-HCS separators.

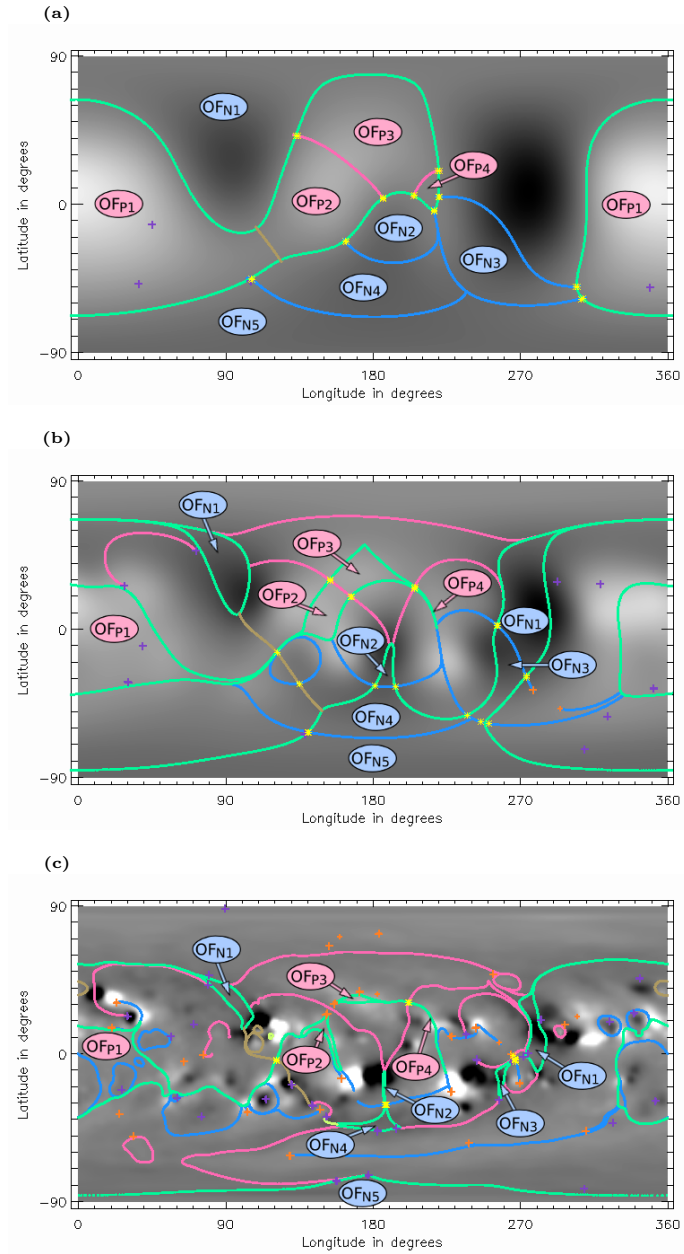


Figure 4.10: Cuts in the separatrix surfaces at heights in the corona for Carrington rotation 1957. (a) is at $r = R_{ss} = 2.5R_{\odot}$, (b) is at $r = 1.44R_{\odot}$ and (c) is at $r = 1.02R_{\odot}$. The same notation as Figure 4.3 is used. There are nine different areas of open field labelled OF_{N1-5} for the negative polarity open-field regions and OF_{P1-4} for the positive polarity open-field regions.

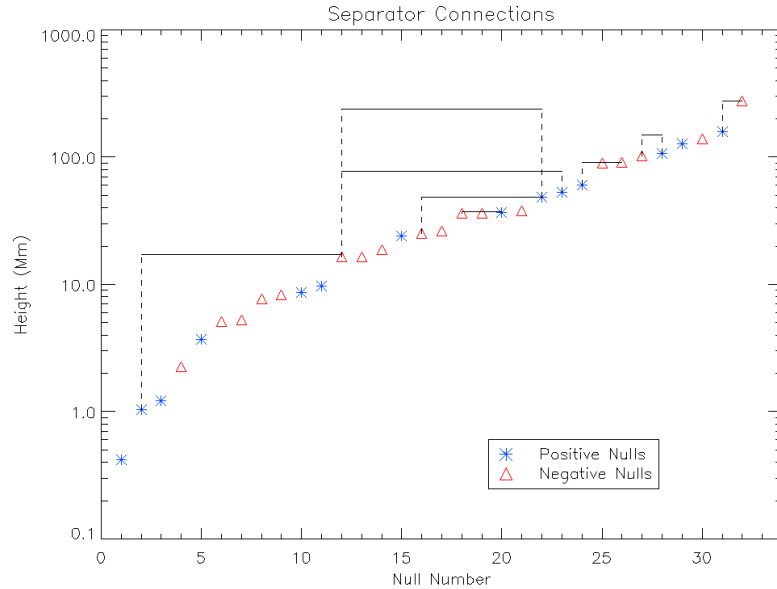


Figure 4.11: Diagram of separator connections between null points for Carrington rotation 1957. Null points are represented as blue stars and red triangles for positive and negative null points, respectively. If there exists a separator between two nulls a line is drawn from the first null up to the maximum height above the photosphere reached by the separator and then along and down to the second null.

4.4 Cycle variations in topological properties

The global structure of the coronal magnetic field varies significantly throughout the solar cycle. This section quantifies these variations through a statistical study of the topological properties found in the potential-field source-surface model of the corona over 37 years. This allows us to consider the global magnetic topology over three solar cycles and not only compare maxima with minima, but also compare between different maxima and minima. The first Carrington rotation we have data for is CR1645 which began on August 17th 1976 and we study data up to Carrington rotation 2144 which began on November 21st 2013. We have 4 missing Carrington rotations, namely CR2015, CR2016, CR2041 and CR2042. This gives us a total of 496 Carrington rotation synoptic maps from which to extrapolate.

4.4.1 Tilt angle of the HCS

The location and shape of the HCS changes greatly over the course of a solar cycle. At solar minimum it lies close to the equator and is almost circular whereas at solar maximum it can become very distorted and can stretch up to the poles.

We measure the tilt angle of the HCS by taking the arithmetic mean of the displacement of the HCS null line to the north and to the south of the equator. Here,

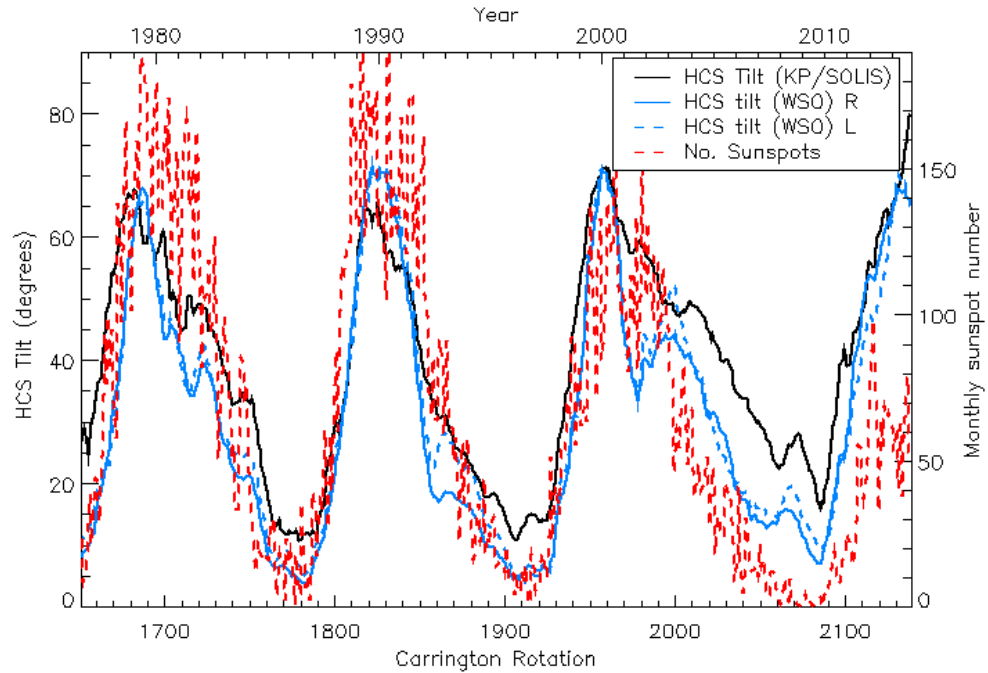


Figure 4.12: Variation of 12 Carrington rotation running mean of the HCS tilt against time. Dashed line shows the sunspot number to indicate the location of maxima and minima. Blue lines show the data from the Wilcox Solar Observatory (WSO).

we consider the tilt angle of the HCS from our PFSS model using KP/SOLIS data and compare it against the HCS tilt angles found using the two Wilcox Solar Observatory (WSO) data sets (<http://wso.stanford.edu/Tilts.html>). WSO produces one data set from line-of-sight measurements using polar field correction and a source surface at $2.5R_{\odot}$ (blue dashed line in Figure 4.12) and one data set from radial magnetic field measurements without polar correction and with a higher source surface at $3.25R_{\odot}$ (blue solid line in Figure 4.12). There are several differences between the WSO data and the KP/SOLIS data. Firstly, the KP/SOLIS data have higher resolution and, hence, higher harmonics are included in our PFSS extrapolations of the coronal field. Secondly, different instruments have different sensitivities which could cause discrepancies in the results and lastly, between the WSO data sets differing source surface heights and polar correction will both cause differences in the results.

The black solid line in Figure 4.12 shows the tilt angle of the HCS in the KP/SOLIS extrapolations against time. The dashed line represents sunspot number² and is plotted to indicate the solar cycles. The tilt angle of the HCS in all models closely follows the trends in sunspot number during cycles 21, 22 and the first half of cycle 23.

²Sunspot data comes from the Royal Greenwich Observatory up until 1977 and then afterwards from the US Air Force Solar Optical Observing Network: http://solarscience.msfc.nasa.gov/greenwch/spot_num.txt

During the decline phase of cycle 23 and through the beginning of cycle 24, there is a big difference between the trends in the HCS in the PFSS model from the KP/SOLIS data and the number of sunspots. Here the HCS reaches higher latitudes than would be suggested by the number of sunspots, this is due to the weaker polar field strength at this time [e.g., Wang et al., 2009]. A weak field strength at the poles means that only a few or even weak active-region magnetic fields can dominate the global magnetic field structure instead of the global dipole.

It can be noted that towards the end of 2013 and into 2014 the tilt angle of the HCS has grown to the same level it was during the previous maxima even though the sunspot number is much lower in this cycle. These higher than expected tilt-angles have previously been noticed by Owens and Lockwood [2012] who studied proxies for the long-term HCS tilt and sunspot number back to the last Maunder minimum. They found that the HCS tilt angle varies only with cycle phase and not with cycle strength.

From our models from the previous two minima compared to the most recent minimum, it seems that the increase in the HCS tilt angle is caused by the small-scale mixed-polarity equatorial fields having greater global influence. These small-scale features are encapsulated in the high-order harmonics of our PFSS extrapolation (this is a possible reason why the tilt angle from WSO is less than that from KP/SOLIS as WSO only uses 30 harmonics and so their PFSS field cannot replicate small field variations). During solar maxima the polar fields reverse, thus are weak, and the strong fields from active regions disperse to dominate at all latitudes. So, due to this dispersal of the active-region fields the global dipole field is not particularly dominant. The equatorial quiet-sun fields during the solar minimum between cycles 23 and 24 were known to be weaker than in previous cycles [Thornton, 2010] however the polar fields at this time are also weak. This means the low-latitude quiet-sun fields have a greater global presence than in the previous two minima where the polar fields were strong.

4.4.2 Closed separatrix curtains

In Chapter 3 we described separatrix surface structures known as closed separatrix curtains. These separatrix surfaces emanate from nulls that have a global significance in the sense that they have separatrix surfaces that create disconnected open field regions. A measure of the number of large-scale topological features can be made by looking at the number of closed separatrix curtains in each Carrington rotation over the solar cycle as shown in Figure 4.13. Closed separatrix curtains are most abundant during solar maximum when the weak polar-field strength has greatly distorted the HCS and the global magnetic field is dominated by low-latitude active-region fields. Also from Figure 4.13 we can see that during the most recent solar minimum the number of closed curtains is also high, this is due to the weaker polar fields allowing small-scale features to have a global influence.

The presence of closed separatrix curtains also implies the presence of discon-

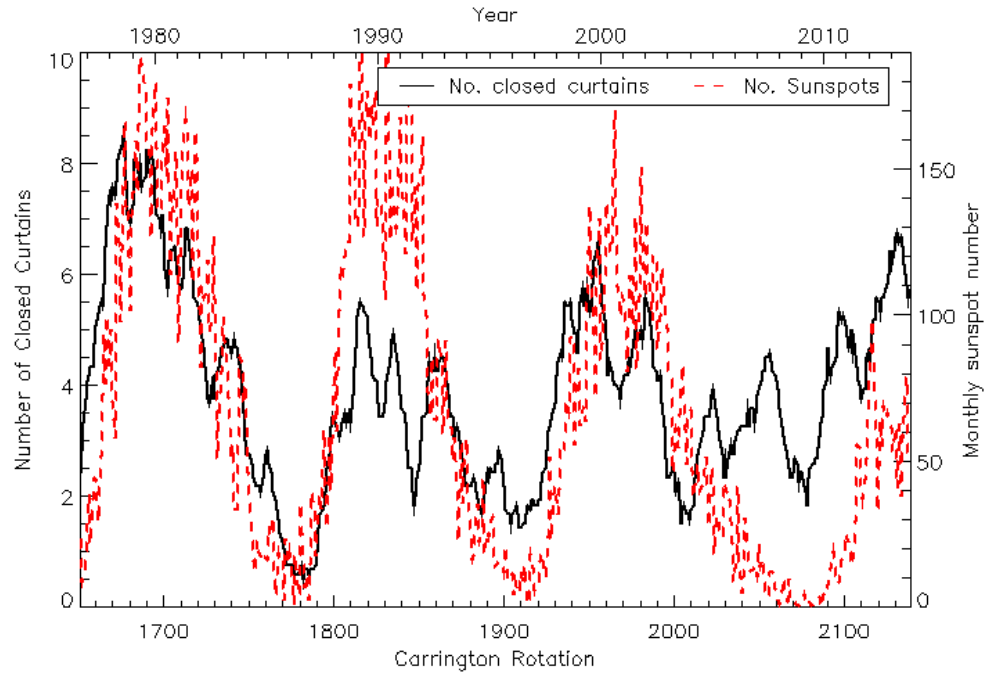


Figure 4.13: 12 CR running mean of the number of closed separatrix curtains (or proxy for the number of disconnected open-field regions) against time. The red dashed line shows the monthly sunspot number.

nected open-field regions at the photosphere (see Sections 3.5.4 and 3.5.5). Hence, from Figure 4.13 we can infer that there are more disconnected open-field regions at maximum than at minimum and also that in the minimum between cycles 23 and 24 there are more disconnected open-field regions than in the previous two minima.

As discussed in Wang et al. [2007] and in Section 3.1 of this thesis, the HCS null line is associated with helmet streamers. However, separatrix curtains are associated with pseudostreamers (see Sections 3.5.5 and 3.5.6). The number of closed separatrix curtains provides us with a proxy for the number of pseudostreamers which (from Figure 4.13) we can see varies in phase with the solar cycle in agreement with Owens et al. [2013]. It has been noted before that pseudostreamers could be sources of the slow solar wind [Wang et al., 2012, Crooker et al., 2012], although Panasenco and Velli [2012] suggest they may instead be sources of the fast solar wind depending on the geometric nature of the associated open-field region.

Our findings agree with Owens et al. [2013] in that pseudostreamers are more abundant in the declining phase of cycle 23 in comparison to the declining phase in the two previous cycles. They claim that this can largely be attributed to the extended length of the cycle 23. However, from our study of the topology of the global magnetic field we believe it is a result of the dipole fields not being replenished after the polar reversal at maximum in cycle 23. The weak solar dipole that persisted between cycles 23 and 24 led to the mixed polarity low-latitude quiet-sun fields gaining

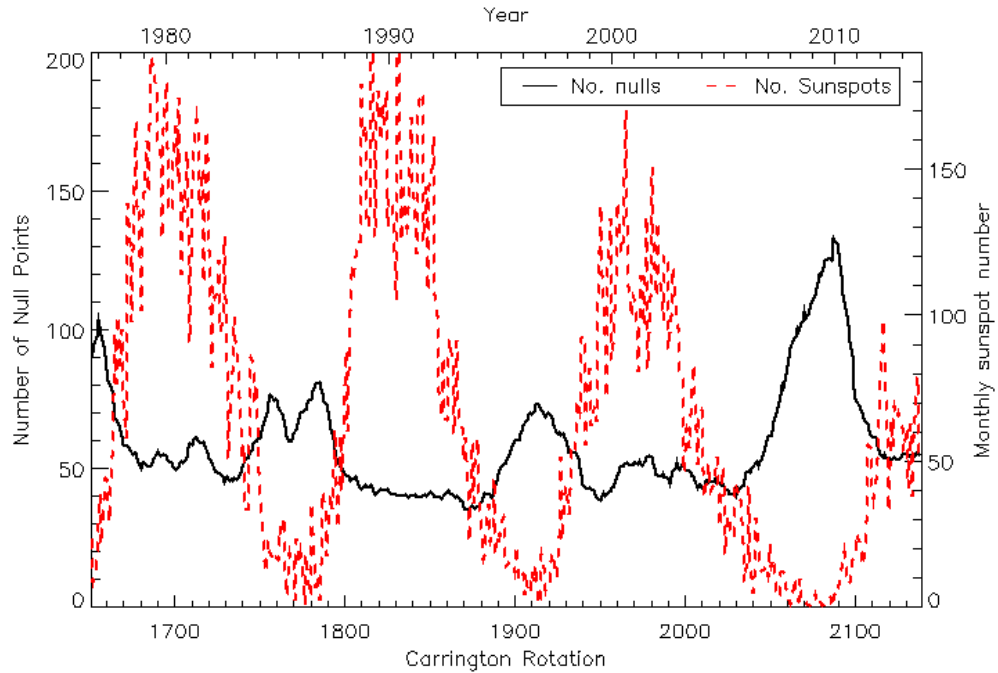


Figure 4.14: Variation in a 12 Carrington rotation running mean of number of coronal null points over time. Dashed line shows the monthly sunspot number to indicate the location of maxima and minima.

a global presence (higher harmonics becoming important).

4.4.3 Null Points

The number of coronal null points shows considerable variation over the course of a solar cycle (see Figure 4.14). There are many more coronal null points at solar minimum than at solar maximum. This is because, during the minimum of a solar cycle, the photospheric field becomes more mixed in the absence of active regions. This is contrary to the findings of Cook et al. [2009] which suggested more null points occur at solar maxima than solar minima. This discrepancy is the result of a combination of factors. First, the PFSS model shown here has a higher resolution than that used by Cook et al. [2009]. Secondly, the magnetograms used by Cook et al. [2009] were synthesised by emerging bipolar regions into a smooth dipole field which neglects the quiet-Sun mixing that accounts for most of the nulls found in our PFSS extrapolations.

The most recent minimum shows the greatest number of nulls in the time period considered. This could be an effect of the low numbers of active regions at this time and also a longer period of solar minimum so the photospheric field can become more mixed on small scales. Fewer active regions mean that mixed field will occur across more of the surface of the Sun and hence more null points will form in the

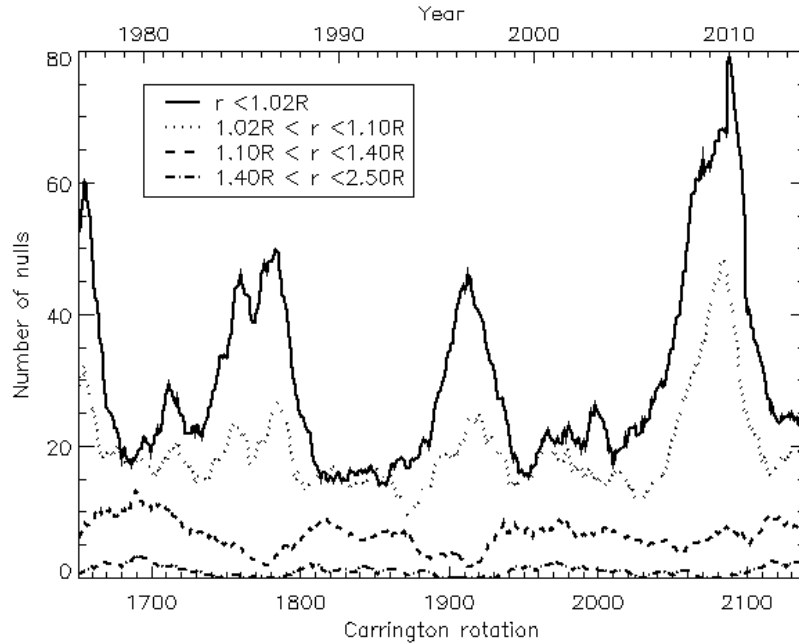


Figure 4.15: Variation in the number of nulls in different ranges of heights in the corona, 12 Carrington rotation running mean. The solid line shows the number of nulls below $1.02R_{\odot}$, the dotted line shows the number of nulls between $1.02R_{\odot}$ and $1.1R_{\odot}$ and the dashed and dash-dotted show the number of nulls between $1.1R_{\odot}$ and $1.4R_{\odot}$ and $1.4R_{\odot}$ and $2.5R_{\odot}$, respectively.

corona. Additionally, the weaker polar field will allow null points to form higher in the atmosphere allowing them to be more easily found in our model.

The size and flux of the photospheric magnetic feature associated with a null point can dictate the height of the null point. Figure 4.15 shows the number of null points in four different coronal height ranges. We can see that at all times most of the null points present occur below $1.02R_{\odot}$ (solid line) and that the number of null points at these low heights is at its highest during solar minimum. This is because even though small-scale polarity mixing can occur on almost any patch of quiet sun at any time through the solar cycle, during solar maximum there is less quiet-Sun over which these nulls can form. A very similar trend is apparent in the number of nulls between $1.02R_{\odot}$ and $1.1R_{\odot}$ as nulls at these heights are also mostly associated with quiet-Sun fields.

Considering null points between $1.1R_{\odot}$ and $1.4R_{\odot}$ (dashed line in Figure 4.15) there are fewer null points in this height range at minimum than at maximum except in the case of the cycle 23/24 minimum. During the cycle 23/24 minimum the number of null points with heights between $1.1R_{\odot}$ and $1.4R_{\odot}$ stays at approximately the same level as at the cycle 23 maximum. This is caused by the weakness of the polar field during this minimum. The weak polar field allows field structures from small-scale

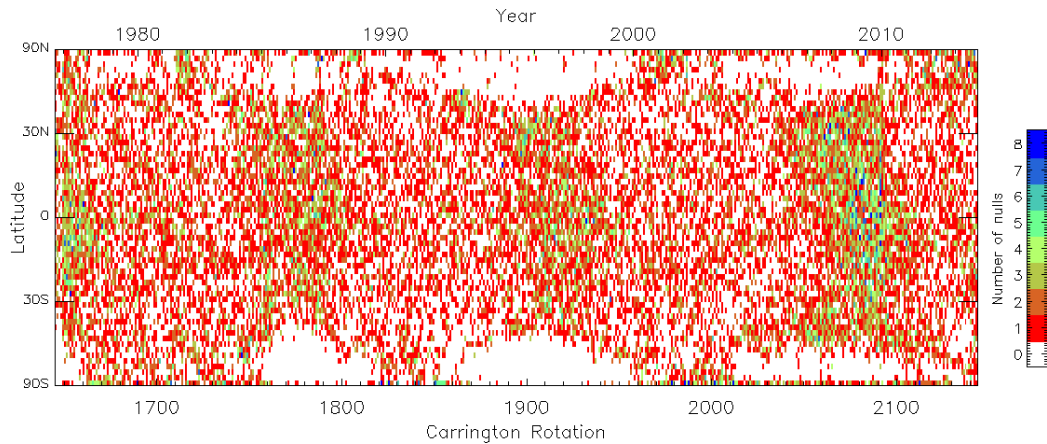


Figure 4.16: “Butterfly” plot of the number of nulls present at each latitude against time. The colour represents the number of nulls in a particular latitudinal range for each synoptic map. The y axis is scaled with the sine of the latitude so that every pixel represents the same area on the sun.

flux elements to expand and allows null points to sit higher in the corona.

There are very few null points above $1.4R_{\odot}$ at all times during the solar cycle however it can be seen that the numbers of these nulls varies in phase with the solar cycle. These nulls are associated with active regions and it is nulls in this height band that were found by Cook et al. [2009] in their simulations of the global magnetic field.

As well as the distribution in height of null points, we also consider their distribution in latitude. Figure 4.16 shows a “butterfly” diagram of the number of nulls in the corona at a given latitude over time (this can be compared with Figure 1.5). Here we plot with a sine-latitude scaling which means that we give less weight to the polar field regions where the magnetogram measurements may not have such good coverage. The highest concentration of null points near the equator occurs at solar minimum. This is because, at solar minimum, the poles are usually strong unipolar regions above which null points do not form in our model owing to the poor resolution of the poles in the original magnetograms. Few nulls appear near the poles and they mostly occur at solar maximum when the poles are in the process of magnetic reversal. However, during the solar minimum in cycle 23/24 there was not such a drop in the number of high latitude null points, this is due to the increased distortion of the heliospheric current sheet and the weakening of the poles allowing mixed field closer to the poles that would be expected at solar minimum.

Figure 4.16 also shows the motions of mixed polarity field towards the poles in the run-up to each polar field reversal. This migration is not always symmetric about the equator and in the current cycle the stream of nulls from the northern hemisphere began before the stream of nulls from the southern hemisphere.

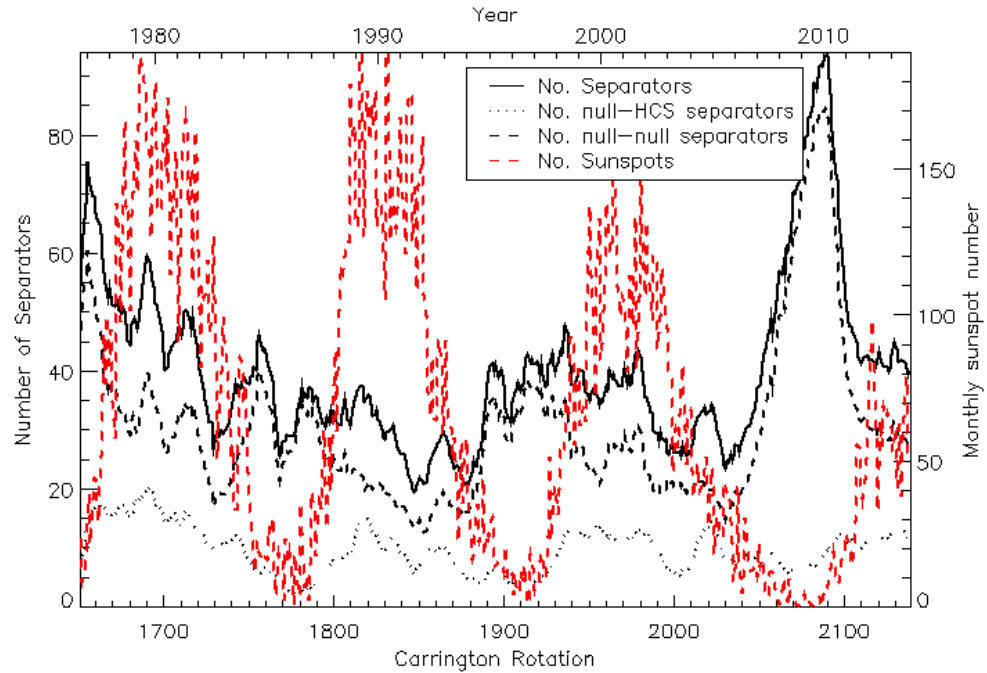


Figure 4.17: Variation in the number of separators against time, 12 Carrington rotation running mean. Solid black line shows the total number of separators, dotted black line shows the number of null-HCS separators, dashed black line shows the number of null-null separators and dashed red line shows the sunspot number to indicate the solar cycles.

4.4.4 Separators

Another topological feature to consider are the field lines that connect null points, i.e., *separators*. Separators are important sites for magnetic reconnection [e.g Priest and Titov, 1996, Galsgaard et al., 2000, Longcope, 2005, Parnell et al., 2010] which is thought to be the main mechanism through which stored magnetic energy is released into the corona. We will examine how the number, height and length of these vary over the solar cycle.

There are two kinds of separator in this model: separators which connect two coronal null points (null-null separators) and separators which connect a coronal null point to the null line at the base of the HCS (null-HCS separators). Figure 4.17 shows the variation in the numbers of separators over time. The total number of all separators is highest at solar minimum (black solid line, Figure 4.17) this is because of the increased number of null-null separators at solar minimum (black dashed line), which is linked to the greater mixed polarity field on the solar surface at these times creating a large numbers of nulls (see Figure 4.14).

There is some evidence to suggest that the number of null-HCS separators is greater during solar maximum. This is caused by the relative strength of fields at the

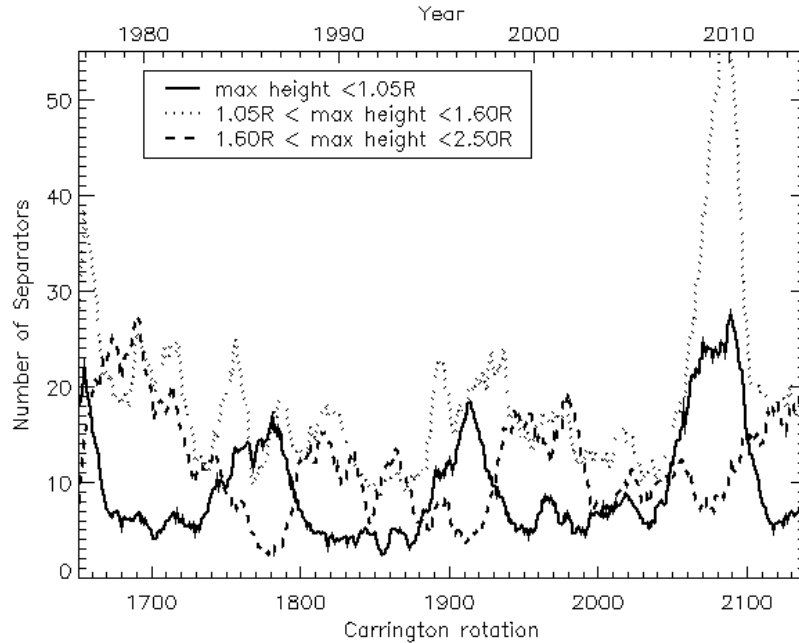


Figure 4.18: Variation in the number of separators reaching maximum heights against time. 12 Carrington rotation running mean: lower than $1.05 R_{\odot}$ (solid line), between $1.05 R_{\odot}$ and $1.6 R_{\odot}$ (dotted); and between $1.6 R_{\odot}$ and $2.5 R_{\odot}$ (dashed)

equator compared to those at the poles which distort the HCS current sheet and allow more separatrix surfaces to form outside the HCS curtain. Some of these separatrix curtains connect to the HCS neutral line and form null-HCS separators. However, during the minimum between cycle 23 and 24 the number of null-HCS separators remains high due to the weaker polar field at this time allowing the HCS to distort more than expected for a minimum (see Figure 4.12).

Figure 4.18 shows the variation of the number of separators in different height ranges over the solar cycles. The height of a separator is taken to be the maximum height to which it reaches along its length. Most separators at solar minimum are low-lying (Figure 4.18, solid line) and connect null points that form over quiet sun regions. The heights of the separators found are, in general, much higher than the nulls they connect, since they tend to arch up high in the atmosphere. The separators with the highest maximum heights are naturally the null-HCS separators.

In three dimensions, reconnection can occur along the length of a separator [e.g., Galsgaard et al., 2000, Parnell et al., 2010]. This means that separators could be important reconnection sites. The variation in the number of separators of different lengths is shown in Figure 4.19. Separators shorter than 500 Mm are most common at solar minimum. These occur between pairs of low-lying null points where the separator is also low-lying. The difference between the numbers of long separators between cycle minimum and cycle maximum is much less pronounced. There is some

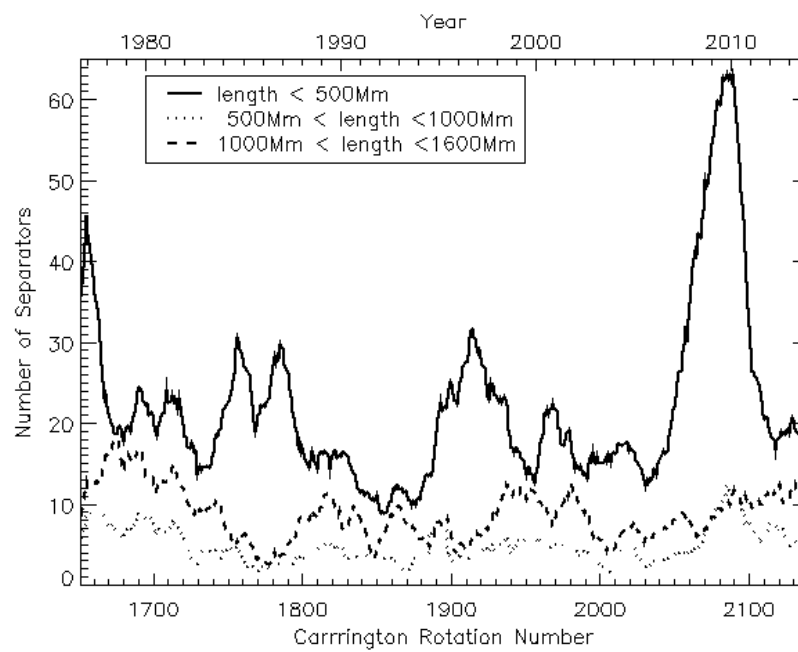


Figure 4.19: The 12 Carrington rotation running-mean time variation of the number of separators of different lengths. Shorter than 500 Mm (solid line), between 500 Mm and 1000 Mm (dotted line) and between 1000 Mm and 1600 Mm, which is the maximum length found in our model (dashed line).

evidence to suggest that “medium length” separators (Figure 4.19 dotted line) occur more often at solar maximum. This could be because they connect null points high in the atmosphere. The dashed line in Figure 4.19 shows the number of separators that are longer than 1000Mm. These separators either loop high in the atmosphere above the nulls they are connecting or they connect low-altitude nulls to the HCS. The longest separators are up to 1600 Mm long with most of these found during solar maxima. Although, during the recent solar minimum, the number of long separators has remained high. This is because the weak polar fields cause a distortion of the HCS curtain (Figure 4.12) which can produce more separatrix curtains, which in turn form null-HCS separators when they intersect the HCS curtains.

4.5 Discussion

Globally, the magnetic topology in the corona is very different at solar maximum than at solar minimum. At solar maximum the fields associated with active regions dominate over the weak polar fields and produce large-scale topological structures that can vary widely depending on the active regions present on the sun. In general there are few null points present and those that are present are often associated with large active regions and so can form high in the atmosphere. The position of the HCS is effected by the active regions and does not lie close to the equator.

At solar minimum, globally, the field looks dipolar, but the topological structures vary depending on the strength of the polar field. During all solar minima there are many null points present as the lack of active regions presents a large expanse of quiet-Sun field of mixed polarity above which many null points can form.

In the minima between cycles 21 and 22 and between cycle 22 and 23 the global dipole was strong and the topology reflected this by having the topological complexity concentrated low in the atmosphere. This contrasts with the last minimum (between cycles 23 and 24) where the global dipole was weak and magnetic structures moved higher in the atmosphere than would be expected.

In every solar maximum and in those solar minima where the polar field is weak many disconnected open-field regions form. These often come from very small regions on the photosphere and funnel out to large regions at the source surface.

We can quantify many topological features such as null points and separators over the solar cycle and a marked difference is seen during the cycle. Null point numbers are at their highest at solar minimum as is the number of separators. If we subdivide null points and separators by height then we can see high-altitude null points and separators are most common at solar maximum as they are associated with features that contain a strong flux. The nulls that are high in the atmosphere are likely to sit over a region with high magnetic flux which could potentially be important for the magnetic breakout model for CMEs [Antiochos et al., 1999].

As well as seeing a difference in the height of topological features through the cycle, the latitude of features also shows cyclic variation. During minima most of

the complex topology occurs at lower latitudes as near the poles the field is unipolar. At maximum the polar fields have little or no influence on the global topology and complex magnetic structure can be seen at all latitudes.

Chapter 5

Long-term Trends in Topological Structures

In Chapter 3, we described various different magnetic configurations made up of separatrix surfaces and, in Chapter 4, we analysed the long term variations of some topological features. In this Chapter, we bring together the knowledge gained about different magnetic structures from Chapter 3 with the topological analysis from Chapter 4 by considering the trends in the separator connections between null points to see what this can tell us about the magnetic structure. Finding the number and type of separator connections that a null point has, combined with details about the null point's spines and separatrix surfaces, allows us to draw conclusions about the types of topological structures that exist in the corona and to classify them.

In Chapter 3, we described the topology of a separatrix dome structure where separatrix surfaces from one or more nulls close down to the photosphere forming a closed ring containing all the magnetic field underneath the separatrix dome. Such structures can form in areas of closed field, e.g., under the HCS curtains. In these cases both spines of the nulls whose separatrix surfaces form the dome intersect with the photosphere. Separatrix domes can also form in areas of open field in which case one spine from each of the dome nulls extends up to the outer boundary. If we have a dome in an open field region made of the separatrix surfaces from more than one null, then an open separatrix curtain will form, piercing the dome (see Section 3.5.2 for more details).

Separatrix curtains are separatrix surfaces that intersect with the source surface, the outer boundary of our model. There are two types of separatrix curtain: open and closed. Closed separatrix curtains are bounded on both sides by the HCS curtains and so create a region of disconnected open field. A closed separatrix curtain will produce two null-HCS separators. Although, in the case where we have a closed separatrix curtain formed from the separatrix surfaces of multiple nulls (e.g., example in Section 3.5.4) these null-HCS separators will not connect to the same null.

Open separatrix curtains do not create disconnected open-field regions. They are either bounded by the HCS curtains on only one end or are completely bounded

by spines. If they are bounded by the HCS curtain on one end then they will be associated with only one null-HCS separator.

We can strip back the magnetic skeleton and only consider the null points, the separators and the HCS null line. This enables us to easily see which topological structures are linked and which are separate. From simply considering the separator connections between nulls we can quickly classify particular kinds of features.

In Section 5.1, we consider the numbers of separatrix domes involving only one null point and their variation through the cycle. We also consider the variation in the number of nulls whose separatrix surfaces intersect with the upper boundary and hence form all or part of a separatrix curtain.

Following this, in Section 5.2, we consider networks of nulls and separators and examine what certain parts of these networks can tell us about the global structure of the corona.

Finally, in Section 5.3, we consider particular structures that we can easily classify from the separator networks and investigate the variation of their numbers with time.

5.1 Isolated separatrix domes from one null and open separatrix surfaces

A separatrix dome from one null point (see Section 3.5.1) is the only separatrix-surface configuration in the solar corona which consists of a null point with no associated separators. Figure 5.1a shows the variation in the number of separatrix domes formed from a single separatrix surface with time. At solar minimum, there are greater numbers of null points than at solar maximum and, hence, greater numbers of isolated separatrix domes (black line) are seen at this time. Most of these domes are formed in closed field regions and such domes are identified by both of their spines being closed (green line). The number of domes in open-field regions i.e., those with open spines, (blue line) do not show any clear cyclic variation.

Instead of looking at the numbers we can see how the proportion of null points that form isolated domes varies over the solar cycle (Figure 5.1b). From this graph, we can see that the proportion of isolated domes is still higher at solar minimum than at solar maximum. However, if we consider the proportion of isolated domes with open spines, i.e., isolated domes in open-field regions, (blue line in Figure 5.1b) we see that in all cycles the highest proportion of these isolated domes occurs just after the peak of cycle maximum which is also the time when the polar fields undergo reversal. At this time the HCS is very warped leading to open field at all latitudes, this means low-latitude null points can form in open-field regions producing isolated separatrix domes with open spines.

The numbers of nulls whose separatrix surfaces close down to the photosphere forming separatrix domes can be compared with the numbers of nulls with separatrix surfaces that intersect with the source surface and form all or part of a separatrix curtain. Figure 5.2 shows the proportion of nulls that have such separatrix surfaces.

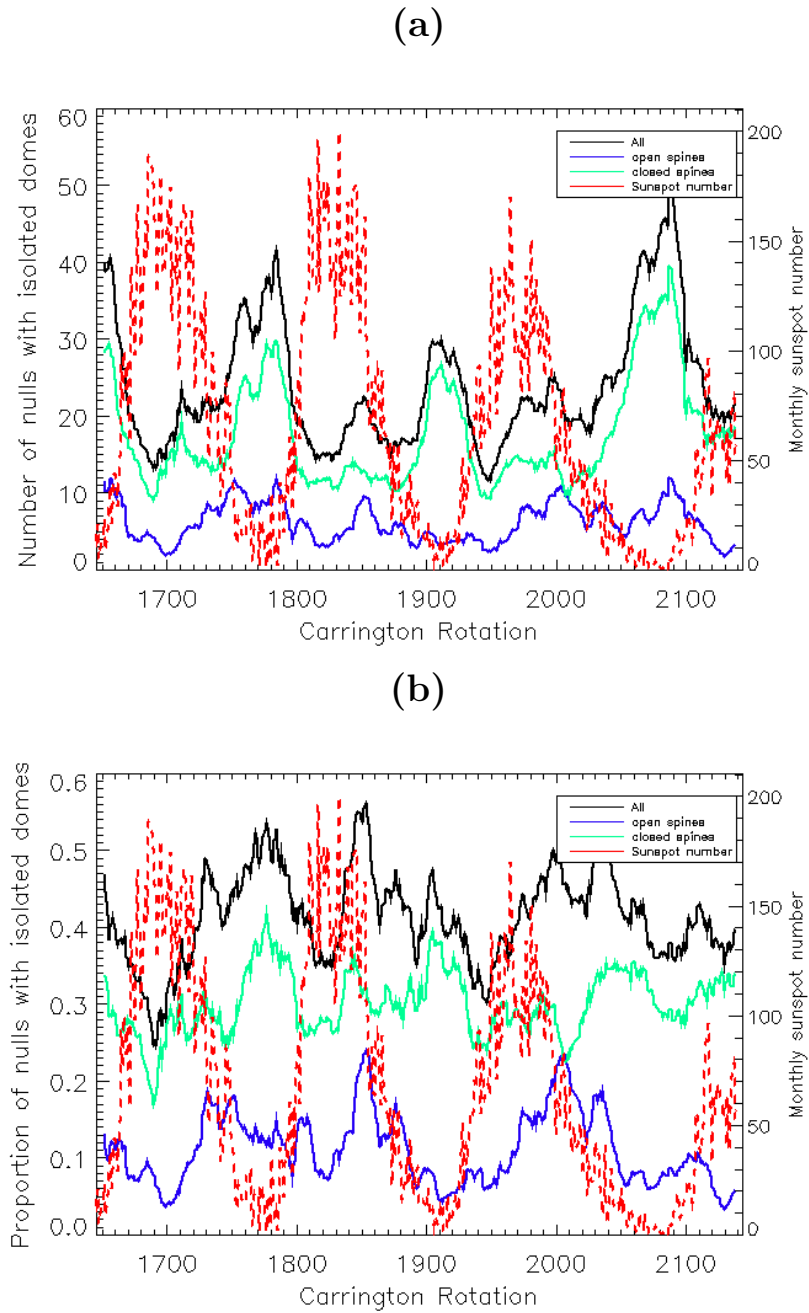


Figure 5.1: (a) shows the variation in the number of separatrix domes from single null points (12CR running mean) and (b) shows the proportion of null points that form isolated separatrix domes (12CR running mean). The black line shows the total, the green line shows domes formed in a closed field region, the blue line shows the domes formed in an open-field region and the red dashed line shows monthly sunspot number to indicate the solar cycles.

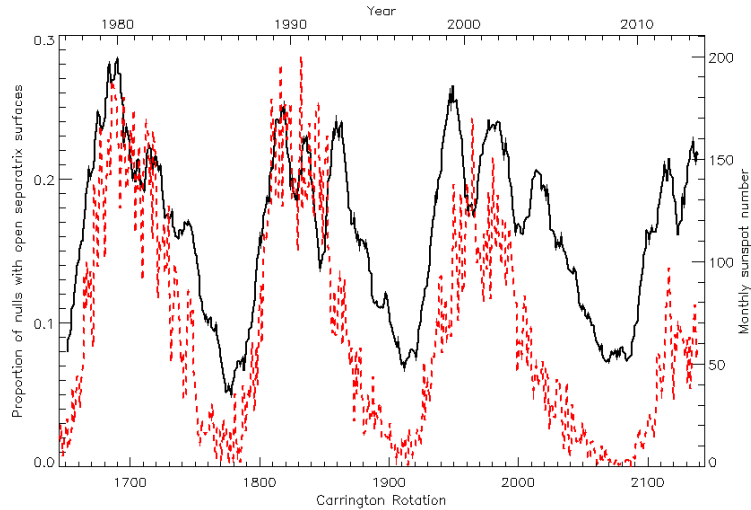


Figure 5.2: 12 CR running mean of the proportion of null points with separatrix surfaces that intersect with the source surface (black line). Monthly sunspot number is plotted to indicate the solar cycles (red dashed line).

The numbers of these nulls vary in phase with the solar cycle with between 10% and 30% of the total number of nulls present in each Carrington rotation associated with separatrix curtains at all times. This means that there are around 40% of nulls that do not form isolated domes and do not form separatrix curtains.

5.2 Null-Separator networks

As well as considering the nulls that have no separators we can also consider networks of separators and the clusters of null points within them. It is possible that changes in the topology around one nullpoint or separator in the network could have consequences for the rest of the network.

For each Carrington rotation PFSS extrapolation we have a null-separator map in which all the null points are vertices, in addition there is a vertex for the HCS null line and a vertex for a bald patch (if present). If there is a separator between two nulls then an edge is drawn between the corresponding vertices, similarly for separators between a null and the HCS null line or a bald patch. Once all the edges have been drawn the map is partitioned into connect sets of nulls and separators that we call separator networks.

Figure 5.3 shows the null point and separator networks for the three Carrington rotations whose global coronal topologies were examined in detail in Chapter 4: the strong solar dipole minimum case is CR1904 (top), the solar maximum case is CR1957 (middle) and the weak solar dipole minimum case is CR2083 (bottom). In all cases, the HCS null line (green circle) is connected to the largest connected separator

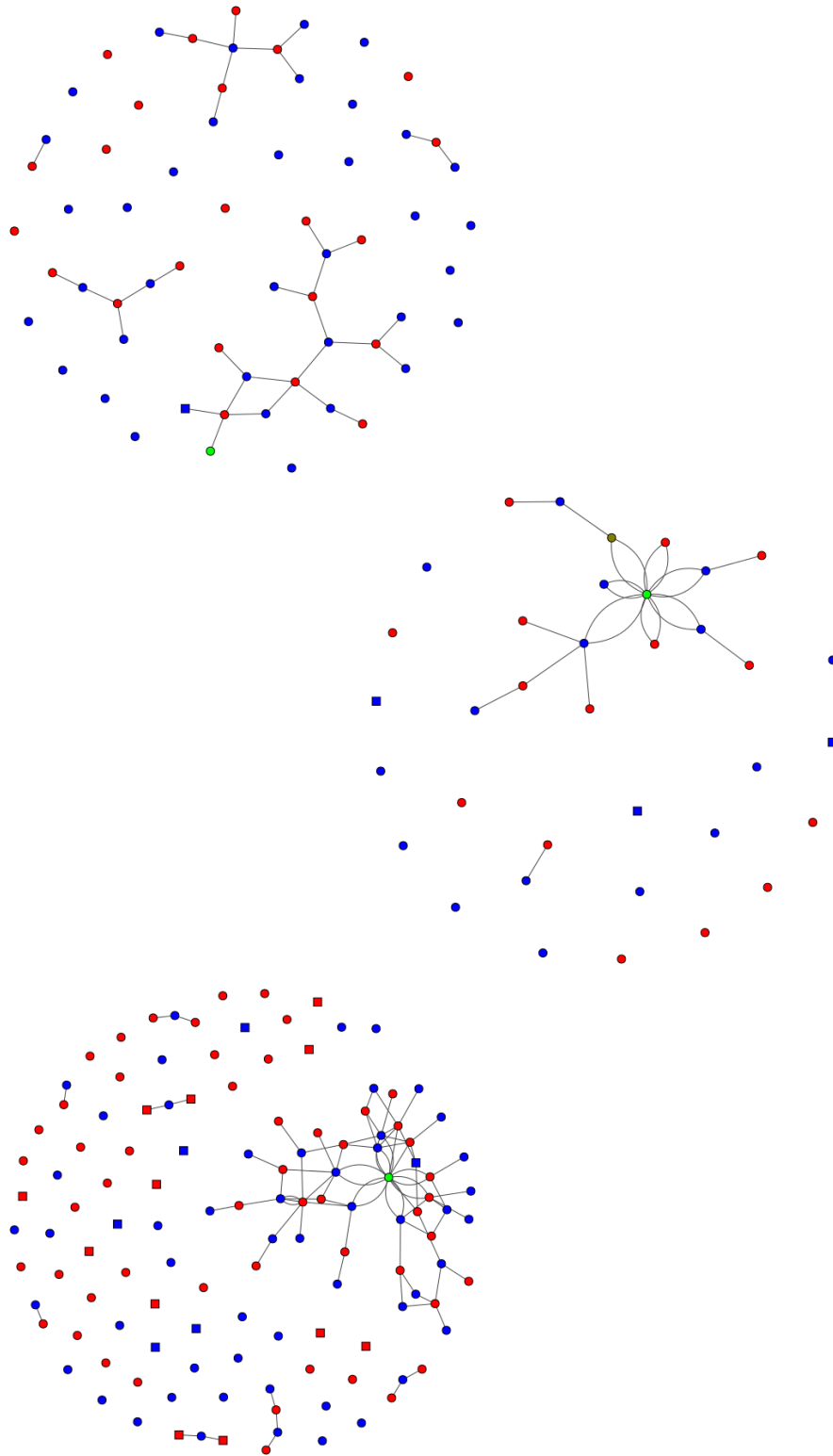


Figure 5.3: Null-Separator maps for KP/low-res SOLIS extrapolations for (left) CR1904, (middle) CR1957 and (right) CR2083. Red and blue symbols are positive and negative null points respectively (squares indicate nulls with open spines, circles indicate nulls with closed spines). Olive circles represent bald-patches and the green circle represents the HCS null line. Black edges indicate separator connections between null points.

network. Indeed in CR1957 and CR2083 (Figure 5.3 middle and bottom) the HCS null line has many more edges (separators) connected to it than any other null. This is to be expected since it is really a line of infinitely many null points. However, in CR1904 (Figure 5.3 top panel) even though the vertex representing the HCS null line only has one separator connection, it is still part of the largest separator network.

In CR1904 (Figure 5.3 top), which occurred in the solar minimum with the strong global dipole, there are other networks of nulls that contain many null points other than the network that includes the HCS null line. However, in both the weak solar dipole minimum and the solar maximum case there are very few nulls connected together other than those connected to the HCS null line.

In all three cases there are very few nulls with open spines (squares). In the strong global dipole solar minimum example (Figure 5.3 top) there are two large networks that are not connected to the HCS, however, all the nulls in these networks have closed spines which tells us that these complex networks must lie underneath the HCS curtains.

We can consider the trends in the proportion of nulls that are part of the network that is connected (by separators) to the HCS null line. Figure 5.4b shows the proportion of null points that are connected to the HCS null line by any chain of separator connections (i.e., are part of the HCS separator network). This proportion is highest at solar maximum during cycles 21, 22 and 23 and also during the extended solar minimum between cycles 23 and 24. The proportion of null points connected via the separator network to the HCS is greater at maximum because, at solar maximum, nulls points form that are associated with large scale magnetic features such as active regions. These nulls are higher in the atmosphere and are more likely to have global connections and, hence, be connected to the HCS null-line thus increasing the size of the network connected to the HCS.

It is interesting that during the recent solar minimum (cycle 23/24) there is a high proportion of nulls that have separator connections to the HCS. There are many more nulls present during this extended solar minimum than in the previous two minima and there is also a higher proportion of nulls that are connected through a separator network to the HCS. This means that, during this time, the HCS null line is part of a very large complex network of nulls and separators, an example of one of these from CR2083 is shown in Figure 5.3 (bottom panel).

Figure 5.4a shows the number of null-HCS separators which follows a similar pattern to the size of the HCS null-separator network.

In addition to counting the null-HCS separators we can also count the number of null points that have at least one null-HCS separator (Figure 5.5). The number of nulls connected to the HCS is highest at solar maximum and also during the recent weak dipole solar minimum. This agrees with what we see in Figure 5.3: CR1919 (strong dipole minimum) has only one null connected to the HCS whereas CR1957 (solar maximum) and CR2083 (weak dipole solar minimum) both have many nulls connected to the HCS. The number of null-HCS separators shows a peak during the cycle 23/24 minimum whereas the number of nulls connected to the HCS shows a

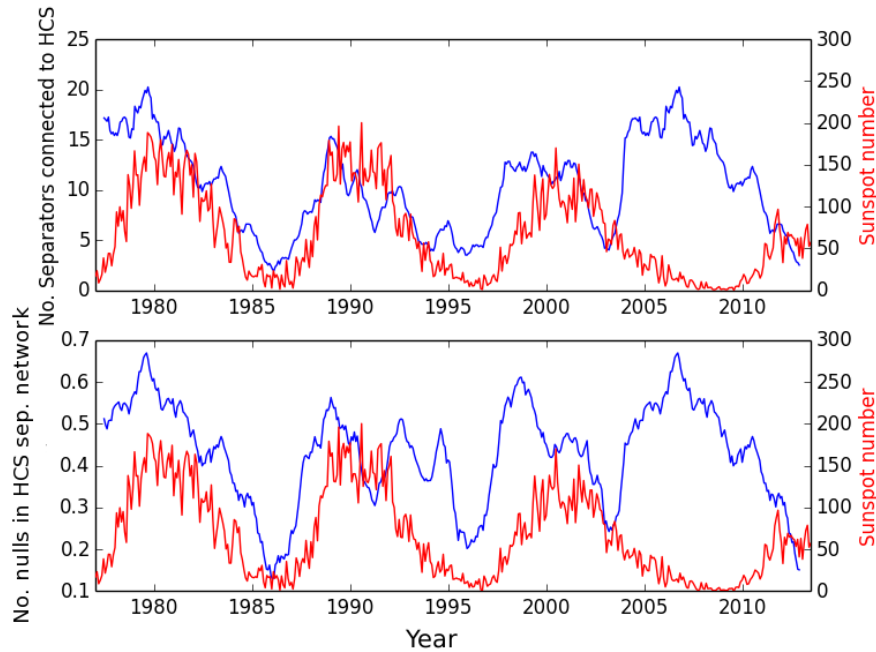


Figure 5.4: 12 Carrington rotation running mean of number of separators connected to the HCS (top) and proportion of nulls that are in the HCS null line separator network i.e., are nulls that are connected to HCS null line via a chain of separators (bottom). Sunspot number is plotted in red to indicate the solar cycles.

slight dip during the cycle 23/24 minimum. This suggests that during this weak minimum more of the nulls connecting to the HCS had multiple null-HCS separators.

In Figure 5.3 top panel we see that in some cases large connected networks of nulls can form that are not connected to the HCS null line. Figure 5.6 (top) shows the variation in the number of nulls in the largest network that is not connected to the HCS null line. The largest networks not connected to the HCS are found during the minima between cycle 21 and 22 and between cycle 22 and 23. This could be due to a large connected network of nulls and separators associated with quiet-sun field forming under the HCS curtains. However, the weak dipole solar minimum between cycle 23 and 24 does not show a peak in the size of the largest network that is not connected to the HCS like the previous minima. This is due to the weak global dipole in this minimum allowing structures associated with the quiet-sun to expand and hence allowing them to interact with and form separator connections to the HCS null line.

Figure 5.6 (bottom) shows the mean number of nulls in a connected separator network (including those networks connected to the HCS null line). This seems to peak twice during each cycle: once just before the peak in cycle maximum and once during the decline phase of the cycle. These two peaks have different explanations. The peak just prior to cycle maximum occurs because, at this time (just before polar

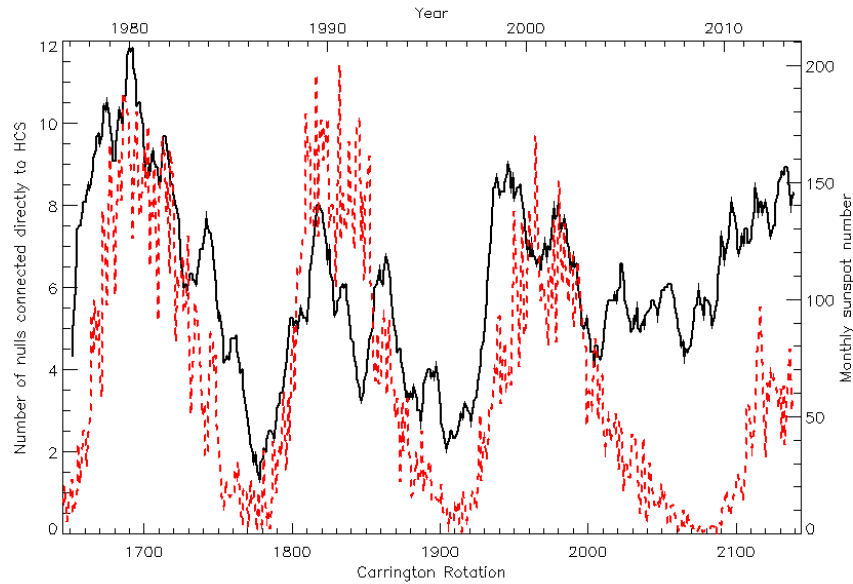


Figure 5.5: Plot of the number of nulls that have a null-HCS separator (12 Carrington rotation running mean). The monthly sunspot number is shown to illustrate the solar cycles (red line).

field reversal), the HCS null line becomes very distorted so many separatrix curtains that connect to the HCS can form creating separator connections to the HCS. This means there is one very large connected network of nulls which shifts the mean. The peak in the mean number of nulls per separator network in the decline phase of the cycle is caused by the mixing of field which allows many small networks of nulls to form that are not connected to the HCS thus increasing the average.

We can classify the types of networks formed by splitting them into linear networks and networks that are branching or contain loops. Figure 5.7 shows the numbers of linear and branching networks. Here all single nulls with no separator connections are ignored. We can see that at all times linear networks are more common than branching networks and, in most cases, there is only one branching network which is usually the network connecting to the HCS null line. We see that during the minima between cycles 21/22 and 22/23 there are both more branching networks and more linear networks than there are in the maxima of those cycles. This trend does not, however, continue into the minimum between cycles 23 and 24. Considering our example case from the cycle 23/24 minimum, CR2083 (Figure 5.3 bottom), we can see that during this Carrington rotation there are many nulls connecting to the HCS null line forming one large network and very few other networks with more than one null. This is typical for the cycle 23/24 minimum where the weak polar field allowed magnetic structures to expand and thus interact the the HCS null line forming one large separator network.

Figure 5.8 shows histograms of the number of separator networks (per Carrington

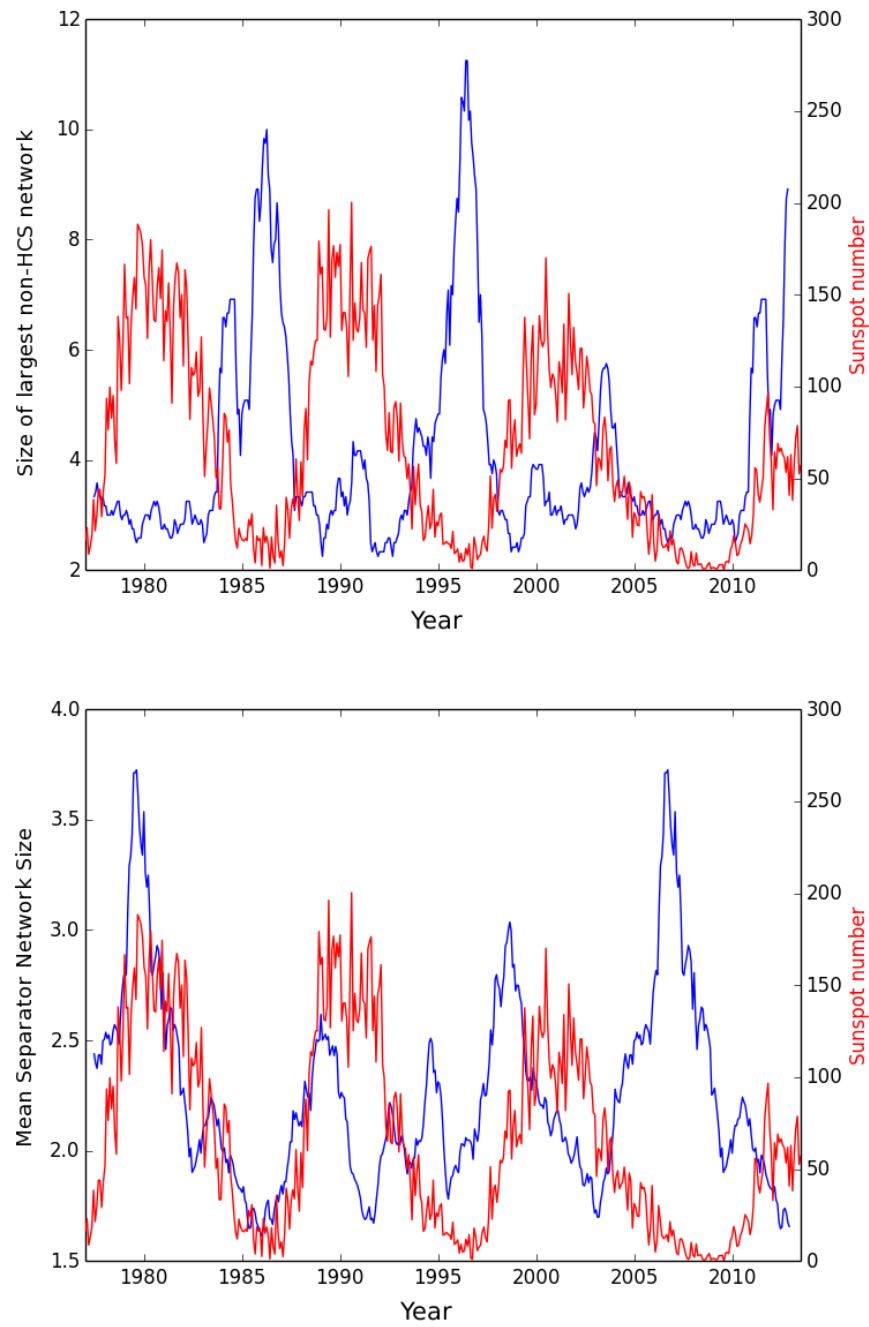


Figure 5.6: 12 Carrington rotation running mean of (top) number of nulls in the largest separator network that is not connected to the HCS and (bottom) mean number of nulls in a separator network (including HCS separator network). Red line shows sunspot number to indicate solar cycles.

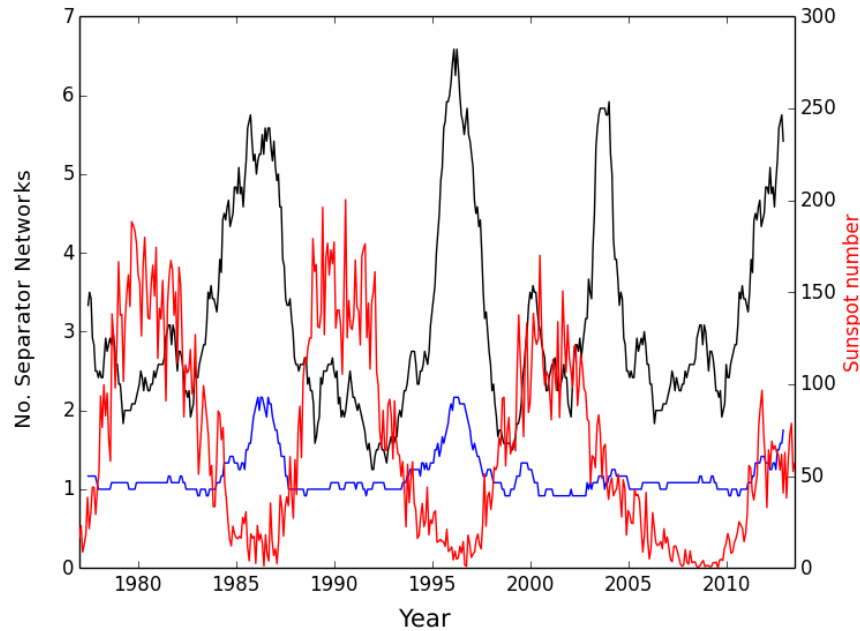


Figure 5.7: 12 Carrington rotation running mean of the number of linear networks (black line) and branching networks (blue line). Red line shows sunspot number to indicate the solar cycles.

rotation) against the network size. From the data set 51 consecutive frames have been selected from each of the two types of solar minimum and from solar maximum. During the strong dipole minimum (Figure 5.8 top), there are many networks that contain between one and ten nulls and a several networks that contain between ten and twenty nulls and few networks that are larger. In the case of a weak dipole minimum and at solar maximum (Figure 5.8 middle and bottom) there are fewer separator networks with sizes between ten and twenty but more networks with larger sizes. These larger sized separator networks correspond to the large HCS separator networks such as those seen in Figure 5.3 (centre and bottom).

5.3 Classifying topological structures

It is possible to use information about individual separator networks described in the previous section to classify types of topological structure such as a double separatrix cave and a dome-tunnel. We describe these features in this section and explain how they can be identified, as well as looking at how their numbers vary over the solar cycle.

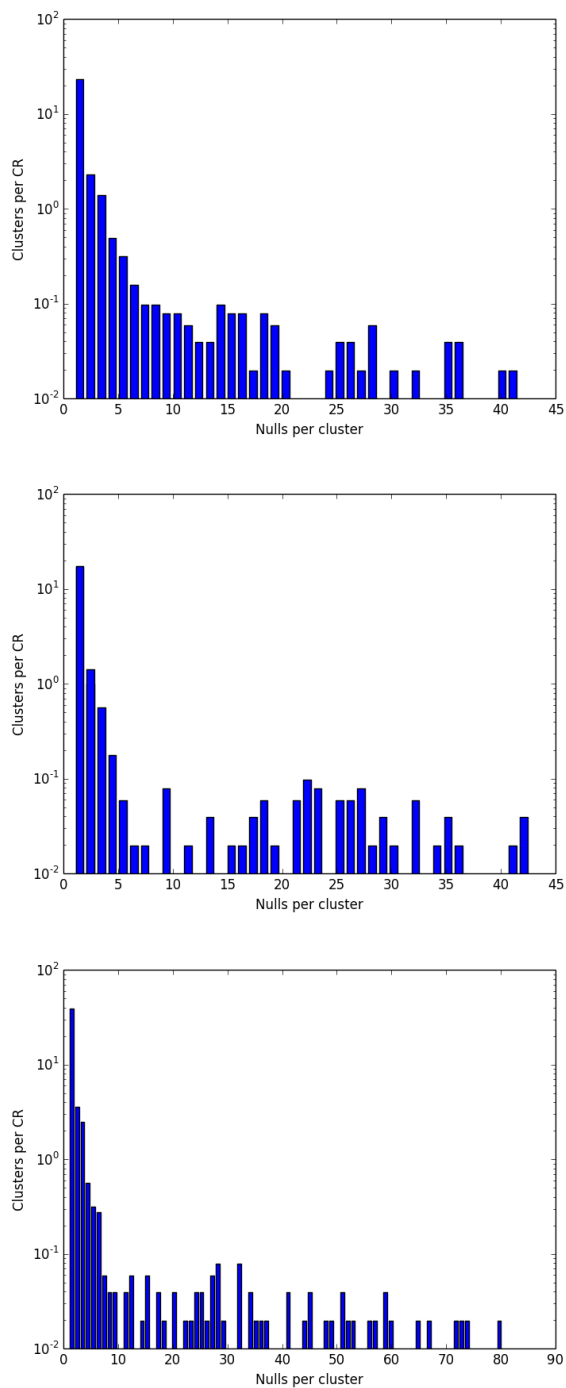


Figure 5.8: Histograms of the numbers of separator networks of different sizes. Top shows results from Carrington rotations during a strong dipole minimum (CR1880-CR1930), middle shows results from Carrington rotations during solar maximum (CR1940-CR1990) and bottom shows results from Carrington rotations during a weak dipole minimum (CR2050-CR2100).

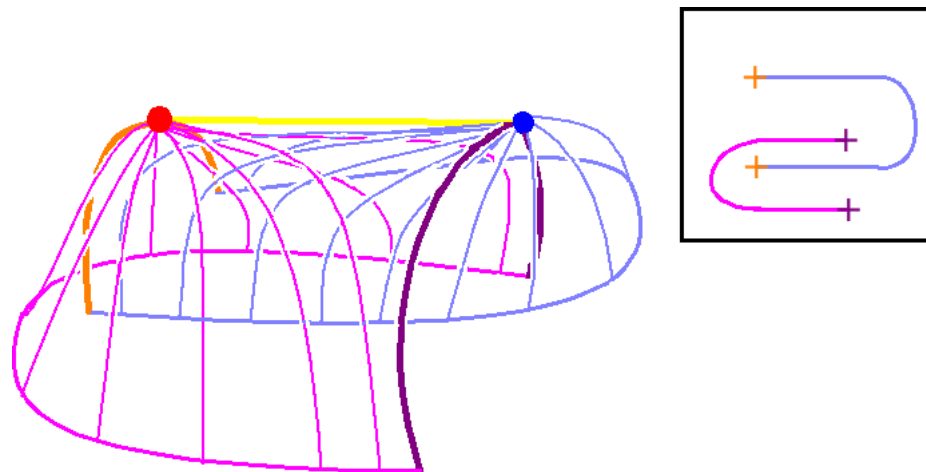


Figure 5.9: Sketch of a double cave structure. Pink and blue lines are field lines in the separatrix surfaces of a positive (red dot) and negative (blue dot) null, respectively. The spines of these nulls are coloured orange and purple for positive and negative and the separator is coloured yellow. The intersection of this structure with the photosphere is shown in the black box.

5.3.1 Double caves

The only way we can have a situation in which two nulls are just connected to each other by a single separator and are not connected to any other nulls or the HCS null line is the case where we have a double cave. Figure 5.9 illustrates this configuration. This differs from the separatrix cave we saw in Section 3.5.3 because neither of the separatrix surfaces from these two nulls forms a separatrix curtain which would be bounded either by another spine (which would cause the structure to be connected by a separator to another null point) or by the HCS curtain (which would cause the structure to have a separator connection to the HCS null line).

If we have a linear network of null points with an even number of nulls that is greater than two, then we get an elongated double cave structure. Such a structure is complex so for ease of understanding only its intersection with the solar surface has been drawn in Figure 5.10.

We can count the number of double separatrix caves by determining the number of connected separator networks that are linear (not branching) and that have an even number of null points.

Figure 5.11 shows the variation in the numbers of double caves with time. The number of double caves is at its greatest during the minimum between cycle 22 and 23. Separatrix caves are closed structures and will therefore form underneath the HCS curtains or possibly underneath large separatrix dome structures. During a strong global dipole minimum the HCS curtains encompass almost all the field within $\pm 60^\circ$ of the equator providing a good environment for these double cave structures to form. It should be noted, however, that the numbers of these structures are still low at all

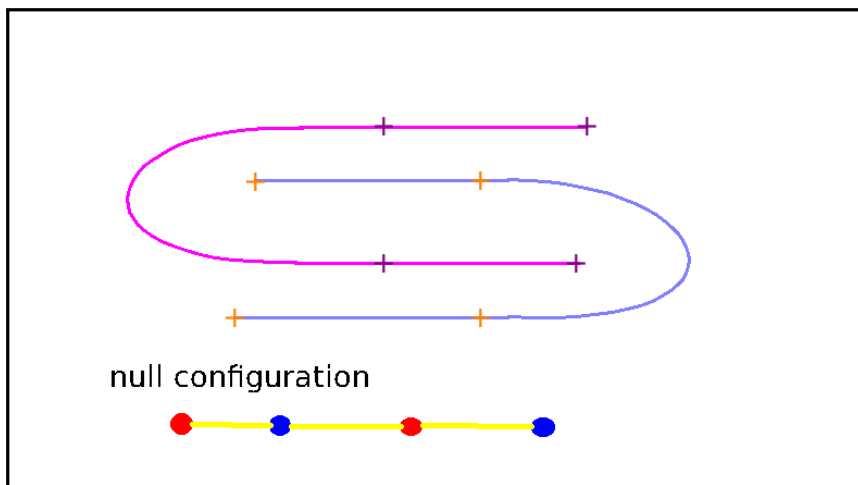


Figure 5.10: Sketch of the intersection of the solar surface with a double separatrix cave formed from the separatrix surfaces of 4 null points. Blue and pink lines are the intersection of the separatrix surfaces from negative and positive nulls, orange and purple crosses are the intersection of the positive and negative spines with the solar surface. The null configuration is also shown in which red and blue dots represent the positive and negative nulls and yellow lines represent the separators.

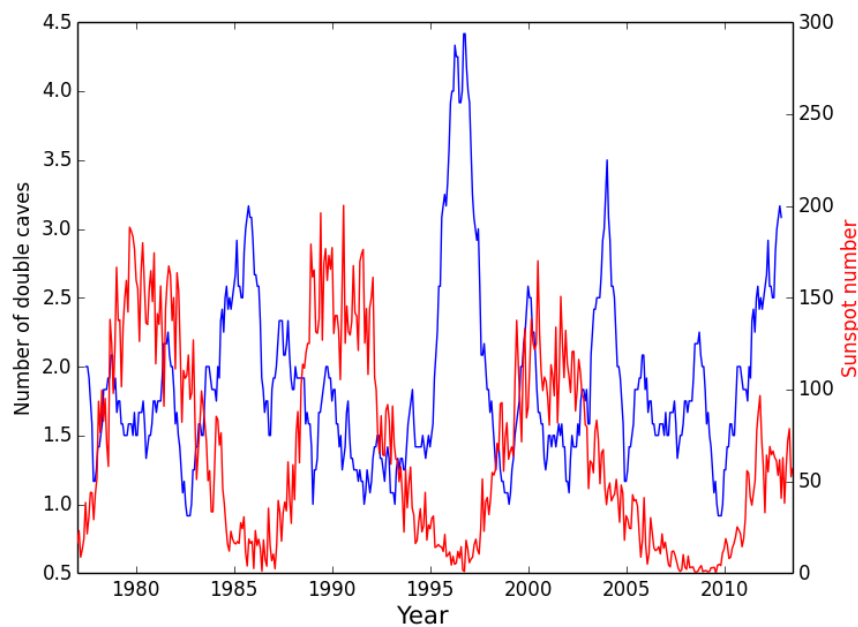


Figure 5.11: 12 Carrington rotation running mean of the number of double caves (blue line). Sunspot number is plotted (red line) to indicate the solar cycles.

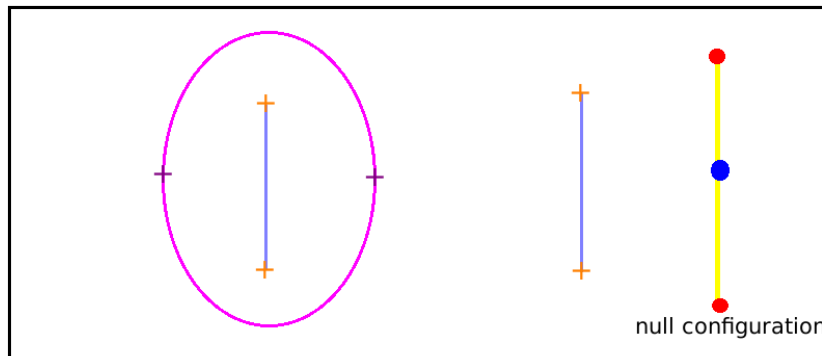


Figure 5.12: Sketch of the footprint on the photosphere of a separatrix dome and tunnel structure formed from the separatrix surfaces of three null points. Pink lines represent positive separatrix surfaces, blue lines represent negative separatrix surfaces, orange and purple crosses are positive and negative spines, respectively. The null separator configuration is also illustrated. Red and blue dots are positive and negative nulls, respectively. Yellow lines are separators.

times (at most four or five per Carrington rotation).

5.3.2 Dome-Tunnels

In Section 3.5.2, we considered a separatrix dome created from the separatrix surfaces of two null points stitched together along the spine lines of a third null. The separatrix surface from the third null point formed an open separatrix curtain. In the example shown in Figure 3.9, the separatrix dome occurred in a region of open field, however, these double-null domes can also occur in regions of closed field. In a closed-field region the separatrix surface that forms the open separatrix curtain folds back down to the photosphere creating a tunnel structure. Figure 5.12 shows the footprint of such a structure on the photosphere.

Similarly to the double cave configuration the dome-tunnel configuration can form from extended chains of nulls with the proviso that there are an odd number of nulls in the chain and that none of the spines of these nulls are open. If there are open spines then a dome and open separatrix curtain structure will form such as that seen in Section 3.5.2.

Figure 5.13 shows the 12 Carrington rotation running mean of the number of these dome-tunnel structures over the solar cycle. These structures are not as common as the double-cave structures with fewer than one occurring per Carrington Rotation. There does not seem to be a clear cyclic variation of the numbers of dome-tunnels, but considering the very low numbers of these this is not particularly surprising.

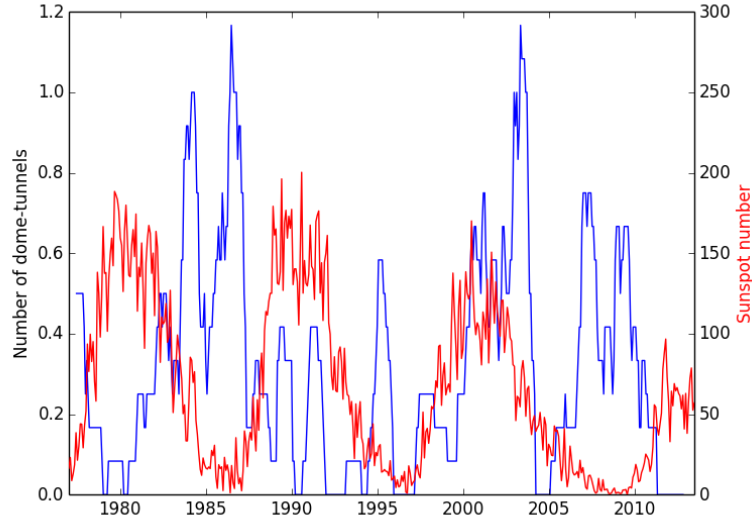


Figure 5.13: Number of dome tunnels with time (12CR running mean). Sunspot number is plotted to indicate the solar cycles (red line).

5.4 Discussion

In the recent extended solar minimum we have seen very different behaviour in the magnetic skeleton to that seen in previous solar minima. In all solar minima there are more isolated separatrix domes than at solar maxima. These domes can form over small magnetic features in the quiet sun and can often be nested within one another or nested under a larger more complex separatrix structure. In the recent extended solar minimum there are many more isolated dome structures than the previous two solar minima where the global dipole was stronger. There is also an increase in the number of nulls that have separator connections to the HCS in the weak dipole solar minimum compared to the strong dipole solar minima. This means that, during the cycle 23/24 minimum, most null points are likely to be either isolated domes or part of the separator network that connects to the HCS null line.

A large network of null points connected to the HCS null line via separator connections could mean that reconnection around any of these null points or separators could have global consequences in terms of allowing closed field under the HCS curtain to become open field leading to a change in the tilt of the HCS.

The network of nulls connected to the HCS contains a large proportion of the total number of nulls that are present for each rotation at both solar maximum and during the recent weak solar minimum. This is due to the warping of the HCS because of the weakening of the global solar dipole field allowing separatrix curtains that are connected to the HCS to form. These will have one connection to the HCS if they are open and two connections to the HCS if they are closed.

The null-separator connections graphs shown in Figure 5.3 reveal that in all cases shown the HCS null line is part of the largest connected separator network. In many instances there are no connected separator networks of more than two nulls other than the HCS null line network.

We find that at solar minimum, when the global dipole is strong, large connected networks of nulls that are not connected to the HCS null line can exist. However, at solar maximum and during the weak dipole minimum the HCS becomes very distorted and hence many separatrix curtains intersect with the HCS curtains and thus most null points are part of the HCS separator network.

The double separatrix cave structure is one example of a structure that we can easily identify simply by considering the separator network. Such structures are most prevalent during solar minima where the global dipole is strong and hence there is much low-level magnetic structure that is enclosed under, and does not interact with, the HCS curtains.

Chapter 6

Data Comparison

In this thesis, several different data sets comprising magnetograms taken from both ground-based and satellite observatories are considered. These magnetograms can vary both in their sensitivity and resolution. In this Chapter, two data sets of PFSS models with different resolutions but which are extrapolated from magnetograms from the same instrument are compared in order to understand the effect that varying resolution can have on the magnetic topology both at local scales, as well as globally.

6.1 Magnetogram data

This section will consider data from the SOLIS telescope at the low resolution described in Chapter 4 and also at a higher resolution. These data sets begin at CR2007 (starting August 30th 2003) and continue to the present. This gives us nearly 11 years worth of data. The low resolution maps have a resolution of 360 by 180 pixels in longitude and sine latitude. The PFSS models from these low-resolution data have a maximum number of harmonics $l_{max} = 81$. This gives an extrapolation resolution of 329 grid points in longitude, 165 in latitude and 48 exponentially spaced in the radial direction. The high-resolution maps have a resolution of 1800 pixels in equal steps of longitude and 900 pixels in equal steps of sine latitude. We can perform the PFSS extrapolation on this data using 301 harmonics. This gives us a resolution of 1209 grid-points in equal steps of longitude, 605 grid-points in equal steps of latitude and 177 grid-points exponentially spaced between $1.00R_{\odot}$ and $2.5R_{\odot}$.

6.2 SOLIS high-res vs. low-res

By considering individual Carrington rotations from the two SOLIS data sets we can extrapolate the global coronal magnetic fields using the PFSS model and then compare the topologies visually and statistically. We will examine one Carrington rotation during the recent extended solar minimum (cycle 23/24) and one from around the maximum of cycle 24.

6.2.1 Solar minimum comparison - CR2083

First we will consider CR2083 (beginning 3rd may 2009) which was studied in detail in the low-resolution data in Section 4.3.1. This Carrington rotation occurred during the weak dipole minimum between cycles 23 and 24.

Figure 6.1 shows the 3D global topologies of the SOLIS low-resolution PFSS extrapolation (top panel) and the SOLIS high-resolution PFSS extrapolation (bottom panel). The first thing to note is that the high-resolution extrapolation gives a much more complex topology both inside and outside the HCS curtains than the low-resolution topology. In particular, there are many more null points near the poles in the high-resolution model than in the low-resolution model that produce tiny isolated separatrix domes with spines extending to the source surface (purple and orange lines). For instance, there are 8 nulls with open spines above 65° in Northern hemisphere of the low resolution extrapolation and 45 nulls with open spines above 65° in the high resolution, similarly, below -65° there are 4 nulls with open spines in the low-resolution model and 52 in the high-resolution model. The large-scale structure, such as the configuration of closed separatrix curtains and the distortion of the HCS, found in the low-resolution extrapolation appears to be a stripped down basic version of the topology of the high-resolution extrapolation. In the high-resolution extrapolation more open separatrix curtains and more closed separatrix curtains are seen than in the low-resolution extrapolation (see below for more detailed discussion on this).

The complexity in the topology of the high-resolution extrapolation makes it difficult to see all the features in the 3D representation of the coronal topology shown in Figure 6.1. With this in mind, we look at cuts in the topological features at different levels in the atmosphere (Figure 6.2).

At the source surface (Figure 6.2a and b) the pattern of the magnetic skeleton from the low-resolution and high-resolution extrapolations is approximately the same, with two notable exceptions: the number of open spines is much greater in the high-resolution model (as discussed earlier) and also in some cases the open-field regions in the low-resolution extrapolation have been split into multiple regions in the high-resolution extrapolation by additional separatrix surfaces very close to one another.

In a cut midway through the model (Figure 6.2c, low-res and 6.2d, high-res) we see much more detail in the extrapolation from the high-resolution data. There are many more large rings between the HCS curtains which correspond to large separatrix domes, as well as a complex web of separatrix surfaces that form the separatrix curtains. Once again, though, there are clear similarities between these cuts. The high-resolution extrapolation shows more separatrix surfaces at this height but they lie in approximately the same location as the separatrix surfaces in the low-resolution extrapolation.

The high-resolution cut in the topological structures at the base of the model (Figure 6.2f) shows a highly complex network of small scale separatrix domes and spines. The small-scale mixing of flux that is resolved in the high-resolution extrap-

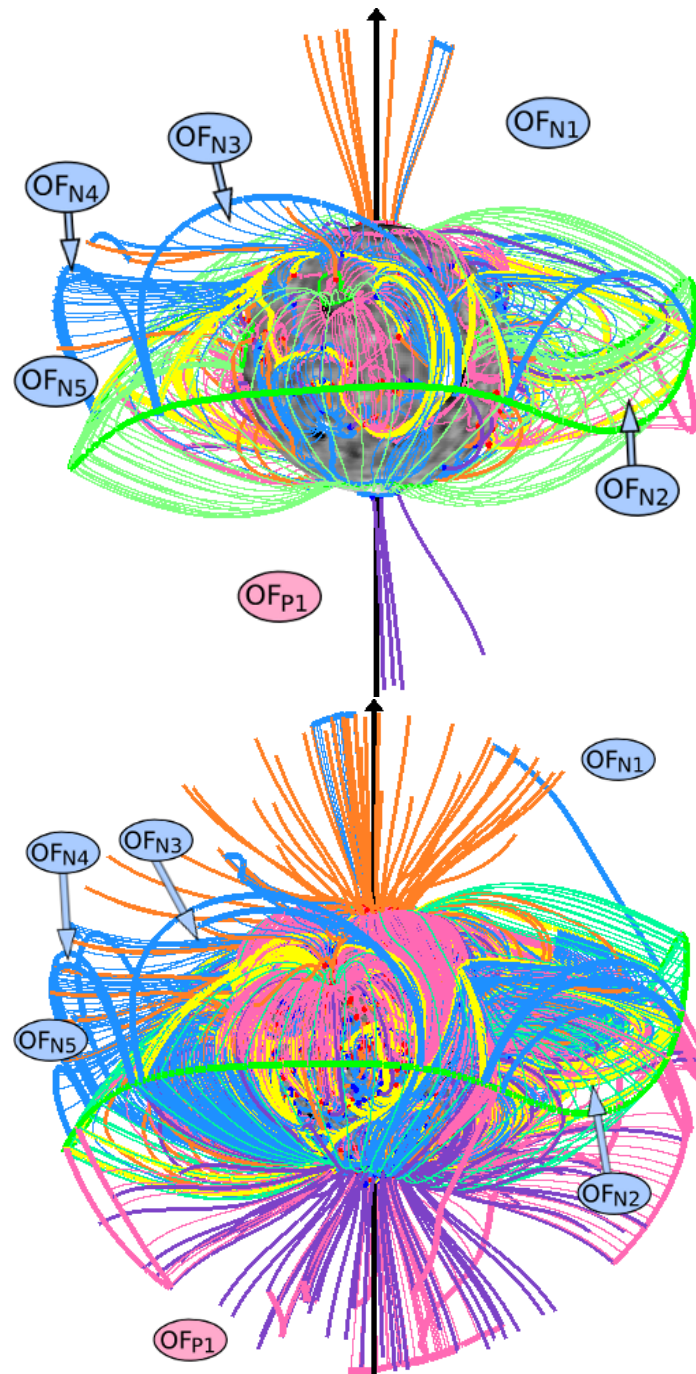


Figure 6.1: Weak global dipole minimum topology of PFSS extrapolation from Carrington rotation 2083. Top panel shows low-resolution SOLIS and bottom panel shows high-resolution SOLIS. Features are coloured as in Figure 4.2. In the low-res model there are 5 negative open-field regions visible labelled OF_{N1-5} and one positive open-field region visible, labelled OF_{P1} . So as to not make the image too cluttered, in the high-res model, only the corresponding open-field regions to these are labelled.

olation creates a complex web of the separatrix surfaces at the photosphere which is very different to the pattern of separatrix surfaces seen at the photosphere in the low-resolution extrapolation (Figure 6.2e). It is interesting to note that around the three active regions that were present at this time the low altitude structure is still fairly simple. This is because the magnetic field in the active regions is organised into large areas of positive and negative field rather than consisting of complex mixed polarity field such as is found in the quiet sun. This means that the potential field topology extrapolated around active regions is stable to increases in resolution.

In order to study the similarities and differences between the structures that form the closed separatrix curtains, we focus in on particular regions of the model. The negative open-field region that was referred to as OF_{N2} (100-150 degrees longitude) in the low-resolution model has split into multiple open-field regions in the high-res model as more nulls whose separatrix surfaces form closed separatrix curtains are found in the higher resolution. Figure 6.3 shows cuts in the separatrix surfaces at the same three radial heights as in Figure 6.2, but zoomed in on the region around the open-field region labelled OF_{N2} in the low resolution model. In the high resolution images (Figure 6.3 b, d and f) we can see that there are now 3 open-field regions (labelled OF_{N21-23}) as opposed to just one seen in the low-resolution cuts (Figure 6.3a, c and e). In Figure 6.3b there are 4 negative separatrix curtains: 3 of these are closed and bound the three open-field regions (OF_{N21-23}) and 1 is open in that it is connected to the HCS curtain on one side and bounded by a spine on the other. The region labelled OF_{N21} is the largest of these open-field regions and can easily be tracked all the way to the photosphere (see Figures 6.3d and f). On the other hand the regions labelled OF_{N22} and OF_{N23} are narrower at all heights and are hardly visible at the photospheric level when plotted at this resolution.

The three open-field regions are divided from the polar open-field region by a negative separatrix curtain emanating from a null at $1.149R_{\odot}$. This corresponds to the closed separatrix curtain found at this location in the low-resolution extrapolation. The other two closed separatrix curtains are from nulls much lower, at heights of $1.002R_{\odot}$ and $1.005R_{\odot}$. Thus, these nulls are not found in the low-resolution extrapolation as they are associated with flux features that are too small to have been resolved in the low-resolution extrapolation.

The structure of the positive open-field regions that were labelled OF_{P3} and OF_{P4} in the low-resolution extrapolation (see Figure 6.2 a, c and e) are also much more complex in the high-resolution extrapolation. In the low-resolution extrapolation, we had two closed separatrix curtains which create two positive open-field regions, OF_{P3} and OF_{P4} (see Figure 6.2 a, c and e). In the high-resolution extrapolation, we have 5 closed separatrix curtains in this region producing 5 disconnected positive open-field regions. These regions are labelled OF_{P31-32} and OF_{P41-43} in Figure 6.4 b, d and f which show zoomed in images of the cuts through the separatrix surfaces at different radial distances. The open-field region with the largest area at the photosphere is OF_{P41} , whereas OF_{P43} has shrunk to only a line of open field when plotted at this resolution.

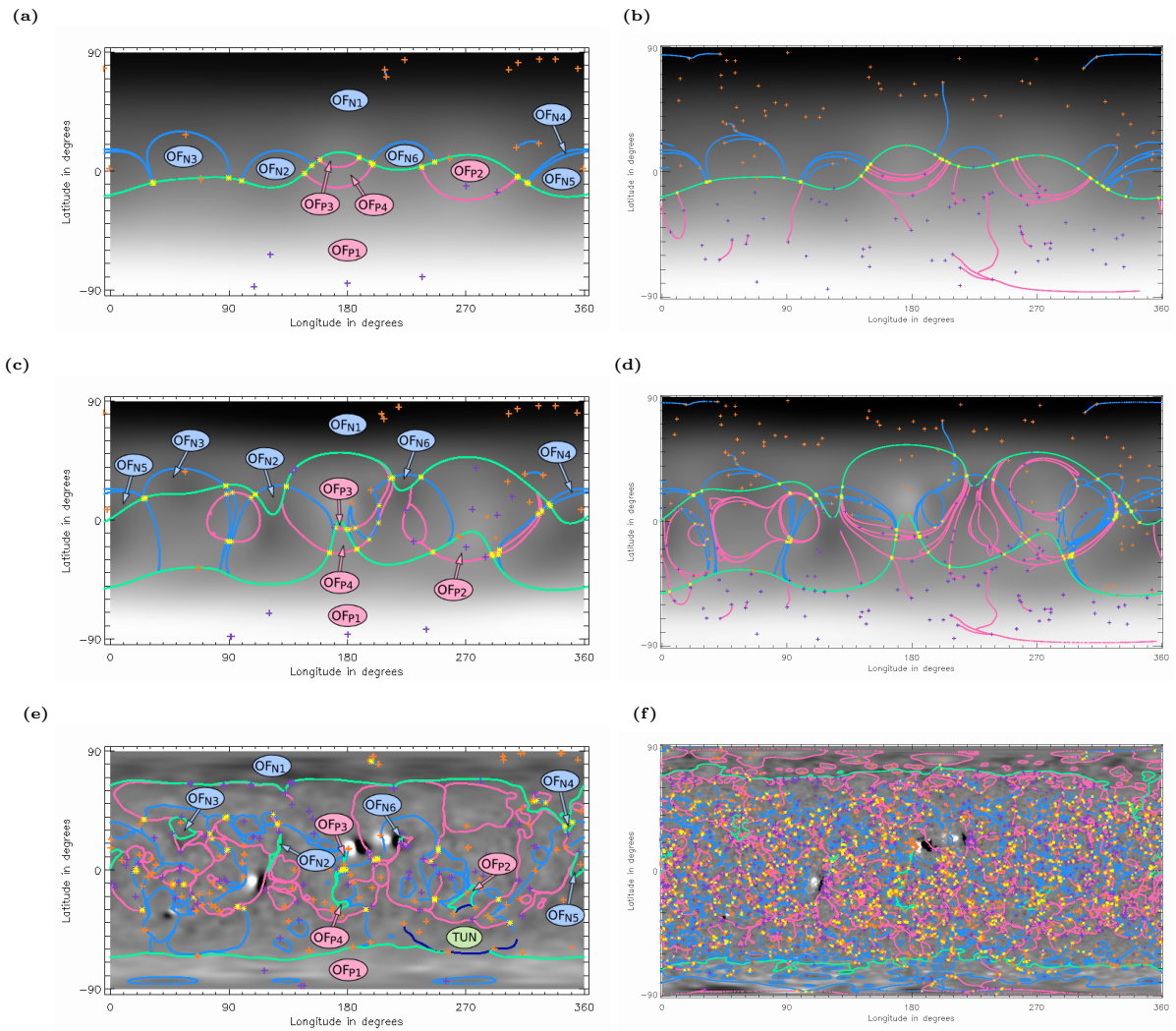


Figure 6.2: Cuts in the separatrix surfaces at heights of (a) $r = R_{ss} = 2.5R_{\odot}$, (b) $r = 1.44R_{\odot}$ and (c) $r = 1.02R_{\odot}$. Features are coloured as in Figure 4.3.

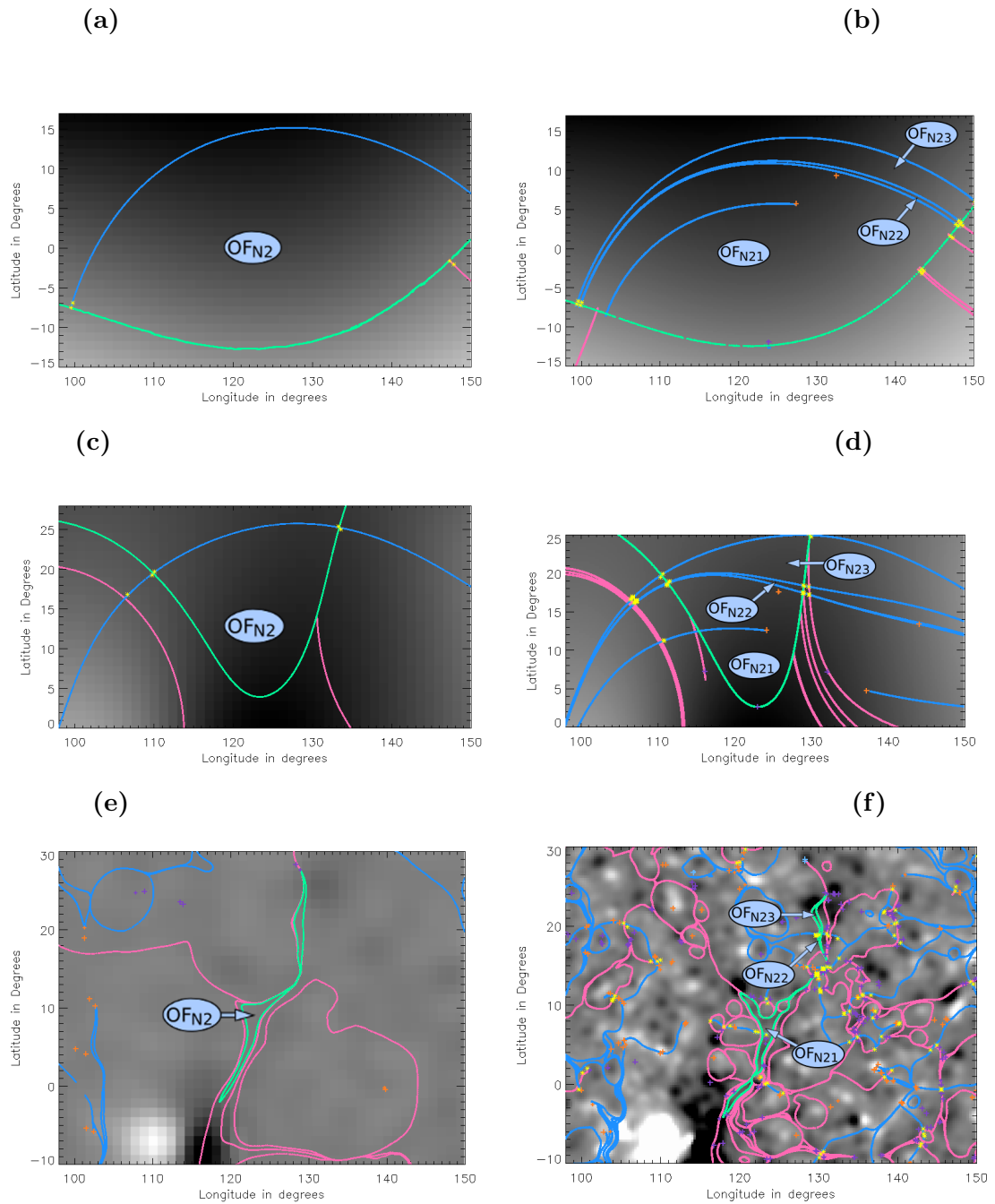


Figure 6.3: Cuts in the separatrix surfaces around a set of negative open-field regions at heights of (a) $r = R_{ss} = 2.5R_{\odot}$, (b) $r = 1.44R_{\odot}$ and (c) $r = 1.02R_{\odot}$. Left panels are from low-res extrapolation, right panels from high-res extrapolation. Features are coloured as in Figure 4.3.

The separatrix curtains that bound these five disconnected open-field regions mostly emanate from nulls that are below $1.01R_{\odot}$. The exceptions to this are the separatrix curtain that bounds OF_{P41} to the south which is from a null at a height of $1.117R_{\odot}$ and the separatrix curtain that bounds OF_{P32} to the south and OF_{P43} to the north which is made up from two separatrix surfaces from nulls with heights of $1.011R_{\odot}$ and $1.022R_{\odot}$. The fact that we have two closed separatrix curtains that result from nulls that are reasonably high in the corona is what we would expect since in the low-resolution extrapolation there were only two closed separatrix curtains.

Counting up all the open-field regions in the high-resolution extrapolation we find that there are 21 open-field regions in total. In the low-resolution extrapolation there are 10 open-field regions in total.

6.2.2 Solar maximum comparison - CR2130

The period of observation for SOLIS mostly covers the recent extended minimum between cycle 23 and cycle 24 however, as we are now coming to a maximum in cycle 24, we can examine and compare a frame from a period of greater solar activity. We choose Carrington rotation 2130 for this purpose which began 4th November 2012.

Figure 6.5 shows the global 3D topologies for the low-resolution model (top) and the high-resolution model (bottom). Similarly to the solar minimum comparison case, the HCS null line is in approximately the same place. There are many more separatrix curtains (both open and closed) in the high-resolution model than in the low-resolution model. There are also many more separators (thick yellow lines) visible in the high-resolution model, both connecting to the HCS null line and connecting between null points, than in the low-resolution model.

If we consider a plot of the heights of null-null separators for Carrington Rotation 2130 in both low-resolution and high-resolution (Figures 6.6 and 6.7) we can see that it is not just the number of low-lying null points and separators that change. Small-scale magnetic features on the photosphere which are better replicated by the high-resolution model than the low-resolution model are likely to be associated with low-lying null points. There is a slight change in the number of high-altitude null points and a large change in the number of high-altitude separators between the low-resolution and high-resolution models, as many separators reach up much higher up above the nulls that they connect.

If we compare cuts through the low-res and high-res topologies at three levels in the solar atmosphere (Figure 6.8) we can see both the similarities and the differences between the two cases. In the low-resolution case (Figure 6.8a, c and e) all the open-field regions have been tracked through the three cuts from the source surface to the photosphere and labelled: there are 5 positive open-field regions (labelled OF_{P1-5}) and 4 negative open-field regions (labelled OF_{N1-4}). These open-field regions have been matched to the open-field regions in the high-resolution extrapolation. In the high-resolution extrapolation (Figure 6.8b, d and f) the area that we referred to as OF_{P1} in the low-resolution extrapolation is divided into 3 positive open-field regions

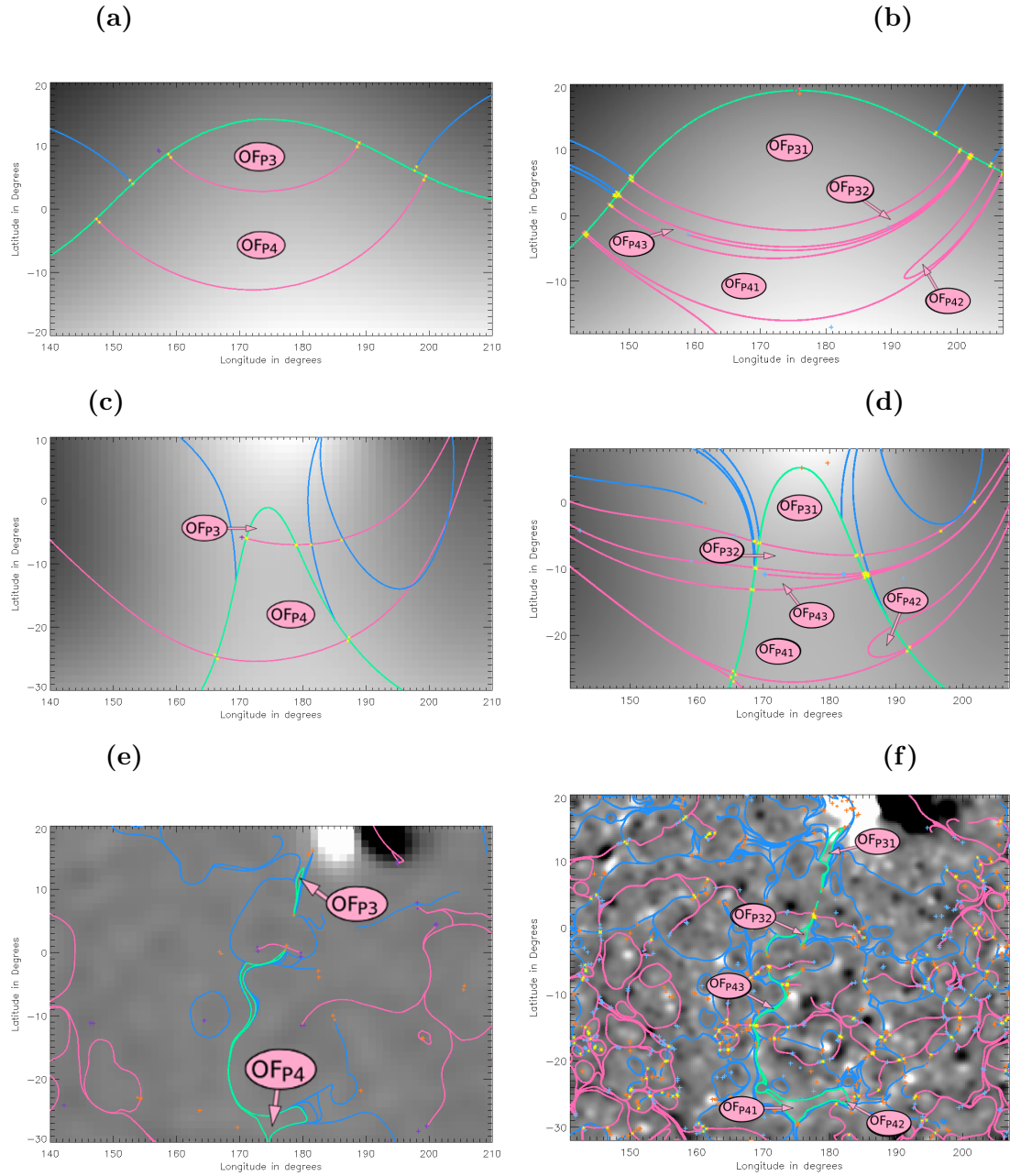


Figure 6.4: Cuts in the separatrix surfaces around a set of positive open-field regions at heights of (a) $r = R_{ss} = 2.5R_{\odot}$, (b) $r = 1.44R_{\odot}$ and (c) $r = 1.02R_{\odot}$. Features are coloured as in Figure 4.3.

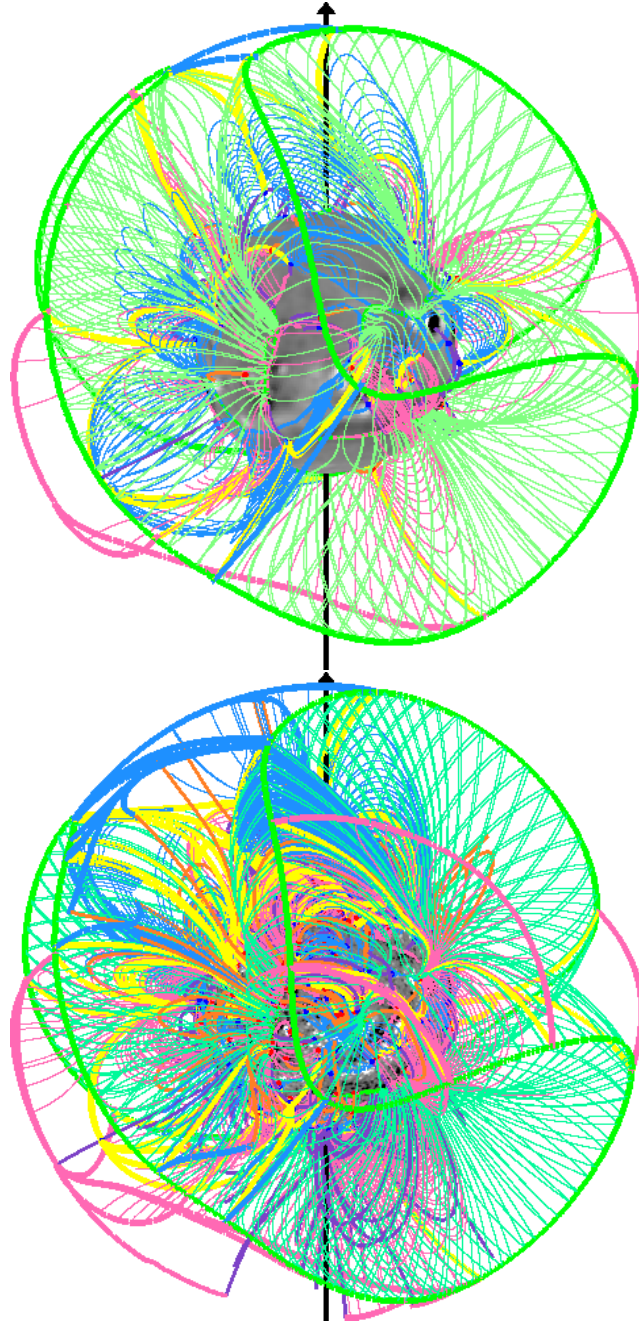


Figure 6.5: Solar maximum topology of PFSS extrapolation from Carrington rotation 2130. Top panel shows low-resolution SOLIS and bottom panel shows high-resolution SOLIS. Features are coloured as in Figure 4.2.

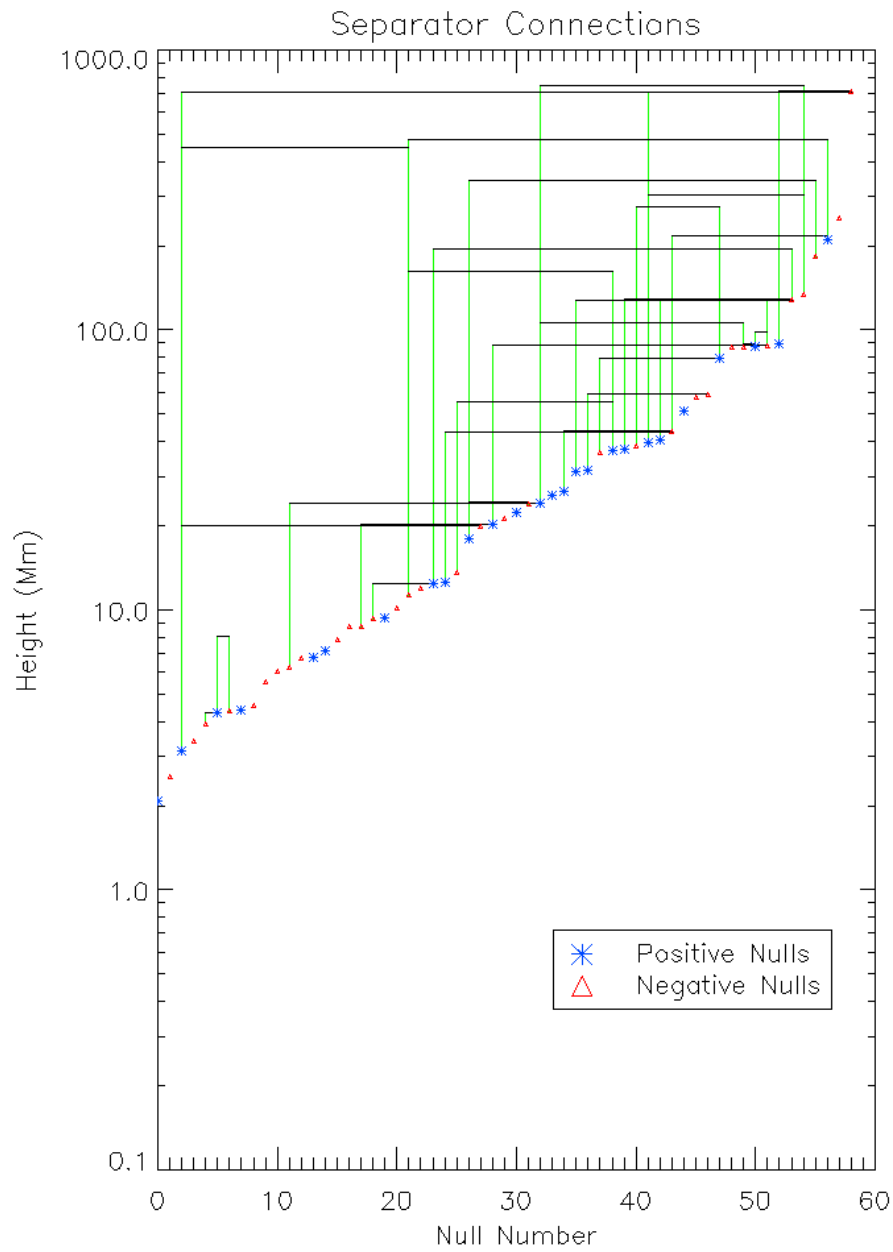


Figure 6.6: Heights of null points and the separators connecting between them for CR2130 for low-resolution SOLIS extrapolation. Positive null points are represented by blue stars, negative null points are represented by red triangles. If two nulls are connected by a separator, a line is drawn up to the maximum height reached by the separator and then along and down to the other null.

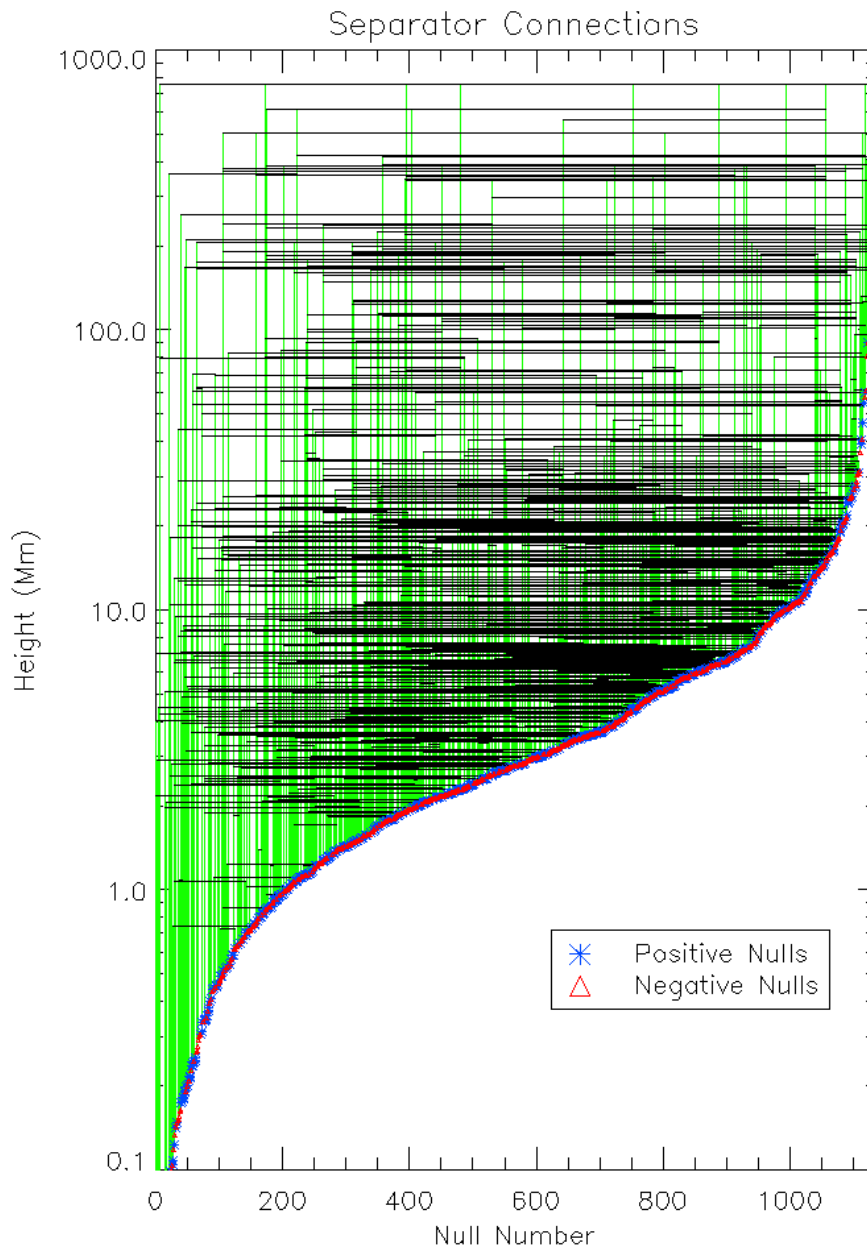


Figure 6.7: Heights of null points and the separators connecting between them for CR2130 for high-resolution SOLIS extrapolation. Positive null points are represented by blue stars, negative null points are represented by red triangles. If two nulls are connected by a separator, a line is drawn up to the maximum height reached by the separator and then along and down to the other null.

	Solar Min CR2083		Solar Max CR2130	
	low-res	high-res	low-res	high-res
HCS tilt	16.9	19.2	76.7	74.7
No. nulls	124	1964	60	1131
No. nulls above $1.1R_{\odot}$	10	20	13	10
No. nulls below $1.1R_{\odot}$	114	1944	47	1121
No. separators	86	1997	44	808
No. null-null separators	69	1946	31	765
No. null-HCS separators	17	51	13	43
No. open spines	21	134	1	26
No. isolated domes	60	574	22	434
No. isolated domes with open spines	16	80	0	14
No. closed curtains	8	18	7	20
No. -ve closed curtains	5	9	3	12
No. +ve closed curtains	3	9	4	8
No. open curtains	2	19	0	8
No. -ve open curtains	2	8	0	4
No. +ve open curtains	0	11	0	4
Size of HCS null network	40	1094	19	400
Size of largest non-HCS network	2	21	4	10

Table 6.1: Details on the numbers of different topological features in each of the example cases CR2083 from solar minimum and CR2130 from solar maximum.

by the creation of 2 additional closed separatrix curtains: these new regions are labelled OF_{P11-13} . Similarly, OF_{P2} has split into 3 regions, OF_{P3} has split into 2 regions and OF_{N4} has split into 2 regions. OF_{P5} is not found at the higher-resolution due to a slight change in the position of the HCS null-line. Also, OF_{N3} has split into 8 regions, the majority of which are too narrow to see when plotted at this resolution, even on the source surface (see Figure 6.8b) and so have not been labelled. The open-field regions OF_{N1} , OF_{N2} and OF_{P4} have not been changed by the increase in resolution of the extrapolation and each remains as a single flux domain. This means that overall there are 19 open-field regions in the high resolution extrapolation compared to 9 open-field regions in the low-resolution extrapolation.

6.2.3 Quantitative comparison of low-resolution and high-resolution structures

Table 6.1 collates the numbers of some of the topological features found in the low-resolution and high-resolution extrapolations. The variation in the HCS tilt is very small between the low-resolution and high-resolution models for both the solar maximum and the solar minimum case. This is to be expected because the HCS tilt is a global property and should not be effected by resolution of small-scale features.

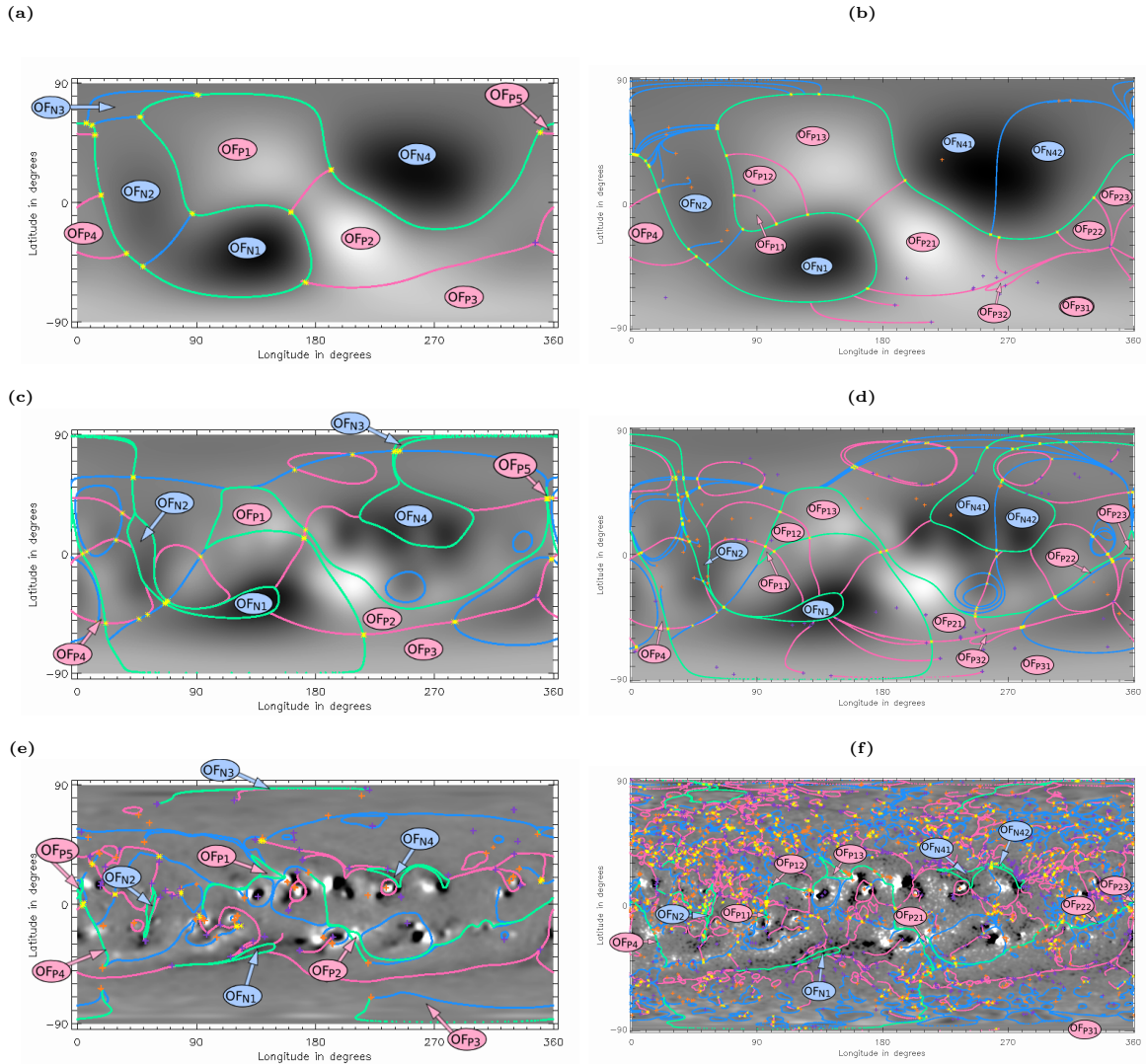


Figure 6.8: Cuts in the separatrix structures at 3 heights in the solar atmosphere ($2.5R_{\odot}$, $1.44R_{\odot}$ and $1R_{\odot}$) for the low-resolution (a), (c) and (e) and the high-resolution extrapolations (b), (d) and (f) of the coronal magnetic field at Carrington Rotation 2130. In the low-resolution extrapolations the open-field regions have been labelled OF_{P1-5} for the 5 positive open-field regions and OF_{N1-4} for the 4 negative open-field regions. The features are described using the colours and symbols introduced in Figure 4.3

The numbers of nulls varies greatly with the resolution. There are 16 times as many nulls in the high-resolution model than in the low-resolution model for solar minimum. Likewise, there are 19 times more nulls in the high-resolution model than in the low-resolution model for solar maximum. However, almost all these extra null points form below $1.1R_{\odot}$.

The numbers of separators also varies greatly with varying resolution with the numbers of null-null separators showing the greatest difference between low and high resolution (Table 6.1). The number of null-HCS separators do not show such a dramatic change: in both the solar maximum and solar minimum case there is approximately a threefold increase in the number of null-HCS separators between the low-resolution and high-resolution models.

In the previous chapter we considered the size of the separator network in terms of nulls that are connected to one another or connected to the HCS via a separator or a chain of nulls and separators. The number of nulls in the HCS network is much greater in the high-resolution model than in the low-resolution model (Table 6.1). This is because there are more open and closed separatrix curtains in the high-resolution model than in the low-resolution model and also these curtains can have more complex interactions with other null points near to the solar surface in the high-resolution model. The size of the largest network of nulls that is not connected to the HCS does not show much of an increase between the low-resolution and high-resolution extrapolations as the increase in the size of the HCS separator network does. This tells thus that extra complexity is mainly forming around the existing complex structures such as the HCS null network.

6.2.4 Temporal comparison

One of the easiest topological features to compare between the low-resolution and high-resolution models over a time series is the number of null points. Here the topology from extrapolations from 124 synoptic magnetograms over 10 years is examined. The number of nulls varies greatly depending on the number of small-scale features that can be resolved on the photosphere. Figure 6.9 shows the numbers of nulls in the extrapolations for the low-resolution and high-resolution data. At the peak in the number of nulls in the low-resolution model (black solid line) approximately 200 null points are found, but in the high-resolution model (black dot-dashed line) approximately 2000 null points are found which is an order of magnitude greater. However, the number of null points in the high-resolution model is not simply a scaling from the low-resolution model. An apparent floor in the number of nulls is at around 1100 for the high-resolution data and around 40 for the low-resolution data (see Figure 4.14 in Chapter 4 for more detail on this). This would imply that in periods of greater solar activity a larger proportion of null points are missed in the low-resolution data than are missed when the Sun is quiet.

We hypothesise that this is due to the small-scale field that is affected by the change in resolution and that the large-scale field, which is described by the lower-

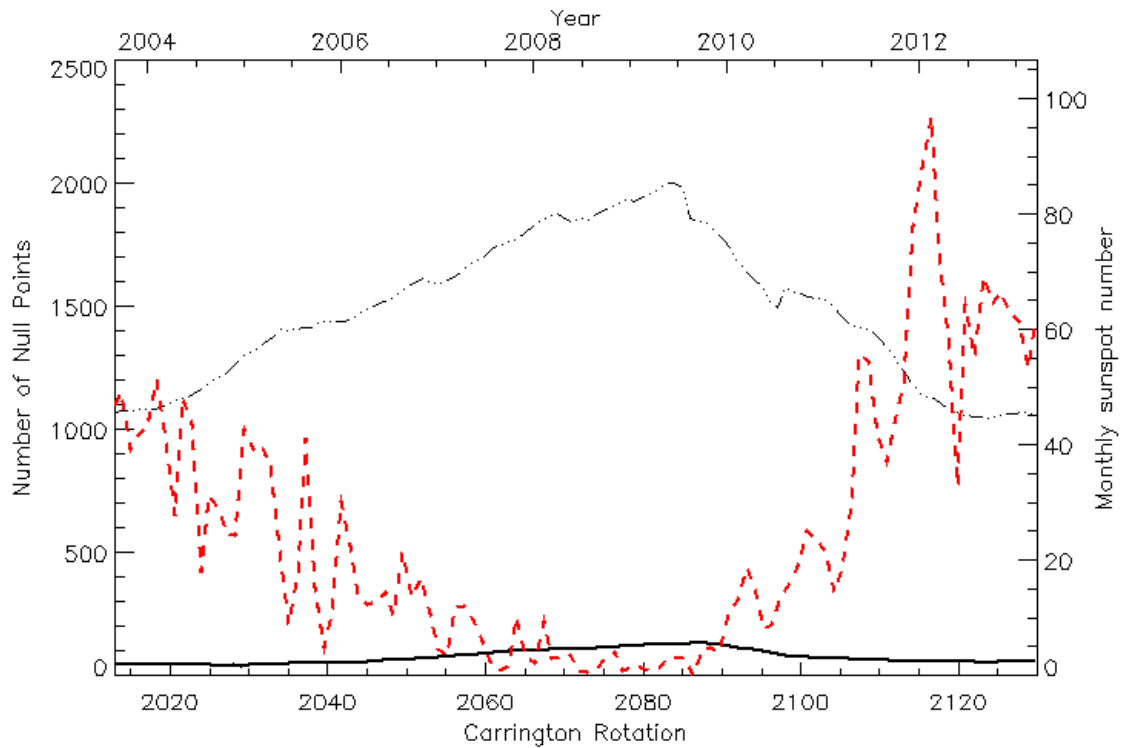


Figure 6.9: 12 Carrington Rotation running mean of the number of null points found in our model. The black solid line shows the SOLIS low-res data and the black dot-dashed line shows the SOLIS high-res data. The red dashed line shows the monthly sunspot number for comparison.

order harmonics in the PFSS models, is predominantly the same. To investigate this we look at the numbers of nulls above and below $1.1R_{\odot}$ for the two extrapolation resolutions. Figure 6.10a shows the number of null points below $1.1R_{\odot}$ for both resolutions. There are many more null points below $1.1R_{\odot}$ in the high-resolution extrapolation than in the low-resolution extrapolation. However, if we consider null points above $1.1R_{\odot}$ (Figure 6.10b) we see that there are practically the same number of null points above this height for both the low resolution and the high-resolution data. The only difference is during the solar minimum where there are still slightly more null points in the high-resolution extrapolations than in the low-resolution extrapolations.

As well as the number of null points, we can also consider the numbers of separators. Figure 6.11 shows the number of separators against time for the high-resolution and low-resolution extrapolations. The total number of separators is much greater in the high-resolution extrapolation than in the low-resolution extrapolation. The peak number of separators occurs at solar minimum and at this time there are about 2000 separators in the high-resolution extrapolation and about 180 separators in the low-resolution extrapolation.

We can divide the separators into two types: separators that connect a pair of null points (null-null separators) and separators that connect a null point to the HCS null line (null-HCS separators). The number of null-null separators is shown in Figure 6.12a. There are many more null-null separators in the high-resolution extrapolation than in the low-resolution extrapolation. This is due to there being many more null points in the high-resolution extrapolation than in the low-resolution. Most separators are null-null separators so the null-null separators show the same pattern as the total number of separators.

There are far fewer null-HCS separators than null-null separators. Figure 6.12b shows the variation in the number of these separators. There is not such a big difference in the numbers of null-HCS separators between the low-resolution and high-resolution models as in the numbers of null-null separators. This is because many of the large-scale magnetic features responsible for the formation of separatrix curtains that are associated with null-HCS separators are correctly replicated in the low-resolution model.

6.3 Conclusions

Looking at the global 3D images (Figures 6.1 and 6.5) there are obvious differences but also obvious similarities in the structure of the topology of PFSS extrapolations from differing resolutions from the same instrument (SOLIS). There are far greater numbers of null points in the high-resolution extrapolations, but most of these extra null points are low in the corona. However, some of these null points low in the corona can have separatrix surfaces and separators that stretch high up in the atmosphere, even to the source surface. There are low down nulls in the high-resolution extrapolations

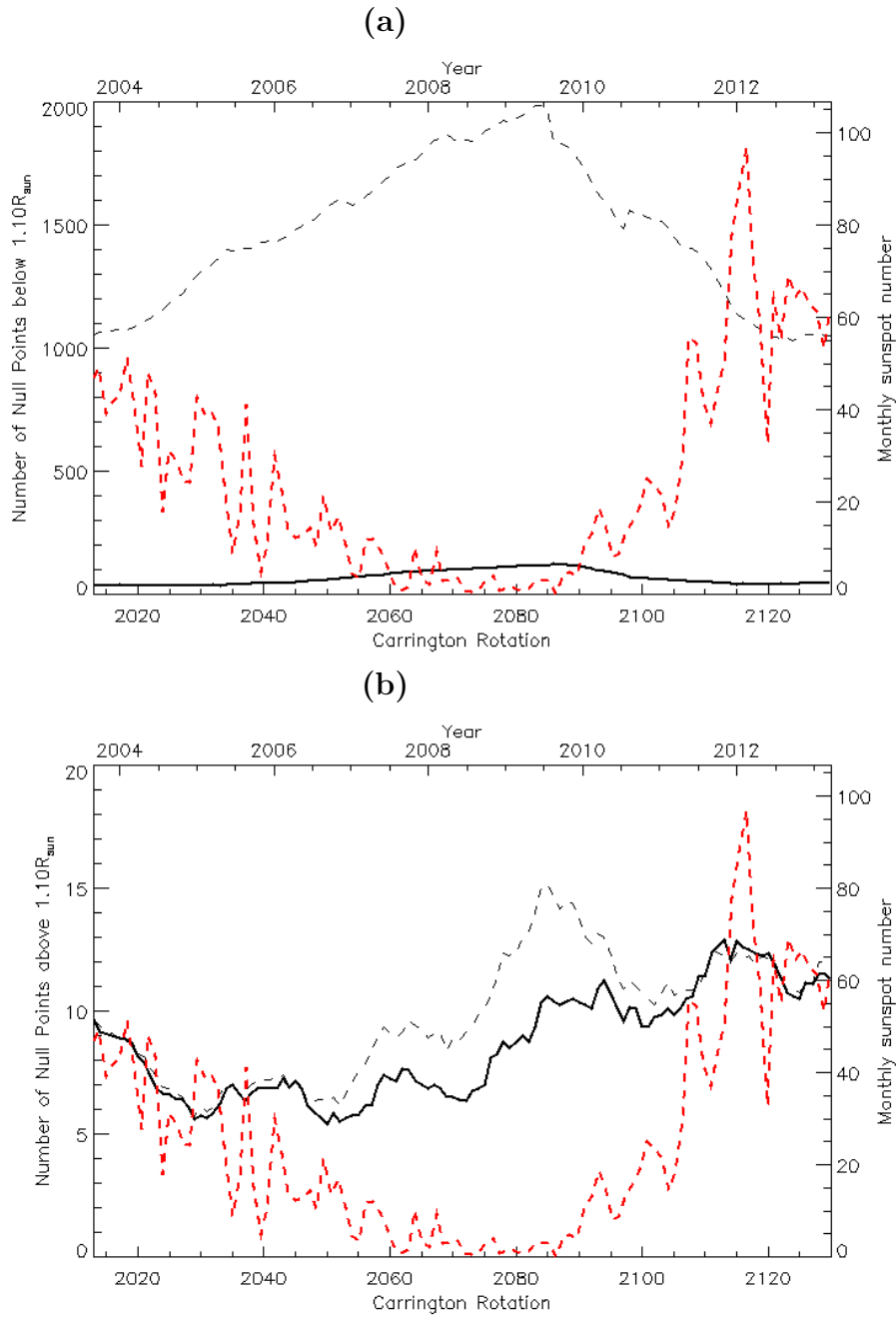


Figure 6.10: Number of nulls by height for low-res SOLIS (black solid line) and high-res SOLIS (black dashed line). (a) nulls below $1.10R_{\odot}$ and (b) nulls above $1.10R_{\odot}$. Red dashed line shows sunspot number to indicate solar cycles.

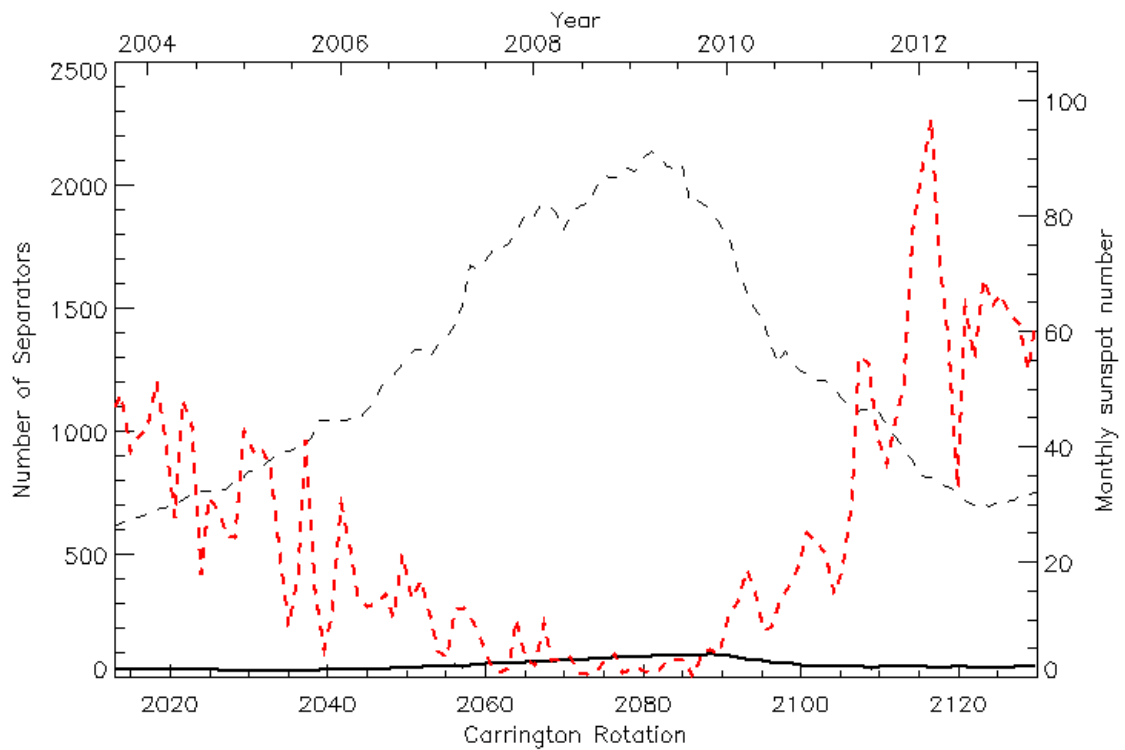


Figure 6.11: 12 Carrington Rotation running mean of the number of separators found in our model. The black solid line shows the SOLIS low-res data and the black dot-dashed line shows the SOLIS high-res data. The red dashed line shows the monthly sunspot number for comparison.

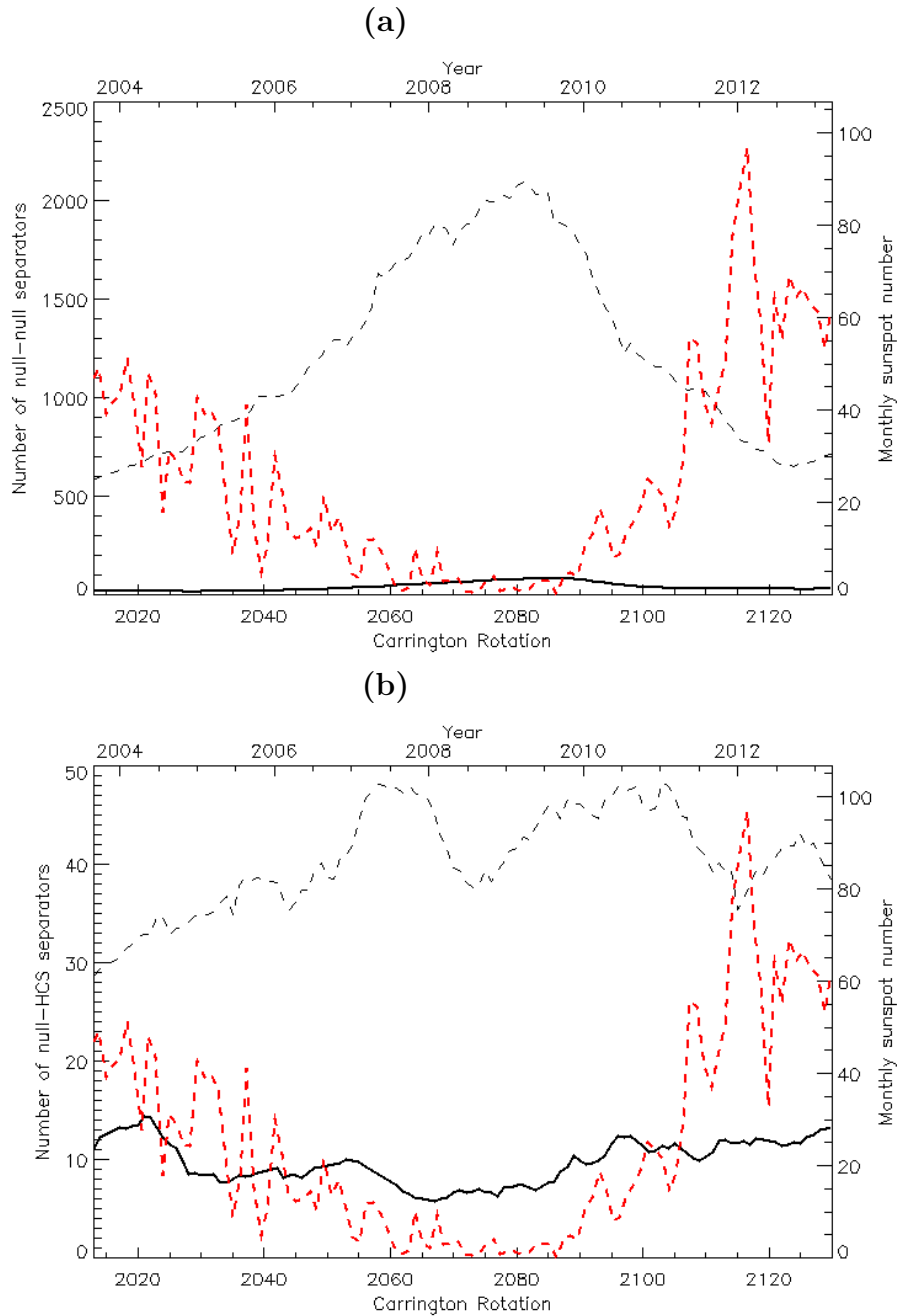


Figure 6.12: Number of separators for low-res SOLIS (black solid line) and high-res SOLIS (black dashed line). (a) null-null separators and (b) null-HCS separators. Red dashed line shows sunspot number to indicate solar cycles.

that have separatrix surfaces which have a global effect, e.g., they form open or closed separatrix curtains. These additional separatrix curtains nearly always lie close to the separatrix surfaces of nulls that are found in the low-resolution extrapolation so they often subdivide open-field regions found in the low-resolution extrapolations into multiple regions in the high-resolution extrapolations, thus do not completely change the overall global structure.

The number of null points increases with the resolution of the extrapolation. However the number of null points above $1.1R_{\odot}$ is very similar in the two extrapolations even though one has a much higher resolution. This shows that changing the resolution does not change the number of high-altitude null points. This is discussed in more detail in Chapter 7.

The number of separators also increases with the increased resolution. Overall there are about 10 times more separators in the high-resolution extrapolations. This trend is the same for the number of null-null separators. There are more null-HCS separators in the high-resolution extrapolation than in the low-resolution extrapolation but the difference in the numbers of these is not so pronounced. There are approximately two to three times as many null-HCS separators in the high-resolution model in comparison to the low-resolution model. This shows that whilst there are still extra large-scale structures (i.e., separatrix curtains that produce null-HCS separators) in the high-resolution model that we fail to find in the low-resolution model, the fraction of these structures that we are missing is smaller than for the small-scale structures.

Chapter 7

Null point distribution and density

Chapters 4 and 5 considered a variety of topological properties of the global solar corona as measured through a 37 year study using low-resolution PFSS extrapolations from Kitt-Peak/SOLIS data. This chapter considers PFSS extrapolations of high-resolution synoptic magnetograms taken by the Michelson Doppler Imager (MDI) aboard the SOlar and Heliospheric Observatory (SOHO) over its 15 year observational period. From these extrapolations, the variation in the number and distribution of null points in the global corona is investigated. Here we move away from using the Kitt-Peak/SOLIS low-resolution synoptic maps to higher resolution synoptic maps so we can get better resolution in our potential field extrapolations.

The density of null points in the corona has previously been considered (particularly in relation to quiet-sun regions) by many authors [e.g. Schrijver and Title, 2002, Close et al., 2004, Régnier et al., 2008, Longcope and Parnell, 2009, Cook et al., 2009].

Schrijver and Title [2002] considered a numerical model of a simulated patch of the quiet-sun corona with point sources distributed on the base with varying fluxes taken from an exponential distribution. They found an exponential fall off in the number of null points with height. The disadvantages of this study are that simulated, as opposed to observed, magnetograms were used as the lower boundary condition. Thus their results are heavily dependent on the spatial spread and distribution of fluxes used in simulating the quiet-sun field.

In order to compare with, and improve on, the Schrijver and Title [2002] model, Close et al. [2004] investigated the number of separators above a patch of quiet-sun field initially in a model with an exponential source distribution similar to that of Schrijver and Title [2002] and then by considering a sequence of observed MDI magnetograms with a size of 240Mm by 240Mm. In these observed magnetograms the field above is calculated by treating every magnetic fragment as a set of point sources. Only the number of null points in the inner 80 by 80 by 40Mm region are found. By considering only the central section of the box, boundary effects are significantly reduced. From the observed data they found 1.051 ± 0.007 nulls per source (fragment), however, due to the use of point sources 96% of these were in the source plane and only 4% above the plane, in the corona.

Régnier et al. [2008] considered a patch of quiet-sun field observed by Hinode/SOT (Solar Optical Telescope) with dimensions 102Mm by 116Mm. A potential field was extrapolated directly from this observed data in which 80 null points were found, none of which lay in the photospheric plane. Of these 80 nulls, only 2 were above 3.5Mm and so were classified as coronal null points. It should be noted, however, that the extrapolation of the potential field relies on assumptions which do not hold in the photosphere and the chromosphere and therefore the discrimination between chromospheric and coronal nulls is purely nominal. The number of null points was found to fall off linearly with height, however, the small field-of-view of the magnetogram used for the extrapolation precludes the possibility of having null points high in the atmosphere. High altitude nulls require larger regions of magnetic field or regions with either stronger or larger flux sources present than those found in the SOT magnetic field observed by Régnier et al. [2008].

Longcope and Parnell [2009] extended the study of null points in the quiet-Sun corona by analysing the potential magnetic field extrapolated directly from 562 small field-of-view magnetograms of quiet sun taken by MDI during cycle 22/23 minimum and cycle 23/24 minimum. This larger study allows a thorough investigation that is more stable to differences in individual observations. They calculated the null column density, which is defined to be the number of nulls present in the atmosphere per unit area of solar surface. The null column density was found to fall off as one over the square of the height above the solar surface with the relation

$$N_d(z) = \frac{0.021}{(z + 1.6)^2}, \quad (Mm)^{-2} \quad (7.1)$$

where N_d is the column density of nulls above the height z (Mm). A similar relationship was found for the fall off of the null density (measured in nulls per Mm^3) with height, except with an inverse cubic rather than an inverse quadratic fall off:

$$\rho_N(z) = \frac{0.040}{z^3}, \quad (Mm)^{-3} \quad (7.2)$$

where ρ_N is the number density of null points and z is the height above the solar surface.

Here, we present results from studying the null-point distribution throughout the entire solar corona. To do this we use PFSS extrapolations from synoptic magnetogram data primarily from the Michelson Doppler Imager (MDI). These magnetograms have a resolution of 3600 by 1080 pixels and are produced once every Carrington rotation. The method of extrapolation is described in Section 2.2 and a maximum harmonic number, $l_{max} = 351$ is used to produce the global potential fields.

For comparison, we also consider data from the high-resolution SOLIS magnetograms and also the Heliospheric Magnetic Imager (HMI). These extrapolations are performed using $l_{max} = 301$ for the SOLIS data and $l_{max} = 351$ for the HMI data. A more thorough description of these data sets is outlined in Section 2.3.

First, in Section 7.1, we consider how the integrated column density of null points changes throughout the solar cycle. In Section 7.2, we look at the fall off in the null

column density with height and following this, in Section 7.3, we fit the fall off in the number of null points with height to several standard statistical distributions to find the best fit. Section 7.4.1 examines the changes in the latitude of null points throughout the solar cycle and also the relationship between height and latitude at different times. Finally, in Section 7.5, we examine individual Carrington rotations to compare between HMI, MDI and SOLIS data, as well as considering MDI extrapolations from different times in the solar cycle.

7.1 Null point column density with time

Here we determine the distribution of null points in order to compare with previous null point studies. The integrated column density of null points, $N_d(z)$, is the average number of coronal null points per unit area of the photosphere above a height, z . Here, the total integrated column density, $N_d(0)$, is plotted in Figure 7.1 for each Carrington rotation during the observational period of MDI. Naturally this follows the same variation over the solar cycle as the number of nulls. The integrated null column density varies from a high of 0.0013 nulls per Mm^2 at solar minimum down to 0.0005 nulls per Mm^2 at solar maximum (Figure 7.1). Null points are also detected in extrapolations from the HMI synoptic magnetograms and a comparable number of null points are found in the HMI data (red line in Figure 7.1) to those found in the MDI extrapolations. This is to be expected since the same number of harmonics are used in both the extrapolations. Unfortunately, it is not possible to directly compare the HMI and MDI null numbers since there is very limited overlap in their observational periods.

As expected the extrapolations from the high-resolution SOLIS data produce fewer null points (blue line in Figure 7.1) than found in the HMI and MDI data due to the lower resolution of this data in comparison to the MDI and HMI data sets, however, the same cyclic trend in null column density is found in all the data sets.

The integrated null column density we find is at all times much lower than that found by Régnier et al. [2008] (0.0068 Mm^{-2}) and Longcope and Parnell [2009] (0.007 Mm^{-2}). This is due to a combination of the lower resolution in our model and the fact that we are including active regions and polar regions where there are fewer null points than in quiet-sun regions.

7.2 Null point column density

Longcope and Parnell [2009] found that the null column density, $N_d(z)$ - the variation with height of the density of null points per unit area of photosphere, follows a power-law type behaviour with index -2 above 1.5Mm. As discussed in the following section, we see a similar behaviour for the null points in our model (compare green line in Figure 7.2). Figure 7.2 shows the column density of null points against height for the MDI extrapolations (black line) in comparison to the HMI null column density

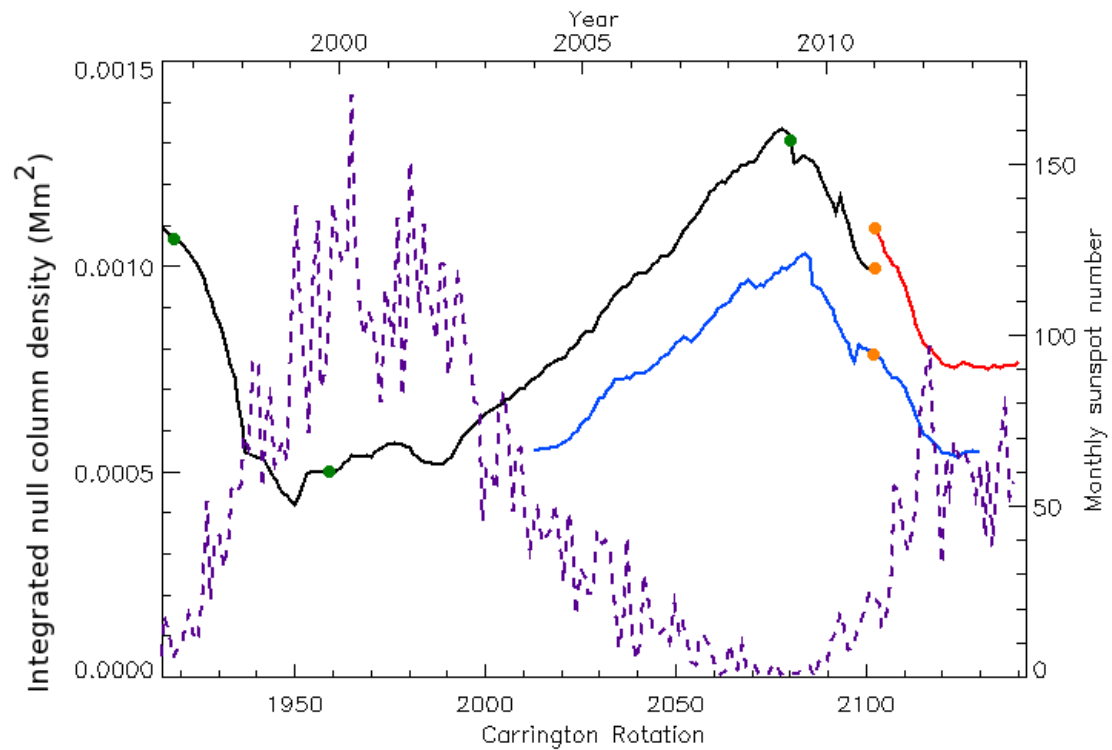


Figure 7.1: Integrated null column density per Mm^2 of the photosphere against time for: MDI extrapolations (black line), high-res SOLIS extrapolations (blue line) and HMI extrapolations (red line). Purple dashed line shows the sunspot number to indicate cycle phase. Green dots show the times of the case studies examined in Section 7.5.2 and orange dots represent the case studies in Sections 7.5.1.

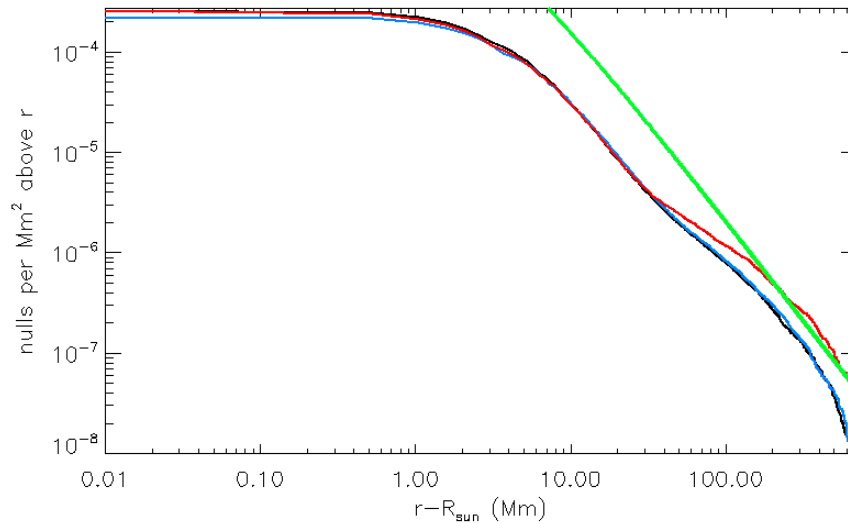


Figure 7.2: Variation of the column density of null points with height for MDI extrapolations (black line), SOLIS high-resolution extrapolations (blue line) and HMI extrapolations (red line). Green line shows power law found by Longcope and Parnell [2009].

(red line) and the high-resolution SOLIS null column density (blue line). The column density is about 30% less for low altitude null points found in the SOLIS extrapolations compared to the null density found in the MDI and HMI extrapolations because fewer harmonics are used in the SOLIS extrapolations since the initial data is of a lower resolution than the HMI and MDI data.

The column densities of null points found high in the atmosphere are larger for HMI extrapolations than for MDI or SOLIS extrapolations. This is mostly due to the fact that the period of observations for MDI and SOLIS encompasses more solar minimum Carrington rotations than the HMI data. Additionally, the only solar minimum for which HMI was operational was the recent solar minimum between cycles 23 and 24 during which time a weak polar field allowed magnetic structures to expand in the atmosphere and thus many nulls formed at high altitudes (this was discussed in Chapter 4).

We see that the null column density has approximately the same slope as the relations found by Longcope and Parnell [2009] but the density is lower in our model for all heights. This is to be expected since we are considering a model with a lower-resolution than that used by Longcope and Parnell [2009].

7.3 Statistical analysis of null point distribution

So far, in this chapter we have seen that the number of null points in the corona falls off with height. This section investigates this further by considering several standard statistical distributions and fitting them to the null point position data from our MDI extrapolations.

The *cumulative distribution function* (CDF) is a measure of the probability that a random variable X will have a value less than x . In our case, we look at the cumulative distribution function of null points with height so the random variable is height of a particular null point.

For the MDI extrapolations we would like to characterise the distribution as one of the standard statistical distributions. We choose 4 distributions to test, these are given below.

Distribution 1: The *exponential distribution* assumes an exponential fall off in the independent variable (in our case this is height) which gives a probability density function (pdf):

$$f_{exp}(h; \alpha_{exp}) = \alpha e^{-\alpha_{exp}(h-h_0)}, \quad h \geq h_0. \quad (7.3)$$

where h_0 is the minimum height of the nulls that we consider. The parameter α_{exp} is determined from the observational data. The pdf can be integrated to find the cumulative distribution function (CDF), $F(h)$:

$$F(h; \alpha_{exp}) = \int_{h_0}^h \alpha_{exp} e^{-\alpha_{exp}(t-h_0)} dt, \quad (7.4)$$

$$= [-e^{-\alpha_{exp}(t-h_0)}]_{h_0}^h, \quad (7.5)$$

$$= 1 - e^{-\alpha_{exp}(h-h_0)}. \quad (7.6)$$

Clearly, as $h \rightarrow \infty$ then $F(h) \rightarrow 1$, as expected.

We use the method of maximum likelihood estimation to find the parameters in our distributions. We define the likelihood function $L(\alpha)$, where α is the parameter we want to constrain, as:

$$L(\alpha) = \prod_{i=1}^n f(h_i; \alpha). \quad (7.7)$$

The h_i are the heights of the nulls, and n is the number of data points. To find the maximum likelihood estimate of our parameters we first take the log of the likelihood function (7.7) to give the log-likelihood function, $l(\alpha)$:

$$l(\alpha) = \log\left(\prod_{i=1}^n f(h_i; \alpha)\right) = \sum_{i=1}^n \log(f(h_i; \alpha)). \quad (7.8)$$

If we then differentiate this function with respect to the parameter, α , and set it to zero, we will find the maximum of the log-likelihood function which is the same

as the maximum of the likelihood function i.e., we find the value of the parameter α which produces the best fit to the data for the pdf of the given form. This means we want to solve the following equation for α :

$$\frac{dl}{d\alpha} = \sum_{i=1}^n \frac{1}{f(h_i; \alpha)} \frac{\partial f}{\partial \alpha}(h_i; \alpha) = 0. \quad (7.9)$$

For the exponential distribution we have:

$$\frac{dl}{d\alpha_{exp}} = \sum_{i=1}^n \frac{1}{\alpha_{exp} e^{-\alpha_{exp}(h_i - h_0)}} [-\alpha_{exp}(h_i - h_0)e^{-\alpha_{exp}(h_i - h_0)} + e^{-\alpha_{exp}(h_i - h_0)}] = 0 \quad (7.10)$$

$$\Rightarrow 0 = \sum_{i=1}^n \frac{1}{\alpha_{exp}} - (h_i - h_0) \quad (7.11)$$

$$\Rightarrow 0 = \frac{n}{\alpha_{exp}} - \sum_{i=1}^n (h_i - h_0) \quad (7.12)$$

$$\Rightarrow \alpha_{exp} = \frac{n}{\sum_{i=1}^n (h_i - h_0)}. \quad (7.13)$$

So in this case α_{exp} is one over the mean of all the $h_i - h_0$.

Distribution 2: The *power-law distribution* assumes that the number of nulls will fall off as a power of height giving a probability density function (pdf):

$$f_{pow}(h; \alpha_{pow}) = \frac{\alpha_{pow} - 1}{h_0} \left(\frac{h}{h_0} \right)^{-\alpha_{pow}}, \quad h \geq h_0, \quad (7.14)$$

where h_0 is the minimum value of h and α_{pow} is a parameter which is found by applying the maximum likelihood method to the observed data.

The cumulative distribution function of the power-law distribution is then given by:

$$F_{pow}(h; \alpha_{pow}) = \int_{h_0}^h f_{pow}(t; \alpha_{pow}) dt = 1 - \left(\frac{h_0}{h} \right)^{\alpha_{pow} - 1}. \quad (7.15)$$

We can then find α_{pow} using maximum likelihood estimation to give:

$$\alpha_{pow} = 1 + \frac{n}{\sum_{i=1}^n \log \left(\frac{h}{h_0} \right)} \quad (7.16)$$

Distribution 3: The *log-normal distribution* assumes that the log of the number of nulls is normally distributed with mean μ and standard deviation σ to give

$$f_{lgn}(h) = \frac{1}{\sigma h \sqrt{2\pi}} e^{\left(-\frac{(\log(h)-\mu)^2}{2\sigma^2}\right)}, \quad h \geq 0. \quad (7.17)$$

Again, to obtain the cumulative distribution function (CDF) of this pdf we integrate:

$$F_{lgn}(h) = \int_0^h \frac{1}{\sigma t \sqrt{2\pi}} e^{\left(-\frac{(\log(t)-\mu)^2}{2\sigma^2}\right)} dt, \quad (7.18)$$

$$= \frac{1}{\sqrt{\pi}} \int_{-\infty}^{(\log(h)-\mu)/(\sqrt{2}\sigma)} e^{-u^2} du, \quad (7.19)$$

$$= \frac{1}{2} + \frac{1}{2} \operatorname{erf} \left(\frac{\log(h) - \mu}{\sqrt{2}\sigma} \right). \quad (7.20)$$

Using maximum likelihood we can confirm that:

$$\mu = \frac{\sum_{i=1}^n \log(h_i)}{n}, \quad (7.21)$$

$$\sigma = \frac{\sqrt{\sum_{i=1}^n (\log(h_i) - \mu)^2}}{n}. \quad (7.22)$$

Distribution 4: The *Weibull distribution* is a probability distribution that behaves as a power law for small $(h - h_0)$ and as an exponential for large $(h - h_0)$. However, the distribution changes depending on the value of the parameter γ . If γ is less than one then the probability is always decreasing with h . If $\gamma > 1$ then this implies that the probability will increase for small $(h - h_0)$ and decrease for large $(h - h_0)$.

The Weibull distribution is defined by a probability distribution function, $f_{wei}(h)$:

$$f_{wei}(h) = \frac{\gamma}{\beta} \left(\frac{h - h_0}{\beta} \right)^{\gamma-1} e^{-\left(\frac{h-h_0}{\beta}\right)^\gamma}, \quad (7.23)$$

for $h > h_0$ and with β and γ parameters that are determined by maximum likelihood estimation from the observed data. Again, the cumulative distribution function comes from integrating:

$$F_{wei}(h) = \int_{h_0}^h \frac{\gamma}{\beta} \left(\frac{x - h_0}{\beta} \right)^{\gamma-1} e^{-\left(\frac{x-h_0}{\beta}\right)^\gamma} dx \quad (7.24)$$

$$= \int_0^{\left(\frac{h-h_0}{\beta}\right)^\gamma} e^{-u} du \quad (7.25)$$

$$= 1 - e^{-\left(\frac{h-h_0}{\beta}\right)^\gamma} \quad (7.26)$$

Using maximum likelihood we find that the parameters β and γ are linked by this pair of equations:

$$\beta = \left(\frac{\sum_{i=1}^N (h_i - h_0)}{n} \right)^{\frac{1}{\gamma}}, \quad (7.27)$$

$$\sum_{i=1}^N \left(\log \left(\frac{h_i - h_0}{\beta} \right) \left[1 - \left(\frac{h_i - h_0}{\beta} \right)^\gamma \right] + \frac{1}{\gamma} \right) = 0. \quad (7.28)$$

These equations then need to be solved numerically to find γ and β .

We fit these four distributions to the empirical CDF for the MDI data. The empirical CDF is calculated by ordering the null points in terms of height and, for the i^{th} element in the list, its value is proportional to the fraction of null points with heights less than it, i.e., $F_i = \frac{i-1/2}{n}$ for $i = 1, \dots, n$.

In Chapter 4, we saw there was a big difference in the distribution of null points at solar minimum and at solar maximum, so to fit the distributions, we pick a sample of Carrington rotations from the solar minima observed by MDI and also from the solar maximum observed by MDI.

Figures 7.3 and 7.4 show the empirical CDF for the MDI data plotted against the 4 fitted model CDFs, such plots are known as p-p (percentile-percentile) plots. Figure 7.3 shows the solar minima Carrington rotations and Figure 7.4 shows the solar maximum Carrington rotations. A perfect fit would be a straight line with a slope of 1 (black line for comparison). So the model CDF that is closest to the black line is considered the best fit to the data of all those considered, although, this does not necessarily mean the model is a good fit.

One method for quantifying the goodness of fit of a model is to use the Kolmogorov-Smirnov statistic by finding the absolute value of the maximum difference between the empirical CDF and the fitted CDF to the model. Since the numbers of null points varies for each plot, we cannot compare these statistics between plots only between models for the same plot. For the case with $h_0 = 0.5\text{Mm}$ we see that the best fit for both the solar minimum and maximum cases is the log-normal distribution. The peak of the log-normal is at 3.6 for the solar minimum case and 3.2 for the solar maximum case which are both just above the boundary of the first grid cell. The distribution falls off sharply towards zero so the fact that this distribution fits our data best tells us that close to the solar surface we are coming across problems with resolution. With this in mind, we move on to consider a h_0 higher in the atmosphere. The first grid cell in our extrapolations is just above 3Mm so we consider the null points above the first grid cell. For $h_0 = 3\text{Mm}$, the best fit is the Weibull distribution for both the solar maximum and solar minimum case.

To be sure we are not missing null points in the chosen domain due to resolution effects we can choose a start height h_0 that is approximately three grid cells into the model at 10Mm (Figures 7.3c and 7.4c). We see that, in both the minimum and

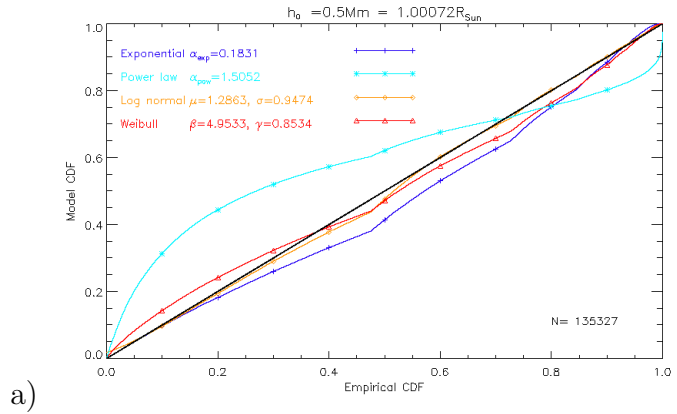
Kolmogorov-Smirnov Statistic Solar minima CR1909-1924 and CR2051-2099

$$D_{exp} = 0.0948$$

$$D_{pow} = 0.245$$

$$D_{lgn} = 0.0382$$

$$D_{wei} = 0.0488$$

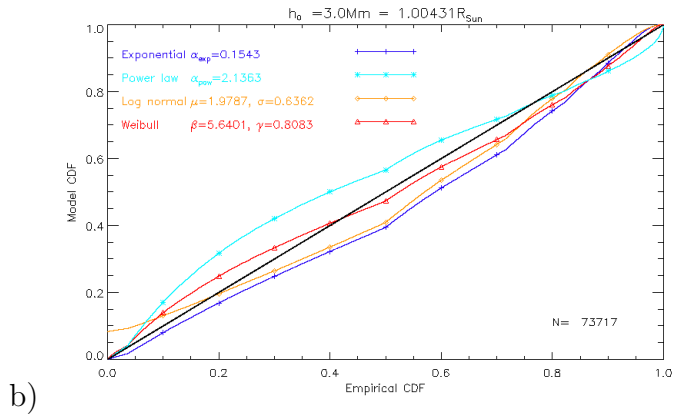


$$D_{exp} = 0.106$$

$$D_{pow} = 0.124$$

$$D_{lgn} = 0.0908$$

$$D_{wei} = 0.0490$$



$$D_{exp} = 0.132$$

$$D_{pow} = 0.0356$$

$$D_{lgn} = 0.140$$

$$D_{wei} = 0.0496$$

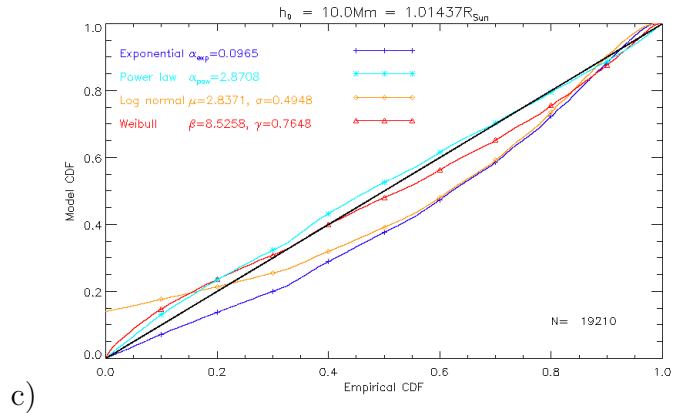


Figure 7.3: P-p plots of the empirical CDF against the model CDF for four standard distributions for solar minima. The blue line is an exponential distribution with parameter α_{exp} , the cyan line is a power law distribution with parameter α_{pow} , the orange line is a log-normal distribution with mean μ and standard deviation θ and the red line is a Weibull distribution with parameters β and γ . The minimum height of the nulls for which the distribution is fitted is (a) $h_0 = 0.5$ Mm, (b) $h_0 = 3$ Mm and (c) $h_0 = 10$ Mm. Null points below h_0 are excluded and the total number of null points, N , is stated on each plot. The Kolmogorov-Smirnov statistic for each distribution is given for each plot.

Kolomogorov-Smirnov Statistic

$$D_{exp} = 0.199$$

$$D_{pow} = 0.226$$

$$D_{lgn} = 0.0525$$

$$D_{wei} = 0.0814$$

a)

$$D_{exp} = 0.253$$

$$D_{pow} = 0.0989$$

$$D_{lgn} = 0.122$$

$$D_{wei} = 0.0924$$

b)

$$D_{exp} = 0.343$$

$$D_{pow} = 0.0679$$

$$D_{lgn} = 0.190$$

$$D_{wei} = 0.104$$

c)

Solar Maximum CR1951-1989

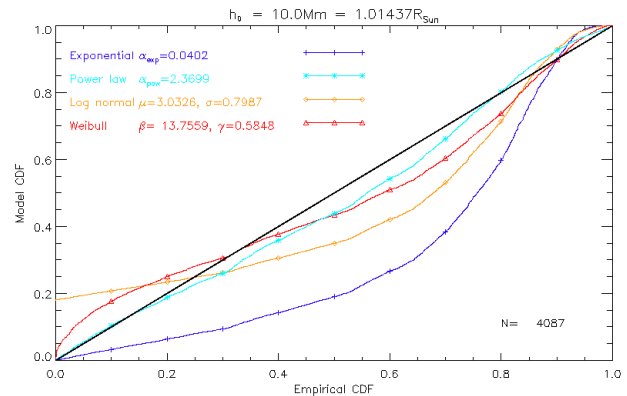
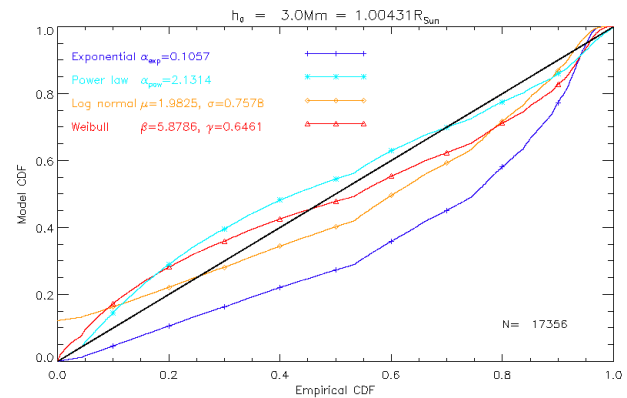
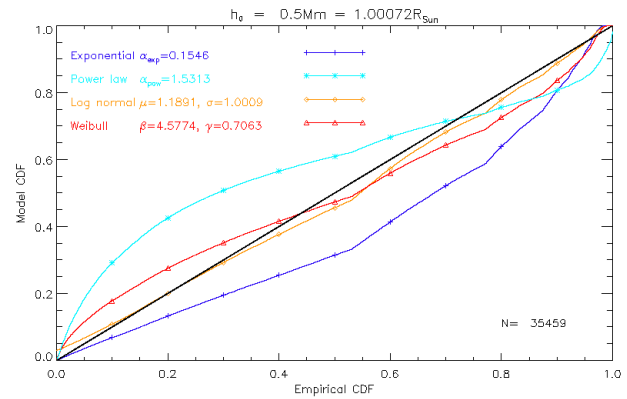


Figure 7.4: P-p plots of the empirical CDF against the model CDF for four standard distributions for solar maximum. The blue line is an exponential distribution with parameter α_{exp} , the cyan line is a power law distribution with parameter α_{pow} , the orange line is a log-normal distribution with mean μ and standard deviation θ and the red line is a Weibull distribution with parameters β and γ . The minimum height of the nulls for which the distribution is fitted is (a) $h_0 = 0.5$ Mm, (b) $h_0 = 3$ Mm and (c) $h_0 = 10$ Mm. Null points below h_0 are excluded and the total number of null points, N , is stated on each plot. The Kolomogorov-Smirnov statistic for each distribution is given for each plot.

maximum cases, that the power law is the best fit. This tells us that the turn over in the number of null points, due to the limitations of the PFSS extrapolation close to the solar surface, is not included here and so with this set of data we can examine the fall off with height.

To eliminate resolution effects we choose to look in depth at the case where we have $h_0 = 10\text{Mm}$ and as such the distribution we consider, in both the solar maximum and solar minimum case, is a power law, since this is found to have the best fit out of the four distributions at which we looked.

The probability distribution function of the number of null points with height is plotted in Figure 7.5 for both the maximum and minimum cases. We calculate the observed pdf (black line) from the data using the following method.

For each data point with a height, h_i , we define the empirical CDF to be $F_i = \frac{i+1/2}{n}$. We know that the cumulative distribution function for a power law (Equation 7.15) and in this case we can write the pdf, f_{pow} in terms of the CDF, F_{pow} , as:

$$f_{pow} = \frac{\alpha_{pow} - 1}{h} (1 - F_{pow}). \quad (7.29)$$

Replacing the F_{pow} with the empirical CDF and h with h_i we get the empirical pdf:

$$f_i = \frac{\alpha_{pow} - 1}{h_i} (1 - F_i). \quad (7.30)$$

The pdf in the solar minima case provides a very good fit for the data. The main divergence is high in the atmosphere where there are fewer null points found in our extrapolations than the model predicts.

The pdf in the solar maximum case does not provide such a good fit for the data as in the solar minima case. At heights of around 100Mm the number of nulls in the atmosphere are underestimated by the model pdf.

The power laws we find for both the solar maximum and the solar minimum case have parameters α_{pow} that are similar, however, the solar minimum has a greater $\alpha_{pow} = 2.87 \pm 0.013$ which gives a steeper fall off with height than the solar maximum case where $\alpha_{pow} = 2.37 \pm 0.021$. This trend is what we expect since there are more null points high in the atmosphere at solar maximum than at solar minimum.

7.4 Null volume density variation with height

The number of null points decreases with height but, because we are working in spherical coordinates, the volume of the column increases with height (or radial distance). To account for this we consider the fall off of the volume density of null points with height. The volume density is calculated by splitting the domain into spherical shells and dividing the number of nulls contained within this shell by the volume of the shell. Figure 7.6 shows this fall off of the volume density of null points with height.

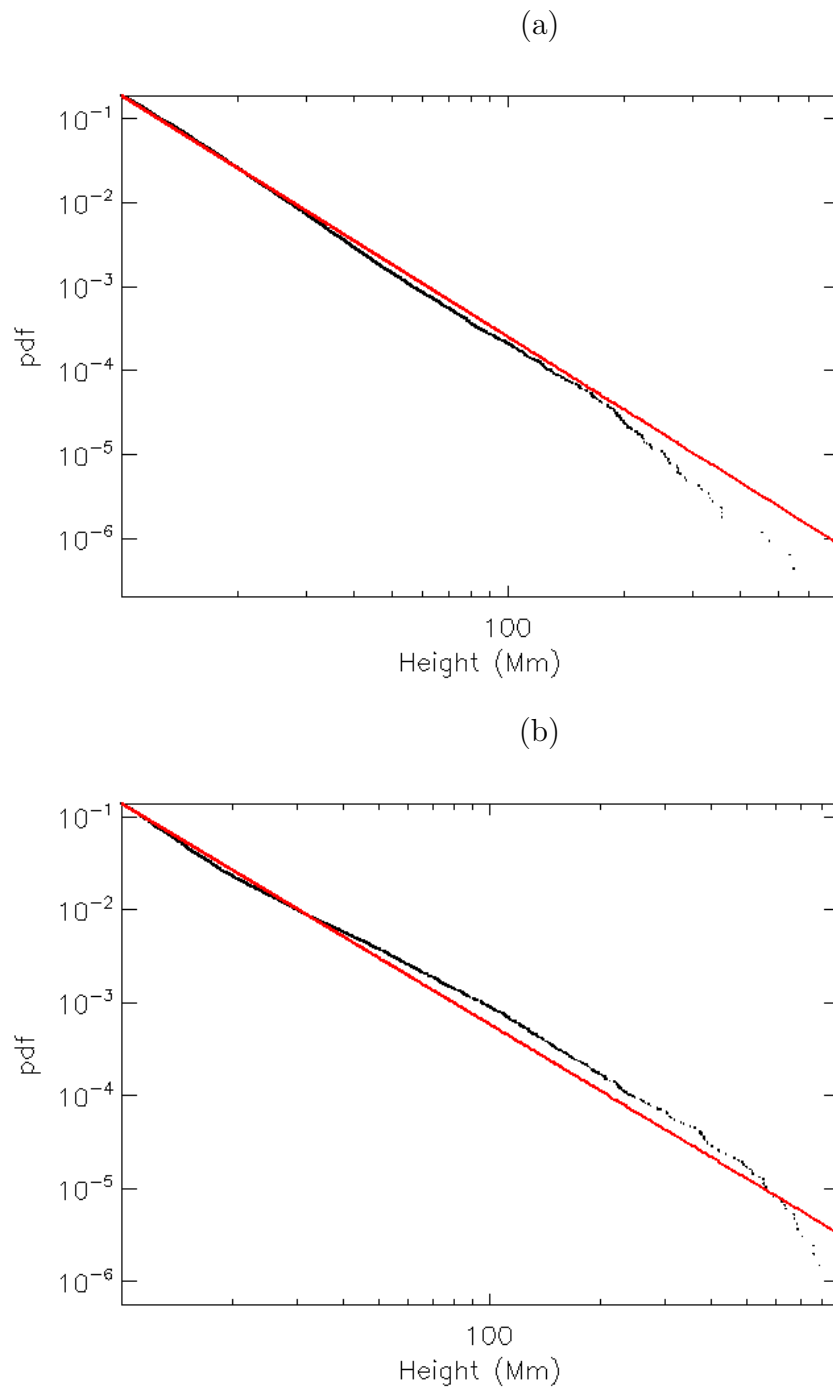


Figure 7.5: pdf of the distribution of null points with height from the data (black line) for solar minimum (a) and solar maximum (b) and model pdf from a power-law distribution with (a) $\alpha_{pow} = 2.87$ and (b) $\alpha_{pow} = 2.37$ (red line).

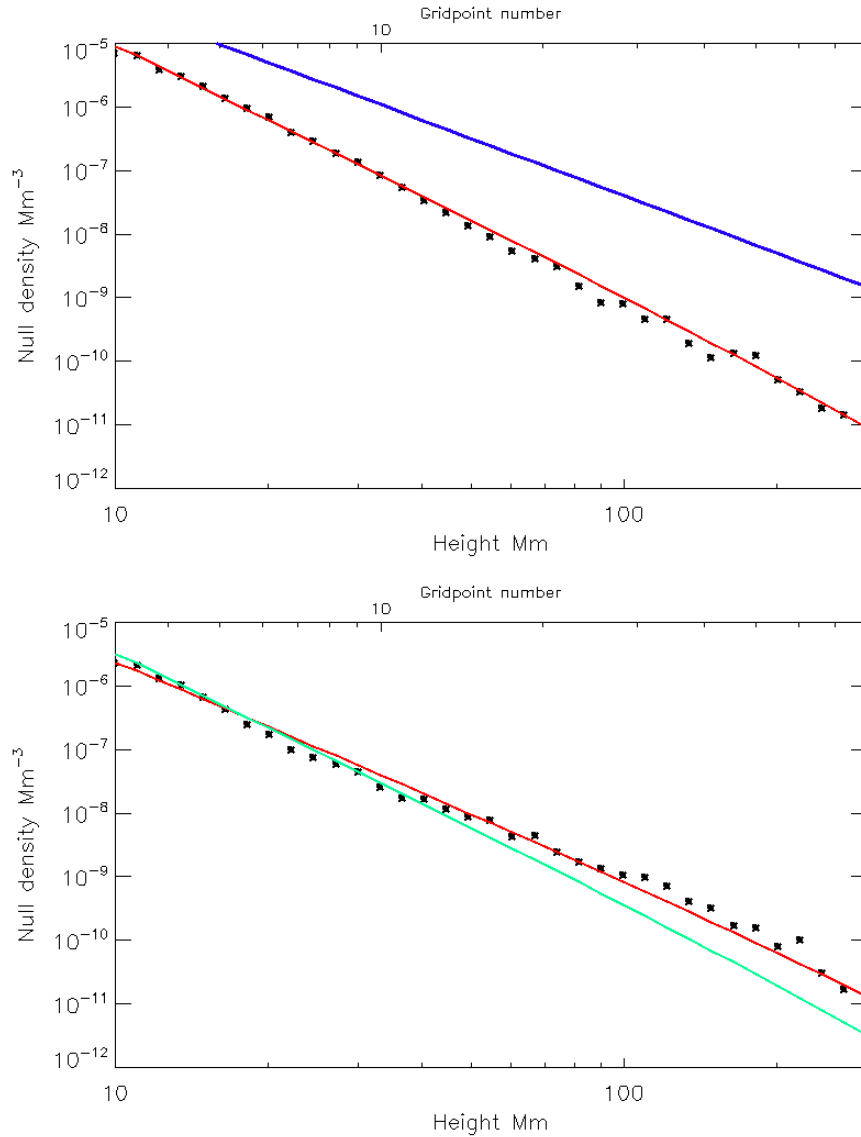


Figure 7.6: Number density per unit volume of the number of null points with height for PFSS extrapolations from MDI (black line) for (a) solar minimum and (b) solar maximum and predicted null density from fitted power law with (a) $\alpha_{pow} = 2.87$ and (b) $\alpha_{pow} = 2.37$ (red line). (a) also shows a blue line which shows the fall off found by Longcope and Parnell [2009], (b) also shows the fit from the solar minima case for comparison (green line).

To find the predicted volume density of null points, N_ρ we first multiply the pdf by the number of nulls per frame, N_F , and then integrate between two heights, h_0 and h_1 and divide by the volume, V , of the corona between those two heights.

$$\rho_N = \frac{N_F}{V(h_{i+1}, h_i)} \int_{h_i}^{h_{i+1}} \frac{\alpha_{pow} - 1}{h_0} \left(\frac{t}{h_0} \right)^{-\alpha_{pow}} dt, \quad (7.31)$$

where,

$$V = \frac{4}{3} \pi [(h_{i+1} + 1)^3 - (h_i + 1)^3]. \quad (7.32)$$

Evaluating the integral in Equation (7.31) gives:

$$\rho_N = -\frac{N_F h_0^{\alpha_{pow}-1}}{V} \left(h_{i+1}^{1-\alpha_{pow}} - h_i^{1-\alpha_{pow}} \right). \quad (7.33)$$

For an α_{pow} greater than one (as in our cases), ρ_N falls off faster with height than the relation given by Longcope and Parnell [2009] but not much faster as can be seen from Figure 7.6a. The blue line shows the relation found by Longcope and Parnell [2009]. As expected the volume density of null points predicted by Longcope and Parnell [2009] is greater than from our model because they use a higher resolution. It is also the case that the relation from our model falls off more steeply at higher heights than that from Longcope and Parnell [2009]. This may be due to the fact that we are using a spherical coordinate system so the volume increases with height whereas they used a Cartesian system where the volume is constant with height.

7.4.1 Null butterfly diagrams

In Chapter 4, we created a “butterfly diagram” of the number of null points found in the PFSS extrapolation of the Kitt-Peak and low-resolution SOLIS synoptic magnetograms over 3 solar cycles (see Figure 4.16). The numbers of null points in the PFSS extrapolations from MDI magnetograms are much greater than the number of null points in the low-resolution extrapolations studied in previous chapters.

Figure 7.7 shows the null butterfly diagram for the MDI extrapolations (top) and the magnetic field butterfly diagram from the MDI data for comparison (bottom). The numbers of null points are lowest (blue and purple on Figure 7.7 top) where there are active regions (strong white and black “wings” on Figure 7.7). This is because, around active regions, there is less mixing of weak polarity field which gives rise to a large number of low-altitude null points. The number of nulls is at its greatest in the quiet sun areas away from the active regions.

To see the variability in the number of null points with latitude clearly, we split the corona into different height bands. The null butterfly diagram for each height band is plotted in Figure 7.8. Figure 7.8a shows the null butterfly diagram for the nulls 69.6Mm or more above the solar surface (radial distance $r > 1.1R_\odot$). Here, there are only a handful of nulls present at this height in each Carrington rotation.

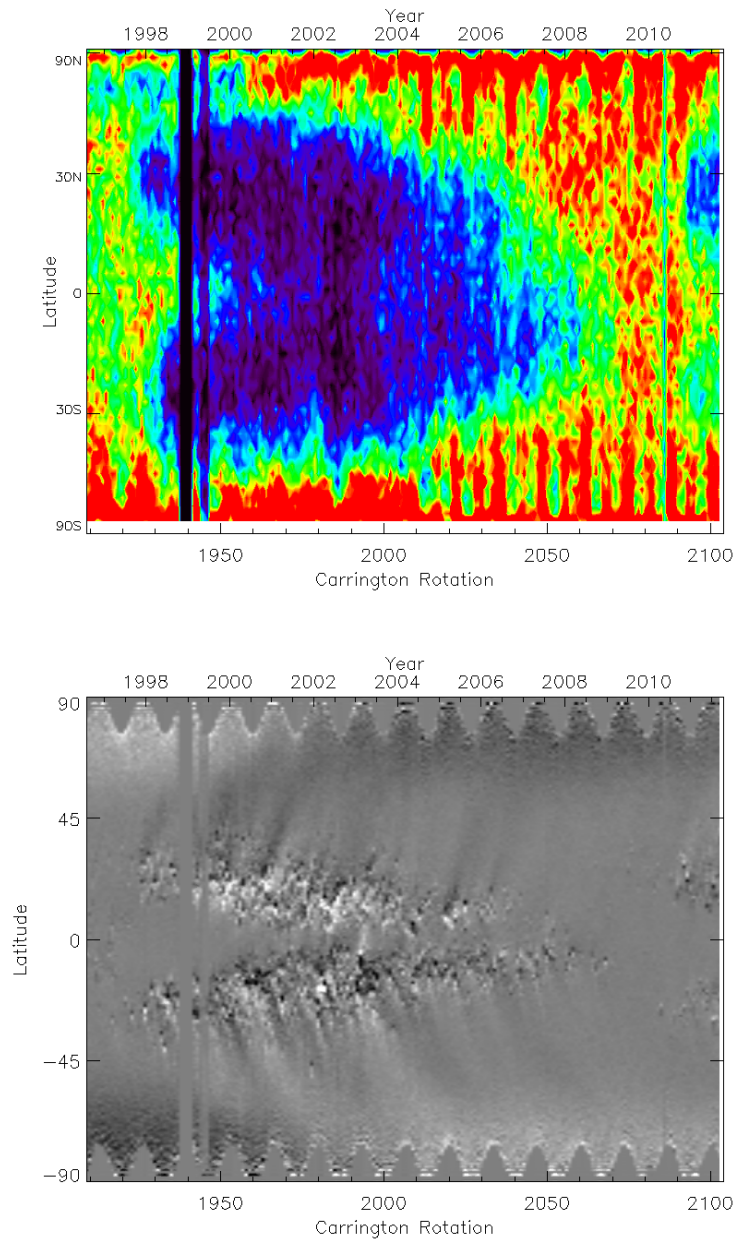


Figure 7.7: Null butterfly diagram for nulls found in PFSS extrapolations from MDI (top) and magnetic field butterfly diagram from MDI data (bottom).

These nulls form over the locations of active regions and also above some regions of mixed polarity field: most specifically they avoid coronal holes. This height band of nulls shows a very similar pattern to the null butterfly diagram for the whole corona from the Kitt-Peak data (see Figure 4.16).

The patterns in each of the other three butterfly diagrams (Figures 7.8b, c and d at heights $6.96 < h < 69.6\text{Mm}$, $0.696 < h < 6.96\text{Mm}$ and $0 < h < 0.696\text{Mm}$, respectively) are approximately the same. The null points are located anywhere on the solar surface, but far fewer form in the active region bands than in the regions of quiet sun and in the polar regions. This is because, around active regions, the field is organised into large-scale positive or negative flux regions and so there is not the small-scale mixing that gives rise to multiple low-altitude null points.

It should be noted here that the pattern of the null butterfly pattern observed by Cook et al. [2009] followed more closely that seen in Figure 7.8a ($h > 69.6\text{Mm}$) with nulls formed over the activity bands. The reason for this discrepancy is that, in the simulations of Cook et al. [2009], they modelled active regions as bipolar regions and neglected all the surrounding quiet-Sun which meant all nulls found were high in the atmosphere and associated with the active-region fields.

Another interesting thing to note is that the bands of heights we take for our null butterfly diagrams increase in size exponentially with height, however the number of null points is at its greatest in the band $0.696\text{Mm} < h < 6.96\text{Mm}$ (Figure 7.8c) which is the second narrowest band. It is probably the case that we are in fact missing many null points in the region $0\text{Mm} < h < 0.696\text{Mm}$ due to this being below the resolution of the first grid cell of our model.

7.5 Example Carrington rotations

As well as examining all the data from the MDI extrapolations together we can examine individual Carrington rotations in order to compare data from different instruments and to compare in more detail the null points at different times during the solar cycle. First we will consider Carrington rotation (CR2100) which is modelled by extrapolations from MDI, SOLIS and HMI synoptic magnetograms (Section 7.5.1). We then consider three different Carrington rotations modelled using the MDI data (Section 7.5.2).

7.5.1 MDI, SOLIS and HMI extrapolations comparison - CR2100

For a comparison of the null points from MDI, SOLIS and HMI PFSS extrapolations, we consider Carrington rotation 2100, which began on the 9th August 2010, since this falls in the brief overlap of all three data sets. The aim of this comparison is to investigate if the overall distribution of null points in 3D space is robust against changes in the instrument that produces the input magnetogram used for the extrapolation.

Figure 7.9 shows the location of the null points superimposed on contours of the

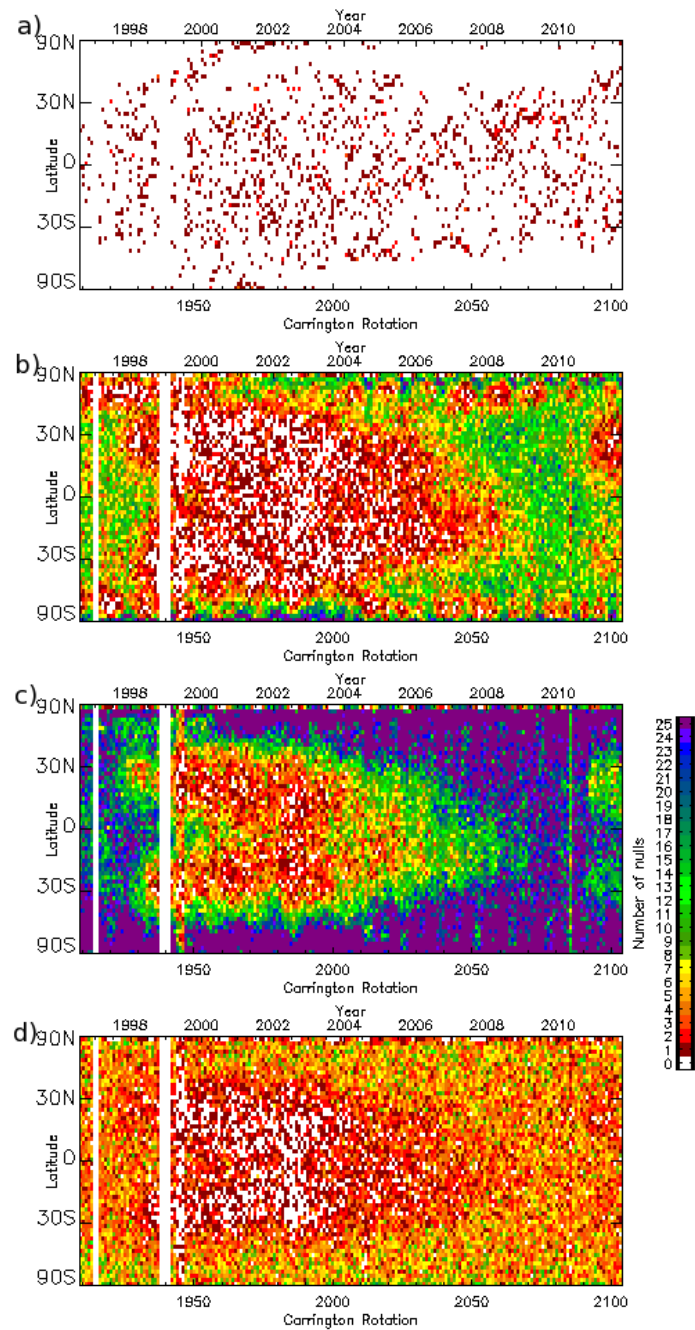


Figure 7.8: Null “butterfly diagram” for different height bands: (a) $h > 69.6\text{Mm}$, (b) $6.96\text{Mm} < h < 69.6\text{Mm}$, (c) $0.696\text{Mm} < h < 6.96\text{Mm}$ and (d) $h < 0.696\text{Mm}$. Colour indicates number of nulls present in a particular latitudinal band in each Carrington Rotation.

	MDI	HMI	SOLIS
Total number of nulls	2034	2113	1524
No. nulls $r > 1.1 R_{\odot}$	9 (0.4%)	6 (0.2%)	6 (0.4%)
No. nulls $1.01 < r < 1.1R_{\odot}$	488 (24.1%)	473 (22.4%)	325 (21.3%)
No. nulls $1.001 < r < 1.01R_{\odot}$	1325 (65.1%)	1379 (65.4%)	995 (65.3%)
No. nulls $1.00 < r < 1.001R_{\odot}$	212 (10.4%)	255 (12.0%)	198 (13.0%)

Table 7.1: Number and proportions of null points in different height ranges for CR2100 for extrapolations from MDI, HMI and SOLIS magnetograms.

radial field at the base for Carrington rotation 2100 for each data set. The position of the null points found in each model are indicated by stars whose colour represents the height band of the null point above the photosphere. For all instruments the distribution of nulls appears to be qualitatively very similar. The locations of the nulls that are above $1.1R_{\odot}$ (red stars) are approximately the same in all frames, which is a good check that the large-scale features are being replicated consistently in the three models. The high altitude nulls that vary between the three data sets are all very close to $1.1R_{\odot}$ so slight differences in the field could cause them to be classified differently.

Table 7.1 shows the number of nulls for each of the height bands for the three extrapolations. There are more null points between $1.01R_{\odot}$ and $1.1R_{\odot}$ (yellow stars) in the MDI extrapolations than in the HMI or SOLIS extrapolations however, in the HMI extrapolations this is balanced out by there being slightly more null points between $1.001R_{\odot}$ and $1.01R_{\odot}$. The height of null points can depend on the strength of the polar field which is one of the hardest parts of the Sun to observe. The different polar field measurements and corrections used in the three data sets probably causes the discrepancy in the number of nulls between $1.01R_{\odot}$ and $1.1R_{\odot}$ and also between $1.001R_{\odot}$ and $1.01R_{\odot}$.

There are fewer null points overall in the SOLIS extrapolation (Figure 7.9) and this is because the resolution of both the extrapolation and the input magnetogram for SOLIS is lower than that for MDI and HMI. We can see from Table 7.1 that the proportion of nulls in each height band in the SOLIS extrapolation is very similar to that of the MDI and HMI. This shows we are not missing off nulls in a particular height range preferentially.

When we look at the distribution of nulls with volume in the atmosphere we have very good agreement between the three instruments (Figure 7.10). The log-log scaling on this plot means that the small differences in the number of nulls found between SOLIS (blue line) and MDI (black line) are not apparent and all the lines follow the same distribution.

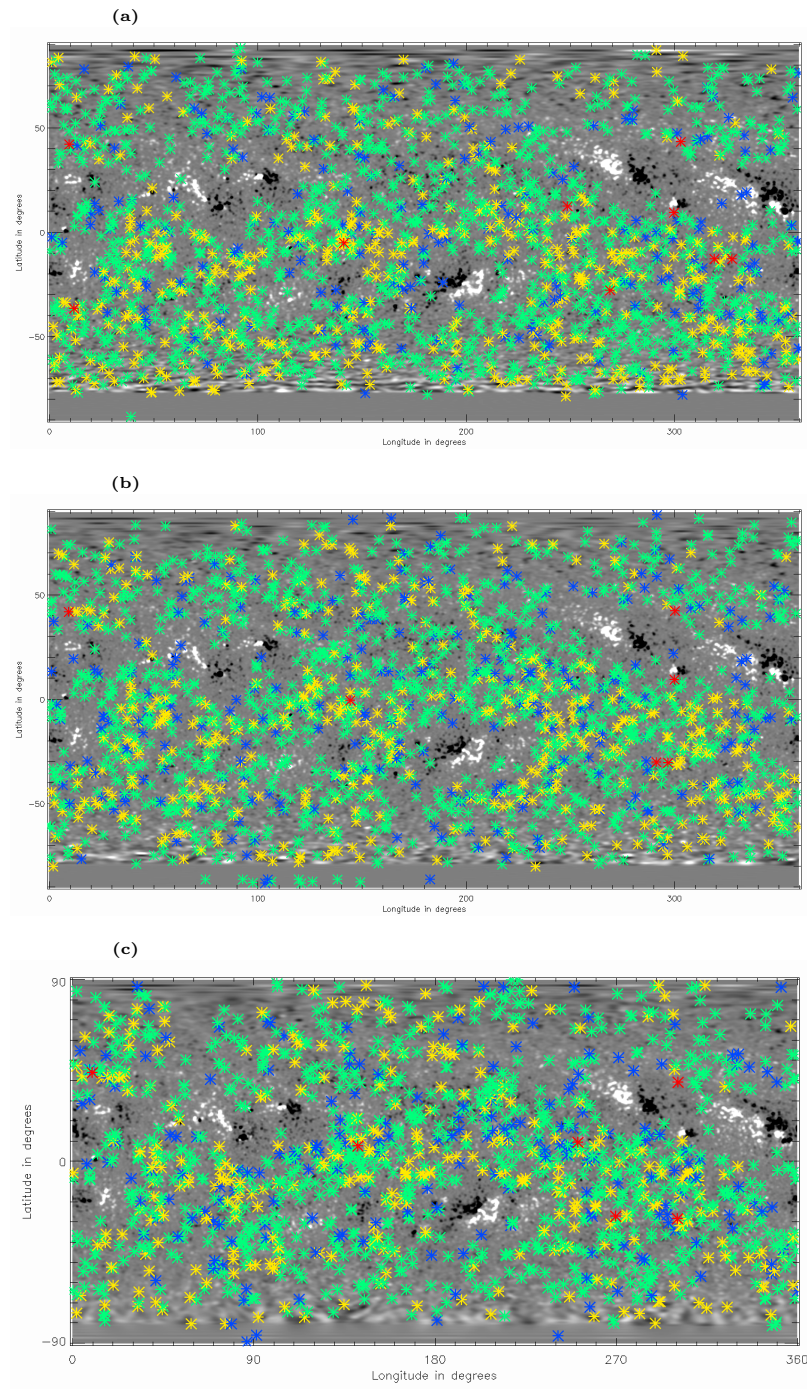


Figure 7.9: Positions of null points for Carrington rotation 2100 in the three models over-plotted on the radial component of the magnetic field at the photosphere for Carrington rotation 2100. Blue stars are nulls below $1.001R_{\odot}$, cyan stars are nulls between $1.001R_{\odot}$ and $1.01R_{\odot}$, green stars are nulls between $1.01R_{\odot}$ and $1.1R_{\odot}$ and red stars are nulls above $1.1R_{\odot}$. The maps are from (a) MDI, (b) HMI and (c) SOLIS

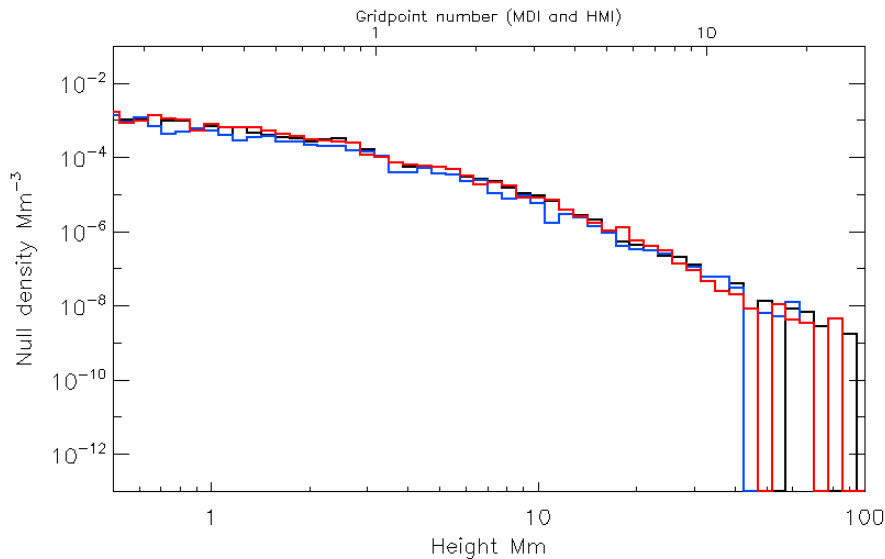


Figure 7.10: Number density of null points with height for PFSS extrapolations from MDI (black line), HMI (red line) and SOLIS (blue line).

7.5.2 MDI sample Carrington rotations

MDI was operational for two solar minima and one solar maximum so we take one frame from each minimum (Carrington rotations (CR) 1919 and 2083) and one from the maximum in between (CR1960) to investigate the null points in detail.

In Figure 7.11, the projected positions of the null points found in each of these extrapolations are labelled as stars, with the star's colour indicating the altitude of the null. The magnetic field in the photosphere at the base of each of these extrapolations is plotted to provide context for the null positions. From these maps it is clear that the data from the magnetogram maps is not very good near the poles for the MDI data so we are wary of drawing conclusions about the null points that are situated polewards of $\pm 70^\circ$ latitude. We can see in the two examples from solar minima (Figures 7.11a and c) that the null points are distributed fairly evenly over the solar surface with most nulls low in the atmosphere. In Figure 7.11b, the example from the solar maximum, the spread of the nulls is found to be very different: far fewer null points form over the active regions than over the surrounding quiet-sun regions. The few null points that do form above active regions are normally found at radial distances greater than $1.1R_\odot$, corresponding to a height of about 69.6Mm above the photosphere (red stars in Figure 7.11). These null points are typically associated with large separatrix domes or separatrix curtains (see Chapter 3). This pattern, in which the low altitude null points avoid the active-region bands, was shown clearly in the null butterfly diagrams (Figure 7.8) with nulls at all radial distances less than $1.1R_\odot$ preferentially situated away from the activity bands.

For each of these individual frames we calculate the cumulative distribution func-

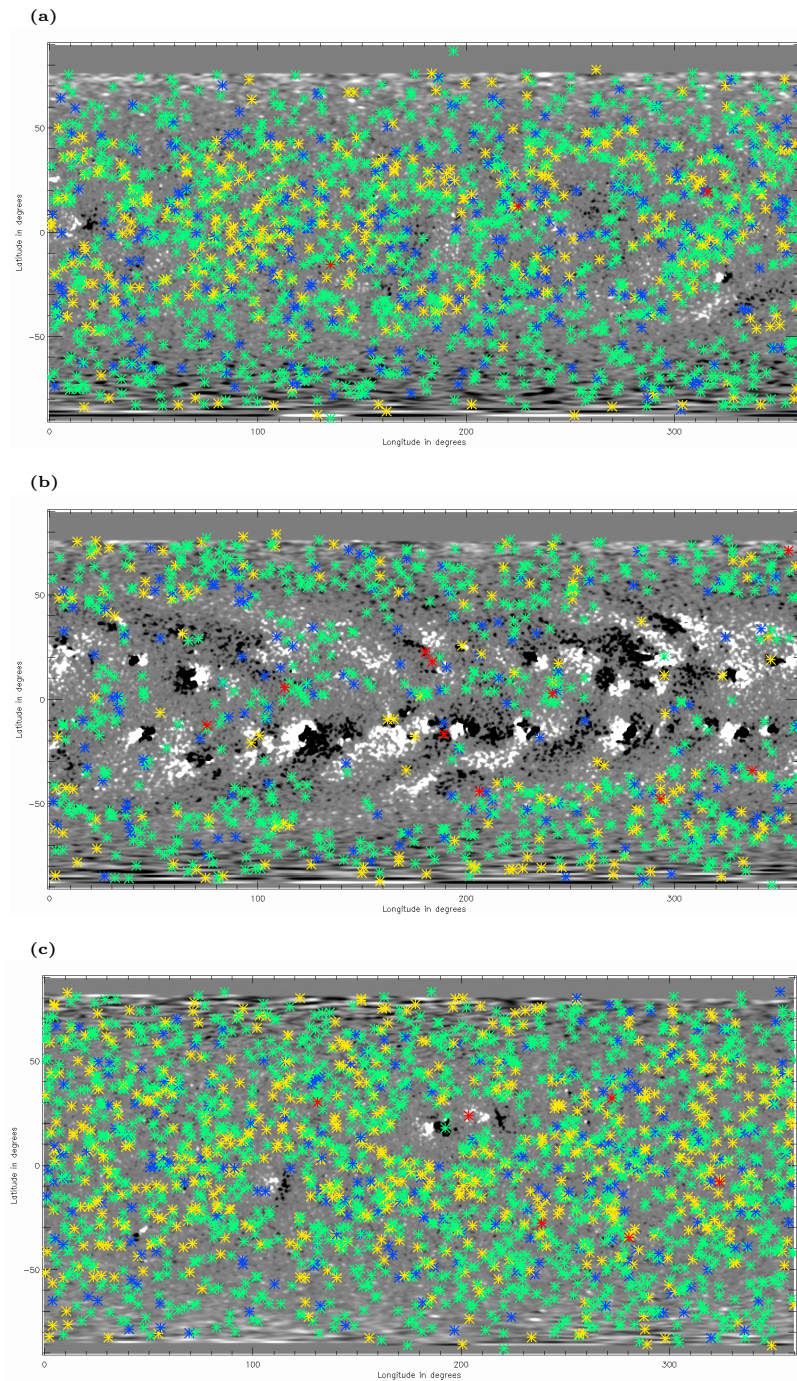


Figure 7.11: Positions of the nulls points found in the PFSS extrapolations of MDI synoptic magnetograms from (a) CR1919, (b) CR1960 and (c) CR2083 over-plotted on the radial component of the magnetic field at the photosphere. The stars show the projected position of the null points: blue stars are below $1.001R_{\odot}$, green stars are nulls between $1.001R_{\odot}$ and $1.01R_{\odot}$, yellow stars are nulls between $1.01R_{\odot}$ and $1.1R_{\odot}$ and red stars are nulls above $1.1R_{\odot}$.

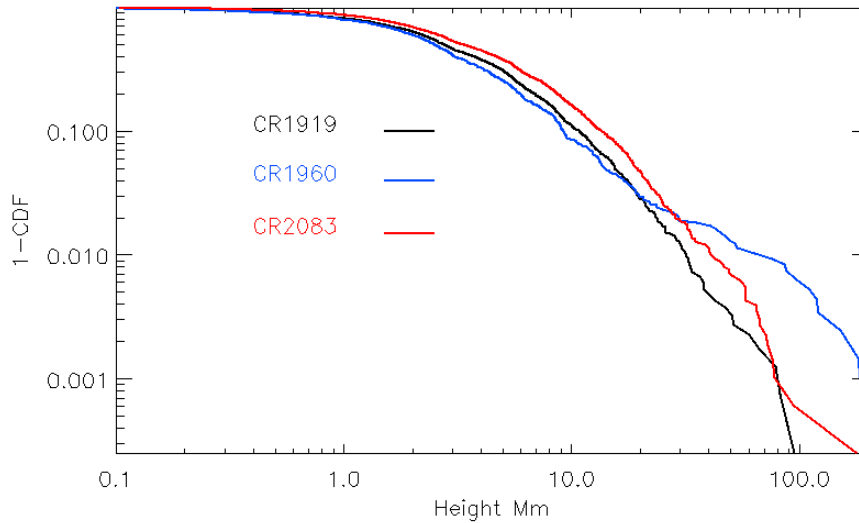


Figure 7.12: Complementary cumulative distribution function of null point heights for CR1919 (black line), CR1960 (blue line) and CR2083 (red line).

tion for the heights of the null points. Figure 7.12 shows a plot of the complementary CDF (1-CDF) against the height. The black line shows the complementary CDF for CR1919 and the red line shows the complementary CDF for CR2083. Since both of these Carrington rotations are from solar minima the largest proportion of null points are found low down in the atmosphere with very few null points formed above about 30Mm. Comparing between the two solar minimum cases, we see that the null points present in CR2083 are, on average, higher in the atmosphere than those present in CR1919. This is due to the weaker polar field strength in the recent minimum in comparison to the previous two minima allowing structures associated with weak-field regions to expand higher into the atmosphere (there is a more thorough discussion of this in Chapter 4).

In the Carrington rotation from solar maximum, CR1960 (blue line), a smaller proportion of null points lie low down in the atmosphere than in the other two Carrington rotations and, also a much more gradual fall off in the number of null points above 30Mm is found. This corresponds to the distributions seen in the synoptic maps of null point locations in that we have a much higher proportion of high-altitude null points at solar maximum than at solar minimum. This is because firstly, there are fewer null points overall at solar maximum since there is less mixed-polarity quiet-sun field than at solar minimum and secondly, there are more high-altitude null points at maximum due to the active regions at this time.

As well as looking at the distribution of null points with height, we also consider their distribution as a function of the magnetic field strength. Figure 7.13 shows the complementary cumulative distribution function of null points against the photospheric magnetic field directly beneath them. In the solar maximum case (CR1960

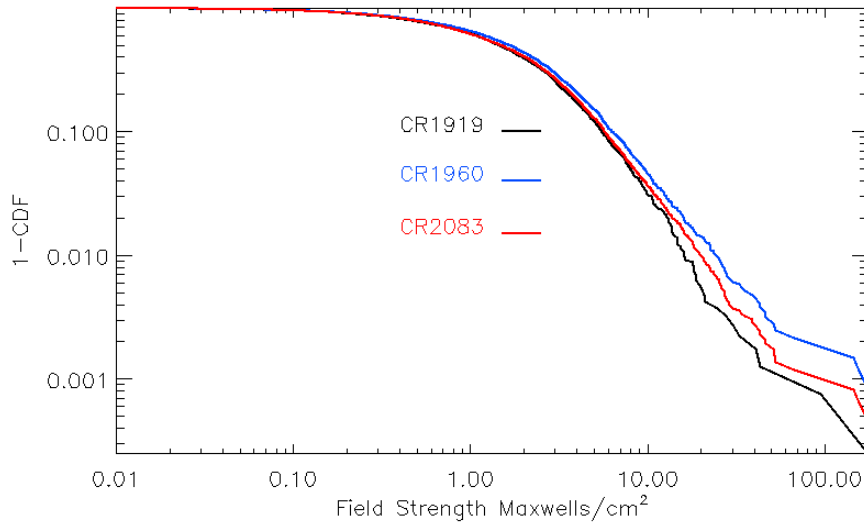


Figure 7.13: Complementary cumulative distribution function of null points with magnetic field strength at the photosphere for the CR1919 (black line), CR1960 (blue line) and CR2083 (red line)

blue line) we see that there are a greater proportion of null points forming over patches of high field-strength than at solar minimum. These nulls also correspond to the nulls that form high in the corona over active regions.

In the weak global dipole solar minimum case (CR2083 red line) we see a greater proportion of nulls forming over strong magnetic field regions than in the strong global dipole minimum case (black line).

Above about 3 Mx/cm² the distribution of nulls with field strength appears to fall off as a power law. With this in mind we have removed all nulls with field strengths less than 3 Mx/cm² and fitted a power law to each of the data sets. Figure 7.14 shows the fitted power law over-plotted on the empirical CDF.

The α_{pow} parameter for the power laws are all very similar. Carrington rotation 1919 during the strong global dipole minimum has the largest α_{pow} which means that out of the three frames considered this shows the steepest fall off with field strength. The example Carrington rotation from the weak global dipole minimum has a parameter $\alpha_{pow} = 2.57 \pm 0.04$. Carrington rotation 1960, during solar maximum, has the parameter $\alpha_{pow} = 2.48 \pm 0.05$. This implies that, in comparison to the solar minimum cases, there are a higher proportion of nulls forming over regions of high field strength. This is because there are many active regions at solar maximum and high-altitude nulls can form over these.

In all cases the power law fits very well to the data between 3 Mx/cm² and 10 Mx/cm² however, for greater field strengths there is deviation from the model. This is partly due to the fact that we have so few data points for these field strengths. We should therefore be wary of extrapolating results from these power laws as we have

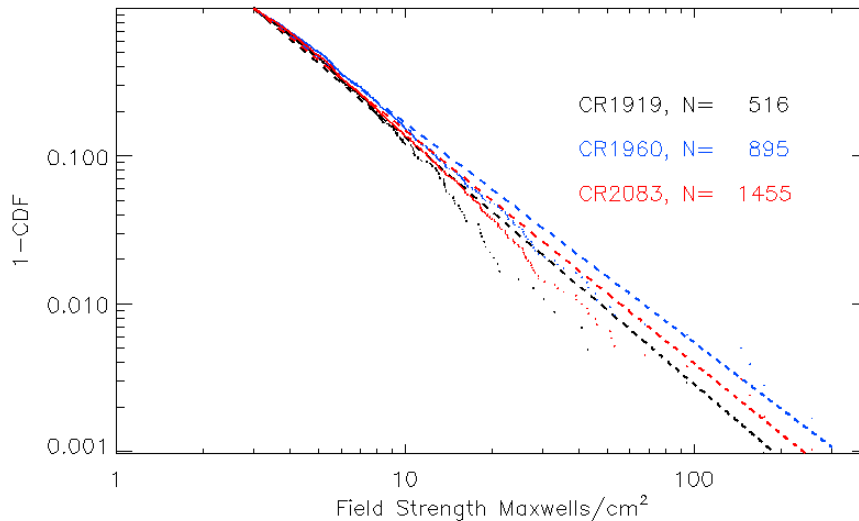


Figure 7.14: Complementary cumulative distribution function of null points with magnetic field strength at the photosphere (dots) and over-plotted CDF from fitted power law (solid line). CR1919 (black) $\alpha_{pow} = 2.67 \pm 0.07$, CR1960 (blue) $\alpha_{pow} = 2.48 \pm 0.05$ and CR2083 (red) $\alpha_{pow} = 2.57 \pm 0.04$.

less than a decade of data in agreement with the model.

7.6 Conclusions

Overall, several conclusions can be drawn about the distribution of null points in the solar atmosphere. To begin with, the total number of null points, as seen in the Chapter 4, varies out of phase with the cycle, but if we consider just high-altitude nulls the number varies in-phase with the solar cycle.

The null points that are present low in the atmosphere preferentially form away from the locations of active regions and instead occur over quiet-sun regions, whereas the high-altitude null points form over active regions and so are more prevalent at solar maximum.

If we consider null points above 10Mm (3 grid cells into the model) we see that the number of null points falls off with height as a power law distribution with parameter $\alpha_{pow} = 2.87$ for solar minimum and $\alpha_{pow} = 2.38$ for solar maximum. When adjusted for the volume the estimated slope of the power-law for solar minimum agrees very well with that of Longcope and Parnell [2009] although the overall density is higher for Longcope and Parnell [2009].

By considering three individual frames from 3 different times in the solar cycle it is clear that the distribution of null points (particularly high in the atmosphere) varies with the solar cycle phase, as well as solar dipole strength. This is in agreement with

the results from the long term study in Chapter 4. If data at a high resolution over a longer time-scale were available a more thorough study of null point distribution could be undertaken to combine both the height variation of null points and their cyclic variation.

By considering data from three Carrington rotations from MDI we were able to compare the distribution of null points with the field strength on the solar surface directly below them. There seems to be a power law relationship between the number of nulls and the field strength on the photosphere with a parameter α_{pow} that varies with the solar cycle. However, we do not have many data points in a single frame to confirm this and a further statistical study of this trend would tell us more about this distribution.

The numbers of nulls found are dependent on the resolution of the model and the instrument used to measure the photospheric magnetic field. This was shown in a comparison of PFSS models of the same Carrington rotation extrapolated from magnetograms from three different instruments. The high-altitude null points do not vary much with resolution or between different magnetogram sources. However, in the single frame which we examined it was found that the proportion of null points found at each height band was approximately the same over all the data sets.

Chapter 8

Open Fields Around Active Regions

8.1 Introduction

This chapter looks at the global magnetic topology of seven large active regions in order to determine if there are specific observational signatures associated with regions of open field. These active regions were observed on the solar disc between August 2011 and September 2012. The global magnetic field associated with these active regions is studied using Potential Field Source Surface (PFSS) extrapolations from high-resolution Heliospheric Magnetic Imager (HMI) data. The locations of magnetic skeleton structures and open-field regions are compared to the locations of upflows observed by the Extreme-Ultraviolet Imaging Spectrometer (EIS) instrument aboard the Hinode spacecraft [Culhane et al., 2007] and to measurements of the density and temperature also calculated using EIS observations. These observations were taken and analysed by Louise Harra and Len Culhane at the Mullard Space Science Laboratory (MSSL) and David Brooks at the Naval Research Laboratory (NRL).

Upflows around active regions were first observed using the Transition Region Coronal Explorer (TRACE) [Winebarger et al., 2001]. These upflows were observed by looking for motions in a time series of images. Following this Sakao et al. [2007] made a similar observation using Hinode/X-Ray Telescope on the 22 February 2007. They proposed that upflowing plasma from the edges of active regions could contribute as much as 25% of the mass of the solar wind. Since then much work has been done to try to establish whether these upflows really are a source of the solar wind [e.g., Harra et al., 2008, Brooks and Warren, 2011, van Driel-Gesztelyi et al., 2012].

Doschek et al. [2008] took measurements of upflows from 2 active regions in 2007 using the EUV Imaging Spectrometer (EIS) aboard Hinode. From this they calculated the plasma in the upflows to have temperatures of 1.3 MK and a number density of $7 \times 10^8 \text{ cm}^{-3}$.

Many authors have looked at the mechanisms that could drive these plasma up-

flows [e.g., Marsch et al., 2008, Baker et al., 2009, Murray et al., 2010]. Baker et al. [2009] found, in the one case they considered, that the upflows corresponded to the locations of Quasi-Separatrix Layers (QSLs) which possibly suggests magnetic reconnection is a driver for these upflows. This idea is supported by the finding of evidence from radio noise storms [Del Zanna et al., 2011] that suggests magnetic reconnection occurs high in the corona around upflows.

Slemzin et al. [2013] found that in the active region they considered in July/August 2009 the observed upflow regions corresponded well with the locations of open field as found using a PFSS model.

van Driel-Gesztelyi et al. [2012] considered upflows observed by EIS from two active regions adjacent to a coronal hole. They calculated the global magnetic skeleton of a PFSS extrapolation of this configuration, as well as a Linear Force-Free Field (LFFF) extrapolation of the local field and examined the relationship between the open field, as predicted by the PFSS model, and the location of observed upflowing plasma. They found that magnetic reconnection along QSLs, some of which surround separatrix surfaces associated with null points, played a part in driving the upflows. They find that since one null point above the active region is associated with a separatrix dome outside the HCS curtains, interchange reconnection could allow loops inside the separatrix dome to open accelerating plasma out along them in the form of the solar wind. However, they find that not all the locations of upflow observed by EIS are associated with structures that could facilitate interchange reconnection. Thus interchange reconnection cannot be the sole mechanism that enables plasma to flow into the solar wind.

The aim of our study is to provide a comparison of multiple active regions and analyse the global topological structure around these. In this Chapter we begin by describing the PFSS extrapolations (Section 8.2) and the observational data (Section 8.3). In the following sections, we then compare seven EIS observations from 2011 and 2012 and the global topology from the PFSS model at these times and discuss our results in Section 8.11. The particular active-regions are chosen for being close to disc centre to allow for good magnetogram measurements and also for the types of observations made by Hinode/EIS.

8.2 PFSS extrapolations from HMI

As the magnetic structure of active-region magnetic field can change quite rapidly we require more of an instantaneous view of the active regions than can be provided from the Carrington rotation averaged synoptic maps. So, here, daily-update synoptic magnetic field maps from the Heliospheric Magnetic Imager (HMI) aboard the Solar Dynamics Observatory (SDO) spacecraft are used.

These maps are created by taking HMI magnetogram data from 60° either side of central meridian on the specified day and replacing the corresponding 120° of the Carrington rotation synoptic maps with this new data. The whole map is then rotated

so these new 120° of data start at zero degrees, which means the central meridian for the date given is now at 60° longitude.

The solar B-angle is a measure of the tilt of the Sun out of the ecliptic plane. For the daily synoptic maps a large B-angle at the time of measurement can lead to missing data values at the poles. To replace these missing data values, first, I look at the corresponding place in the HMI Carrington rotation synoptic map and use these to fill the missing values. If these data are also missing from the Carrington rotation synoptic map then I fill in the missing data values by averaging the values of the nearest neighbours.

The original size of the HMI synoptic maps is 3600 by 1440 pixels. This resolution is too large to process through the PFSS extrapolation routine that I use, so the resolution of the input magnetogram is reduced to a resolution of 1800 by 720 by averaging adjacent pixels. The harmonic number is set to $l_{max} = 351$ which, when run through the PFSS extrapolation code (described in Section 2.2) with the daily-update synoptic map gives a grid with resolution 1409 grid-points equally spaced in longitude, 705 grid-points equally spaced in latitude.

In this study, we are considering the global field around active regions which can be far from potential. It has been shown in previous studies that potential field models underestimate the height of features [e.g., Riley et al., 2006]. This means that what we would consider to be large arching features in our model may actually reach out beyond the source surface and contain open field. With this consideration in mind we use extrapolations where the source surface is at approximately $2.0R_{\odot}$. This gives a resolution of 157 grid-points spaced exponentially between $1R_{\odot}$ and $2.006R_{\odot}$.

8.3 Active Regions and Observational Data

The seven active regions considered in this chapter were observed between August 2011 and September 2012 during the rise phase of cycle 24. Table 8.1 lists the active regions we consider and their positions relative to disc centre on the day of the observation. We consider a mix of northern and southern hemisphere active regions. Most are reasonably close to disc centre although the 29th August 2012 and 17th February 2012 are at high latitudes in the northern and southern hemispheres, respectively.

These active regions are observed using AIA in the 193Å line and then using EIS the intensity in FeXII and the Doppler velocity are measured.

8.4 AR11271 - 21st August 2011

The first active region considered is AR11271 on the 21st August 2011. A full disc AIA image (Figure 8.1 top) shows this active region situated to the North of disc centre on this date and reveals a large coronal hole (lighter patch on AIA image) to the west. There are upflows (blue shifts) observed on both sides of this active region in a Doppler map created from EIS FeXII line data (Figure 8.1, centre middle). The

Date	NOAA AR number	Site of AR from disc centre	Approx. Solar coordinates (arcsec)
21st Aug 2011	11271	N	(-80, 180)
17th Feb 2012	11419	NE	(-220, 580)
2nd Mar 2012	11427	NW	(50, 350)
28th Mar 2012	11445	SE	(-320,-280)
29th Aug 2012	11553	SW	(110,-460)
15th Sep 2012	11569	SE	(-130,-330)
23rd Sep 2012	11575	E	(-370,0)

Table 8.1: Active regions studied and their positions, relative to disc centre, on dates mentioned.

HMI daily-update synoptic magnetogram is used as a lower boundary condition for the PFSS model and this lower boundary is shown in Figure 8.1 (bottom). The active region being considered is circled in red and is fairly isolated from other active regions.

In the PFSS model at this time the HCS has split into two sections (Figure 8.2). The open field in AR11271 (yellow lines in Figure 8.2) sits in between the HCS curtains that map down from the two HCS null line loops. This open field region coincides with the coronal hole observed in the full-disc AIA image. This region of open field is in a similar location to that of the observed upflow to the west of the active region. The area to the east of the active region, which also exhibits upflow in the observations is not open according to the PFSS model, however, the field lines emanating from this region reach very high in the atmosphere (see centre row, right panel of Figure 8.1) This means that they could be open if the source surface was lower. Indeed, it has been suggested that the source surface could be as low as $1.6R_{\odot}$ [Lee et al., 2011].

Figure 8.1 (centre row, centre panel) shows the intersections of the separatrix surfaces with the photosphere overlaid on the EIS Doppler velocity map. The strong blue shifted region to the east of the active region is threaded by a negative separatrix surface that forms part of a large separatrix dome. Field lines near the separatrix surface travel a long distance, either within the dome or around its boundaries. Examples of such field lines can be seen in Figure 8.2 (bottom). In looking at the lengths of these field lines ($l < 300\text{Mm}$ red, $l > 300\text{Mm}$ blue, open yellow), we see that many field lines emanating from around the eastern side of the active region near the negative separatrix surface are longer than 300Mm (blue lines in Figure 8.2 bottom) which means significant plasma flow could happen along these field lines.

8.5 AR11419 - 17th February 2012

On the 17th February 2012, AR11419 was observed by EIS to the North-East of disc centre (see Figure 8.3 top). Figure 8.3 (bottom) shows the radial component of the magnetic field at the lower boundary of the model ($1R_{\odot}$) on which a red circle has

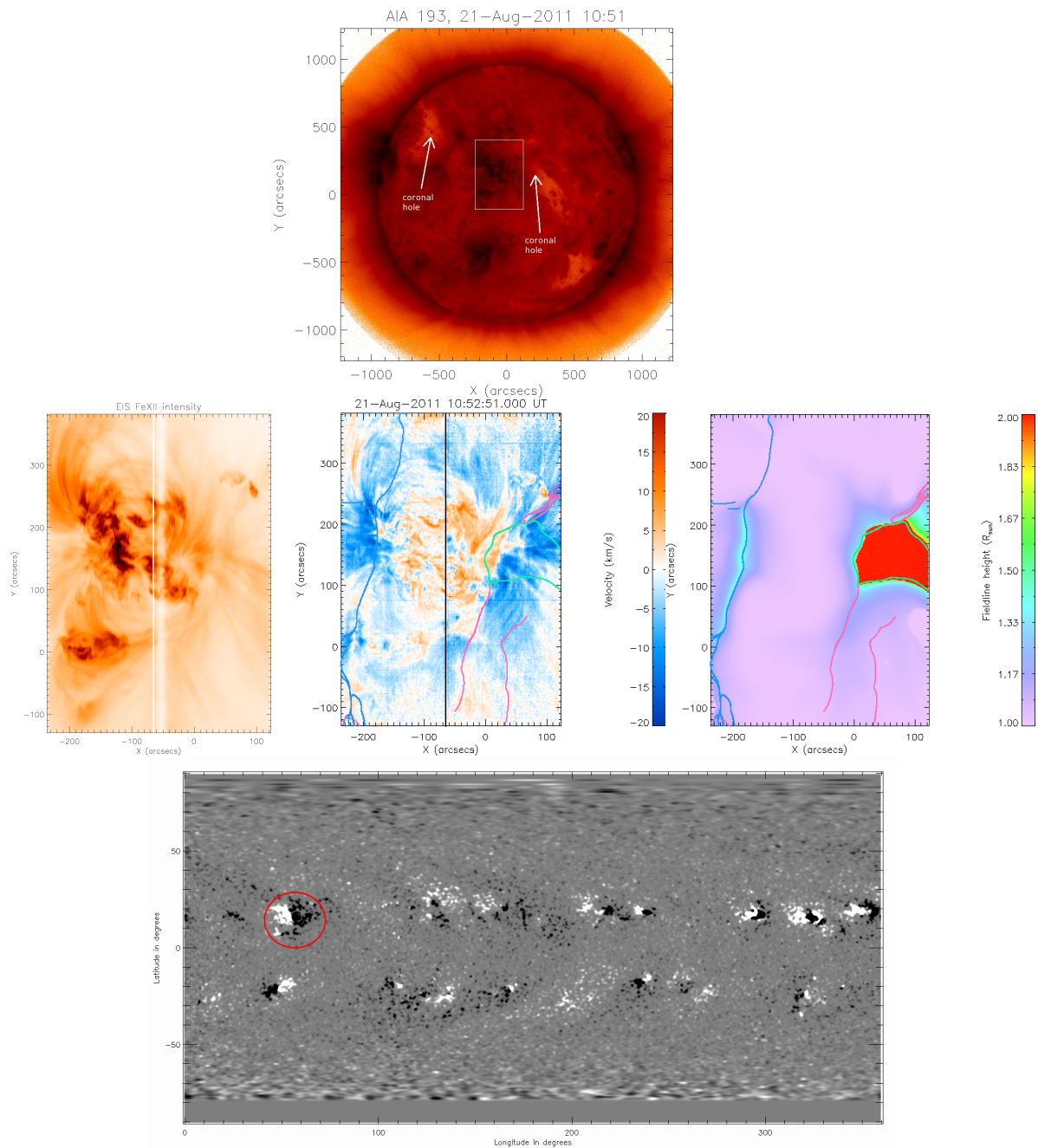


Figure 8.1: Top: AIA 193Å image on the 21st August 2011 for active region AR11271. The white box shows the position of the EIS raster. Centre row: EIS FeXII intensity image, Doppler velocity map and map of heights reached by field lines. Over-plotted on the Doppler and field line height maps are the intersection of the separatrix surfaces with the photosphere, green: HCS curtains, blue: negative separatrix surfaces, pink: positive separatrix surfaces. Bottom: the radial component of the magnetic field at the base of the PFSS model. AR11271 is circled in red.

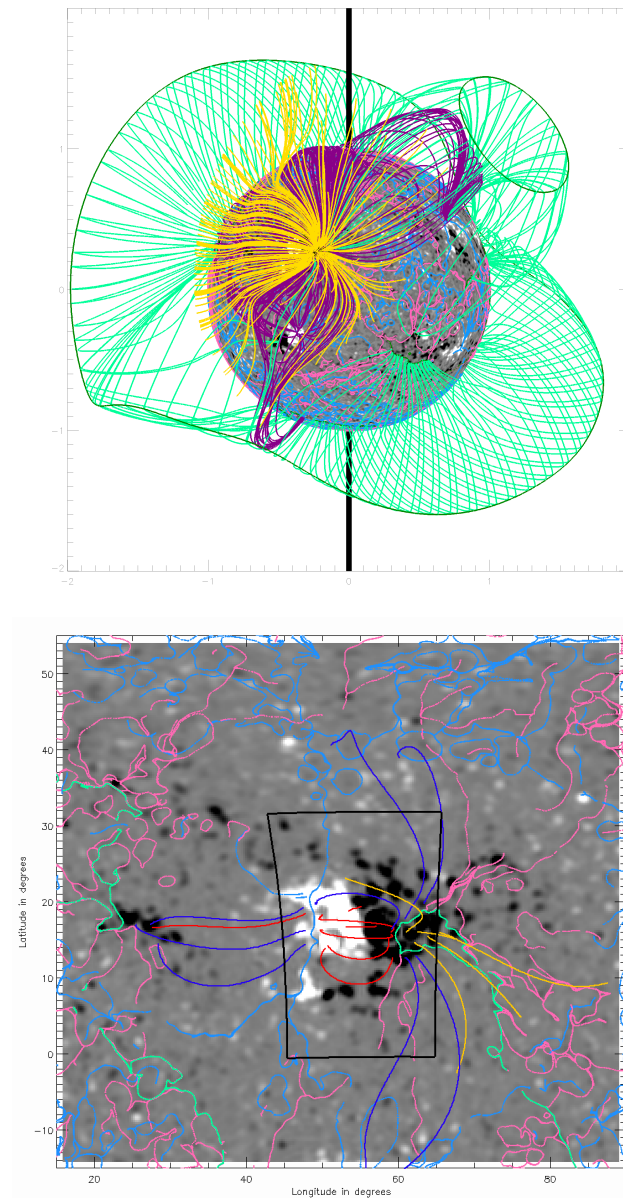


Figure 8.2: Top: 3D image of the PFSS extrapolation of the Sun from 21st August 2011. Field lines are traced from around AR11271. The green lines are field lines in the HCS, the yellow and purple lines are lines traced from the active region (yellow lines are open and purple lines are closed). The surface of the Sun is coloured with the radial component of the magnetic field. Bottom: Photospheric magnetic field from the PFSS extrapolation around AR11271 for the 21st August 2011. Light blue and light pink lines are the intersection of negative and positive separatrix surfaces, respectively, with the photosphere, light green lines are the intersection of the HCS curtains with the photosphere. Red lines are example field lines shorter than 300 Mm. Dark blue lines are example field lines longer than 300 Mm. Yellow lines are example open field lines. Black box shows EIS field-of-view.

been drawn to highlights AR11419. It is a large active region to the North of a cluster of smaller active regions and is tilted in the opposite direction to that predicted by *Hale's Law*. AR11419 began its transit of the solar disc on the 12th February and disappeared off the western limb on the 23rd February. The observations indicate that this active region is not near to a coronal hole so we would not expect to find any large open-field regions near this active region in the PFSS extrapolation.

The magnetic field of the global solar corona is calculated using the PFSS model and as expected, around AR11419, there are very few open-field lines. The area surrounding the active region has only a few field lines that make it out to the source surface (see Figure 8.4). These open-field lines originate from such a small photospheric area that it is unlikely that this region would produce a clear coronal hole in the observations. Most of the field in the active region is comprised of closed loops which are low lying (purple lines in Figure 8.4 top). Towards the south of the active region are the foot-points of field lines that reach high in the atmosphere before eventually closing. This patch (cyan in Figure 8.3 centre row, right panel) occurs near to where the upflow was seen in the EIS Doppler velocity data. It also corresponds to the intersection of a large negative separatrix surface with the photosphere (blue line in Figure 8.3 centre row, centre panel). This could suggest that reconnection about the null point associated with this separatrix surface is a driver for the upflow.

Figure 8.4 (bottom) shows a sample of field lines emanating from the active region over-plotted on a subsection of the photospheric magnetic field map. Most of the field lines traced in Figure 8.4 (bottom) are coloured red, signifying field lines shorter than 300 Mm. All of the sample field lines that are longer than 300 Mm (dark blue lines) have foot points near to the intersection of a negative separatrix surface (light blue line) with the photosphere. This is also the location of upflow (see Figure 8.3 centre row, middle panel). The negative separatrix surface that threads this blue-shifted region is part of a large separatrix dome so it could be the case that reconnection around such a dome could drive upflowing plasma.

8.6 AR11427 - 2nd March 2012

On the 2nd March 2012, the active region, AR11427, circled in red in Figure 8.5 (bottom) was observed by HMI, EIS and AIA. It is situated to the north of disc centre. There is a coronal hole to the north east of the active region, but this is outside the field-of-view of EIS (Figure 8.5 top). From the HMI daily update magnetogram (Figure 8.5 bottom) it is apparent that the active region is surrounded by diffuse and decaying active regions.

According to the PFSS model, on the 2nd March 2012, AR11427 has two narrow channels of open field either side of the active region (yellow field lines in Figure 8.6 (top) whose foot-points are along the green lines in Figure 8.5 centre row, centre panel). These do not appear to line up with the locations of the observed upflows. However, if a map of the maximum height reached by field lines with foot-points

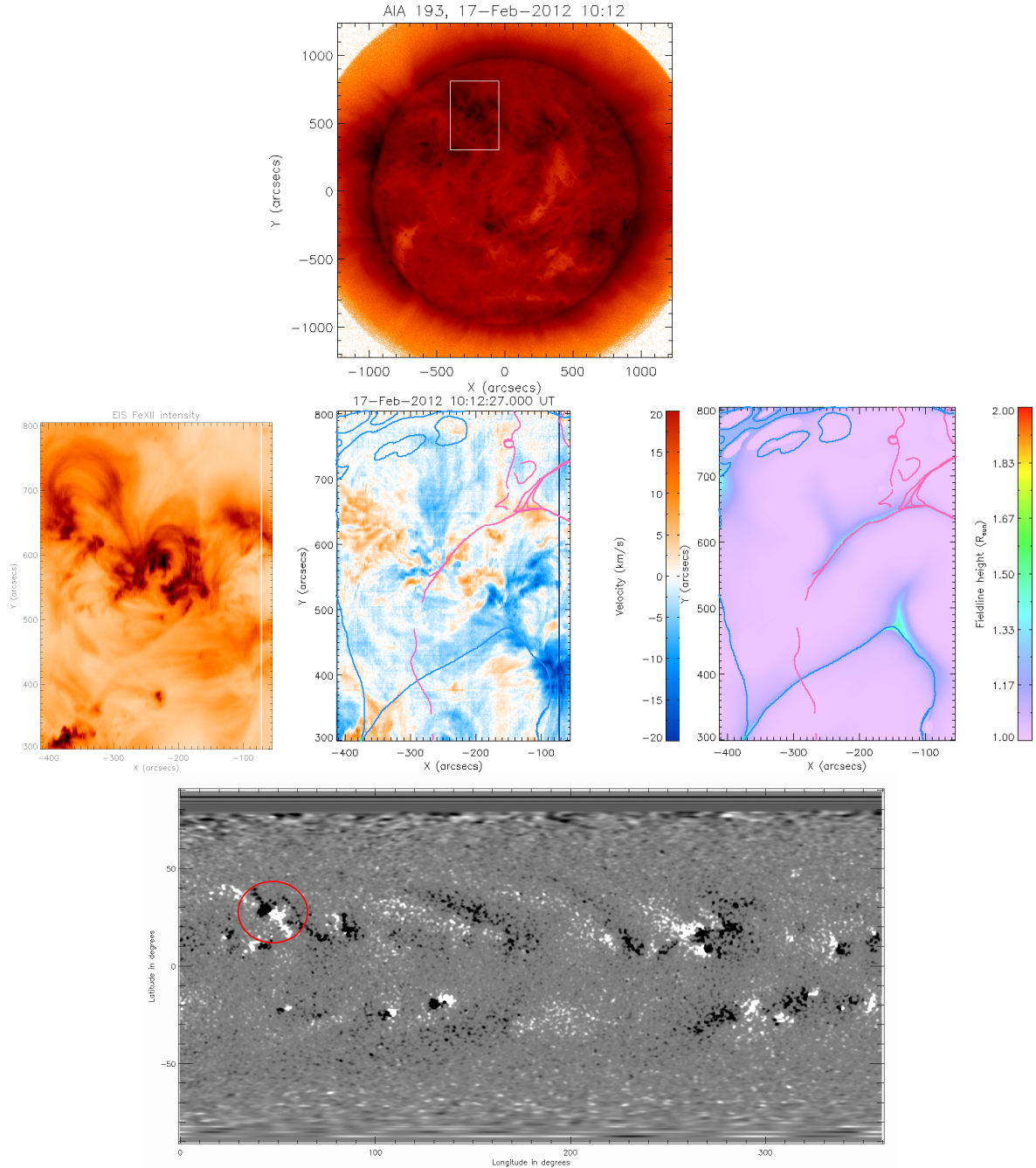


Figure 8.3: Top: AIA 193Å image on the 17th February 2012 for active region AR11419. The white box shows the position of the EIS raster. Centre row: EIS FeXII intensity image, Doppler velocity map and map of heights reached by field lines. Over-plotted on the Doppler and field line height maps are the intersection of the separatrix surfaces with the photosphere, green: HCS curtains, blue: negative separatrix surfaces, pink: positive separatrix surfaces. Bottom: the radial component of the magnetic field at the base of the PFSS model, AR11419 is circled in red.

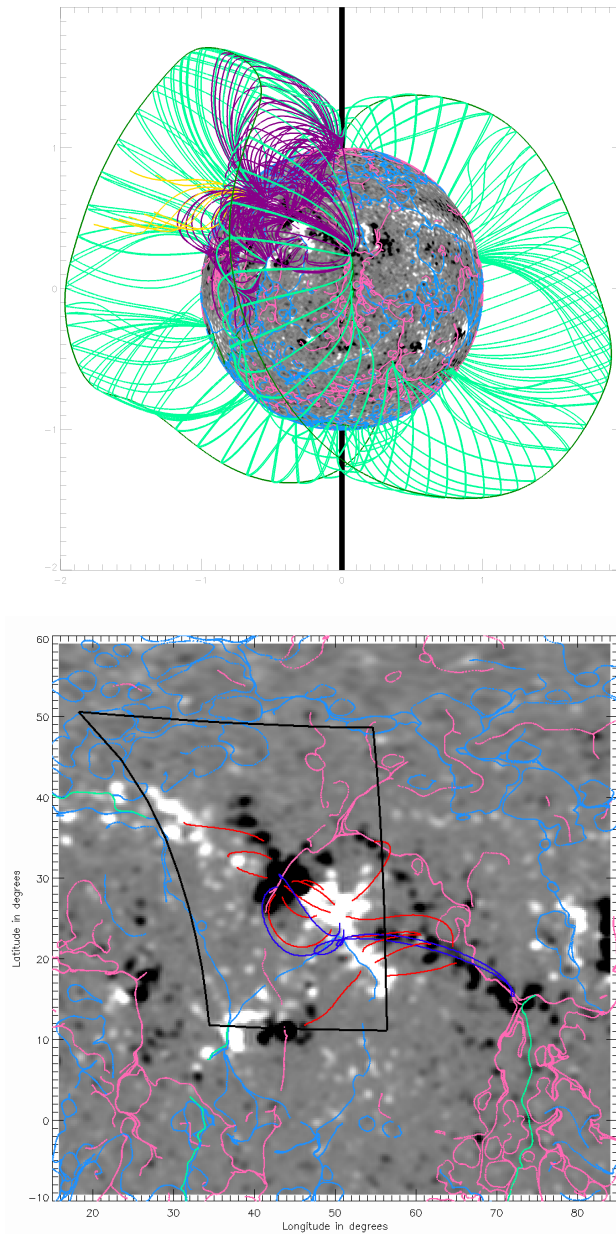


Figure 8.4: Top: 3D image of the PFSS extrapolation of the Sun from 17th February 2012. Field lines are traced from around AR11419. The green lines are field lines in the HCS, the yellow and purple lines are lines traced from the active region (yellow lines are open and purple lines are closed). The surface of the Sun is coloured with the radial component of the magnetic field. Bottom: Photospheric magnetic field from the PFSS extrapolation around AR11419. Light blue and light pink lines are the intersection of negative and positive separatrix surfaces, respectively, with the photosphere, light green lines are the intersection of the HCS curtains with the photosphere. Red lines are example field lines shorter than 300 Mm. Dark blue lines are example field lines longer than 300 Mm. Black box shows EIS field-of-view.

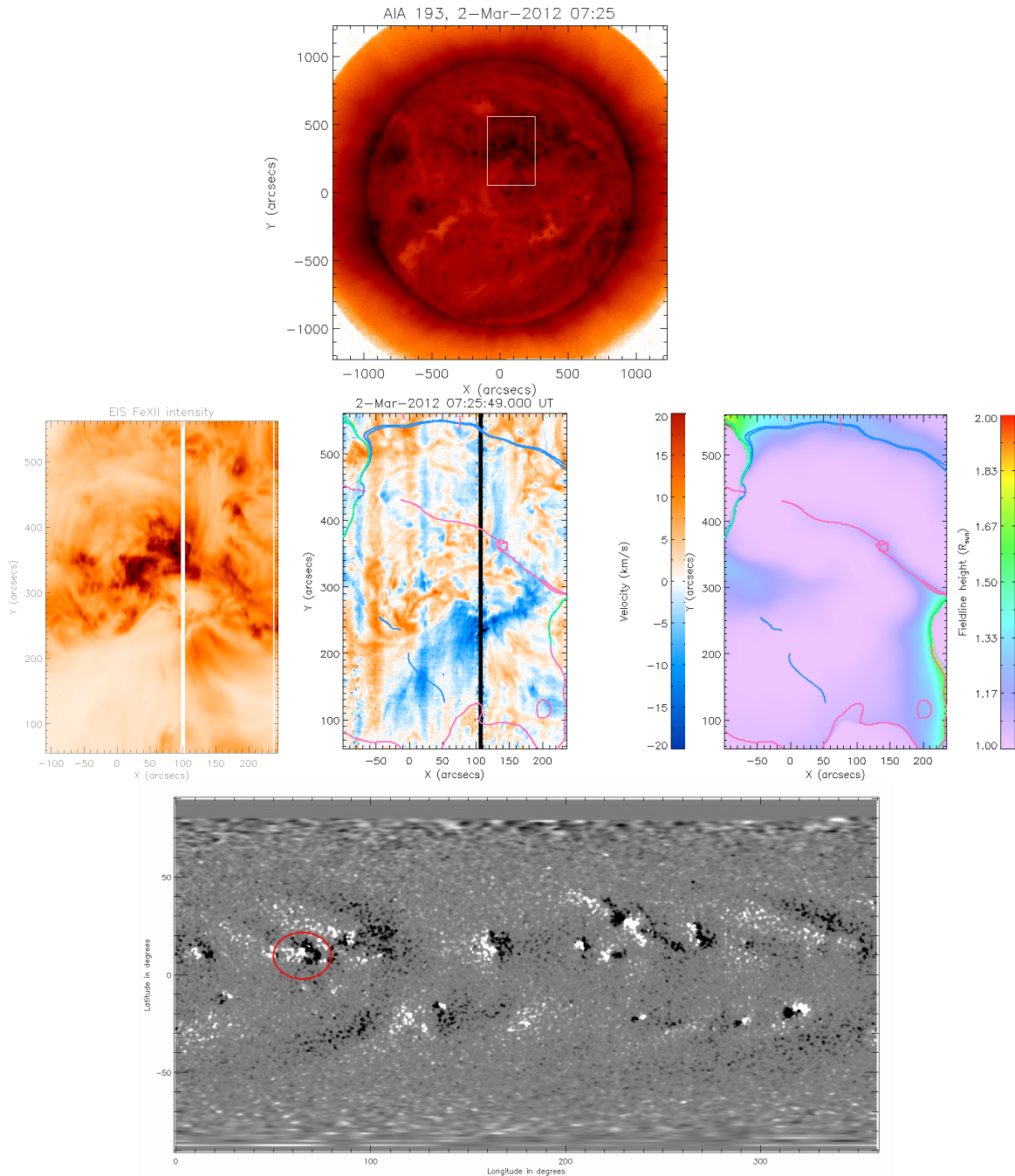


Figure 8.5: Top: AIA 193Å image on the 2nd March 2012 for active region AR11427. The white box shows the position of the EIS raster. Centre row: EIS FeXII intensity image, Doppler velocity map and map of heights reached by field lines. Over-plotted on the Doppler and field line height maps are the intersection of the separatrix surfaces with the photosphere, green: HCS curtains, blue: negative separatrix surfaces, pink: positive separatrix surfaces. Bottom: the radial component of the magnetic field at the base of the PFSS model, AR11427 is circled in red.

around the active region is plotted (Figure 8.5, centre row, right panel), it is possible to see that there is a patch of field lines to the south west of the active region that reach higher up into the atmosphere than the surrounding field lines (see Figure 8.5 centre row, right panel) and this is in roughly the same location as the upflow region. This could indicate that the upflow is flowing along large closed loops rather than providing an outflow into the solar wind or that the complex structure is not being well replicated in the potential field model.

Figure 8.6 (bottom) shows a selection of field lines over-plotted on a patch of the photospheric magnetic field at the base of the PFSS model from the 2nd March 2012. Closed field lines longer than 300Mm are coloured dark blue and shorter closed field lines are coloured red, the intersection of positive and negative separatrix surfaces and the HCS curtains with the photosphere are shown as pink, light blue and green lines, respectively. The longest field lines arch up near to the base of the heliospheric current sheet and either connect the two polarities of AR11427 or connect the negative polarity of AR11427 to a diffuse active region to the east of AR11427. The region where the strongest upflow is observed corresponds to where some of these large arching loops are anchored in the negative polarity of AR11427.

8.7 AR11445 - 28th March 2012

The next active region considered is AR11445 was observed on the 28th March and lies in the southern hemisphere. Figure 8.7 (bottom panel) shows the radial component of the magnetic field at the photosphere on this date with active region AR11445 circled in red. It lies to the south east of central meridian and is very close to another active region. No coronal holes were observed near AR11445 on the 28th March 2012 so we do not expect to find any large areas of open field in our PFSS model.

From the PFSS model, a short and narrow channel of open field is found to the North West of the active region. Open field lines from this channel are coloured yellow in Figure 8.8 and have foot points along the green line in Figure 8.7 (centre row, centre panel). This region of open field sits in the centre of the upflow region observed by EIS (Figure 8.7 centre row, centre panel). The field lines around the open-field channel reach high into the atmosphere before closing within AR11445 (if they are to the left of the open channel) or to a diffuse active region to the north (if they are to the right of the open channel). If the source surface in our PFSS model was lower or more non-potential effects were taken into account it is likely that a larger area of open field would be found which might encompass the whole of the observed upflow region. For this reason it is possible that a large proportion of the upflowing plasma identified by EIS might make it into the solar wind.

A sample set of field lines are traced to see their connections and their length. Figure 8.8 (bottom) shows a selection of field lines over-plotted on the radial magnetic-field map at the photosphere. The longest field lines (blue lines) have foot points close to the intersection of HCS curtains with the photosphere. Here also a blue shifted

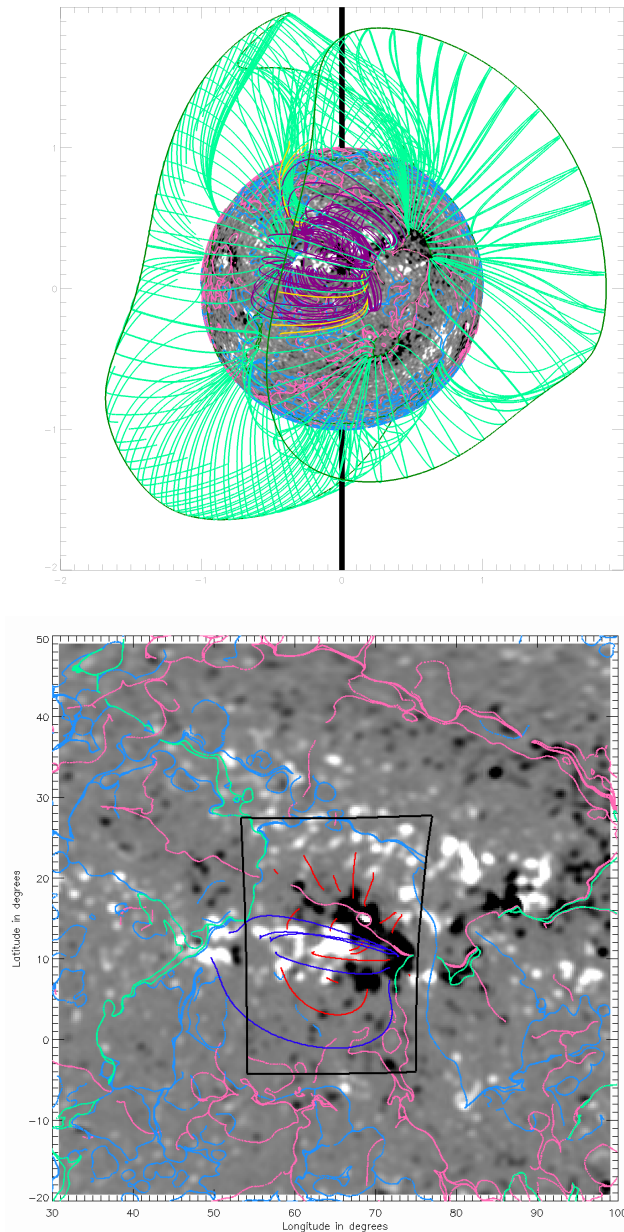


Figure 8.6: Top: 3D image of the PFSS extrapolation of the Sun from 2nd March 2012. Field lines are traced from around AR11427. The green lines are field lines in the HCS, the yellow and purple lines are lines traced from the active region (yellow lines are open and purple lines are closed). The surface of the Sun is coloured with the radial component of the magnetic field. Bottom: Photospheric magnetic field from the PFSS extrapolation around AR11427. Light blue and light pink lines are the intersection of negative and positive separatrix surfaces, respectively, with the photosphere, light green lines are the intersection of the HCS curtains with the photosphere. Red lines are example field lines shorter than 300 Mm. Dark blue lines are example field lines longer than 300 Mm. Black box shows EIS field-of-view.

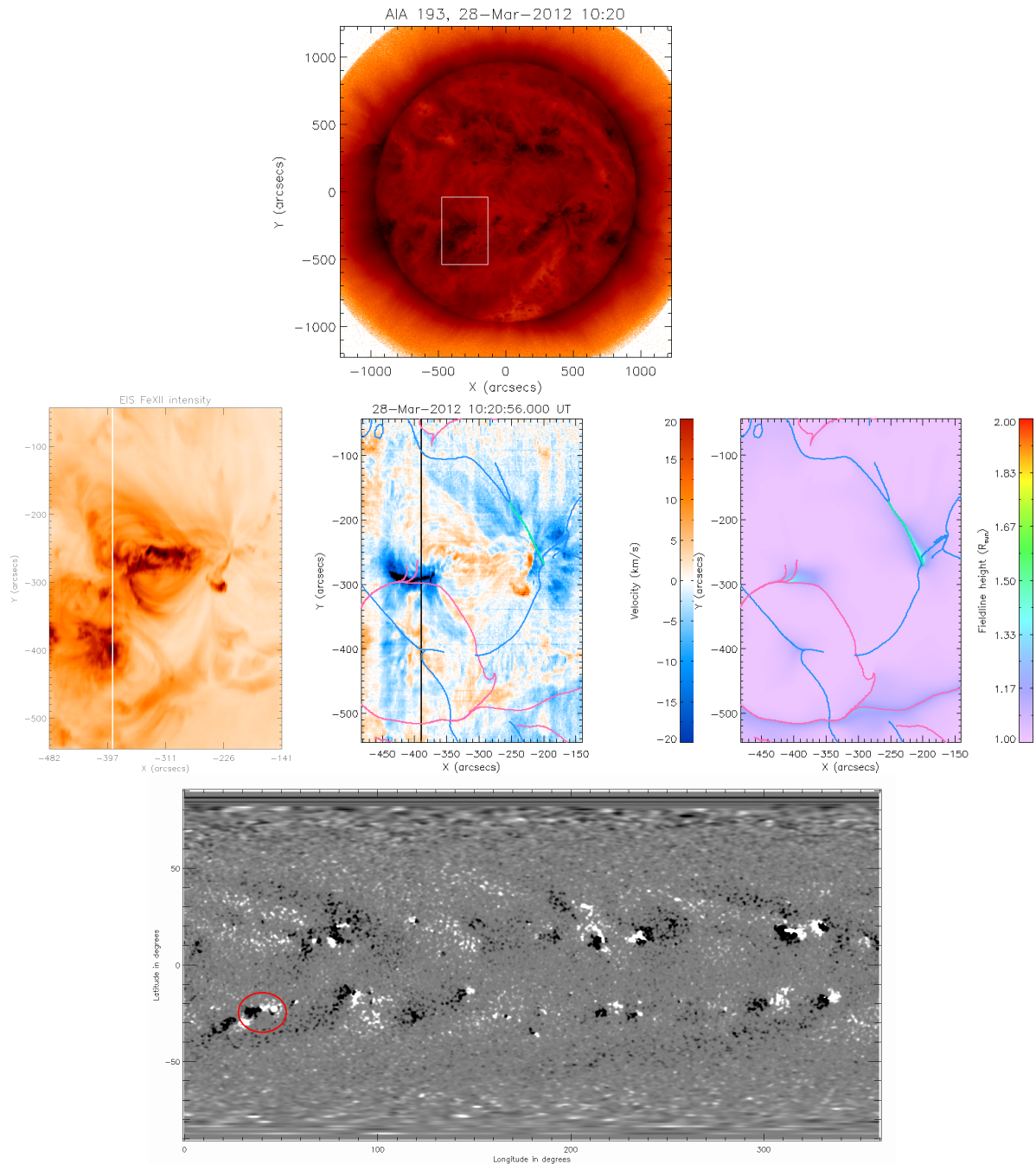


Figure 8.7: Top: AIA 193Å image on the 28th March 2012 for active region AR11445. The white box shows the position of the EIS raster. Centre row: EIS FeXII intensity image, Doppler velocity map and map of heights reached by field lines. Over-plotted on the Doppler and field line height maps are the intersection of the separatrix surfaces with the photosphere, green: HCS curtains, blue: negative separatrix surfaces, pink: positive separatrix surfaces. Bottom: the radial component of the magnetic field at the base of the PFSS model, AR11445 is circled in red.

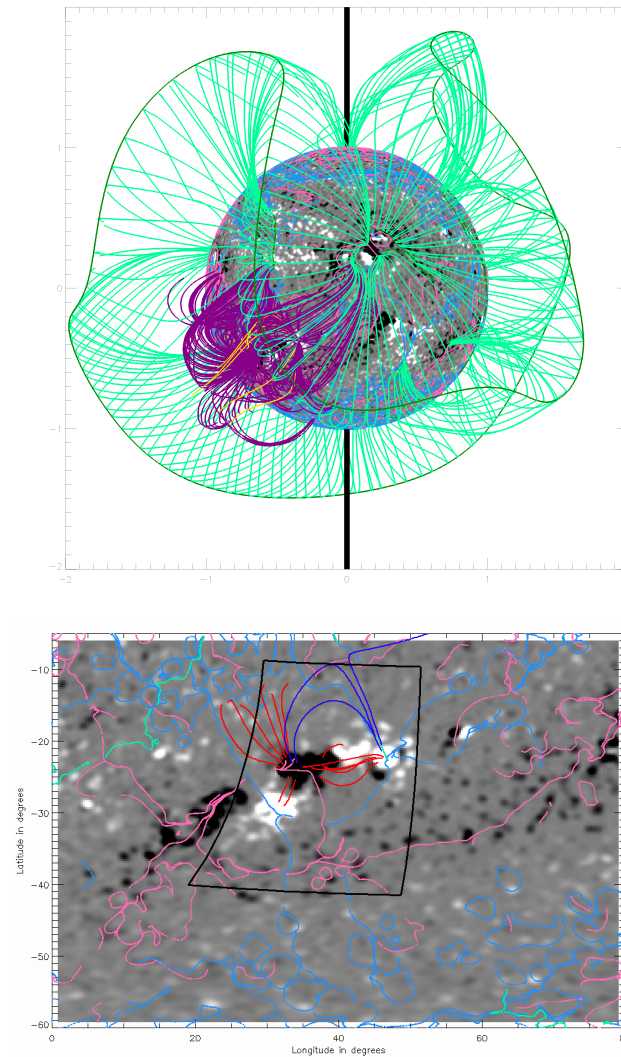


Figure 8.8: Top: 3D image of the PFSS extrapolation of the Sun from 28th March 2012. Field lines are traced from around AR11445. The green lines are field lines in the HCS, the yellow and purple lines are lines traced from the active region (yellow lines are open and purple lines are closed). The surface of the Sun is coloured with the radial component of the magnetic field. Bottom: Photospheric magnetic field from the PFSS extrapolation around AR11445. Light blue and light pink lines are the intersection of negative and positive separatrix surfaces, respectively, with the photosphere, light green lines are the intersection of the HCS curtains with the photosphere. Red lines are example field lines shorter than 300 Mm. Dark blue lines are example field lines longer than 300 Mm. Black box shows EIS field-of-view.

region is seen (Figure 8.7 centre row, centre panel). The field lines starting in the blue shifted region to the east of the active region are mostly under 300 Mm in length in our extrapolation (red lines in Figure 8.8 bottom).

8.8 AR11553 29th August 2012

On the 29th August 2012, AR11553 was visible to the south west of disc centre. This active region is circled in red in the radial photospheric magnetic field from HMI for this date Figure 8.9 (bottom) and outlined by the white box on the AIA 193 Å image in Figure 8.9 (top). The active region consists of a positive polarity region to the north west of a smaller negative polarity region. It has an orientation consistent with Joy’s Law and Hale’s Law. AR11553 lies between a large and diffuse active region to the west and the remnant negative polarity region of a decaying active region to the east. No coronal holes near AR11553 are observed so we would not expect any large open-field regions to be found in the PFSS extrapolation.

Two open-field regions near AR11553 are found in the PFSS model. These lie to the north west and south east of the active region. Open field lines (yellow) are traced from these two regions in Figure 8.10 (top). The foot-points of these field lines lie in red shaded regions plotted in Figure 8.9 (centre row, right panel). The PFSS open-field region to the north west does not line up with the upflow region observed by EIS and the open-field region to the south east occurs in a region where the EIS Doppler velocity data shows a red shift indicating a down flowing plasma.

The direction and length of a few sample field lines traced from the active region can be seen in Figure 8.10 (bottom). Open field lines (yellow lines) are found to the north-west and south-east of the active region and the longest field lines (blue lines) are found to be arching above the active region connecting the opposite-polarity regions of AR11553. This is to be expected since in Figure 8.10 (top) we have seen that the HCS (green line) runs parallel to the polarity inversion line in this active region and the associated HCS curtains touch down either side of the active region.

For this case it does seem that the observations of both locations of coronal holes and of upflows do not agree well with our PFSS model. We see that in the PFSS model at this time the HCS has split into three distinct loops (green lines Figure 8.10 top). It has been noted by others [Wang et al., 2014] that the HCS was observed as two loops for much of 2012 and these three loop structure imply there is even more complexity in the global coronal magnetic field. In such a complex field it is likely that many of the magnetic field structures will become twisted and hence it is unlikely that a potential field will accurately model the coronal magnetic field which is probably the cause of the discrepancy between the PFSS model and the observations.

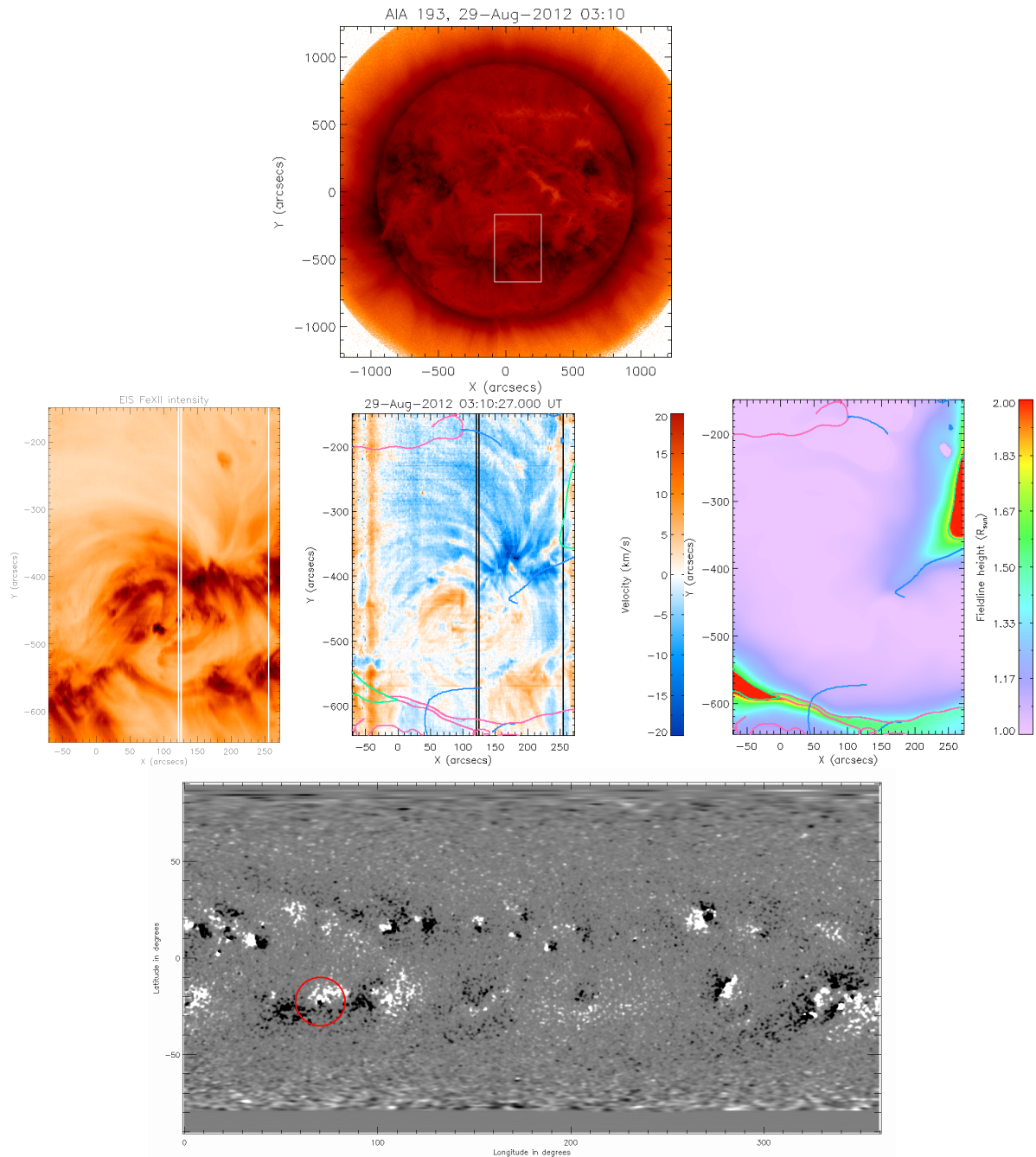


Figure 8.9: Top: AIA 193Å image on the 29th August 2012 for active region AR11553. The white box shows the position of the EIS raster. Centre row: EIS FeXII intensity image, Doppler velocity map and map of heights reached by field lines. Over-plotted on the Doppler and field line height maps are the intersection of the separatrix surfaces with the photosphere, green: HCS curtains, blue: negative separatrix surfaces, pink: positive separatrix surfaces. Bottom: the radial component of the magnetic field at the base of the PFSS model, AR11553 is circled in red.

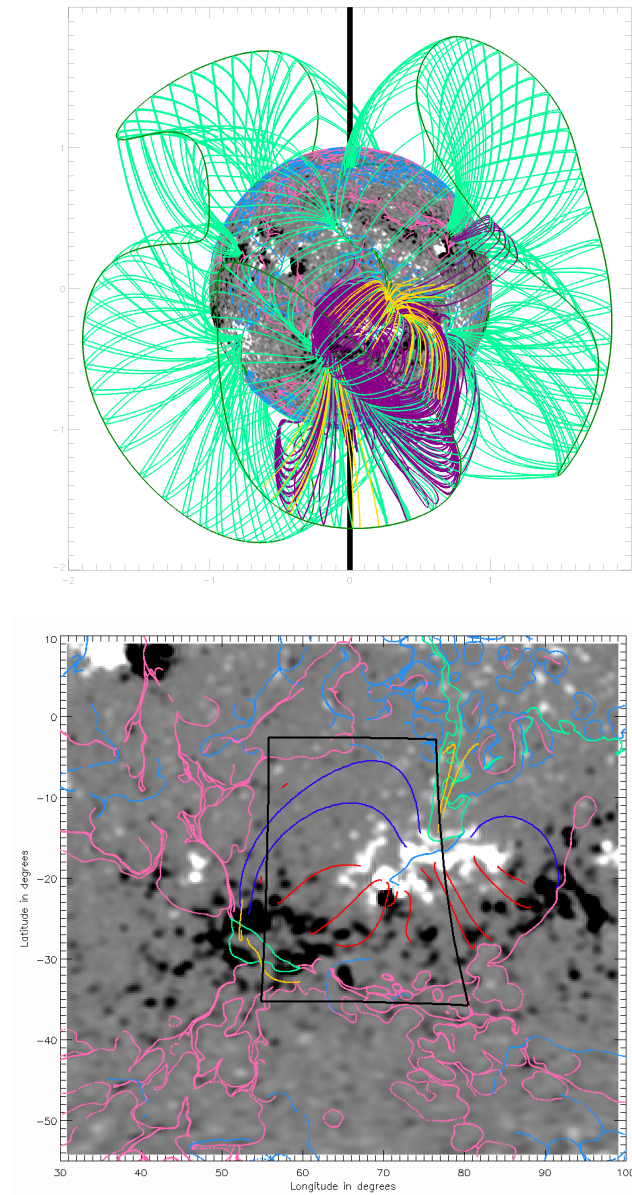


Figure 8.10: Top: 3D image of the PFSS extrapolation of the Sun from 29th August 2012. Field lines are traced from around AR11553. The green lines are field lines in the HCS, the yellow and purple lines are lines traced from the active region (yellow lines are open and purple lines are closed). The surface of the Sun is coloured with the radial component of the magnetic field. Bottom: Photospheric magnetic field from the PFSS extrapolation around AR11553. Light blue and light pink lines are the intersection of negative and positive separatrix surfaces, respectively, with the photosphere, light green lines are the intersection of the HCS curtains with the photosphere. Red lines are example field lines shorter than 300 Mm. Dark blue lines are example field lines longer than 300 Mm. Yellow lines are example open field lines. Black box shows EIS field-of-view.

8.9 AR11569 15th September 2012

On the 15th September 2012 a pair of active regions were visible to the south east of disc centre (see Figure 8.11 top). We examine the active region which is the closest to disc centre of this pair (AR11569) and is adjacent to a large coronal hole. This active region is circled in red on the photospheric magnetic field map in Figure 8.11, bottom.

Again we extrapolate the magnetic field in the corona by applying the PFSS model to the daily update synoptic magnetogram map from HMI. The HCS null-line found in the source surface of our PFSS model runs parallel to a photospheric polarity inversion line between the active region we are considering and another active region to the east (see Figure 8.12 top). This means that the HCS curtains map down to the photosphere leaving an area of open field to the west of the active region (yellow field lines in Figure 8.12 top and originating from the red area in Figure 8.11 centre row, right panel).

From the plot of the Doppler velocities (Figure 8.11 centre row, centre panel) we see upflow close to the intersection of a positive separatrix surface with the photosphere to the east of the active region. Field lines around this separatrix surface reach high up into the atmosphere: up to $1.2R_{\odot}$ which is approximately 140Mm above the photosphere. On the western side of the active region the PFSS extrapolation predicts open field, however, the Doppler velocities show a down flow. This may be due to the PFSS extrapolation not replicating the complex (non-potential) connections between active regions. The field line connections from these regions can be seen by tracing sample field lines with foot points in the active region (see Figure 8.12 bottom). The longest closed field lines begin in the west positive pole of the active region near to the open-field region (blue lines, Figure 8.12 bottom). These field lines lie close to the HCS curtain and so they reach high in the atmosphere and also map back down to the photosphere a long distance from their foot points.

8.10 AR11575 23rd September 2012

On the 23rd September, AR11575 was visible to the north east of disc centre (see the AIA full disc 193 Å image Figure 8.13 top). From the photospheric magnetic field from the HMI daily-update synoptic map we can see that there is a polarity-inversion line through the active region is oriented in the North-South direction. The active region is to the west of a cluster of smaller, weaker magnetic features than found in the active region itself (Figure 8.13 bottom panel).

The PFSS model extrapolated from the HMI daily update synoptic map suggests that there is a channel of open field running from the north east to the southern centre of the active region. This open-field region (yellow field lines in Figure 8.14 top) forms close to where two HCS curtains reach the photosphere very close to one another. Its location does not coincide with the location of the strongest upflow as observed from the EIS Doppler velocity plot (Figure 8.13 centre row, centre panel).

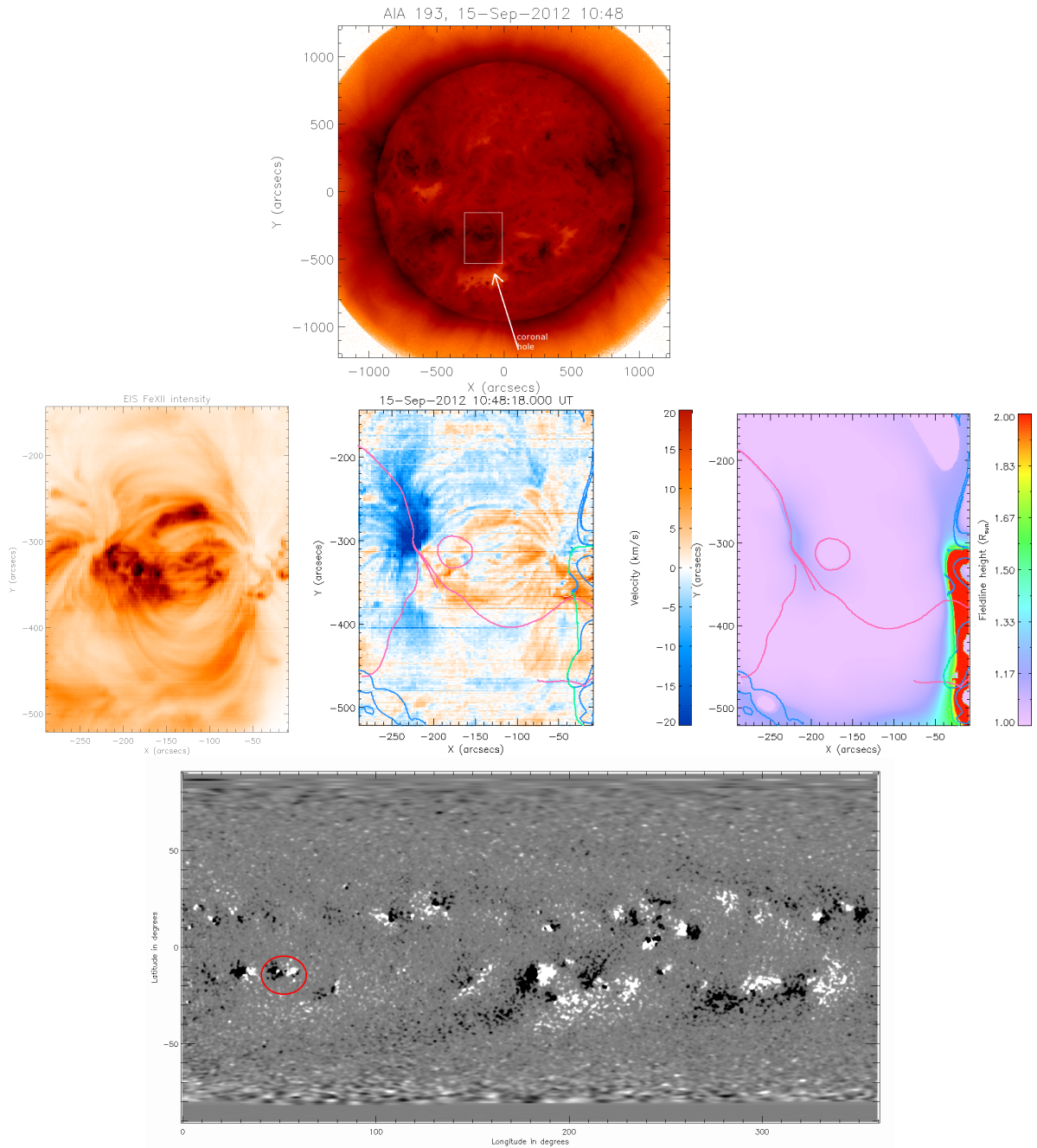


Figure 8.11: Top: AIA 193Å image on the 15th September 2012 for active region AR11569. The white box shows the position of the EIS raster. Centre row: EIS FeXII intensity image, Doppler velocity map and map of heights reached by field lines. Over-plotted on the Doppler and field line height maps are the intersection of the separatrix surfaces with the photosphere, green: HCS curtains, blue: negative separatrix surfaces, pink: positive separatrix surfaces. Bottom: the radial component of the magnetic field at the base of the PFSS model, AR11569 is circled in red.

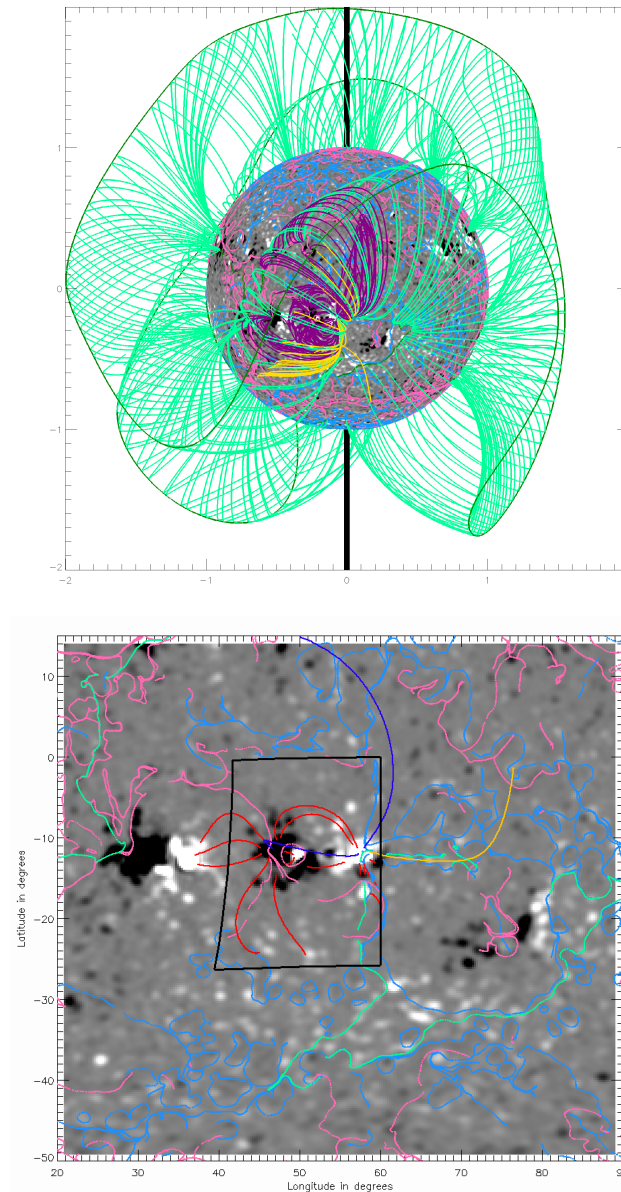


Figure 8.12: Top: 3D image of the PFSS extrapolation of the Sun from 15th September 2012. Field lines are traced from around AR11569. The green lines are field lines in the HCS, the yellow and purple lines are lines traced from the active region (yellow lines are open and purple lines are closed). The surface of the Sun is coloured with the radial component of the magnetic field. Bottom: Photospheric magnetic field from the PFSS extrapolation around AR11569. Light blue and light pink lines are the intersection of negative and positive separatrix surfaces, respectively, with the photosphere, light green lines are the intersection of the HCS curtains with the photosphere. Red lines are example field lines shorter than 300 Mm. Dark blue lines are example field lines longer than 300 Mm. Yellow lines are example open field lines. Black box shows EIS field-of-view.

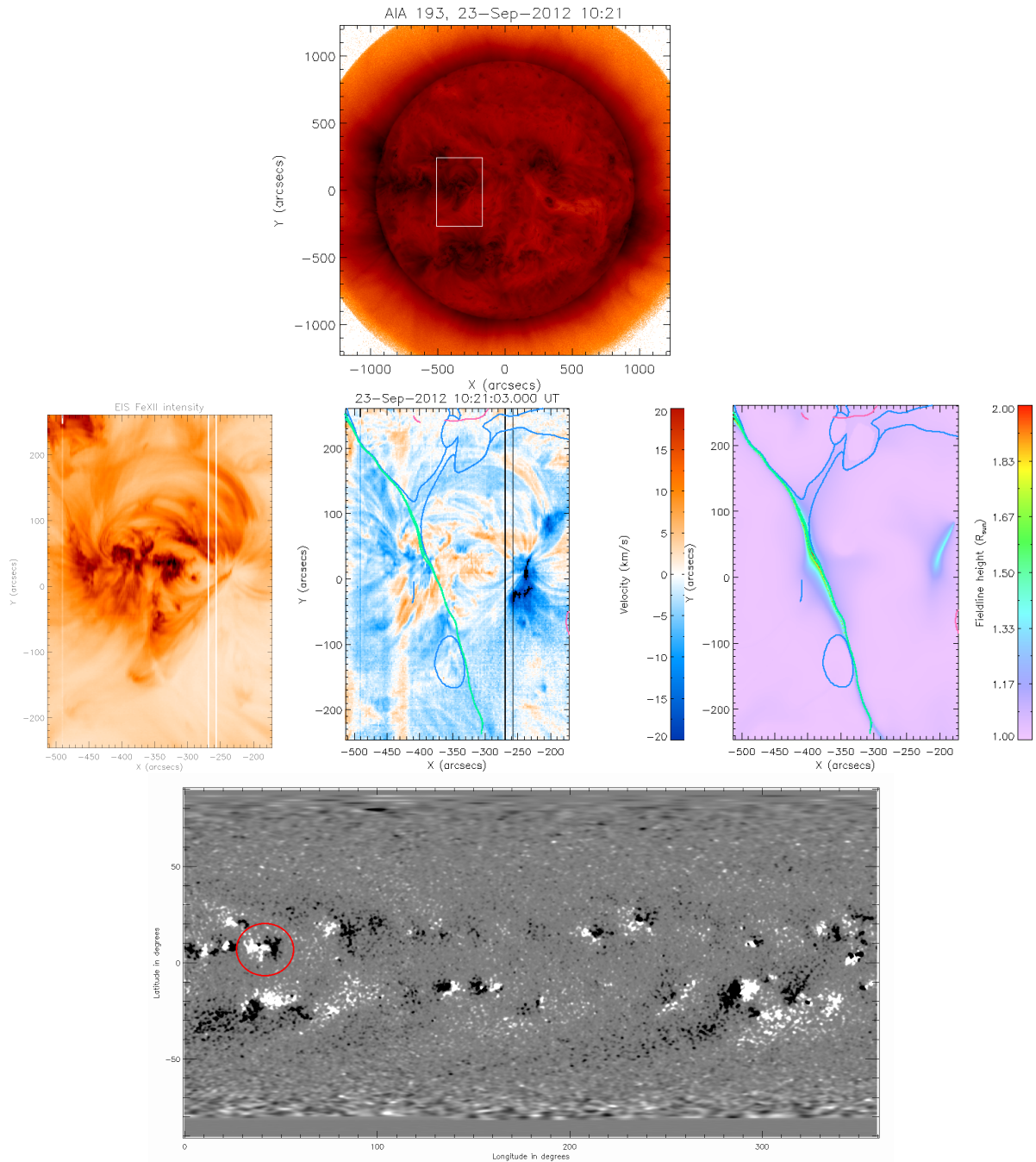


Figure 8.13: Top: AIA 193Å image on the 23rd September 2012 for active region AR11575. The white box shows the position of the EIS raster. Centre row: EIS FeXII intensity image, Doppler velocity map and map of heights reached by field lines. Over-plotted on the Doppler and field line height maps are the intersection of the separatrix surfaces with the photosphere, green: HCS curtains, blue: negative separatrix surfaces, pink: positive separatrix surfaces. Bottom: the radial component of the magnetic field at the base of the PFSS model, AR11575 is circled in red.

Figure 8.13 (centre row right panel) shows the heights reached by field lines from the PFSS model. From this plot, we see that there is a small group of field lines that reach high into the corona at approximately the same location as the observed upflow. Note, though that if a lower source surface had been used in the PFSS extrapolation then it is probable that the upflow region west of the active region could be associated with open field and thus be a region of outflow into the solar wind.

The field lines mapped from the east of the open-field channel are very far reaching (blue lines in Figure 8.14 bottom) with foot points far from the active region, but the field lines mapped from the west of the open field channel close back down to the photosphere within the active region, giving much shorter loop lengths (red lines in Figure 8.14 bottom).

8.11 Discussion and Conclusions

A potential field extrapolation provides a first approximation of the magnetic field around an active region as, in such a region, current accumulations and plasma effects are likely to have an impact on the magnetic field structure. With that in mind, we draw some conclusions about the relationship between observed regions of plasma upflows within active regions with extrapolated PFSS magnetic field configurations of the global corona.

In this study, we considered observations from EIS of upflows from seven active region in the rise phase of cycle 24 and compared then to PFSS extrapolations from HMI daily-update synoptic magnetic field maps.

It is clear from our results that not all plasma upflows are sources of the solar wind. Many of the upflowing plasma sites appear to be associated with field lines that form large loop structures that either reach high into the atmosphere or reach far across the solar surface (or both). However, there are also regions with long extended loops that do not coincide with upflows.

Our active region studies also suggest that, in most cases, the intersection of large (global) separatrix surfaces (as predicted by the PFSS extrapolations) with the photosphere occur within the upflow region. This is in agreement with Baker et al. [2009] who found that upflow regions are threaded by QSLs. By applying the separatrix-surface finding method [Haynes and Parnell, 2010] we have found that in some cases the upflow regions correspond to the locations of separatrix surfaces. Therefore, it is likely that the layers of high squashing factor that were found by Baker et al. [2009] to thread upflow regions are associated with topological separatrix surfaces as opposed to geometric features in the magnetic field.

Our results from this potential-field study suggest that, out of all upflow sites, only a small portion contain open-field regions and thus are associated with the solar wind. The best example we have is the AR11271 from the 21st August 2011. This active region also happened to be beside a coronal hole (as observed in the AIA 171 Å full-disc image). Previous work comparing observed upflow regions to global magnetic

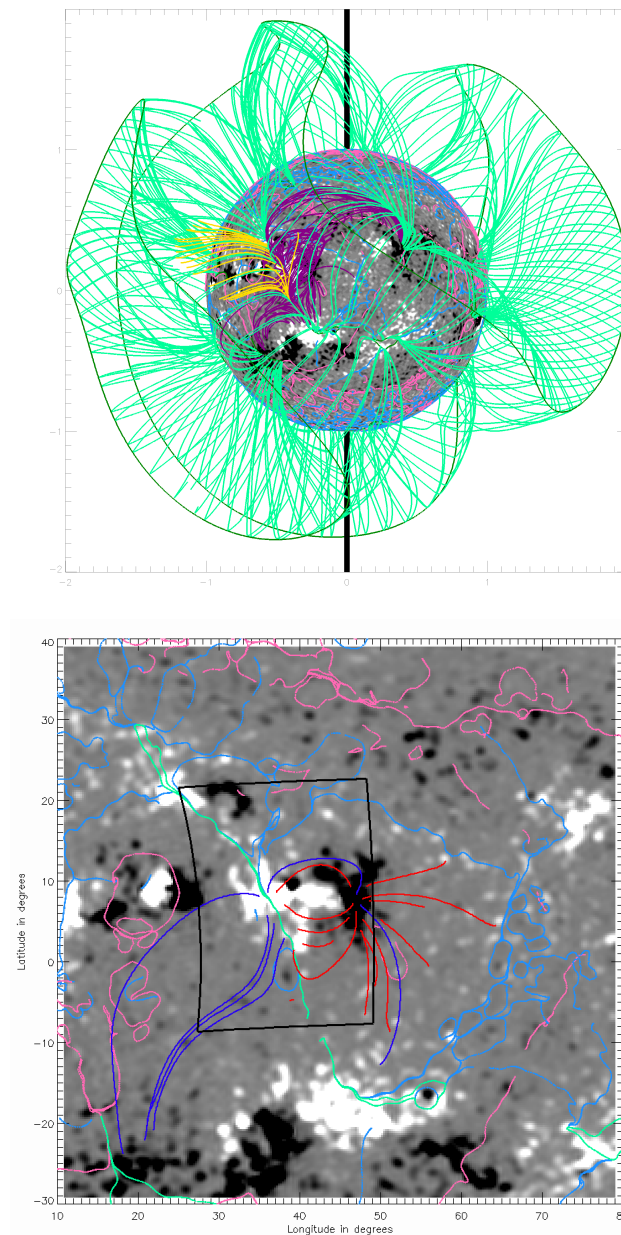


Figure 8.14: Top: 3D image of the PFSS extrapolation of the Sun from 23rd September 2012. Field lines are traced from around AR11575. The green lines are field lines in the HCS, the yellow and purple lines are lines traced from the active region (yellow lines are open and purple lines are closed). The surface of the Sun is coloured with the radial component of the magnetic field. Bottom: Photospheric magnetic field from the PFSS extrapolation around AR11575. Light blue and light pink lines are the intersection of negative and positive separatrix surfaces, respectively, with the photosphere, light green lines are the intersection of the HCS curtains with the photosphere. Red lines are example field lines shorter than 300 Mm. Dark blue lines are example field lines longer than 300 Mm. Yellow lines are example open field lines. Black box shows EIS field-of-view.

field structures by van Driel-Gesztelyi et al. [2012] examined two active regions either side of a coronal hole. They found that the upflowing plasma regions corresponded to the locations of open field. Thus by only including examples that are in close proximity to a coronal hole the results of a study on the association of upflows and open field may become skewed. The only other example we have that is adjacent to a coronal hole is AR11569 on the 15th September 2012. However, in this case the upflow does not correlate with the open field found in the PFSS model.

It is therefore difficult to say whether some particular conditions in AR11271 on the 21st August 2011 enabled the field to become open in the same location as the upflow for this case or if its favourable observational conditions (located almost exactly at disc centre) allowed us to better model it using a PFSS extrapolation from a daily synoptic map. To further this study it would be advantageous to automate the process of comparing open-field regions(as predicted by a PFSS model) to observed plasma outflows and in this way undertake a statistical study of a much greater number of active regions.

The main problem we have encountered in trying to discover the relationship between open-field regions and plasma upflows around active regions is that the potential field model is not valid where the magnetic field becomes twisted and currents build up. This is the case around active regions and so, in order to get a proper idea about this, non-potential effects need to be taken into account. In particular, the use of a high-resolution non-linear force-free field model instead of a PFSS model would greatly improve the results.

Chapter 9

Summary and Future Work

This thesis has investigated the global solar corona through potential field source surface extrapolations from observed magnetograms. These extrapolations of the global magnetic field have then allowed us to study the topology of the resulting fields in terms of the magnetic skeleton.

The main conclusion we have to draw from this work is that the coronal magnetic field topology, even from a simple potential field extrapolation, is incredibly complicated. In Chapter 4 PFSS extrapolations were produced from a relatively low-resolution magnetogram and still a magnetic skeleton containing a complex web of many separators was formed. We found that the complexity varied throughout the solar cycle with more low-lying small scale features at cycle minimum and more large high-altitude features at cycle maximum.

9.1 Topological Configurations and Cycle Variations

Understanding the magnetic skeleton of a magnetic field is very important for understanding how the field lines are connected in 3D space. It enables us to find sites that could be important for magnetic reconnection and also breaks the field down into its building blocks allowing us to find all the features without tracing all the field lines in the domain.

In Chapter 3 various different simple topological configurations were considered and classified. We described well established topological features such as the separatrix dome and separatrix curtain as well as exploring variations on these like the separatrix cave and the separatrix tunnel. Separatrix curtains are separatrix surfaces that reach out into interplanetary space which, in our case, means up to the source surface. These curtains can be classified as closed if they connect at both ends to the HCS and open if they do not. Closed separatrix curtains are a type of structure that could be associated with a pseudostreamer.

Chapter 4 identified two different types of global solar minimum topology and one

type of global solar maximum topology. The topology of solar maximum is characterised by a warped Heliospheric Current Sheet (HCS) which means the open-field regions move away from the poles and open field occupies a much smaller proportion of the solar surface. During solar minima, the characteristics of the global magnetic topology depend on the strength of the global magnetic dipole. During the last minimum (between cycles 23 and 24) the global dipole was weak and in the previous two minima the global dipole was strong. When there is a strong global dipole at solar minimum the HCS is not very warped and sits close to the equator, there are few null points high up in the atmosphere and few separatrix curtains. On the other hand, when the global dipole is weak, null points that are associated with weak field regions can form higher in the atmosphere and their separatrix surfaces can form closed separatrix curtains which divide open field regions of the same polarity.

In Chapter 5 the work from the previous two chapters was brought together as we provided a method for classifying particular topological structures such as isolated domes and double caves. We found that the numbers of isolated domes varies out of phase with the solar cycle whereas, when we considered the number of isolated domes with open spines we see that their numbers peak during the decline phase of each cycle. In this chapter we also investigate the global separator network and draw a map of the connections of all the separators and null points. We find that at solar maximum and during the weak dipole solar minimum there is usually only one large connected network of null points and that this is connected to the HCS null line. We find that networks not connected to the HCS null line are relatively rare and complex clusters not connected to the HCS null line are only seen during a strong dipole solar minimum.

In Chapter 6 the differences between the global coronal magnetic skeleton from low-resolution and high-resolution SOLIS extrapolations were investigated. It was found that there was more complexity both on small-scales (low-altitude null points) and on large scales (closed separatrix curtains) in the high-resolution extrapolation than the low-resolution extrapolation. The extra closed curtains that form in the high-resolution extrapolation that are not present in the low-resolution extrapolation all form very close to existing closed separatrix curtains in the low-resolution extrapolation. This means that the global topology looks similar in both the high-resolution and low-resolution cases.

9.1.1 Future work

To continue this study one next step would be to take the separator networks as found in Chapter 5 and classify structures that are connected to the HCS null line. So far in this thesis, we have only been able to classify types of linear networks that are not connected to the HCS. However, using only the information we have about the separator networks, it should be possible to classify almost all topological configurations that can be found in a potential field.

It would be good to continue the study into the long term trends in topological

structures into the future. In particular, it would be interesting to see if the next minimum follows the same trends as the cycle 23/24 minimum or is more like the cycle 21/22 and 22/23 minima. In particular, it would be good to study the global topological structure of the magnetic field including the separator network through multiple cycles for high-resolution extrapolations, such as those from SOLIS or a combination of MDI and HMI.

9.2 Null point statistics

As well as high-resolution SOLIS data we also have extrapolations from MDI and HMI synoptic magnetograms that are also at a high-resolution. Chapter 7 investigated the distribution of null points in these high-resolution extrapolations, giving particular attention to the PFSS extrapolations from MDI synoptic magnetograms. Many previous studies have looked at the distribution of null points, particularly above regions of quiet sun and we sought to add to this body of work by looking at the distribution of nulls in the entire corona. It is found that the number of null points above 10Mm falls off as a power law with $\alpha_{pow} = 2.36$ for solar maximum and $\alpha_{pow} = 2.87$ for solar minimum. This is in close agreement with the relation found by Longcope and Parnell [2009].

It is found that the distribution of null points with latitude varies over time with the majority of the null points found forming away from active regions and forming over the quiet-sun field.

Through a study of a extrapolations from SOLIS, HMI and MDI synoptic magnetograms from the the same Carrington rotation, we find that the distribution of null points in all three data sets is very similar.

9.2.1 Future work

There are many improvements and additions we could make to our study of the prevalence of null points in the solar atmosphere. First, if we could get a higher-resolution in the synoptic maps we could resolve the locations of null points closer to the solar surface. In this way we would be able to directly compare with the results found by others who studied the distribution of null points on a much smaller scale.

In Chapter 7 we briefly considered the distribution of null points depending on the photospheric magnetic field directly below them. This could be examined more closely using all of the MDI data instead of just a single frame.

9.3 Active region topology

The final study in this thesis considered the global coronal topology extrapolated from HMI daily synoptic maps and compared with observations of upflows around active regions. Seven cases were considered from 2011 and 2012 in the rise phase of cycle 24

and it was found that open field predicted by the PFSS model does not always line up with the locations of strong upflows. In many instances it is the case that upflows occur around separatrix surfaces and long field lines that are high-reaching or are very long, connecting between active regions rather than within active regions. However, the potential nature of the extrapolated field made it difficult to approximate well the magnetic field close to the active regions.

9.3.1 Future Work

The main improvement that could be made in this study would be to use a more complex field than a PFSS extrapolation. In active regions the magnetic field is often very complex and twisted which we are not able to determine from our extrapolations. To use a high-resolution non-linear force-free model would greatly improve the validity of our results.

Bibliography

- H. Alfvén. On the existence of electromagnetic-hydrodynamic waves. *Ark. Mat. Astron. Fys.*, 29(2):1–7, 1943.
- M. D. Altschuler and G. Newkirk. Magnetic Fields and the Structure of the Solar Corona. I: Methods of Calculating Coronal Fields. *Solar Phys.*, 9:131–149, September 1969. doi: 10.1007/BF00145734.
- S. K. Antiochos, C. R. DeVore, and J. A. Klimchuk. A Model for Solar Coronal Mass Ejections. *Astrophys. J.*, 510:485–493, January 1999. doi: 10.1086/306563.
- S. K. Antiochos, C. R. DeVore, J. T. Karpen, and Z. Mikić. Structure and Dynamics of the Sun’s Open Magnetic Field. *Astrophys. J.*, 671:936–946, December 2007. doi: 10.1086/522489.
- S. K. Antiochos, Z. Mikić, V. S. Titov, R. Lionello, and J. A. Linker. A Model for the Sources of the Slow Solar Wind. *Astrophys. J.*, 731:112, April 2011. doi: 10.1088/0004-637X/731/2/112.
- M. J. Aschwanden. *Physics of the Solar Corona. An Introduction with Problems and Solutions (2nd edition)*. Springer, December 2005.
- G. Aulanier, E. E. DeLuca, S. K. Antiochos, R. A. McMullen, and L. Golub. The Topology and Evolution of the Bastille Day Flare. *Astrophys. J.*, 540:1126–1142, September 2000. doi: 10.1086/309376.
- G. Aulanier, L. Golub, E. E. DeLuca, J. W. Cirtain, R. Kano, L. L. Lundquist, N. Narukage, T. Sakao, and M. A. Weber. Slipping Magnetic Reconnection in Coronal Loops. *Science*, 318:1588–, December 2007. doi: 10.1126/science.1146143.
- H. D. Babcock. The Sun’s Polar Magnetic Field. *Astrophys. J.*, 130:364, September 1959. doi: 10.1086/146726.
- H. W. Babcock. The Topology of the Sun’s Magnetic Field and the 22-YEAR Cycle. *Astrophys. J.*, 133:572, March 1961. doi: 10.1086/147060.
- D. Baker, L. van Driel-Gesztelyi, C. H. Mandrini, P. Démoulin, and M. J. Murray. Magnetic Reconnection along Quasi-separatrix Layers as a Driver of Ubiquitous

- Active Region Outflows. *Astrophys. J.*, 705:926–935, November 2009. doi: 10.1088/0004-637X/705/1/926.
- P. J. Baum and A. Bratenahl. Flux linkages of bipolar sunspot groups - A computer study. *Solar Phys.*, 67:245–258, September 1980. doi: 10.1007/BF00149805.
- G. Baumann, K. Galsgaard, and Å. Nordlund. 3D Solar Null Point Reconnection MHD Simulations. *Solar Phys.*, 284:467–487, June 2013. doi: 10.1007/s11207-012-0168-5.
- C. Beveridge and D. W. Longcope. On Three-Dimensional Magnetic Skeleton Elements Due to Discrete Flux Sources. *sp*, 227:193–206, April 2005. doi: 10.1007/s11207-005-2558-4.
- L. Biermann. Kometenschweife und solare Korpuskularstrahlung. *ZAp*, 29:274, 1951.
- L. Biermann. Solar corpuscular radiation and the interplanetary gas. *The Observatory*, 77:109–110, June 1957.
- D. H. Brooks and H. P. Warren. Establishing a Connection Between Active Region Outflows and the Solar Wind: Abundance Measurements with EIS/Hinode. *Astrophys. J.*, 727:L13, January 2011. doi: 10.1088/2041-8205/727/1/L13.
- M. E. Burton, N. U. Crooker, G. L. Siscoe, and E. J. Smith. A test of source-surface model predictions of heliospheric current sheet inclination. *J. Geophys. Res.*, 99: 1–9, January 1994. doi: 10.1029/93JA02100.
- R. C. Carrington. Description of a Singular Appearance seen in the Sun on September 1, 1859. *Mon. Not. Roy. Astron. Soc.*, 20:13–15, November 1859.
- J. Clerk Maxwell. A dynamical theory of the electromagnetic field. *Phil. Trans. R. Soc. Lond.*, 155, January 1865. doi: 10.1098/rstl.1865.0008.
- R. M. Close, C. E. Parnell, and E. R. Priest. Separators in 3D Quiet-Sun Magnetic Fields. *Solar Phys.*, 225:21–46, November 2004. doi: 10.1007/s11207-004-3259-0.
- R. M. Close, C. E. Parnell, and E. R. Priest. Domain structures in complex 3D magnetic fields. *Geophysical and Astrophysical Fluid Dynamics*, 99:513–534, 2005. doi: 10.1080/03091920500410520.
- I. Contopoulos, C. Kalapotharakos, and M. K. Georgoulis. Nonlinear Force-Free Reconstruction of the Global Solar Magnetic Field: Methodology. *Sol. Phys.*, 269: 351–365, April 2011. doi: 10.1007/s11207-011-9713-x.
- G. R. Cook, D. H. Mackay, and D. Nandy. Solar Cycle Variations of Coronal Null Points: Implications for the Magnetic Breakout Model of Coronal Mass Ejections. *Astrophys. J.*, 704:1021–1035, October 2009. doi: 10.1088/0004-637X/704/2/1021.

- S. W. H. Cowley. A qualitative study of the reconnection between the Earth's magnetic field and an interplanetary field of arbitrary orientation. *Radio Sci.*, 8:903–913, 1973.
- I. J. D. Craig, R. B. Fabling, S. M. Henton, and G. J. Rickard. An Exact Solution for Steady State Magnetic Reconnection in Three Dimensions. *Astrophys. J. Lett.*, 455:L197, December 1995. doi: 10.1086/309822.
- N. U. Crooker, G. L. Siscoe, S. Shodhan, D. F. Webb, J. T. Gosling, and E. J. Smith. Multiple heliospheric current sheets and coronal streamer belt dynamics. *J. Geophys. Res.*, 98:9371–9381, June 1993. doi: 10.1029/93JA00636.
- N. U. Crooker, S. K. Antiochos, X. Zhao, and M. Neugebauer. Global network of slow solar wind. *Journal of Geophysical Research (Space Physics)*, 117:A04104, April 2012. doi: 10.1029/2011JA017236.
- J. L. Culhane, L. K. Harra, A. M. James, K. Al-Janabi, L. J. Bradley, R. A. Chaudry, K. Rees, J. A. Tandy, P. Thomas, M. C. R. Whillock, B. Winter, G. A. Doschek, C. M. Korendyke, C. M. Brown, S. Myers, J. Mariska, J. Seely, J. Lang, B. J. Kent, B. M. Shaughnessy, P. R. Young, G. M. Simnett, C. M. Castelli, S. Mahmoud, H. Mapson-Menard, B. J. Probyn, R. J. Thomas, J. Davila, K. Dere, D. Windt, J. Shea, R. Hagood, R. Moye, H. Hara, T. Watanabe, K. Matsuzaki, T. Kosugi, V. Hansteen, and Ø. Wikstol. The EUV Imaging Spectrometer for Hinode. *Solar Phys.*, 243:19–61, June 2007. doi: 10.1007/s01007-007-0293-1.
- G. Del Zanna, G. Aulanier, K.-L. Klein, and T. Török. A single picture for solar coronal outflows and radio noise storms. *Astron. Astrophys.*, 526:A137, February 2011. doi: 10.1051/0004-6361/201015231.
- E. E. Deluca and P. A. Gilman. *The solar dynamo*, pages 275–303. 1991.
- P. Démoulin, E. R. Priest, and D. P. Lonie. Three-dimensional magnetic reconnection without null points 2. Application to twisted flux tubes. *J. Geophys. Res.*, 101: 7631–7646, April 1996. doi: 10.1029/95JA03558.
- M. L. DeRosa, C. J. Schrijver, and G. Barnes. Topology of Coronal Fields from Potential Field Models. In *AAS/Solar Physics Division Abstracts #42*, page 1810, May 2011.
- C. R. DeVore and S. K. Antiochos. Homologous Confined Filament Eruptions via Magnetic Breakout. *Astrophys. J.*, 680:740–756, June 2008. doi: 10.1086/588011.
- G. A. Doschek, H. P. Warren, J. T. Mariska, K. Muglach, J. L. Culhane, H. Hara, and T. Watanabe. Flows and Nonthermal Velocities in Solar Active Regions Observed with the EUV Imaging Spectrometer on Hinode: A Tracer of Active Region Sources of Heliospheric Magnetic Fields? *Astrphys. J.*, 686:1362–1371, October 2008. doi: 10.1086/591724.

- C. Downs, I. I. Roussev, B. van der Holst, N. Lugaz, I. V. Sokolov, and T. I. Gombosi. Toward a Realistic Thermodynamic Magnetohydrodynamic Model of the Global Solar Corona. *Astrophys. J.*, 712:1219–1231, April 2010. doi: 10.1088/0004-637X/712/2/1219.
- J. A. Eddy. The Maunder Minimum. *Science*, 192:1189–1202, June 1976. doi: 10.1126/science.192.4245.1189.
- X. Feng, C. Jiang, C. Xiang, X. Zhao, and S. T. Wu. A Data-driven Model for the Global Coronal Evolution. *Astrophys. J.*, 758:62, October 2012. doi: 10.1088/0004-637X/758/1/62.
- K. Galsgaard, E. R. Priest, and Å Nordlund. Three-dimensional separator reconnection - How does it occur? *Solar Phys.*, 193:1–16, 2000.
- E. G. Gibson. The quiet sun. *NASA Special Publication*, 303, 1973.
- R. G. Giovanelli. A Theory of Chromospheric Flares. *Nature*, 158:81–82, July 1946. doi: 10.1038/158081a0.
- J. D. Haigh. The Sun and the Earth’s Climate. *Living Reviews in Solar Physics*, 4:2, October 2007. doi: 10.12942/lrsp-2007-2.
- G. E. Hale, F. Ellerman, S. B. Nicholson, and A. H. Joy. The Magnetic Polarity of Sun-Spots. *Astrophys. J.*, 49:153, April 1919. doi: 10.1086/142452.
- L. K. Harra, T. Sakao, C. H. Mandrini, H. Hara, S. Imada, P. R. Young, L. van Driel-Gesztelyi, and D. Baker. Outflows at the Edges of Active Regions: Contribution to Solar Wind Formation? *Astrophys. J. Lett.*, 676:L147–L150, April 2008. doi: 10.1086/587485.
- D. H. Hathaway. The Solar Cycle. *Living Reviews in Solar Physics*, 7:1, March 2010. doi: 10.12942/lrsp-2010-1.
- A. L. Haynes and C. E. Parnell. A trilinear method for finding null points in a three-dimensional vector space. *Physics of Plasmas*, 14(8):082107, August 2007. doi: 10.1063/1.2756751.
- A. L. Haynes and C. E. Parnell. A method for finding three-dimensional magnetic skeletons. *Physics of Plasmas*, 17(9):092903, September 2010. doi: 10.1063/1.3467499.
- M. Hesse and K. Schindler. A theoretical foundation of general magnetic reconnection. *J. Geophys. Res.*, 93:5559–5567, June 1988. doi: 10.1029/JA093iA06p05559.
- R. Hodgson. On a curious Appearance seen in the Sun. *Mon. Not. Roy. Astron. Soc.*, 20:15–16, November 1859.

- R. A. Howard and M. J. Koomen. Observation of sectorized structure in the outer solar corona - Correlation with interplanetary magnetic field. *Sol. Phys.*, 37:469–475, August 1974. doi: 10.1007/BF00152504.
- F. Hoyle. *Some recent researches in solar physics*. 1949.
- Y.-T. Lau and J. M. Finn. Three-dimensional kinematic reconnection in the presence of field nulls and closed field lines. *Astrophys. J.*, 350:672–691, February 1990. doi: 10.1086/168419.
- C. O. Lee, J. G. Luhmann, J. T. Hoeksema, X. Sun, C. N. Arge, and I. de Pater. Coronal Field Opens at Lower Height During the Solar Cycles 22 and 23 Minimum Periods: IMF Comparison Suggests the Source Surface Should Be Lowered. *Solar Phys.*, 269:367–388, April 2011. doi: 10.1007/s11207-010-9699-9.
- R. Lionello, J. A. Linker, and Z. Mikić. Multispectral Emission of the Sun During the First Whole Sun Month: Magnetohydrodynamic Simulations. *Astrophys. J.*, 690:902–912, January 2009. doi: 10.1088/0004-637X/690/1/902.
- D. W. Longcope and I. Klapper. A General Theory of Connectivity and Current Sheets in Coronal Magnetic Fields Anchored to Discrete Sources. *Astrophys. J.*, 579:468–481, November 2002. doi: 10.1086/342750.
- D. W. Longcope and C. E. Parnell. The Number of Magnetic Null Points in the Quiet Sun Corona. *Sol. Phys.*, 254:51–75, January 2009. doi: 10.1007/s11207-008-9281-x.
- Dana W. Longcope. Topological methods for the analysis of solar magnetic fields. *Living Reviews in Solar Physics*, 2(7), 2005. doi: 10.12942/lrsp-2005-7. URL <http://www.livingreviews.org/lrsp-2005-7>.
- D. H. Mackay and A. A. van Ballegoijen. Models of the Large-Scale Corona. I. Formation, Evolution, and Liftoff of Magnetic Flux Ropes. *Astrophys. J.*, 641: 577–589, April 2006. doi: 10.1086/500425.
- Duncan Mackay and Anthony Yeates. The sun’s global photospheric and coronal magnetic fields: Observations and models. *Living Reviews in Solar Physics*, 9(6), 2012. URL <http://www.livingreviews.org/lrsp-2012-6>.
- C. H. Mandrini, P. Démoulin, L. van Driel-Gesztelyi, B. Schmieder, G. Cauzzi, and A. Hofmann. 3D Magnetic Reconnection at an X-Ray Bright Point. *Solar Phys.*, 168:115–133, September 1996. doi: 10.1007/BF00145829.
- E. Marsch, H. Tian, J. Sun, W. Curdt, and T. Wiegmann. Plasma Flows Guided by Strong Magnetic Fields in the Solar Corona. *Astrophys. J.*, 685:1262–1269, October 2008. doi: 10.1086/591038.

- S. Masson, E. Pariat, G. Aulanier, and C. J. Schrijver. The Nature of Flare Ribbons in Coronal Null-Point Topology. *Astrophys. J.*, 700:559–578, July 2009. doi: 10.1088/0004-637X/700/1/559.
- S. Masson, G. Aulanier, E. Pariat, and K.-L. Klein. Interchange Slip-Running Reconnection and Sweeping SEP Beams. *Solar Phys.*, 276:199–217, February 2012. doi: 10.1007/s11207-011-9886-3.
- E. W. Maunder. Spoerer’s law of zones. *The Observatory*, 26:329–330, August 1903.
- N. Meyer-Vernet. *Basics of the Solar Wind*. Cambridge University Press, January 2007.
- M. J. Murray, D. Baker, L. van Driel-Gesztelyi, and J. Sun. Outflows at the Edges of an Active Region in a Coronal Hole: A Signature of Active Region Expansion? *Solar Phys.*, 261:253–269, February 2010. doi: 10.1007/s11207-009-9484-9.
- M. Neugebauer and C. W. Snyder. Solar Plasma Experiment. *Science*, 138:1095–1097, December 1962. doi: 10.1126/science.138.3545.1095-a.
- M. J. Owens and M. Lockwood. Cyclic loss of open solar flux since 1868: The link to heliospheric current sheet tilt and implications for the Maunder Minimum. *Journal of Geophysical Research (Space Physics)*, 117:A04102, April 2012. doi: 10.1029/2011JA017193.
- M. J. Owens, N. U. Crooker, and M. Lockwood. Solar origin of heliospheric magnetic field inversions: Evidence for coronal loop opening within pseudostreamers. *Journal of Geophysical Research (Space Physics)*, 118:1868–1879, May 2013. doi: 10.1002/jgra.50259.
- O. Panasenco and M. Velli. Pseudostreamers and Twin Filaments in the Solar Corona. In *American Astronomical Society Meeting Abstracts #220*, volume 220 of *American Astronomical Society Meeting Abstracts*, page 202.12, May 2012.
- E. N. Parker. Dynamics of the Interplanetary Gas and Magnetic Fields. *apj*, 128:664, November 1958. doi: 10.1086/146579.
- E. N. Parker. Dynamical Properties of Stellar Coronas and Stellar Winds. III. The Dynamics of Coronal Streamers. *Astrophys. J.*, 139:690, February 1964. doi: 10.1086/147795.
- C. E. Parnell, J. M. Smith, T. Neukirch, and E. R. Priest. The structure of three-dimensional magnetic neutral points. *Physics of Plasmas*, 3, 1996.
- C. E. Parnell, A. L. Haynes, and K. Galsgaard. Structure of magnetic separators and separator reconnection. *J. Geophys. Res.*, 115(A14):2102, 2010.

- D. I. Pontin, E. R. Priest, and K. Galsgaard. On the Nature of Reconnection at a Solar Coronal Null Point above a Separatrix Dome. *Astrophys. J.*, 774:154, September 2013. doi: 10.1088/0004-637X/774/2/154.
- E. Priest and T. Forbes. *Magnetic Reconnection*. June 2000.
- E. R. Priest. *Solar Magnetohydrodynamics*. D. Reidel Publishing Company, 1982.
- E. R. Priest and P. Démoulin. Three-dimensional magnetic reconnection without null points. 1. Basic theory of magnetic flipping. *J. Geophys. Res.*, 100:23443–23464, December 1995. doi: 10.1029/95JA02740.
- E. R. Priest and V. S. Titov. Magnetic Reconnection at Three-Dimensional Null Points. *Royal Society of London Philosophical Transactions Series A*, 354:2951–2992, December 1996. doi: 10.1098/rsta.1996.0136.
- E. R. Priest, D. P. Lonie, and V. S. Titov. Bifurcations of magnetic topology by the creation or annihilation of null points. *Journal of Plasma Physics*, 56:507, December 1996. doi: 10.1017/S0022377800019449.
- L. A. Rachmeler, S. J. Platten, C. Bethge, D. B. Seaton, and A. R. Yeates. Observations of a Hybrid Double-streamer/Pseudostreamer in the Solar Corona. *Astrophys. J. Lett.*, 787:L3, May 2014. doi: 10.1088/2041-8205/787/1/L3.
- S. Régnier, C. E. Parnell, and A. L. Haynes. A new view of quiet-Sun topology from Hinode/SOT. *Astron. Astrophys.*, 484:L47–L50, June 2008. doi: 10.1051/0004-6361:200809826.
- P. Riley, J. A. Linker, Z. Mikić, R. Lionello, S. A. Ledvina, and J. G. Luhmann. A Comparison between Global Solar Magnetohydrodynamic and Potential Field Source Surface Model Results. *Astrophys. J.*, 653:1510–1516, December 2006. doi: 10.1086/508565.
- T. Sakao, R. Kano, N. Narukage, J. Kotoku, T. Bando, E. E. DeLuca, L. L. Lundquist, S. Tsuneta, L. K. Harra, Y. Katsukawa, M. Kubo, H. Hara, K. Matsuzaki, M. Shimajo, J. A. Bookbinder, L. Golub, K. E. Korreck, Y. Su, K. Shibasaki, T. Shimizu, and I. Nakatani. Continuous Plasma Outflows from the Edge of a Solar Active Region as a Possible Source of Solar Wind. *Science*, 318:1585–, December 2007. doi: 10.1126/science.1147292.
- K. H. Schatten, J. M. Wilcox, and N. F. Ness. A model of interplanetary and coronal magnetic fields. *Solar Phys.*, 6:442–455, March 1969. doi: 10.1007/BF00146478.
- K. Schindler, M. Hesse, and J. Birn. General magnetic reconnection, parallel electric fields, and helicity. *J. Geophys. Res.*, 93:5547–5557, June 1988. doi: 10.1029/JA093iA06p05547.

- C. J. Schrijver and A. M. Title. The topology of a mixed-polarity potential field, and inferences for the heating of the quiet solar corona. *Solar Phys.*, 207:223–240, June 2002. doi: 10.1023/A:1016295516408.
- M. Schwabe. Sonnenbeobachtungen im Jahre 1843. Von Herrn Hofrath Schwabe in Dessau. *Astronomische Nachrichten*, 21:233, February 1844.
- V. Slemzin, L. Harra, A. Urnov, S. Kuzin, F. Goryaev, and D. Berghmans. Signatures of Slow Solar Wind Streams from Active Regions in the Inner Corona. *Solar Phys.*, 286:157–184, August 2013. doi: 10.1007/s11207-012-0004-y.
- L. Thornton. *Small-scale Magnetic Features observed by SoHO/MDI and Hinode/SOT*. PhD thesis, University of St Andrews, 2010.
- V. S. Titov. Generalized Squashing Factors for Covariant Description of Magnetic Connectivity in the Solar Corona. *Astrophys. J.*, 660:863–873, May 2007. doi: 10.1086/512671.
- V. S. Titov, E. R. Priest, and P. Demoulin. Conditions for the appearance of "bald patches" at the solar surface. *aa*, 276:564, September 1993.
- V. S. Titov, Z. Mikic, J. A. Linker, and R. Lionello. 1997 May 12 Coronal Mass Ejection Event. I. A Simplified Model of the Preeruptive Magnetic Structure. *Astrophys. J.*, 675:1614–1628, March 2008. doi: 10.1086/527280.
- V. S. Titov, Z. Mikić, J. A. Linker, R. Lionello, and S. K. Antiochos. Magnetic Topology of Coronal Hole Linkages. *The Astrophysical Journal*, 731:111, April 2011. doi: 10.1088/0004-637X/731/2/111.
- V. S. Titov, Z. Mikic, T. Török, J. A. Linker, and O. Panasenco. 2010 August 1-2 Sympathetic Eruptions. I. Magnetic Topology of the Source-surface Background Field. *Astrophys. J.*, 759:70, November 2012. doi: 10.1088/0004-637X/759/1/70.
- Ilya G. Usoskin. A history of solar activity over millennia. *Living Reviews in Solar Physics*, 10(1), 2013. doi: 10.12942/lrsp-2013-1. URL <http://www.livingreviews.org/lrsp-2013-1>.
- A. A. van Ballegoijen, N. P. Cartledge, and E. R. Priest. Magnetic Flux Transport and the Formation of Filament Channels on the Sun. *Astrophys. J.*, 501:866, July 1998. doi: 10.1086/305823.
- A. A. van Ballegoijen, E. R. Priest, and D. H. Mackay. Mean Field Model for the Formation of Filament Channels on the Sun. *Astrophys. J.*, 539:983–994, August 2000. doi: 10.1086/309265.

- L. van Driel-Gesztelyi, J. L. Culhane, D. Baker, P. Démoulin, C. H. Mandrini, M. L. DeRosa, A. P. Rouillard, A. Opitz, G. Stenborg, A. Vourlidas, and D. H. Brooks. Magnetic Topology of Active Regions and Coronal Holes: Implications for Coronal Outflows and the Solar Wind. *Solar Phys.*, 281:237–262, November 2012. doi: 10.1007/s11207-012-0076-8.
- Y.-M. Wang, N. R. Sheeley, Jr., and N. B. Rich. Coronal Pseudostreamers. *Astrophys. J.*, 658:1340–1348, April 2007. doi: 10.1086/511416.
- Y.-M. Wang, E. Robbrecht, and N. R. Sheeley, Jr. On the Weakening of the Polar Magnetic Fields during Solar Cycle 23. *Astrophys. J.*, 707:1372, December 2009. doi: 10.1088/0004-637X/707/2/1372.
- Y.-M. Wang, R. Grappin, E. Robbrecht, and N. R. Sheeley, Jr. On the Nature of the Solar Wind from Coronal Pseudostreamers. *Astrophys. J.*, 749:182, April 2012. doi: 10.1088/0004-637X/749/2/182.
- Y.-M. Wang, P. R. Young, and K. Muglach. Evidence for Two Separate Heliospheric Current Sheets of Cylindrical Shape During Mid-2012. *Astrophys. J.*, 780:103, January 2014. doi: 10.1088/0004-637X/780/1/103.
- T. Wiegmann. Computing Nonlinear Force-Free Coronal Magnetic Fields in Spherical Geometry. *Sol. Phys.*, 240:227–239, February 2007. doi: 10.1007/s11207-006-0266-3.
- A. R. Winebarger, E. E. DeLuca, and L. Golub. Apparent Flows above an Active Region Observed with the Transition Region and Coronal Explorer. *Astrophys. J. Lett.*, 553:L81–L84, May 2001. doi: 10.1086/320496.
- A. R. Yeates and D. H. Mackay. Chirality of High-latitude Filaments over Solar Cycle 23. *Astrophys. J. Lett.*, 753:L34, July 2012. doi: 10.1088/2041-8205/753/2/L34.
- Q. M. Zhang, P. F. Chen, Y. Guo, C. Fang, and M. D. Ding. Two Types of Magnetic Reconnection in Coronal Bright Points and the Corresponding Magnetic Configuration. *Astrophys. J.*, 746:19, February 2012. doi: 10.1088/0004-637X/746/1/19.

*"The sun has gone to bed and so must I. So long, farewell, auf wiedersehen,
goodbye."*

- Gretl, The Sound of Music